UNIVERSITÀ DEGLI STUDI DI TRIESTE

XXXIII CICLO DEL DOTTORATO DI RICERCA IN

Scienze della Terra, Meccanica dei Fluidi e Matematica Interazioni e Metodiche

PO FRIULI VENEZIA GIULIA – FONDO SOCIALE EUROPEO 2014/2020

LITHOSPHERIC STRUCTURE AND TECTONIC EVOLUTION OF INTRACRATONIC BASINS: THE CONGO BASIN A NATURAL LABORATORY

SSD: GEO/10

DOTTORANDA

Francesca Maddaloni

COORDINATORE

PROF. Stefano Maset

FIRMA

SUPERVISORE DI TESI

PROF. Carla Braitenberg

FIRMA

CO-SUPERVISORE DI TESI

PROF. Magdala Tesauro

FIRMA

ANNO ACCADEMICO 2019/2020

"...Going up that river was like traveling back to the earliest beginnings of the world, when vegetation rioted on the earth and the big trees were kings. An empty stream, a great silence, an impenetrable forest. The air was warm, thick, heavy, and sluggish. There was no joy in the brilliance of sunshine. The long stretches of the waterway ran on, deserted, into the gloom of overshadowed distances."

(Joseph Conrad – Heart of Darkness)

Contents

Abstract

The aim of this thesis is to identify the tectonic processes that lead to the long-term topography variations of the cratonic areas that contain the memory of the past deformation. These areas are the intracratonic basins (*ICBs*), which are usually very large basins, characterized by long-term subsidence. Among them, the Congo Basin (*CB*) occupies a large part of the Congo Craton, derived from the amalgamation of different cratonic pieces. The *CB* is a typical intracratonic basin, due its slow and long-lived subsidence history and the largely unknown formation mechanisms. It recorded the history of deposition of up to one billion years of sediments, above a metamorphic basement, one of the longest geological records on Earth. Thus, it can be considered a natural laboratory, suitable to achieve the objectives of my thesis project. To improve our knowledge on the interplay between shallow and deep tectonic processes, which lead to the formation of the *CB*, I first reconstructed the stratigraphy and depths of the main seismic horizons of the basin, using geological and exploration geophysical data. The results revealed that the *CB* formed very probably as a failed rift in late Mesoproterozoic (about 1200 Myr) and evolved during the Neoproterozoic and Phanerozoic, under the influence of far-field compressional tectonic events, global climate fluctuations, between icehouse and greenhouse conditions, and drifting of Central Africa through the South Pole towards its present-day equatorial position. These events caused the migration over time of the sedimentary depocenters within the central part of the basin (Cuvette Centrale). Afterwards, I analyzed gravity data, using the seismic data and density of sedimentary samples as constraints, in order to investigate the shallow crustal structure of the basin. The results lead to the identification of the continuity of the *NW-SE* oriented tectonic structures and of small basins in areas uncovered by seismic data. From the analysis of the gravity anomalies, I could further hypothesize the location of high-density crustal bodies, likely related to the extensional tectonics of the *CB*. Using all the knowledge acquired during the previous analyses, I tested the hypothesis of the formation of the *CB* as multi-extensional rift in a cratonic area, through 3D numerical simulations, based on a finite difference approach. The results reproduce the first order heterogeneities characterizing the *CB* basement depth, in particular a series of small basins and highs, aligned along a preferential direction, within a large topographic depression. The results of the numerical models were used to implement forward gravity models, which I compared with the observed gravity field. Such a comparison shows a similarity between the trends of the modelled and observed gravity anomalies, likely related to the density and topography variations produced by the extensional tectonics. The obtained results can be considered as benchmarks for further studies on the long-term evolutions of the continental interiors.

CHAPTER 1

- Introduction -

1.0 Introduction of the chapter

In this chapter, I give an overview of the current knowledge of the Congo Basin (*CB*) in terms of the geodynamics of the basin, based on the geological and geophysical studies carried out since the '50s. The chapter is partly based on Delvaux et al. (2021), in which I contributed by writing the manuscript.

1.1 Scope of the thesis

The thesis aims to contribute to the understanding the processes that drive the long-term evolution of the tectonic plate interiors. The most suitable areas to reach this aim are the parts of cratons overlaid by a long record of sedimentary deposition. These areas, named intracratonic basins (*ICBs*), contain the memory of the processes that are responsible for the past deformation. The *ICBs* are usually large basins (they can reach the order of million km^2), circular or oval in plan view, characterized by continental, limnic or shallow marine sediments (Hartley and Allen, 1994). They have been moving downwards (i.e. subsiding) over long periods (typically >200 Myr), but despite their longevity they are characterized by very low subsidence rates (20-30 m/Myr). Subsidence curves of *ICBs* are at first sight similar to those of sea floor subsidence, approximately exponential in shape, as the cooling plate moves away from the oceanic spreading centers. However, they lack a rapid initial tectonic subsidence phase and have much longer decay constants (Hartley and Allen, 1994; Allen and Armitage, 2012). These deviations from idealized thermal subsidence are more pronounced than passive margins ones. These suggest that *ICBs* experienced periods of tectonic reactivation (Hartley and Allen, 1994; Allen and Armitage, 2012). The formation and evolution of the *ICBs* is commonly related to stresses induced by plate tectonics (e.g., Lithgow-Bertelloni and Gurnis, 1997). In addition, local tectonic events and intraplate heterogeneities may have also influenced their subsidence (Korsch and Lindsay, 1989). Hence, the sedimentary record of *ICBs* reflects the imprints of this complex (and still not understood) interaction between their lithospheric structure and global/local tectonic events. Starting from these considerations, I chose as a study area the Congo Basin (*CB*), which represents a natural laboratory, where I can reach the objectives of my thesis project. Indeed, the *CB* is one of the greatest *ICBs* and has been repeatedly reactivated by extensional and compressional tectonic events, determining the deposition of a thick sedimentary cover (up to ~9 km), during about one billion years.

1.2 Thesis outline

This section summarizes the outline of this thesis work, describing the main steps of the research and the methodology used (Fig. 1.1).

Chapter 1 – Introduction

In this chapter, I give an overview on the previous geological and geophysical studies and current knowledge of the geodynamics of the *CB*.

Chapter 2 – Exploration geophysics, stratigraphy and 3D model of sediments

In this chapter, I implemented a 3D model of sediments in terms of thickness and depth of the stratigraphic layers composing the *CB*, in order to identify its mechanisms of formation and evolution. The results were obtained during my first year of my *PhD* project, in which I spent two months in Belgium, at the Royal Museum of Central Africa (*RMCA*, Tervuren). The data that I used to reconstruct the stratigraphy and tectonic evolution of the *CB* are reflection and refraction seismic profiles, borehole, and field data. In particular, at *RMCA*, I interpreted about 2600 km of seismic reflection profiles, well-log data, located inside the central part of the *CB* (named "Cuvette Centrale"), analyzed the rock samples from drilling cores, and revised the existing literature. The results consist in the review of the previous sismostratigraphic model and reconstruction of the basement depth and main seismic horizons, as well as in the interpretation of the spatial-temporal evolution of the *CB* in the frame of the geodynamics of the entire African continent, during the last 1.2 billion years.

Chapter 3 – Potential field analysis

In this chapter, I used the available aeromagnetic and gravity data to delineate the main structures of the basement and overlying sedimentary deposits and to investigate the shallow crustal structure of the *CB*. The gravity analyses give me also the chance to reconstruct the basement depth in areas between the seismic reflection profiles, suppressing the artefacts produced by the interpolation of uneven seismic data distribution (Chapter 2). To this aim, I first used the isopach maps of the sedimentary sequences (Chapter 2) and their densities obtained from representative core samples (currently located at the *RMCA*) to calculate the gravity effect of sediments. In this way, I could separate the effects of the sediments from that of the underlying shallow crust in the residuals obtained from the regression analysis between the topography and Bouguer anomalies. Therefore, I inverted the gravity residuals, corrected for the effect of the shallow crust, for the basement depths, using the seismic data as constraints, and two different density contrasts between the shallowest sedimentary layer and crystalline basement. The results evidence *NW-SE* trending structures, also revealed by magnetic and seismic data, corresponding to the alternation of highs and sediments filled topographic depressions. I noticed also a good consistency between the seismic and gravity basements along the seismic profiles. On the other hand, the analyses of the gravity residuals related to the shallow crust, evidence the possible presence of high-density bodies in some parts of the basin, related to the first phase of extension.

Chapter 4 – 3D Numerical Modelling

In this chapter, the data and results obtained in the first part of my *PhD* project have been used as input for numerical simulations on the formation of the *CB*. I performed seven numerical models, using the thermomechanical *I3ELVIS* code, developed by *ETH-Zurich*, where I spent four months during my second year of the *PhD*. The initial rift phases, affecting the *CB* formation, were first simulated using four cratonic blocks, representing the different pieces composing the Congo Craton, surrounded by not cratonic lithosphere. Other numerical tests were carried out considering a single cratonic area with a circular weak zone in the central part, representing the suture zone between the different cratonic pieces. The numerical models were

run applying extensional divergent velocities of 2.5 mm/yr for each side, acting in East-West and North-South direction. I tested the influence of different parameters (size of cratons and weak zones, continental geotherm, lithospheric thickness outside the cratonic areas) on the extensional deformation produced by the multidirectional velocities. The resulting surface topographies show a series of highs and lows inside a central depressed area, quite consistent with those observed from the seismic basements variations. Among all the numerical tests performed, I chose the two models that are apparently more consistent with the results obtained from the analysis of the geological and geophysical data, as input for forward gravity models. The modelled gravity signal, induced by the multi-extensional tectonics, was compared with the observed gravity field, giving the chance to validate the results of the numerical simulations performed.

Chapter 5 – What does the Congo Basin tell us?

In this final chapter, I present a discussion on the possible tectonic processes that initiated the subsidence of the *CB*, comparing the results obtained during my *PhD* project with those of previous studies. I also present the main conclusions and give an outlook for future researches.

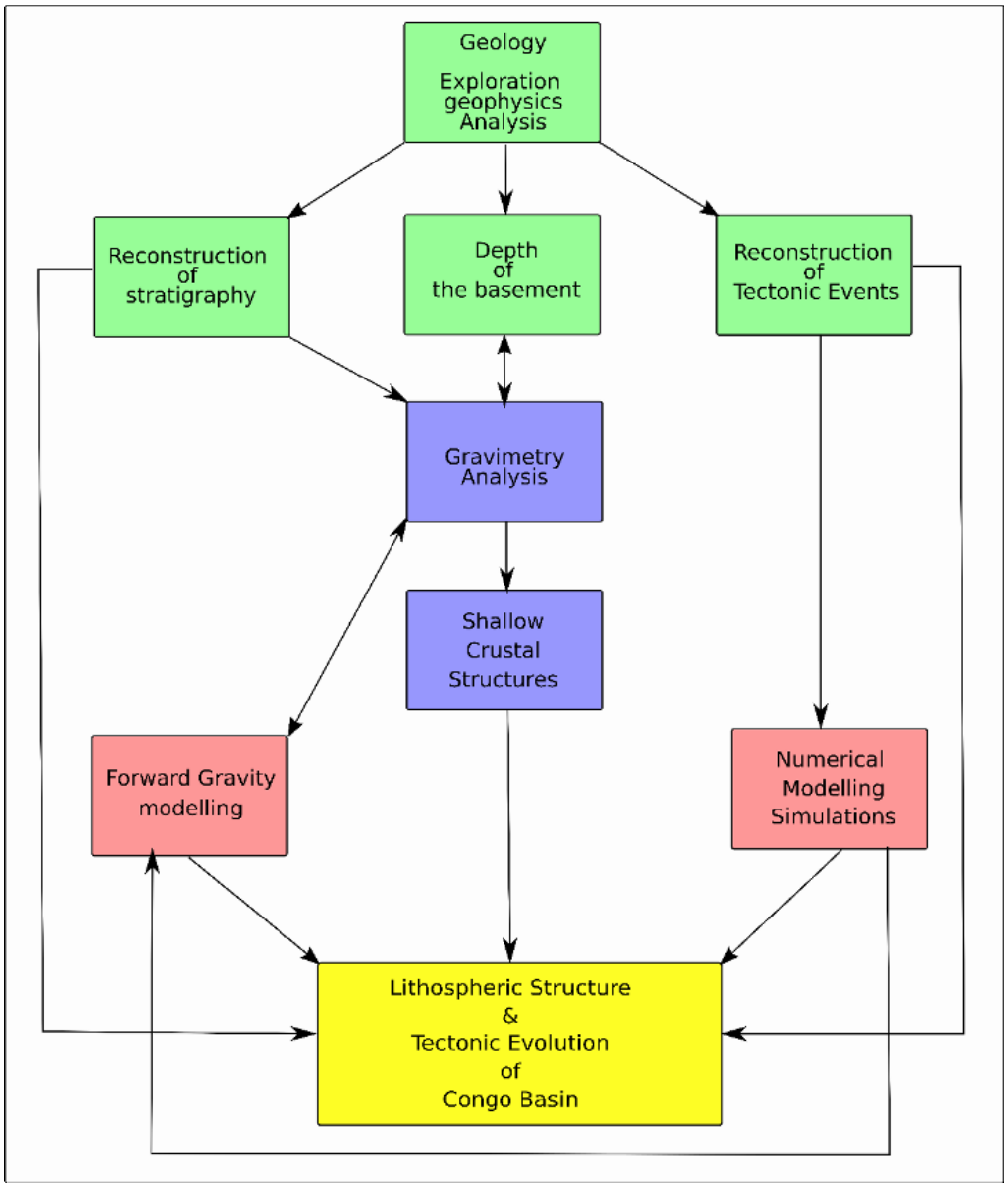

Figure 1.1. *Flowchart summarizing the main steps and methods followed in this PhD thesis.*

1.3 State of art

The Congo Basin (*CB*), named also Cuvette Centrale for its rough circular shape, is located in the center of the African plate, covering approximately 10% of the African continent. It is one of the largest intracratonic basins of the World, extending for about 3.7 million km^2 from the Central African Republic (CAR) in the North to Angola in the South. It occupies most of the Democratic Republic of Congo (DRC) and the Republic of Congo (RC) (Daly et al. 1992; Downey and Gurnis 2009; Crosby et al. 2010; Kadima et al. 2011a, b). Its long and complex history of sediment accumulation, tectonic inversion/reactivations, and erosion makes it a typical intracratonic basin, with a mean elevation of 300-400 m above the sea level and a sedimentary thickness up to about 9 km. The *CB* initiated its subsidence in the Precambrian and evolved with different extensional phases interrupted by short-lived compressional phases (e.g., Linol et al. 2015).

During the first part of its development, it also shared its intraplate history with other intracratonic basin located in the Gondwana supercontinent (Daly et al., 2018) and in particular with the Taoudeni Basin of West Africa (Bertrand-Sarfati et al., 1991; Deynoux et al., 2006) and Paraná Basin in the South American continent (e.g., Milani and De Wit, 2008). According to Kadima et al. (2011a) and Buiter et al. (2012), a large part of the older subsidence history of the *CB* is controlled by post-rift thermal subsidence. Further studies link the *CB* formation to tectonic uplift of swells surrounding the basin (Burke and Gunnell, 2008) or to lithospheric delamination (Downey et al., 2011). Therefore, despite the abundant literature on the *CB* and its huge geo-resources potential (Delvaux and Fernandez, 2015), the existing geophysical and geological data have not been fully exploited at the scale of the basin and important scientific questions concerning its structure and tectonic evolution, within the global plate tectonic and climatic context, remain. Thus, the *CB* is a natural laboratory, where I can investigate the processes that govern the long–term evolution of continental interiors. The hydrocarbon exploration in the *CB*, using geological and geophysical methods, started in the '50s and continued during the following decades (Evrard, 1957; Jones et al., 1960; Lawrence and Makazu, 1988, Daly et al., 1992), with several field campaigns in its peripheral parts (Raucq, 1957, 1970; Verbeek, 1970; Lepersonne, 1977; JNOC, 1984). In the 1950's, field works, gravity surveys, and several seismic refractions profiles were carried out (Evrard, 1957; 1960).

The first exploration campaigns were undertaken between 1952 and 1956 by *REMINA* (Société de Recherche Minière en Afrique), with the drilling of two fully cored stratigraphic wells, in the localities of Samba (2.039 m deep; Cahen et al., 1959) and Dekese (1.856 m deep; Cahen et al., 1960). The resulting data and documentation of these campaigns (original data and notes, publications, geological samples, and the entire cores) were donated to the Royal Museum for Central Africa (*RMCA*) for further use in scientific studies. A second exploration campaign was organized by a consortium of oil companies in the 1970's, acquiring ~2600 km of seismic reflection profiles, airborne aeromagnetic surveys, covering most part of the basin in the DRC, and additional field sampling. Two deep (~4.3-4.6 km) exploration wells, taking mostly drilling cuttings (Mbandaka-1 and Gilson-1) were drilled in 1981 by Esso Zaire. The available geological and geophysical data were used to revise and/or update the stratigraphy and tectonic evolution of the basin (Kadima et al., 2011a, 2015; Sachse et al., 2012; Linol et al., 2015a; 2015b; 2015c; Lucazeau et al., 2015; Caillaud et al., 2017; François et al., 2017). In particular, interpretation of the seismic reflection data identified the main sedimentary

layers deposited inside the *CB* in a series of basins separated by basement highs (e.g. Lawrence and Makazu 1988; Daly et al. 1992). More recently, a new field campaign in the *CB* is started to evaluate its hydrocarbon potential (Delvaux and Fernandez, 2015). At the end of the 80s, satellite gravity missions such as the Gravity Recovery and Climate Experiment (*GRACE*), have provided global knowledge of the gravity and geoid fields. More recently, the availability of a high-resolution global gravity field dataset, derived from the *GOCE* (Gravity field and steady state Ocean Circulation Explorer) satellite, allowed the first time to recover geological features across the entire African continent, also in areas with scarce field observations (Braitenberg, 2014). The satellite gravity data together with several seismic tomography models (e.g. Sebai et al., 2006; Pasyanos and Nyblade, 2007; Begg et al., 2009; Fishwick, 2010) shedded the light on the main structures of the basin. Gravity data, together with other geological and geophysical data, were used by Watts et al. (2018) to compare the structure, subsidence history, and evolution of several intracratonic basins including the *CB*. In this study, it was proposed that the observed gravity anomalies in the *CB* might be explained considering igneous intrusion, which contributed to its subsidence and consequent sediment accumulation. In addition, gravity observations from satellite *GRACE* revealed a huge long-wave negative gravity anomaly centered on the *CB* (Braitenberg and Ebbing, 2009). Several new geodynamic models attempted to explain this anomaly (Downey and Gurnis, 2009; Crosby et al., 2010; Kadima et al., 2011b, Buiter et al., 2012). This is considered as the effect of low-density sediments (Buiter et al., 2012) or the result of the combined effects of sediments and the presence of a high-density body below the crust, which isostatically compensates them (Hartley and Allen, 1994). In contrast, Downey and Gurnis (2009) attributed this anomaly to the presence of a high-density body and according to Crosby et al. (2010), it is the result of the mantle flow down welling in response to the upwelling caused by the mantle plume beneath the East African Rift.

1.4 Tectonic setting and factors controlling the evolution of the Congo Basin

The *CB* started to form in early Neoproterozoic (Kadima et al., 2011b, 2015), or, as I will show in this study, possibly even earlier, in late Mesoproterozoic. It developed within the Precambrian basement of Central Africa (Fig. 1.1), originally defined as the Congo Craton by Cahen (1954). De Waele et al. (2008) and Fernandez-Alonso et al. (2015) expanded the definition of the Congo Craton to the assemblage of several Central-African Archean nuclei plus the Sao-Francisco and Tanzania cratons (Ntem, Bouca-Mboumou-Uganda, Tanzanian-Kibaran, and Cuango-Kasai blocks), all welded together at the end of the Mesoproterozoic by Paleo- and Meso- Proterozoic belts. Others studies named this assemblage the Central African Shield (De Wit and Linol, 2015) or the great Congo Craton (Kadima et al., 2015). I prefer here to keep the Congo Craton term as understood by De Waele et al. (2008) and Fernandez-Alonso et al. (2015). The Congo Craton is surrounded from all sides by Neoproterozoic belts (Abdelsalaam et al., 2002; Frimmel et al., 2006; Gray et al., 2008; Collins and Pisarevsky, 2005; Fritz et al., 2013; Foster et al., 2015).

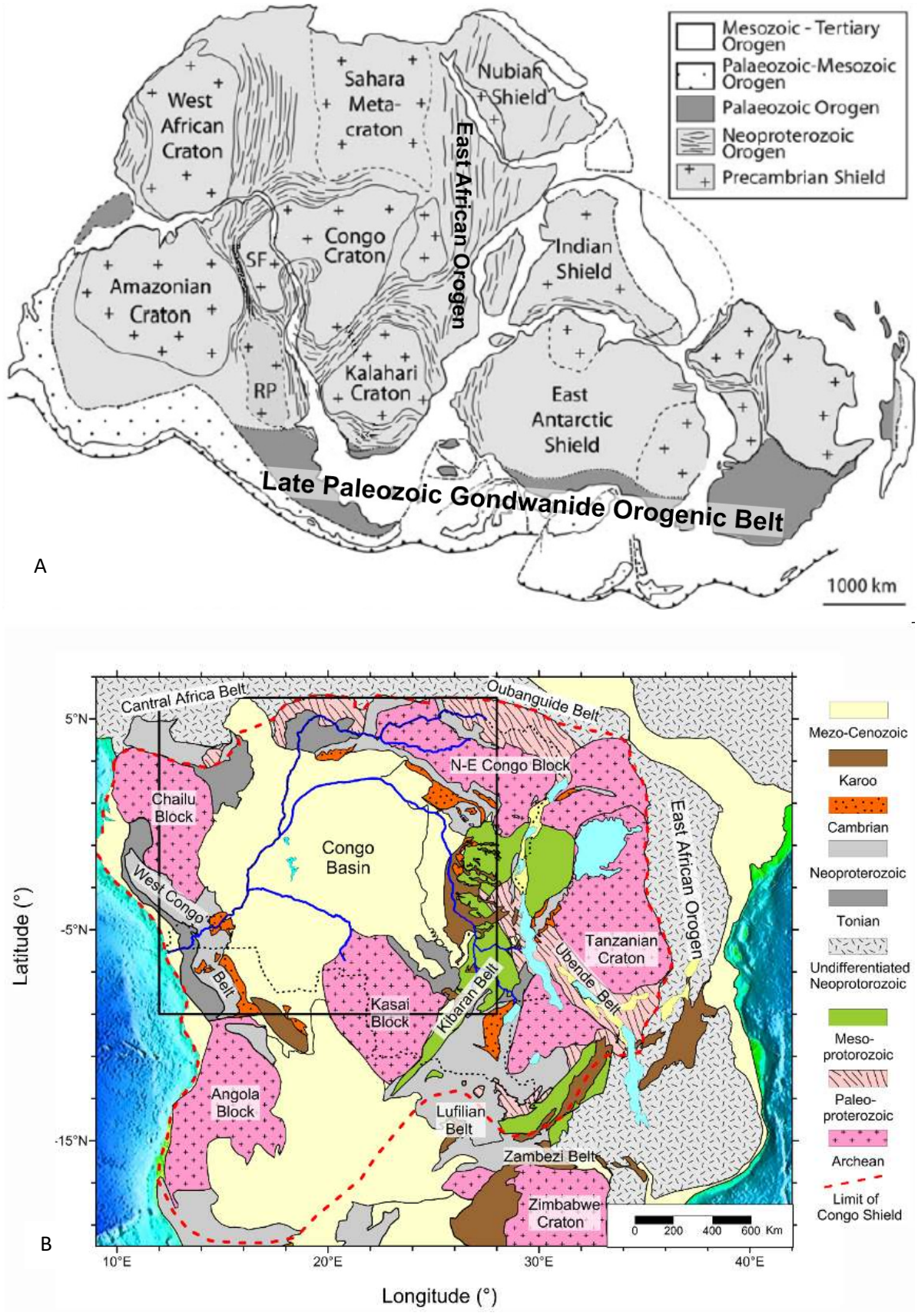

Figure 1.2. *Geological setting of the Congo Basin.* ***A****: Map of Gondwana (modified from Gray et al., 2008), with position of the Gondwanide orogenic belt from Trauw and De Wit (1999).* ***B****: Congo Craton and surrounding Pan-African orogenic belts (modified from Kadima et al., 2015). Black rectangle delimits the Congo Basin as detailed in Figure 2.1 (Delvaux et al. 2021).*

Since the late Mesoproterozoic, as the result of Rodinia amalgamation, the Congo Craton comprised the *NE*-Congo (Gabon, Angola, Kasaï, Tanzania, and S˜ao Francisco cratons, together with the Bangweulu block together with the Bangweulu block (Collins and Pisarevsky, 2005; Fernandez et al., 2015). During Gondwana amalgamation, it interacted between 650 and 540 Ma with the West African Craton along the Central African Orogenic Belt (Toteu et al., 2004; Saha-Fouotsa, 2019). At about 630 Ma, it entered in continental collision with the Sahara Metacraton, generating the Oubanguide Orogen (Poidevin, 1985) and with Neoproterozoic India in the East, generating the East African Orogen (Fritz et al., 2013).

Around about 570 Ma, closure of the ocean embayement between the São Francisco Craton (eastern Brazil) and Gabon-Angola cratonic cores generated the Araçuaí-West Congo Orogen (Pedrosa-Soares et al., 2008; Santiago et al., 2020). Convergence and collision between the southern margin of the Congo Craton and Zimbabwe Craton (small northern part of the Kalahari Craton) generated the Damara Orogen in the west, peaking at about 565 Ma (Frimmel et al., 2011). In the east, the twin Lufilian Orogen, peaking at about 595 Ma (Cailteux and De Putter, 2019) and Zambezi Orogen, peaking at 560-550Ma (Kuribara et al., 2018). Late tectonic convergence between the Dharwar Craton (India) relative to the Congo Craton at ~530 Ma generated intraplate reactivations between the Congo-Bangweulu and the Tanzania cratons (Delvaux et al. 2012) and within the Lufilian Orogen (Kipata et al, 2013; Cailteux and De Putter, 2019). All these tectonic events are likely to have caused late Neoproterozoic (Pan-African) intraplate deformations in the heterogeneous Congo Craton, which could have been recorded in the *CB*.

The *CB* developed over three NW elongated Archean nuclei (Gabon, Kasaï and NE Congo) that form the central core of the Congo Craton, and surround the concealed central part of the Congo Craton (De Wit and Linol, 2015). The presence of a heterogeneous cratonic lithosphere beneath the *CB* has recently been confirmed by seismic tomography of Celli et al. (2020), who identified at least three distinct high-velocity blocks (Ntem, Mboumou-Uganda, and Kasai blocks, respectively). These blocks represent remnants of likely larger Archean nuclei, which were partly eroded (e.g., Liao et al., 2017). Therefore, the original heterogeneous structures of the Archean cratons and their possible successive modifications during geological time are responsible for the primary basement anisotropy and the following development of the *CB*.

After the final junction between East and West Gondwana, at ~about 530 Ma, the *CB* became located in the center of the Gondwana supercontinent. A new paleo-pacific active margin formed along the southern edge of the continent during the Phanerozoic (Milani and De Wit, 2008). Once amalgamated, the entire Gondwana supercontinent drifted first southwards, then northwards, bringing the *CB* first into a polar-centered, and then back into an equatorial position. According to the apparent polar wander curve for Gondwana (Scotese et al., 1999; Torsvik and Cocks, 2011; 2013) the South Pole was located in W Africa (Mali/Algeria) in early Cambrian; NW Africa (Morocco) in early Ordovician; SW Africa (Ivory Coast) in late Ordovician and western coast of Central Africa (Namibia) in early Devonian. Also in Namibia during the late Devonian (Frasnian); Central Africa in late Devonian (Famennian); north of the *CB* in early Carboniferous (Tournaisian-Visean), and central Antarctica (then adjacent to South Africa) in late Carboniferous. From that period, the general tendency for the Gondwana continent was to drift northwards, bringing the *CB* progressively into a more equatorial position. In parallel, the global climate fluctuated with several ice ages (Ice House), during which one or two poles were covered by permanent ice, followed by global warming and warm ages (Hot House),

without permanent ice cover at the poles. Major Ice House periods occurred during the Cryogenian (coinciding with the assembly of Gondwana), late Ordovician - earliest Silurian (brief but extensive), and in late Devonian–Carboniferous to early Permian (Frakes et al., 1992).

The regional paleo climatic conditions of the plate interior were controlled by the latitudinal movement of Gondwana, global climate evolution, and morphology of the plate interior. During the lifespan of the Gondwana supercontinent, interactions with the adjacent plates generated plate-boundary forces that propagated into the continental interior as far-field stresses (Daly et al., 1991; De Wit and Ransome, 1992). Collision with Laurentia on its NW edge in the late Carboniferous – early Permian resulted in the Appalachian-Mauritanian-Variscan orogeny (Kröner and Römer, 2013). Subduction along the southern margin of Gondwana resulted in the Gondwanides orogeny with the Sierra de la Ventana-Cape Fold Belt in the late Permian – early Triassic (Trouw and De Wit, 1999; Milani and De Wit, 2008) and earlier collisions (Ordovician-Devonian) in the NW, along the South American domain (Milani and De Wit, 2008).

Gondwana breakup, which started around 200 Ma ago (early Jurassic), also influenced the tectonic evolution of the *CB*. It involved successively the giant Okavango mafic dyke swarm across NE Botswana emplaced at 178-179 Ma (Le Gall et al., 2005), the late Jurassic opening of the Indian Ocean (Sinha et al., 2019), the early Cretaceous opening of the South Atlantic Ocean (Heine et al., 2013), and the Neogene East African rifting (Macgregor, 2015). According to Kadima et al. (2011a; 2011b), the *CB* started as a failed rift system. The fossil rift would be represented by the *NW-SE* trending Kiri basement high that separates the basin into two parts and coincides with pronounced axial magnetic zone and gravity anomalies. On the other hand, Daly et al. (1989) instead claimed that there is no clear evidence for the presence of extensional structures in the seismic profiles and suggest that the Kiri and Lokonia Highs could be the shortened and uplifted parts of the basin where the Paleozoic (and Neoproterozoic) sequences have been deposited, but have been eroded afterwards.

The Mbuji-Maji Groups (Raucq, 1957; 1970; Delpomdor, 2013a; b; François et al., 2017; Balukiday et al., 2018), which outcrop along the margin of the *CB*, could represent the deepest sediments of the *CB* and, consequently, interpreted as rift deposits. Following Daly et al. (1992), the Kiri High formed by crustal contraction and uplift in the late Paleozoic times, reactivating (inverting) the former rift structure. Kadima et al. (2011a), instead, using combined gravity and magnetic modeling, proposed that the poorly defined seismic zone with transparent seismic facies, which mark the 'basement' of the Kiri High can be adequately modelled by intermediate salt (evaporate) and sediment density, instead of an uplifted crystalline basement. Therefore, they proposed a gradual lateral change in density from the adjacent basins towards the Kiri High. Once initiated, the development of the *CB* was then characterized by regional contraction deformation episodes (Daly et al., 1991; 1992). Late Paleozoic structures have been largely produced from a reactivation of the early Paleozoic structures, but it is not clear the size of the structures. Kadima et al. (2011a) suggested that observed tectonic structures of the *CB* are the typical product mainly of the tectonic inversion processes occurred during the Pan-African deformation.

CHAPTER 2

- Exploration geophysics, stratigraphy and 3D model of sediments -

2.0 Introduction of the chapter

In this chapter, I implemented a new sismostratigraphic model of the *CB*, which made it possible to reconstruct the tectonic evolution of the basin. To this aim, I spent two months in Belgium at the Royal Museum of Central Africa (*RMCA*, Tervuren), during my first year of my *PhD* project, in which I worked on the interpretation of all available exploration geophysical data (seismic reflection, refraction, and well-log data). In particular, I re-interpreted about 2600 km calibrated seismic reflection profiles, acquired along 35 lines inside the Cuvette Centrale, between 1974 and 1976, by an Esso-Texaco consortium and analyzed rock samples from drilling cores. The interpretation of seismic reflection profiles is based on the Two-Way-Travel time (*TWT*)-Depth conversion, which allowed me to compute the thickness of the major sedimentary layers by interpolating the seismic data on a regular grid. The obtained results enabled to identify the main sedimentary depocenters of the *CB* and reconstruct their evolution in a more detailed way than before (e.g. Daly et al., 1992; Kadima, 2011; Kadima et al., 2011a). Furthermore, the analysis of the seismic reflection profiles led me to identify, for the first time, several small tectonic features, reflecting the influence of far-field compressional tectonic events within the basin. Based on the results achieved, I could put the ~1.000 Myr evolution of the *CB* into a broad geodynamic context of supercontinents amalgamation, breakup, and climatic fluctuations. In particular, I identified in the *CB* stratigraphy a major global glacial event occurred during the Paleozoic age. The chapter is mostly based on Delvaux et al., 2021, in which I mostly contributed with the seismic lines digitalization and interpretation, *TWT*-Depth conversion, and by writing the manuscript.

2.1 Data presentation

A first exploration campaign in the Congo Basin was conducted in 1952-1956 by the 'Syndicat pour l'étude Géologique et Meniere de la Cuvette Congolese' with field work, refraction seismic and two c. 2000 m deep stratigraphic wells, fully cored (Samba and Dekese) drilled by the *REMINA*, (Cahen et al., 1959, 1960). The resulting data (outcrop samples, drill cores), reports, and publications are stored in *RMCA* collections and are available for research. Furthermore, between 1970 and 1984, Shell, Texaco, and JNOC oil companies acquired new data with aeromagnetic surveys. They also acquired more additional gravity data, geochemical sampling, and about 2600 km of seismic reflection profiles, in the *CB*, over an area of 500.000 km^2 between the Congo and Kasaï rivers. The seismic profiles were recorded both along watercourses (lines R) and along roads (lines L) (Fig. 2.1).

In 1981, the exploration wells Mbandaka-1 (4350 m; Esso Zaire S.A.R.L., 1981a) and Gilson-1 (4563 m; Esso Zaire S.A.R.L., 1981b) were drilled by the Esso Oil Company (Fig. 2.1). The cuttings of the cores were sampled every 10 m, but they are no longer accessible. The Mbandaka-well terminated in massive salt deposits of Proterozoic age with anhydrite inter-beds, after encountering stromatolitic carbonates, while the Gilson-1 well terminated in massive dolomite. None of the four wells reached the crystalline basement. Only the Jurassic to Recent sediments encountered in the Dekese and Samba wells were accurately dated paleontologically but the stratigraphic position of the deeper deposits is more problematic (Cahen et al., 1959; 1960; Linol et al., 2015b). Analysis of the data lead to a preliminary subdivision of the basin stratigraphy in three major sedimentary sequences (Proterozoic, Paleozoic-Triassic and Jurassic-Cretaceous) separated by major tectonic

unconformities (Pan-African and Basal Jurassic) and allowed to define its global architecture and tectonic evolution (ECL, 1988; Lawrence and Makazu, 1988; Daly et al, 1992; Kadima et al., 2011a). In addition to these deep wells, we used also shallow wells drilled in the periphery of the basin (Fig. 2.1). They are located in Kisangani area (Caillaud et al., 2017), Lukuga coal field along Lake Tanganyika (Cahen and Lepersonne, 1971), Mbuji-Mayi area, and Tshikapa area (Roberts, 2015) in Kasaïi (Delpomdor et al., 2016; François et al., 2014), and in the underground of Kinshasa and Brazzaville (Egoroff and Lombard, 1962). Exploration was also performed on the northwestern side (right bank) of the Congo River in the Republic of the Congo, with aeromagnetic survey, reflection seismic and drilling, but the data (except aeromagnetic) are not available for research.

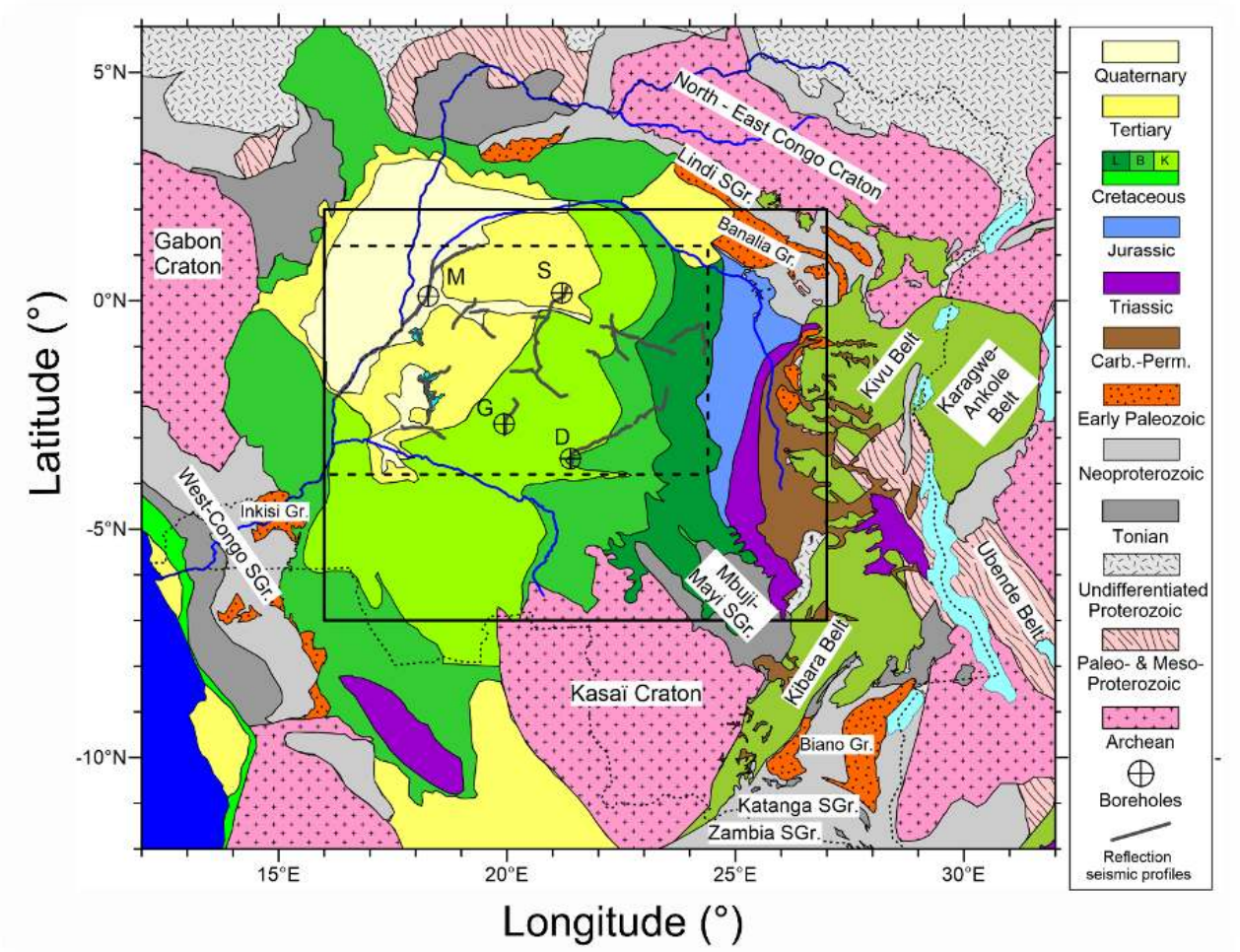

***Figure 2.1**. Surface geology of the Congo Basin (adapted from Kadima et al., 2015). Black circles: deep wells: D (Dekese), G (Gilson-1), M (Mbandaka-1), S (Samba). The continuous black rectangle delimits the zone used for the aeromagnetic data analysis, while the dashed black rectangle delimits the Cuvette Centrale as the study area (modified after Delvaux et al., 2021).*

2.2 Revised stratigraphy

The bowl-shaped central area of the *CB* ("Cuvette Centrale") shows progressively older outcropping geological series towards its periphery (Fig. 2.1). Integrating the analysis of surface outcrops with the well data and thanks' to the remarkable lateral continuity of the stratigraphic units, Daly et al. (1992) proposed a first general stratigraphic column of the *CB*. It was revised by Kadima et al. (2011a, 2015) and Linol et al. (2015b, 2015c) based on the re-analysis of some key seismic profiles and well-log data (Appendixes A and B). The lithostratigraphic units are named according to the last version of the Geological map of the *RDC* at 1/2.500.000 (Fernandez-Alonso et al., 2017), as detailed in his Explanatory Notice (Fernandez-Alonso et al., 2017), published by the Ministry of Mines of the *DRC*.

A series of stratigraphic names has been changed according to the Stratigraphic Guide of the International Commission on Stratigraphy (*ICS*). In particular, in this work, the formations described in the literature as Haute-Lueki, Stanleyville Groups are now respectively named as Lueki, and Kisangani Groups.As previously mentioned, the lithostratigraphy of the *CB* is essentially known from the analyses of four well-log data (Appendix A) and surface outcrops. The good lateral continuity of the sedimentary layers and seismic reflection profiles allows extending the stratigraphic framework over the entire basin. This has been shown already by Daly et al. (1992) for the *CB* and used by Watts et al. (2018) in his comparative study of the Paranaiba, Michigan, and Congo Basin. The Proterozoic to Cambrian sequences are exposed along the margins of the *CB* (Delpomdor and Préat, 2015).

The pre-Jurassic sequences of the deep Gilson and Mbandaka wells are almost unconstrained by biostratigraphy and, therefore, their interpretation is difficult and varies from one study to the other. For these sequences, we preferred to follow the interpretation of Kadima et al. (2011a; 2015), which is based on unpublished exploration reports, instead of the one presented in Linol et al. (2015b). The latter study gives too much emphasis on the late Paleozoic and limits the history of the *CB* to the Late Carboniferous-Mesozoic period, neglecting all the Neoproterozoic to early Paleozoic evolution. The oldest sequences of the *CB* are illustrated by the Mesoproterozoic Mbuji-Maji Supergroup, which is found in two NW-trending depressions between the Kasaï Craton and the Kibara belt of Katanga (Fig. 2.1). They comprise a lower BI Group of mostly clastic sediments, dolomitized on top, and an upper *BII* Group of dolomitic limestones, surmounted by dolerite lava (Raucq, 1957, 1970; Delpmondor, 2013a, b; François et al., 2017; Balukiday et al., 2018). The Neoproterozoic sequences are typified by the Lindi Supergroup, which outcrops in the northern part of the *CB* (Fig. 2.1) and was intensively studied by Verbeek (1970). Their correlation with the well and seismic data in the *CB* was proposed by Daly et al. (1992).

The lower Paleozoic sequences are represented by thick cross-bedded red arkosic sandstones, outcropping along the margin of the *CB* (Fernandez-Alonso et al., 2017) as the Inkisi Group (Alvarez et al., 1995; Affaton et al., 2015), Banalia Group (Verbeek, 1970) and Biano Group (Cailteux and de Putter, 2019). They are also found also in the Samba and Dekese wells (Cahen et al., 1959; 1960). The overlying Karoo series comprises from top to bottom, red-sandstones of the Lueki (ex-Haute-Lueki) Group (Triassic), coal-bearing mudstones and psammitic sandstones of the Upper Lukuga Group (upper Carboniferous to upper Permian), and glacial to periglacial tillites and valval black shales of the Lower Lukuga Group (Upper Permian). Their

age is relatively well constrained by spores and pollens (Boulouard and Calendra, 1963; Boze and Kar, 1976, 1978; Cahen and Lepersonne, 1978). The Lower Lukuga Group is well known in the Dekese well cores (Cahen et al., 1960), with a thickness of up to 1000 m of glacial-lacustrine tillites and periglacial valval black shales (not present in the Samba Well). The entire Karoo series is exposed along the Lukuga River valley and in the Lukuga Coal field (Fourmarier, 1914; Jamotte, 1931), in the Luama graben along the Tanganyika rift valley. The Upper Lukuga Group and its transition to the Lueki Group is well evidenced in a coal exploration drill well (Cahen and Lepersonne, 1971). The Lueki Group is present in small thickness in the Dekese Well, but not in the Samba Well (Lombard, 1961) and known as part of the Casanje Group in Angola (Cahen, 1981). The Lukuga and Lueki sediments are also present in the Gilson and Mbandaka wells, but the dominant clastic facies of these wells do not allow to precise their biostratigraphy correlations.

The Jurassic to Cretaceous series are the best studied ones in terms of biostratigraphy, sequence stratigraphy and lithostratigraphy. They were dated by ostracods (Grekoff, 1957; 1960), phyllopods (Defretin Lefranc, 1967), pelecypods (Cox, 1960), spores/pollen (Boulouard and Calendra, 1963; Masheshwari et al., 1977), and fishes (de Saint-Seine, 1955; de Saint-Seine and Casier, 1962; Casier, 1965; Taverne, 1975a, 1975b). Their biostratigraphy has been revised by Colin (1994) and presented in detail in Linol et al. (2015b; c). Their sequence stratigraphy and depositional environment were studied by Linol (2015c) and Roberts (2015). These series start by the late Jurassic (Kimmeridgian) Kisangani (ex-Stanleyville) Group, well developed along the Lualaba River (i.e. the Congo River upstream Kisangani), where it forms a large basin (Passau, 1923). In this region the series starts by organic-rich lacustrine calcareous siltstones and shales (Type I kerogen; Sachse et al., 2012) and grades upward to more oxidized sandstones and siltstones in a dryer environment (Caillaud et al., 2017). They overly limestones with stromatolitic of probable Neoproterozoic age, themselves resting over quartzite's and gneisses basement.

Jurassic sediments are present in the Samba well (Cahen et al., 1959) consisting of a lacustrine sequence at the base, locally organic-rich, surmounted by red siltstones and sandstones with geochemical evidence for hot and arid conditions (Myers et al., 2011). They have also been recognized in small thicknesses in the Gilson and Samba Wells (Esso-Zaïre SARL, 1981a, 1981b; Linol et al., 2015b), in boreholes in Kinshasa and Brazzaville, lying directly over the Inkisi red sandstones (Egoroff and Lombard, 1962; Defrétin-Lefranc, S., 1967), and in the cover series of the Kasaï Craton in the Tshikapa area (Roberts et al., 2015). Arid conditions then developed, with deposition of aeolian cross-bedded sandstones, recently identified in Dekese and Gilson wells, which define the new Dekese Group (Linol et al., 2015c). Its age is indirectly constrained as early Cretaceous from the surrounding sediments. Conditions that are more humid followed in Albian – Cenomanian, as evidenced by the deposition of sandstones and mudstones of the Loia and Bokungu Groups (Colin, 1994). Deposition started in a lacustrine environment, locally anoxic with black shales (mixture of kerogens of Type I and II; Sachse et al., 2012), then evolved into a shallower, fluvial environment with carbonated mudstones. The Kwango Group is known mainly in the southern and western parts of the basin (Cahen and Lepersonne, 1954; Linol et al., 2015c) and as cover of the Kasaï Craton (Roberts et al., 2015). It may have had a marine influence and its lower part is dated mainly by fishes, suggesting a Cenomanian-Turonian age (Casier, 1965; Taverne, 1976a, b) or Campanian-Maastrichtian (Gobbo-Rodrigues et al, 2003). The cover sequences are regrouped in the Kalahari Group (Linol et al., 2015e; Fernandez-Alonso et al., 2015),

with silcretes, calcretes and ferricretes covered by aeolian sandstones that represent the weathering alteration. They also have been formed under a regional humid and hot climate of Central Africa and are described as 'Polymorph sandstones' by Lepersonne (1945). The thermal evolution modeling constrained by vitrinite data shows that during the late Cretaceous-Paleogene evolution of the landscape (Guillocheau et al., 2015), an estimate of 1000m (Sachse et al., 2012) or more (Lucazeau et al., 2015) of sediments were removed.

2.2.1 New seismo-stratigraphic model

Starting from the existing seismo-stratigraphic models of Kadima et al., (2011a; 2015), in Delvaux et al (2021), the entire seismic stratigraphy of the *CB* was reinterpreted, using a new comprehensive analysis of the seismic profiles developed during my first year of *PhD*, integrated with the most recent studies carried out in collaboration with the *RMCA* researchers. This new stratigraphy of the *CB* with the description of the seismic sequences is displayed in Fig. 2.2. The Mesozoic and late Paleozoic strata are directly constrained by the Samba and Dekese cored wells (Cahen et al., 1959, 1960), but the early Paleozoic and Proterozoic rocks remain poorly dated, as they do not contain datable material, except for the basal series. Their stratigraphic age is indirectly constrained by analogy with the Supergroups outcropping along the margins of the basin, and with the help of the two Gilson-1 and Mbandaka-1 wells (Esso-Zaïre SARL, 1981a, and b) and the first interpretation of the Esso-Texaco reflection seismic profiles.

The "infracambrian" stratigraphy was first correlated with the West Congo and the Katanga Supergroups, respectively to the west and southeast of the *CB* (Lawrence and Makazu, 1988). Daly et al. (1992) correlated it with the Lindi Supergroup (Verbeek, 1970) on the northern side of the *CB*. The seismo-stratigraphy of the *CB* was later revised by Delpomdor et al. (2013b) and Kadima et al. (2015) with additional references to the Mbuji-Mayi Supergroup defined by (Raucq, 1957; 1970). This Supergroup outcrops against the Kasaï Craton along the SE edge of the *CB* in the Sankuru-Mbuji-Mayi-Lomami-Lovoy (*SMLL*) sedimentary basin, which is considered a lateral equivalent of the basal units of the *CB*. The Mbuji-Mayi Supergroup has been deposited in a intracratonic failed-rift basin with a lower clastic sequence (*BI*) and an upper carbonate sequence (*BII*), indicative of a restricted marine carbonate ramp environment (Delpomdor et al., 2013a). It is covered and intruded by dolerite lavas, which mark the end of the deposition for the Supergroup, thus constraining its minimum age. Cahen et al. (1984) obtained a K-Ar age of 940 ± 20 Ma for these dolerites. In contrast, Delpomdor et al. (2013b) dated the depositional interval of the Mbuji-Mayi Supergroup between 1174 ± 22 Ma and ca. 800 Ma, using δ13C of carbonates and obtained an Ar/Ar age of 882.2 ± 8.8 Ma for the dolerites. However, recent U-Th-Pb (François et al., 2017) dating shows that the diagenesis of the BI subgroup is between 1065 Ma and 1030 Ma. Similarly, conventional 207Pb/206Pb ages of 1040 Ma and 1065 Ma for galena samples in the upper part of the *BI* group were obtained by Cahen (1954) and attributed to syngeneic growth of galena during diagenesis. Therefore, we consider that the Mbuji-Mayi Supergroup has a terminal Mesoproterozoic age and correlates with the representing basal series of the *CB*. Despite its age, this sedimentary sequence remained in a low-grade thermal maturity, mostly restricted to the diagenesis domain (Balukiday et al., 2018).

I subdivided the seismic stratigraphy of the *CB* in a similar approach as Kadima et al. (2015), but consider eight sequences (instead of 6), overlying the crystalline/metamorphic basement. Separated by the

prominent Pan-African and Basal Jurassic regional unconformities, identified by Lawrence and Makazu (1988), a first-order subdivision in three age groups can be made: (1) Meso-Neoproterozoic (sequences 0-3), (2) Paleozoic-Triassic (sequences 4-5) and (3) Jurassic-Paleogene (sequences 6-7) (Fig. 2.2).

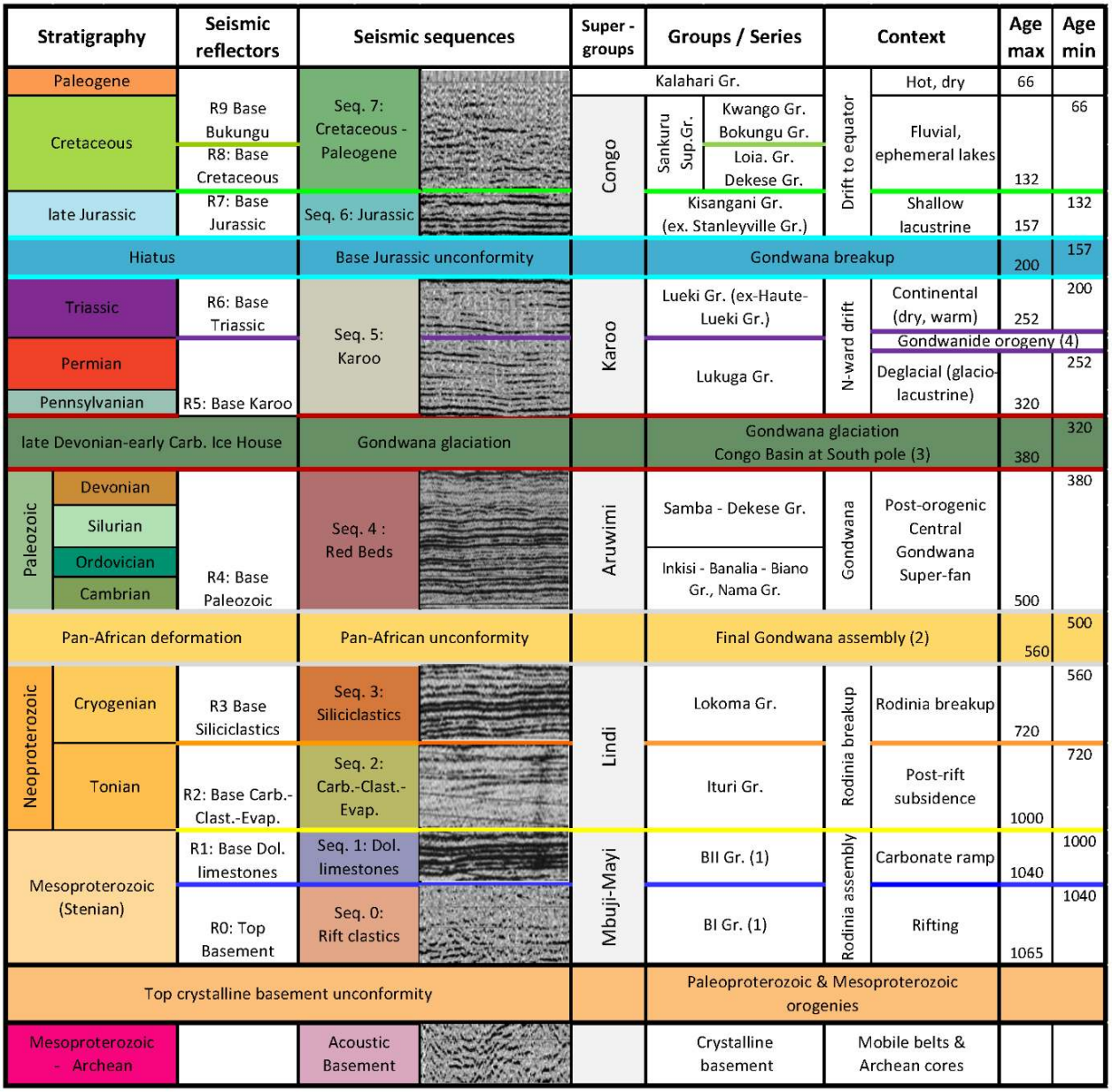

Figure 2.2. *Composite sismostratigraphic model integrating well-log and outcrop data (Appendix A), and seismic reflection profiles (Cahen et al., 1959; Esso-Zaire SARL, 1981a, 1981b; Sachse et al., 2012; Linol 2013; Delvaux and Fernandez-Alonso, 2015; Fernandez-Alonso et al., 2012; 2015; Kadima et al., 2015; Roberts et al., 2015; François et al., 2017; Caillaud et al., 2017). Age estimates are taken from François et al., 2017; Fritz et al., 2011; Torsvik and Cocks, 2011, 2013; Blewett and David, 2016. The thick colored lines refer to the interpreted seismic reflectors in the profiles (Figs. 2.5-2.10).*

2.2.2 Proterozoic (sequences S0-S3)

The Proterozoic sedimentary sequences formed in a succession of rift and post-rift events, during the final stages of the Rodinia supercontinent amalgamation (De Waele et al. 2008).

The Mesoproterozoic corresponds to the syn-rift sequences:

- Sequence 0 (*S0* - rift clastics): represents coarse siliciclastics, by analogy with the lower BI Group of the Mbuji-Mayi Supergroup;
- Sequence 1 (*S1* - dolomitic limestones): almost highly continuous and parallel reflectors on the seismic reflection profiles, they are considered an equivalent to the BII Group of the Mbuji-Mayi Supergroup. The top of this sequence was reached in the Gilson well at 4503 m deep and in the Mbandaka well at 3960 m. The latter stopped in interstratified massive salt, at 4350 m deep.

The Neoproterozoic is marked by continuous subsidence with carbonates and siliciclastics. It has been correlated (Lawrence and Makazu, 1988; Daly et al., 1992) with the Ituri (mostly carbonates) and Lokoma (siliciclastics and carbonates) groups of the Lindi Supergroup, separated by the Akwokwo tillite (Verbeek, 1970):

- Sequence 2 (*S2* - carbonates-evaporates-clastics): transparent seismic pattern with some medium to strong continuous reflectors, which could represent dominant carbonates and clastics (eq. Ituri Gr.), locally with some evaporates.
- Sequence 3 (*S3* - siliciclastics): banded seismic pattern of moderately continuous reflectors representing dominantly siliciclastic sediments (eq. Lokoma Gr.).

As reported in Kadima et al. (2011b), Sr-isotope stratigraphy of the Akwokwo tillite allowed researchers to postulate that it corresponds to a Sturtian event (720 ± 30 Ma), and therefore, the Ituri group would be of Tonian age (1000-720 Ma), and the Lokoma group of Cryogenian age (720-635 Ma). Sequences *S1* to *S3* are locally folded, faulted, and truncated by the Pan-African unconformity. The related tectonic deformation and subsequent denudation are explained as the result of intraplate deformation in response to the amalgamation of the continental blocks against the Congo Craton (Collins and Pisarevsky, 2005; Kadima et al., 2011a), as described above.

2.2.3 Paleozoic-Triassic (sequences S4-S5)

Below the Basal Jurassic unconformity, the whole Paleozoic and Triassic sequences were considered as a single sequence by Kadima et al. (2015). Here, it is further subdivided into two sequences, corresponding respectively to a newly defined Aruwimi Supergroup (see below) and the Karoo Supergroup, separated by the late Devonian – early Carboniferous Ice House event, during which the *CB* was close to the South Pole:

- Sequence 4 (*S4* - Red Beds): moderate to continuous parallel reflectors, wavier on top. The basal part of this sequence has been considered as equivalent to post-Pan-African early Paleozoic red arkoses ("Red Beds") outcropping at the periphery of the *CB*. The upper part of this sequence was reached in the Samba well from 1167 m to 2038 m and in the Dekese well from 1677 m to 1856 m, down to the bottom of the wells. The drill cores did not provide biostratigraphic material for dating. Detrital zircons in the Inkisi Group gave a maximum age of 581 ± 18 Ma (Straathof, 2011). The age of this sequence could be up to the late Devonian, just before the late Paleozoic Icehouse and late Devonian - early Permian "Karoo" glaciation over Gondwana.
- Sequence 5 (*S5* - Karoo): discontinuous to moderately continuous parallel reflectors, more transparent than sequence S4. It was drilled in the Dekese well between 714 and 1677 m. The cores reveal alternating sequences of glacial diamictities (initially described as tillites) and varval clays of late Carboniferous to early Triassic (Karoo) age (Cahen et al., 1960), deposited in a large glacial lake (Linol et al., 2015). They correspond to glacial - deglacial sequences under glacial to cool climate (Lukuga Group), and end in a postglacial environment (Lueki Group), while the South Pole was migrating towards central Antarctica (Wopfner, 1999).

Between sequences *S4* and *S5*, the Dekese well shows a stratigraphic break at 1677 m depth. The cored transition from sequence *S4* to *S5* shows a typical dark-brown diamictities with poorly sorted irregular rock fragments up to 14 cm large overlying, in an irregular contact, massive red-brown micaceous feldspathic sandstone with soft clay pebbles, locally weakly calcareous and cross-bedded downwards. This evidences an episode of erosion (and therefore a hiatus) before the beginning of the deglacial Karoo sequence. The Karoo and Red Beds sequences are locally folded and truncated by the Basal Jurassic unconformity, which is marked by a stratigraphic hiatus, localized tectonic deformation and erosion related to far-field stresses caused by the Gondwanide Orogeny (Trouw and De Wit, 1999). This intracratonic deformation caused tectonic activations in the *CB* (Daly et al., 1991) and in the Cape Fold Belt of South Africa (De Wit and Ransome, 1992).

2.2.4 Jurassic-Paleogene (sequences S6-S7)

The Jurassic-Paleogene sequences appear as a continuous blanket over the entire basin. They overlie the Basal Jurassic unconformity (Lawrence and Makazu, 1988; Kadima, 2011a) that truncates all the Paleozoic to Triassic sequences and correspond to the Sequence 5 of Kadima et al. (2015):

- Sequences 6 (*S6* - Jurassic) and *S7* (Cretaceous): parallel highly continuous reflectors grading upward to wavier reflectors. They correspond to the late Jurassic Kisangani and Cretaceous Dekese (Linol et al., 2016), Loia, Bokungu, and Kwango Groups, assembled into the Congo Supergroup, and a thin Paleogene cover (Kalahari Group) (Linol et al., 2016). They were deposited in tropical to equatorial conditions, in shallow ephemeral-lakes, fluvial-deltaic and aeolian environments (Cahen 1954; Lepersonne 1974; Cahen 1983a, 1983b, Colin, 1994; Linol et al., 2015c; Roberts et al., 2015; Caillaud et al. 2017). This sequence is the best known of the *CB*, as it has been reported in the four deep wells drilled in the *CB* and in outcrops and contains fossils that allow biostratigraphic determinations (for the late Jurassic-Cretaceous).

2.3 Refraction seismic interpretation

Three field geophysical campaigns were conducted by the *REMINA* in the *CB* between 1952 and 1956 (Evrard, 1957). Among the others, a refraction seismic survey was carried out with 117 points regularly positioned over the entire *CB*. The depth of refractors was obtained for these points, and isobaths were traced on a map (Evrard, 1960). The sedimentary sequences characterized by velocities less than 3600 m/s were considered by Evrard (1957; 1960) as “cover series” (Jurassic to Paleogene, sequences 5 and 6) on the base of the correlations with outcropping series and the Samba and Dekese cored wells. The 4200 m/s reflector was correlated with the top of the red arkoses (Red Beds) in the northern part of the basin and the top of the Triassic Lueki and Permian Lukuga groups (Karoo) in the southern part (Sequence 5). The Red Beds define the seismic Sequence 4, which was considered at that time as the top of the Neoproterozoic “substratum” (Veach, 1935; Cahen, 1954; Lepersonne, 1977). Evrard (1957) also recognized the ambiguity of the nature of the substratum deduced from the sole measured velocities. An important outcome of that survey was to recognize that the basin is likely much deeper than originally thought. Here, the isobaths of the 4200 m/s and 5200 m/s refractors were digitized and interpolated using a standard kriging method (SURFER, Golden Software package) with a grid spacing of 0.1 degree. The interpolated maps (Fig. 2.3 A-B), show the internal structure of the basin, with a WNW-ESE structural high separating the *CB* into two parts (the Kiri High), coinciding with the axial magnetic zone (Kadima et al., 2011a). Two main depocenters were identified, that motivated the drilling of the Samba and Dekese wells (Fig. 2.3 A-B). The southern limit of the deep part of the basin remarkably corresponds to the limit of the Kasaï Craton under the sediment cover, as defined using the aeromagnetic data (Chapter 3).

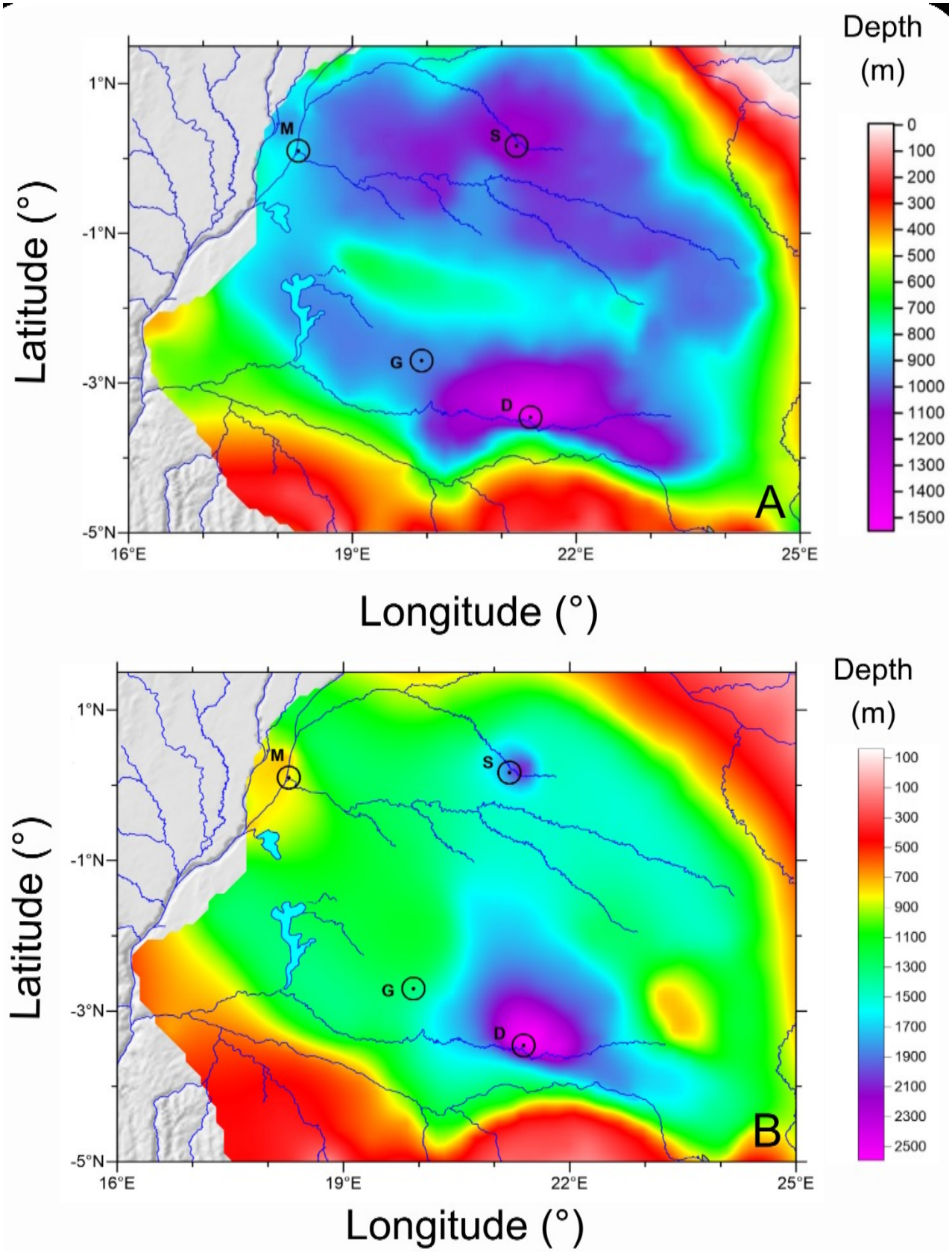

Figure 2.3. *Refraction seismic (Kriging interpolation of the data from Evrard, 1960). Depth of the (**A**) 4200 ms and (**B**) 5200 ms refractor. Black circles show the location of the four wells drilled in the study area: D=Dekese; G=Gilson-1; M=Mbandaka-1; S=Samba (Delvaux et al. 2021).*

2.4 Reflection seismic interpretation

As part of a second field exploration campaign, an extensive coverage of the central part of the *CB* by reflection seismic profiles has been performed by the Compagnie General de Géophysique in 1974. They were recorded with sources at 100 m interval consisting of groups of three vibrators 12.5 m apart, and geophones in series spaced by 5 m. The records were processed by the Geophysical Development Corporation (Houston, Texas) in 1986. Unfortunately, the original (digital) records are lost. The reflection profiles from scanned paper copies and their location map come from Kadima (2011). There are 35 profiles for 2623 km in total (Fig. 2.4), 21 deployed along rivers and lakes (*R* profiles) and 14 along roads (L profiles). They were shot mainly at a high angle to the Kiri High, in order to better image the structure of the basin, with also some transversal lines. They cover in a rather homogeneous way the central part of the basin, from 1°N to 3.5°S and from 16.5°E to 24°E. The profiles were geo-referenced and analyzed using the Golden Software *SURFER* program. The geographic coordinates (*WGS84 UTM Zone 33N*) of the seismic lines were digitized and the line lengths calibrated accordingly.

In a reverse operation, the digitized points of the profile interpretations were re-located as geographic coordinates. The Common Depth Point boxes (*CDP*) giving the relation between *TWT*, seismic velocity and depth were used to compute depth-time curves for each profile by a third degree polynomial interpolation, needed for converting *TWT* to depth. For each profile, the most central *CDP* boxes were used as average for the entire profile.

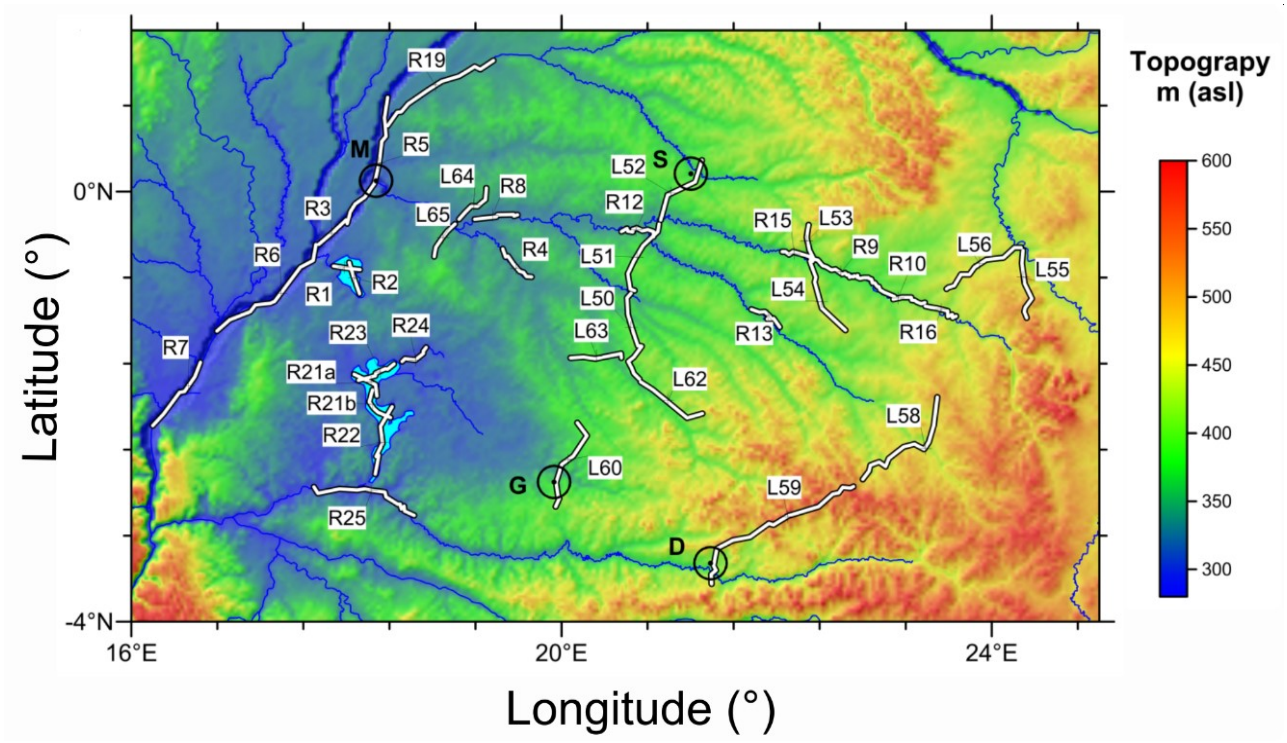

Figure 2.4. *Topography map of the CB using ETOPO 1 (Amante et al., 2009). Black labels show the names of the seismic reflection profiles (white broken line). The hydrological system is displayed in blue. Black circles show the location of the four wells drilled in the study area: D=Dekese; G=Gilson-1; M=Mbandaka-1; S=Samba (Delvaux et al. 2021).*

A preliminary interpretation of the seismic reflection profiles, calibrated with the Mbandaka-1 well, identified three major seismic units separated by major unconformities (Kadima et al., 2011a). Based on the interpretation of all available seismic reflection profiles inside the *CB*, it was possible to identify ten sequence boundaries, based on prominent seismic reflectors (*R0 – R9*), of which seven can be recognized over the entire basin and two correspond to major tectonic unconformities. They define the eight (*S0 - S7*) seismic sequences overlying the acoustic basement (Fig. 2.2). Some profiles have been shot in series or assembled into combined profiles, generally calibrated by one or two wells. Some profiles intersect each other. From NW to SE, we distinguish:

- the *SW-NE* combined profile (*R7-6-3-5-19*), along the Congo River and calibrated by the Mbandaka 4350 m deep well;
- a group of profiles recorded along roads and rivers, near Ingende (*L64-65, R4, R8*);
- the series of profiles along Lake Tumba (*R1, R2*) and Lake Mai-Ndombe (*R22, R24*), together with profile *R25* along the Lukenie river;
- the *N-S* Gilson-Samba combined land profile (*L60-50-51-52*), calibrated by the Gilson (4563 m deep) and Samba (2039 m deep) wells and intersected by three *E-W* oriented profiles (*R12, L63, L62*);
- a series of river and land profiles in the *NE* part of the basin, along the Tshuapa River between Bokungu and Ikela (*R15-9-10-16*) and across it (*L53-54*), along the Lomela River (*R13*) and near Opala on the Lomami River (*L55, L56*);
- Two long *SW-NE* profiles (*L59-L58*), calibrated by the Dekese well (1856 m deep).

All the seismic profiles with the raw seismic line, the interpreted seismic lines, and the depth-converted lines are displayed in the Appendix B. In the following sections, only detailed portions of some seismic profiles are presented, which illustrate the key features of the structure and stratigraphy of the *CB*. The sequence boundaries are laterally extensive basin-wide scale surfaces defining the strata discontinuity. This concept of sequence boundaries was used for lateral correlations in the interpretation of the low-resolution seismic data in the 1970's (Cartwright et al., 1998). Under higher resolution, these sequence boundaries appear as discrete surfaces of onlap, downlap, or toplap, thus representing more closely the real stratigraphy. With low vertical resolution as it is the case here, it becomes hazardous to determine accurately these types of surfaces, but also it becomes easier to make long-distance correlations (Cartwright et al., 1998). Therefore, in this study, the seismic sections are not discussed in terms of strata terminology, as used in modern seismic sequence stratigraphy, but rather in terms of basin-wide lateral correlations with eventually erosional truncation. In some places, the interpretation of the profiles can be hazardous and other interpretations are possible, because of the poor quality of some portions of the profiles, some gaps in the recording, and the junction between the lines. Therefore, other interpretations are sometimes possible.

2.4.1 Congo River seismic profile R7-6-3-5-19

This combined seismic profile, shot along the Congo River, shows an alternation of highs and deep depressions (up to nearly 10 km deep), corresponding from *SW* to *NW* to the Bololo Basin, Inongo High, Lokoro Basin, Kiri High and Busira Basin (Fig. 2.5). Line *R5*, as shown in Kadima et al. (2011a), has been used to calibrate the stratigraphy of the *CB* using the Mbandaka well in the Busira Basin (Fig. 2.5 c). This profile shows on the left (northern) side the full succession of the 8 seismic sequences overlying the acoustic basement in a sub-horizontal and undisturbed way.

There are a series of small reverse faults affecting the Proterozoic layers below the Pan-African unconformity, while the Paleozoic to Triassic sequences are only locally dislocated by younger faults. The highs are overlain by a regular cover of mostly undisturbed post-rift sediments, about 3 km thick over the Kiri High (Figs 2.5 b-c), thinning over the Inongo High (Fig. 2.5 a). Over these structural highs, the syn-rift sequences (*S0, S1*) are almost absent, as well as the entire Paleozoic to Triassic sequences (*S4, S5*). The rift clastics (*S0)* are absent in the Lokoro Basin, south of the Kiri High (Fig. 2.5 b), while they reach up to 23 km thick in the Busira Basin, north to the Kiri High (Fig. 2.5 c). In contrast, the dolomitic limestones (*S1*) are present in the basins on both sides of the Kiri High. Detailed seismic interpretations (Fig. 2.5 b-c) suggest that the synrift sequences do not onlap against the high and/or are not condensed over its top.

The sudden transitions with the adjacent Lokoro (Fig. 2.5 b) and Busira basins (Fig. 2.5 c) were interpreted by Daly et al. (1992) as controlled by normal faulting during the initial failed rift stage, but the seismic profiles do not show clearly the existence of such normal faults. Above the Kiri High (Figs. 2.5 b-c), there are about 2 km of Neoproterozoic sediments (*S2* and *S3*), directly overlying the crystalline basement. The Red Beds (*S4*) overly the Pan-African unconformity along the Kiri High and in adjacent basins with a similar thickness, except for the southern side, where they were probably partly eroded. The Karoo sediments (*S5*), which form a thick layer in all the basins, are instead only present over the Kiri High as a thin sheet on its northern side and are absent on its southern side. The Pan-African unconformity appears weakly marked and passively deformed (Figs. 2.5 b-c). In contrast, the Basal Jurassic unconformity truncates the Paleozoic sediments over the Kiri High and marks the expansion of the basin by regular sedimentation over the deformed pre-Jurassic part of the basin. This pattern led Daly et al. (1991, 1992) to suggest a contraction deformation or 'inversion' of the Kiri High in the late Paleozoic, controlled by the pre-existing "rift" structures, inherited from the initial opening of the *CB*. The latter would have caused uplift of the Kiri High and overlying sediments, which were partly eroded before the deposition of the Jurassic sediments. As there is no clear evidence for a rift structure in the seismic profiles, here the preferred hypothesis is to consider these structures as a product of compressional reactivation of a structure formed during the rift phase, instead of inversion.

As alternative interpretation, the termination of sequences *S0* and *S2* against the Kiri High can also be interpreted as due to a normal fault, but the quality of the profile at that depth does not allow confirming it. All the tectonic structures identified along the combined line remained inactive since the Jurassic, as indicated by the Jurassic to Paleogene layers, lying undisturbed over the Basal Jurassic unconformity over the entire line.

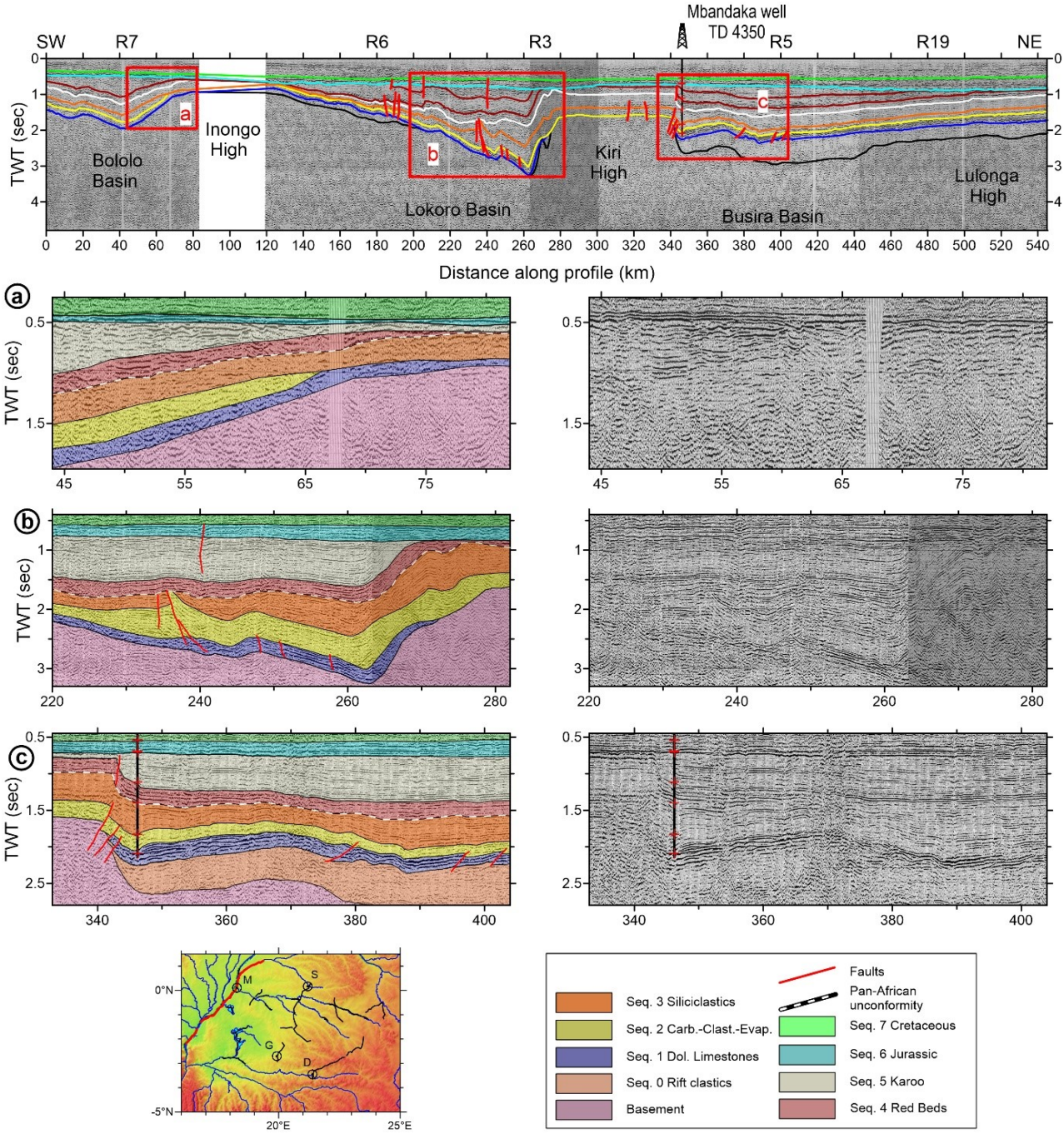

Figure 2.5. *Interpreted seismic profile of combined river lines R7-6-3-5-19 along the Congo River with details of three zones (a-c).* ***Upper****: interpreted profile.* ***Middle****: details with superimposed interpretation (left) and raw profile (right).* ***Lower/Bottom****: profile location and legend. Color of seismic horizons as in Fig. 2.2 (Delvaux et al., 2021).*

2.4.2 Gilson-Samba seismic profile L60-50-51-52

This seismic profile with combined landlines, calibrated by the Gilson-1 and Samba wells, provides a general *SW-NE* section across the central part of the *CB* (Fig. 2.6). It shows a significant lateral variability of the depth of the basement and thickness of the sedimentary sequences up to the Basal Jurassic unconformity. There is unfortunately a gap in seismic recording approximately the Gilson well, but recording was good at the Samba well. On the southern extremity of the profile, just south of the Gilson well, a zone of tectonic deformation caused uplift of the northern compartment (with the Gilson well area) relative to the southern extremity of the profile (Fig. 2.6 a). It affected the entire Proterozoic and Paleozoic series causing a general bending of the Pan-African unconformity, amplified by top-to-the-south reverse and thrust faulting. In contrast, the Basal Jurassic unconformity is not affected.

The Karoo series appear to thicken markedly at the southern extremity of the profile. The possible limit between the Permian Lukuga Group and the Triassic Lueki Group, based on the interpretation of the Gilson well is indicated (Fig. 2.6 a). However, this is poorly constrained, due to the lack of bio-stratigraphic control (Linol et al., 2015 b) in this well. Between km 60 and 100 along profile *L60*, the basement and the overlying very thin rift clastics and dolomitic limestones (sequences *S0-S1*) are deflected downward and deepen up to a maximum depth of about 11 km (Fig. 2.6 b). This area corresponds to an important over thickening of the Neoproterozoic series (sandstones and shales, rare limestones in the well) over a distance of 50 and 100 km along the profile. The Karoo sediments appear truncated by the Basal Jurassic Unconformity. After a hiatus in the profile, the *N*-trending line *L50* shows an intensely folded and faulted crystalline basement and overlying Proterozoic series (*S0-S3*), truncated by the Pan-African unconformity (Figs. 2.6 c-d). This one, in turn, has been (more locally) deformed in continuity with the deformations underneath. This illustrates the presence of well-developed Pan-African compressional structures (reverse faulting and folding) in the center of the basin and suggests a reactivation and influence of these structures on the further evolution of the basin during Paleozoic-Triassic times (sequences *S4-S5*).

Above the Basal Jurassic unconformity, the Jurassic to Paleogene sediments (sequences *S6-S7*) are mainly concordant with the underneath ones. The Samba well in the northern extremity of the section (line *L52*) fixes the limit between the Jurassic-Paleogene sequence (*S6*) and the Red Beds (*S4*) at 1167 m, since the Karoo (*S5*) is entirely missing.

The red sandstones present until the well bottom (2038 m) represent the upper part of the Red Beds (the Samba-Dekese Group as defined below). A pronounced reflector just below the bottom of the Samba well can be identified which correlates with the Pan-African unconformity recognized on the left (southern) side of line *L51* (Fig. 2.6 e). On this segment, the dolomitic limestones and overlying Neoproterozoic series are affected by thrusting deformation, truncated by a prominent reflector in continuity with the Pan-African unconformity seen in line *L50* (Figs. 2.6 c-d).

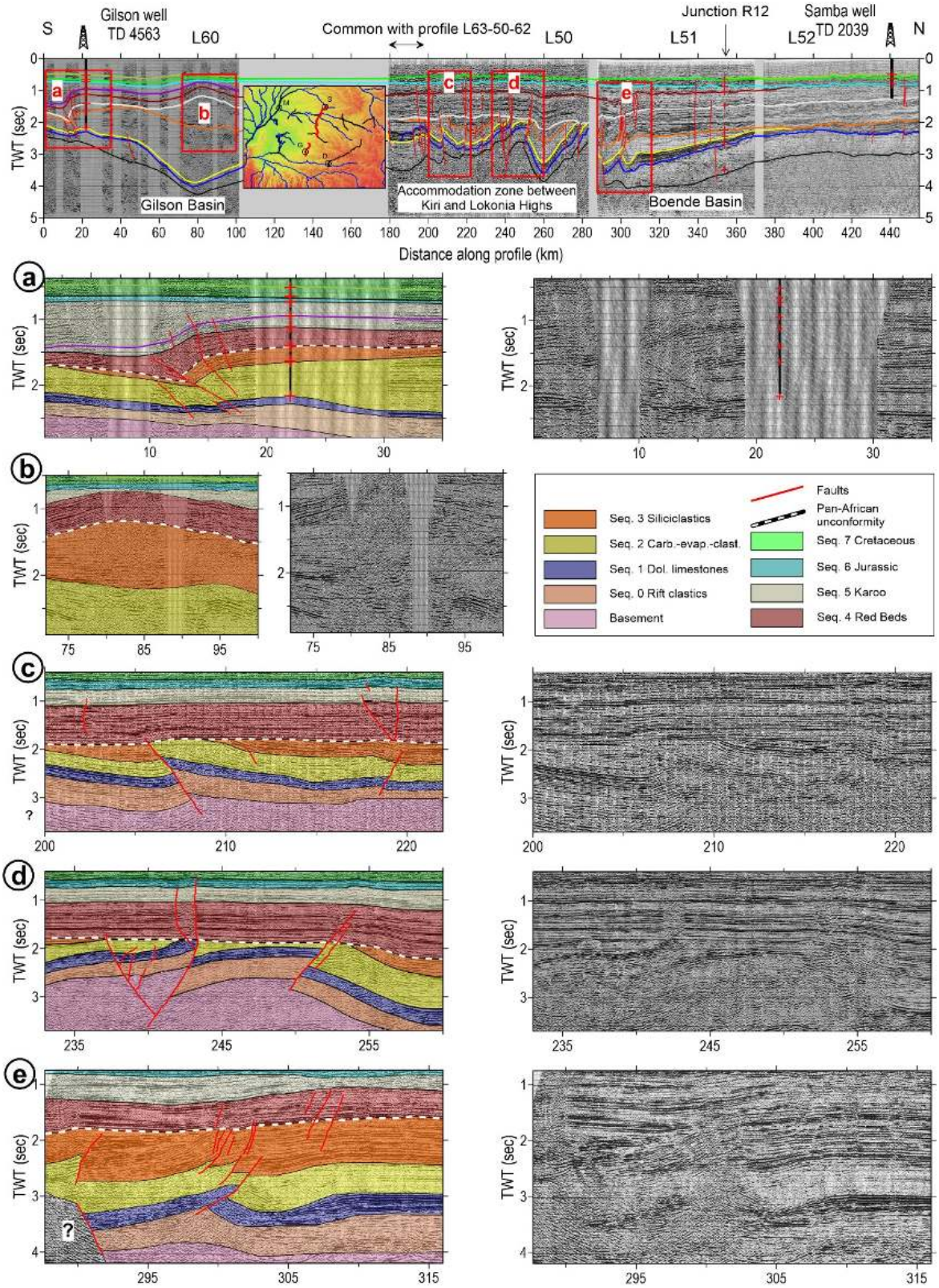

Figure 2.6. *Interpreted seismic profile of combined land lines L60-50-51-52, crossing the Gilson and Samba wells with details of five zones (a-e).* ***Upper****: interpreted profile with location of the profiles.* ***Middle/Lower/Bottom****: details with superimposed interpretation (left) and raw profile (right) with the legend. Part of seismic line L50 is common with profile L63-50-62 (Fig. 2.7, details in 8b). Color of seismic horizons as in Fig. 2.2 (Delvaux et al. 2021).*

2.4.3 E-W combined seismic profile L63-50-62

This seismic profile with combined land lines cross-cuts the previous one in a general E-W orientation (Fig. 2.7), with part of line *L50* in common with profile *L60-50-51-52*. It shows the Pan-African unformity truncating the entire Proterozoic sequences (*S0-S3*). The Neoproterozoic sequences (*S2-S3*) are present only in the central part, as a large and flat depression. On the western side, the Red Beds (*S4*) rest directly over the basement (Fig. 2.7 a) and over the late Mesoproterozoic dolomitic limestones (*S1*) on the eastern side (Fig. 2.7c). The rift clastics (*S0*) are particularly well developed in the central part of the profile and seem to strongly thicken on the *SE* extremity of line *L62*. Here, the deep reflectors are not so clear, but around 120 km along the profile one notices an upwarp deflection of the seismic reflector which then deepens strongly until 130 km (Fig. 2.7 c). This implies that there should be a deep depocenter (Salonga Basin) that developed during the initiation of the basin and accomodated a great thikness (4-5 km) of rift clastics. In line *L50*, the dolomitic limestones layer appears slightly deformed by fault-assisted kinking (Fig. 2.7 b). This deformation does not affect the Pan-African unconformity, but some possible faulting could also exist above it, in the Red Beds and the Karoo.

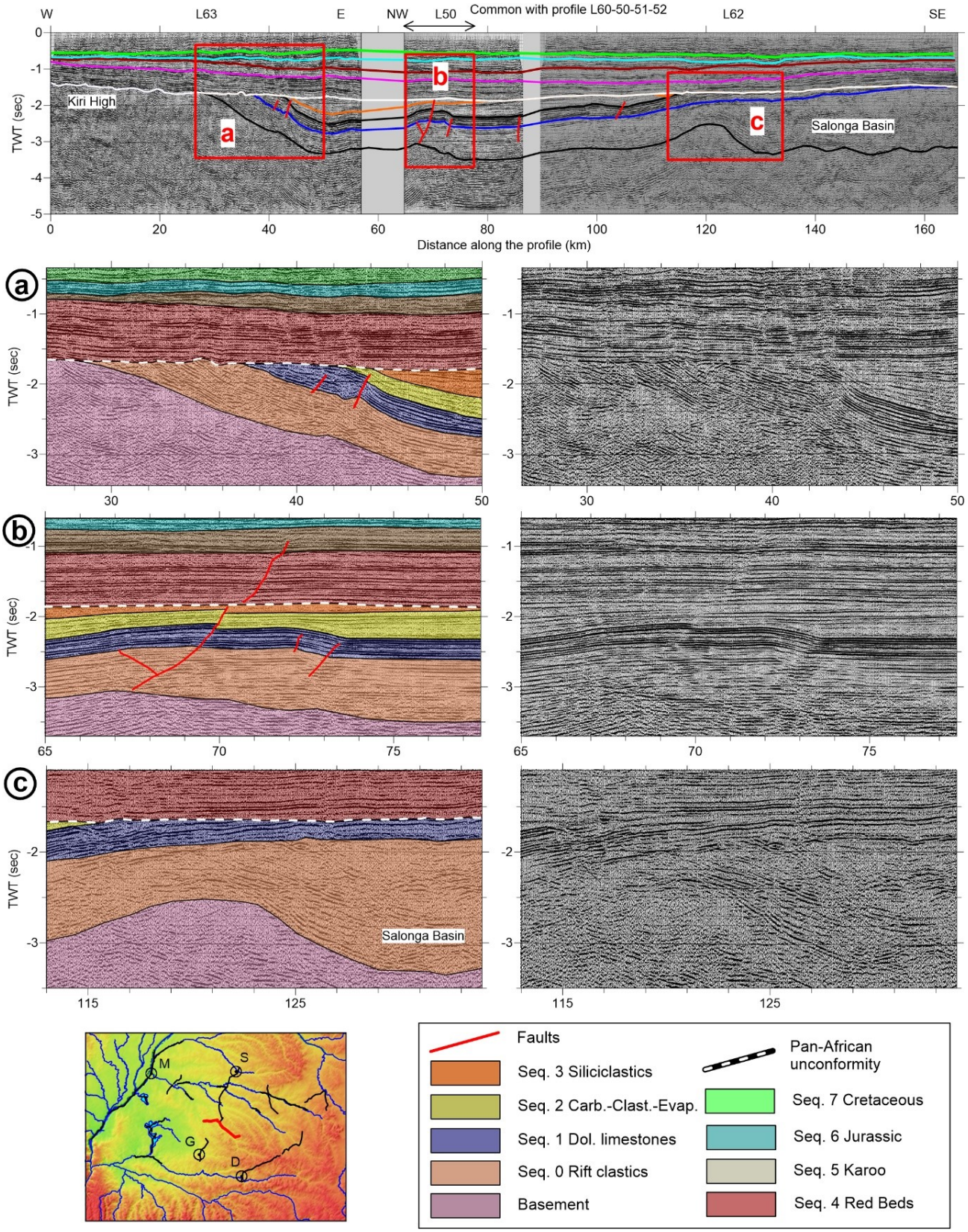

Figure 2.7*. Interpreted seismic profile of combined land lines L63-50-62 with details of three zones (**a-c**). **Upper**: interpreted profile. **Middle**: details with superimposed interpretation (left) and raw profile (right). **Lower/Bottom**: location map and legend. Part of seismic line L50 is common with profile L60-50-51-52 (Fig. 2.6). Color of seismic horizons as in Figure 2.2 (Delvaux et al. 2021).*

2.4.4 Dekese seismic profile L59

This *SW-NE* oriented profile, located in the southeastern part of the *CB* (Fig. 2.8), passes through the Dekese well. The rift clastics reach a thickness of more than 2.5 km in proximity of the Dekese well (Fig. 2.8 a). This depocenter, named Dekese Basin, reaches a maximum depth of about 8 km. Between 100 and 130 km along the profile, the Pan-African unconformity truncates the folded Neoproterozoic sequences (Fig. 2.8 b). Possible onlap of the siliciclastics (*S3*) above the carbonates-clastics (*S2*) at 118-120 km along the profile (white arrow) would suggest deposition of the siliciclastics during deformation. Some small-scale compressional deformation (folds and reverse faults) affects the carbonate level (*S1*), suggesting it behaved during deformation as a mechanically strong layer between weaker layers (km 140-150 along the profile, Fig. 2.8b). The Dekese well, on the *SW* edge of the profile, is located in a highly perturbed zone of the profile, most likely corresponding to a zone of intense tectonic deformation (Fig. 2.8 a). The drill cores of the well show locally intense deformation by folding and faulting, mainly in the Karoo sequence, where some large parts reach verticality. These deformation signs have sometimes been interpreted as due to glacial-tectonic movements (Giresse, 2005; Linol et al., 2015b), but a detailed re-examination of the structures in the cores suggests rather a tectonic origin (Delvaux et al., 2015). It caused also the uplift of the northern part relative to the southern part, involving the basement as seen in the southern extremity of line *L60* near the Gilson well. The syn-rift sediments (*S0-S1*) are reduced to a thickness of few hundred meters in the *SW* side of the profile (toward the Kasaï Craton). They seem partly eroded under the Pan-African unconformity on *NE* side (Lokonia High). The sedimentary sequences deposited above the Pan-African unconformity appear almost undisturbed.

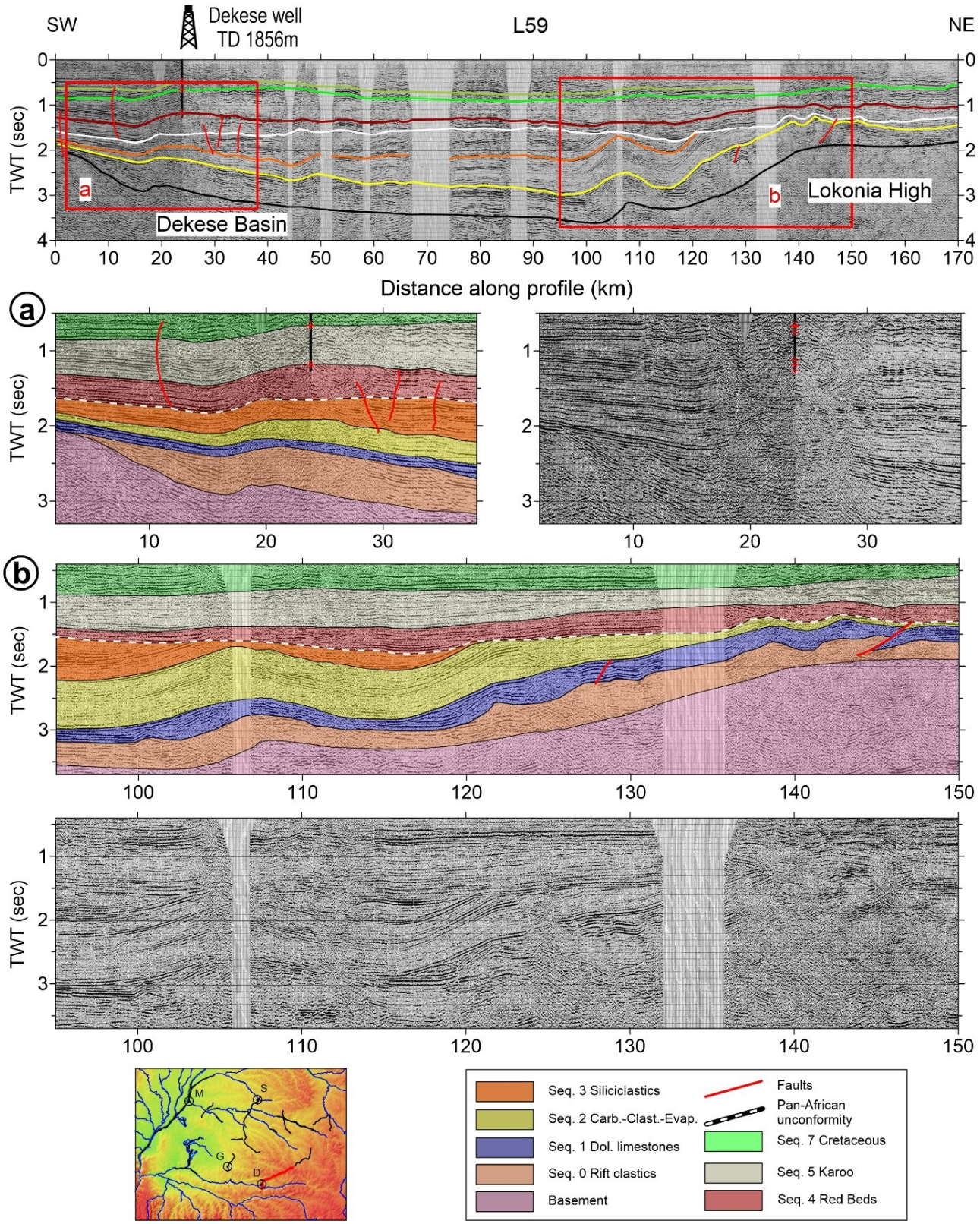

Figure 2.8. *Interpreted profile of land seismic lines L59 trough the Dekese well, with details of two zones (a-b).* ***Upper****: interpreted profile.* ***Middle****: details with superimposed interpretation (left/above) and raw profile (right/below).* ***Bottom****: location map and legend. Color of seismic horizons as in Figure 2.2 (Delvaux et al., 2021).*

2.4.5 Tshuapa River seismic profile R15-9-10-16

This combined WNW-trending profile (Fig. 2.9) is located in the northeastern part of the *CB*, along the Tshuapa River between Boende and Ikela. It shows a long-wavelength anticlinal folding of the entire Precambrian-Paleozoic series (*S0-S5*), which appears regularly stratified. The anticline forms an elevation (Maringa Ridge), which has been truncated by the Basal Jurassic unconformity. It extends laterally in the direction of the *L53* and *L54* seismic lines and thus has a *NW-SE* axis. The southeastern flank of the anticline shows minor faults and reverse faults in the dolomitic limestones level (*S1*). In the central and southeastern part of the profile, the sedimentary sequences lie horizontally undisturbed, forming the Lomami Basin.

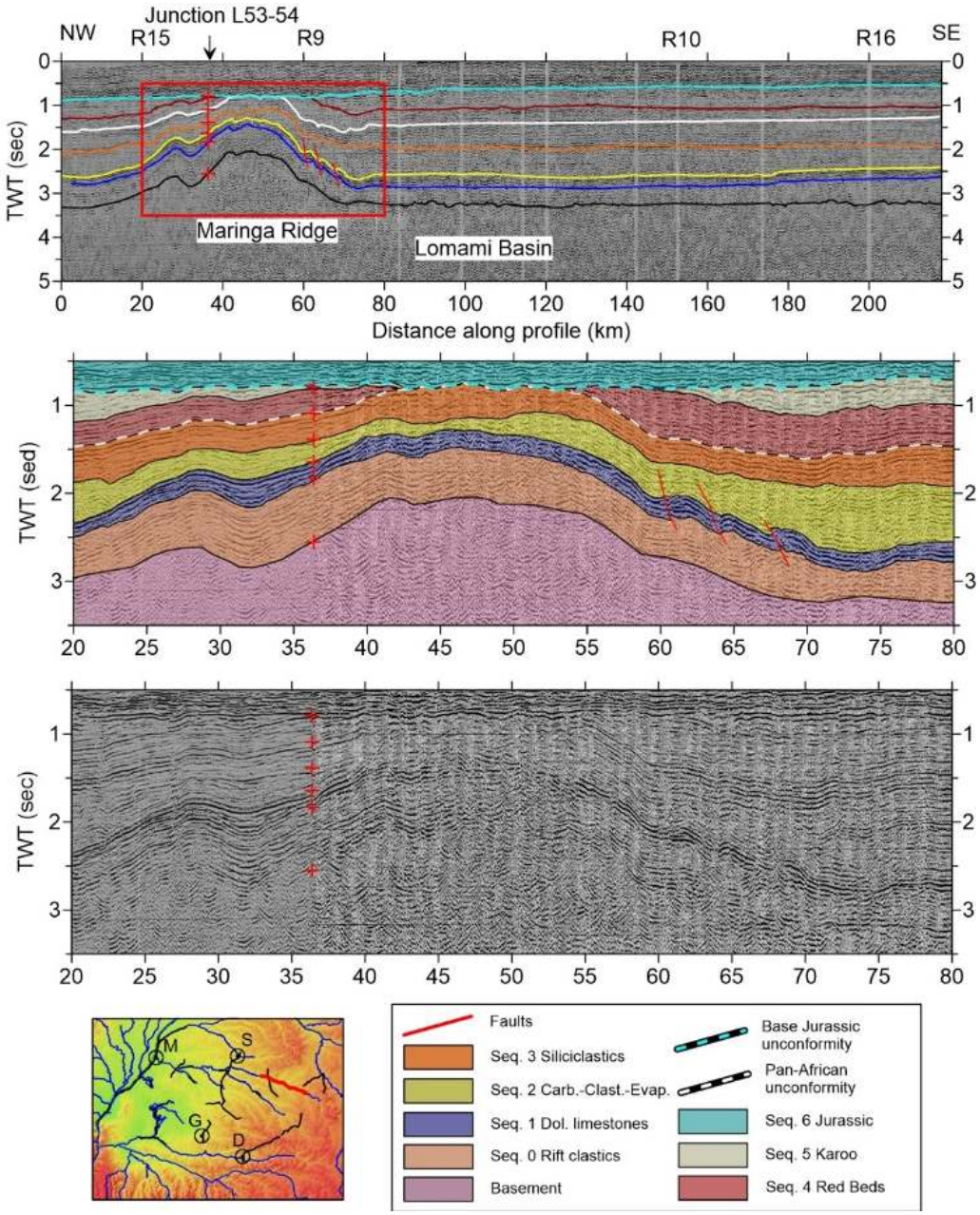

Figure 2.9. *Interpreted seismic profile of Composite River lines R15-R9-R10, with detail of the zone around the Maringa Ridge anticline.* ***Upper****: interpreted profile.* ***Middle****: details with superimposed interpretation.* ***Lower****: raw profile.* ***Bottom****: location map and legend. Color of seismic horizons as in Figure 2.2 (Delvaux et al. 2021).*

2.4.6 Lake Mai-Ndombe seismic profile R22

Along Lake Mai-Ndombe in the southern part of the *CB*, the *NE*-trending line *R22* (Fig. 2.10), shows a northeastward deepening of the basement from about 3.5 to 6.5 km and of the overlying sedimentary sequence. In the northeastern part of the profile, until the junction with line *R21b*, we observe a pattern of small faults dislocating the late Mesoproterozoic dolomitic limestones (*S1*) and overlying Neoproterozoic sediments, while the sedimentary sequences above the Pan-African unconformity lie undeformed. This suggests that the carbonates layer formed a more competent layer relative to the surrounding ones during the Pan-African deformation.

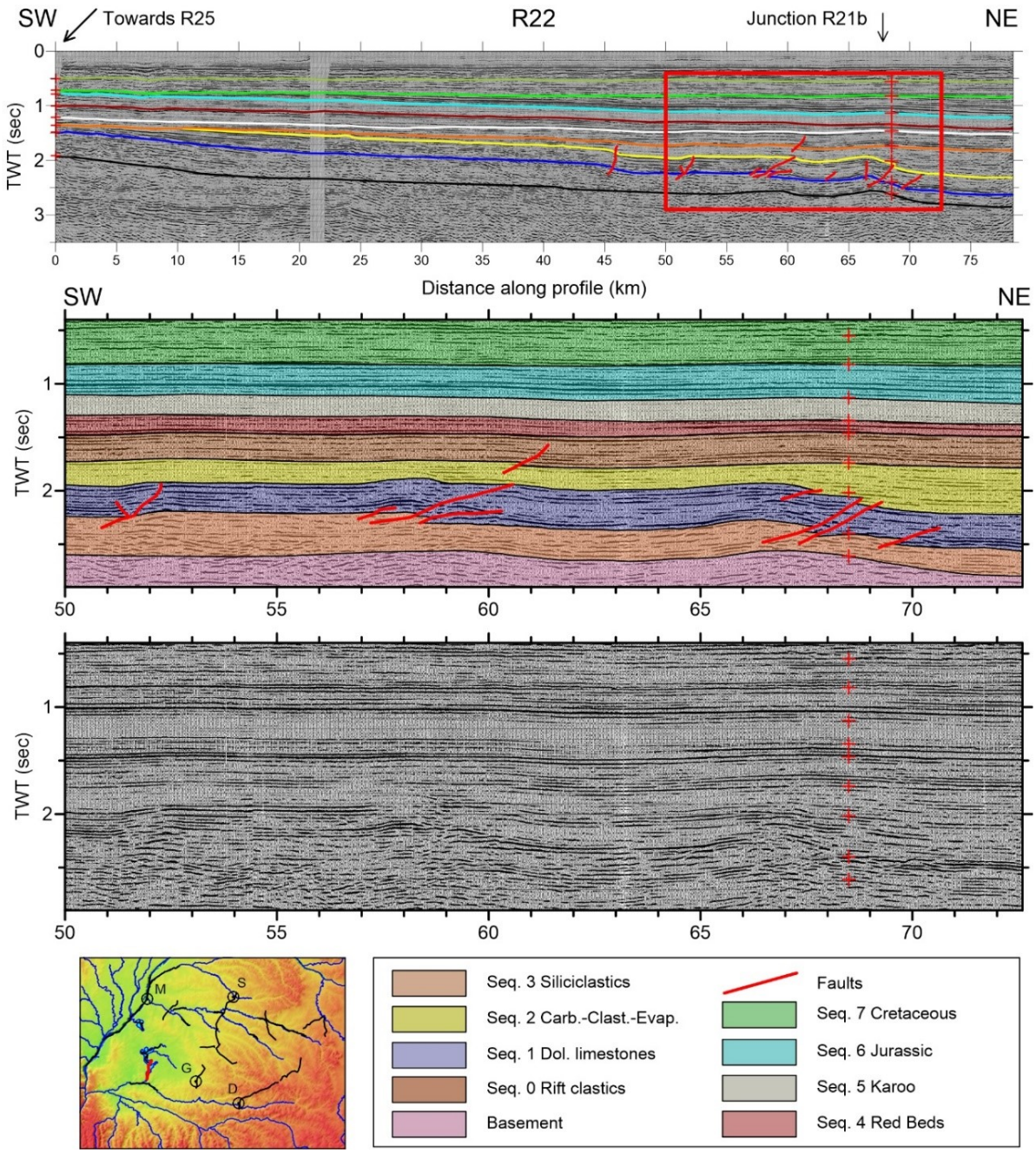

Figure 2.10. *Interpreted profile of land seismic line R22 with detail of the deformed dolomitic limestones sequence.* ***Upper****: interpreted profile.* ***Middle****: details with superimposed interpretation.* ***Lower****: raw profile.* ***Bottom****: location map and legend. Colors are referred to Figure 2.2 (Delvaux et al. 2021).*

2.5 3D model of sediments from seismic reflection interpretations

All the interpreted seismic horizons converted to depth were interpolated using a standard kriging method (*SURFER*, Golden Software package) with a grid spacing of 0.05 degree (about 5.5 km) to generate depth maps of the main seismic horizons, *R0*-*R5* and *R7* (Fig. 2.12). The R6, R8, and R9 seismic horizons, dividing the Karoo and the Mesozoic, have not been recognized in all seismic lines and thus have not been computed. The thickness of the seismic sequences (isopach maps) has been further derived by making the difference between the depth maps of the top and bottom layers. They were computed for each sequences (*S0*-*S7*, Fig. 2.13) and for groups of sequences, obtained considering the four main stages of evolution of the basin (Seq.*S0*-*S1*, *S2*-*S3*, *S4*-*S5* and *S6*-*S7*). They reveal a different behavior of the basin during the successive stages of evolution, with a progressive decrease in the influence of the initial rift structure. Both depth and isopach maps are limited to the data available, between 1.4°*N*-3.8° *S* and 16°*E*-24.5°*E*.

2.5.1 Top of basement architecture and main sedimentary depocenters

The top of the basement depth (reflector *R0*) shows significant variations, with major and minor elevated zones, alternated by several sedimentary depocenters (Fig. 2.11). The *NW*-*SE* Kiri High, well expressed between the Congo River and Line *L63* in the center of the basin, separates the *CB* into two parts. It appears formed by two domes, in the places constrained by data, separated by a saddle, where there are no data. I interpreted this last feature as an artefact of the interpolation and assumed that the Kiri High is probably a continuous high between the Congo River and Line *L63*. In the eastern side of the basin, the Lokonia High appears in a similar orientation as the Kiri High, but with a shift to the north. The relay zone between the two is illustrated by the intensely deformed seismic line *L50* Line (Fig. 2.6). I consider the Kiri and Lokonia Highs as basement highs, in which the basement is elevated respectively to 2.7 km and 1.4 km below the topographic surface. They are interpreted by Daly et al. (1992) as shortened and uplifted parts of the basin during contraction tectonic events. The poorly defined seismic pattern in the core of these uplifts are considered by Kadima et al. (2011a) as indicative for salt pillows within sedimentary layers. However, I do not see signs for salt tectonics with diapirs above these structures, nor evidence for detachment due to a ductile salt layer. The presence of thin salt layers is possible, as found in the bottom of the Mbandaka well, drilled in the Busira Basin, they are probably of relatively small thickness and interlayered with carbonates and clastics.

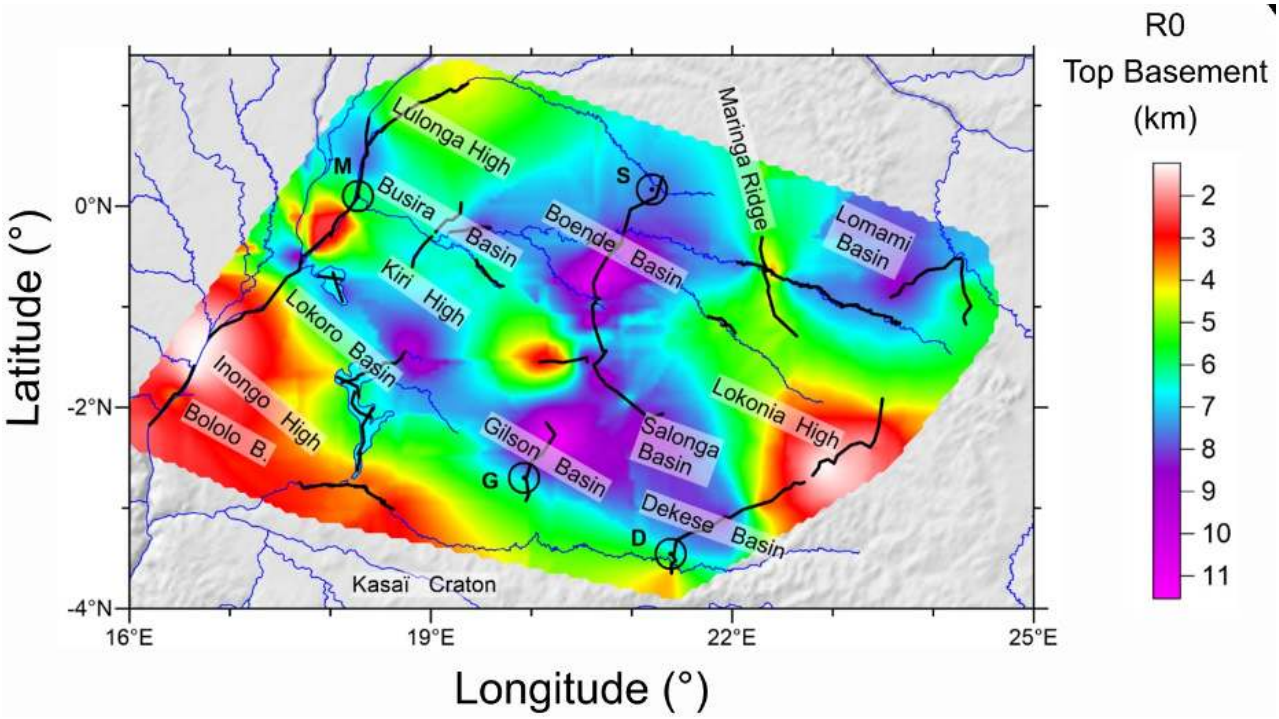

Figure 2.11. *Main tectonic structures identified at the depth of the top of the basement. Broken white lines show location of the seismic reflection profiles. Black circles show the location of the four wells drilled in the study area: D= Dekese; G=Gilson-1; M=Mbandaka-1; S=Samba. (Delvaux et al. 2021).*

The *NW-SE* oriented central elevated zone, formed by the Kiri and Lokonia Highs, separates the *CB* into two major depocenters. On the *SW* side, the depocenter is defined by a continuous alignment of three basins (Lokoro, Gilson, and Dekese basins), with a maximum depth of 11.5 km observed in the Gilson Basin. It is limited to the SW by the Inongo High and, further to the south, by the Kasaï Craton, which rises below the Karoo to the Cretaceous cover. The Lokoro Basin is composed of two main depocenters, one very large in the south (~ 10 km deep) and another smaller and shallower (~ 8 km deep) in the north. The deep Salonga Basin lies in the alignment of the Kiri High, after the relay zone between the Kiri and Lokonia Highs. On the northern side of the axial magnetic zone, the Busira Basin (7.6 km deep) is flanking the Kiri High. The large Boende Basin (10.6 km deep), well evidenced in the seismic line *L51*, is separated from the Gilson Basin by the Kiri High - Lokonia High relay zone. The Lomami Basin (8.6 km deep) on the *NE* extremity is separated from the Boende Basin by the Maringa Ridge. The last one appears to result from an anticlinal folding, followed by erosion of the complete pre-Jurassic series, before the deposition of the Jurassic-recent series (lines *R15-9-10-16*, Fig. 2.9). Therefore, the Boende and Lomami basins could have been formed initially as a single large basin.

2.5.2 Evolution of the depocenters with time

The results of the interpolation of the seismic reflection profiles for the different seismic horizons show the migration of the depocenters from the Proterozoic to Jurassic times (Fig. 2.12) and the lateral thickness variations of the different sedimentary layers (Fig. 2.13).

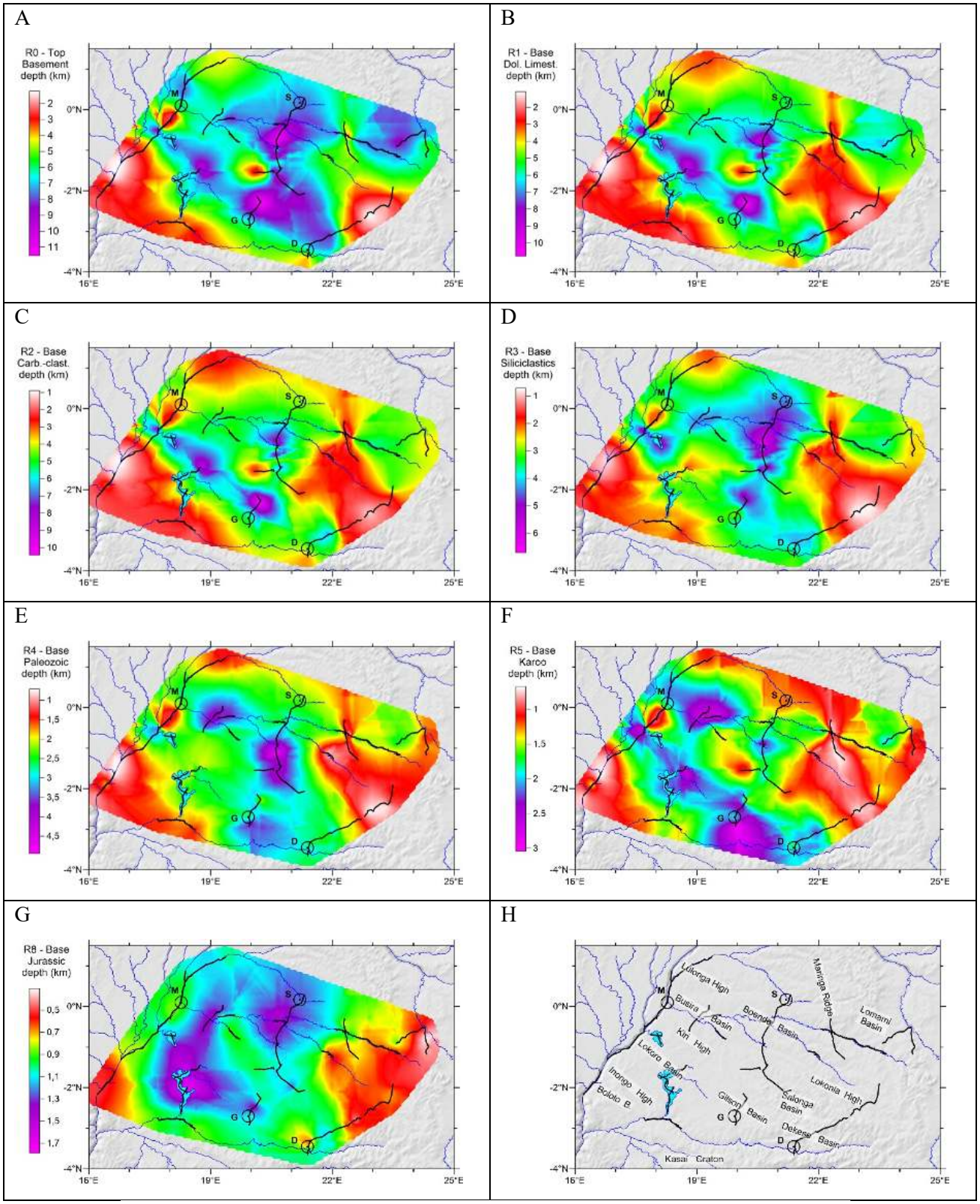

Figure 2.12. *Depths maps of the main seismic horizons (**A-G**). Names of the CB structures (**H**). Broken black lines show location of the seismic reflection profiles (Delvaux et al. 2021).*

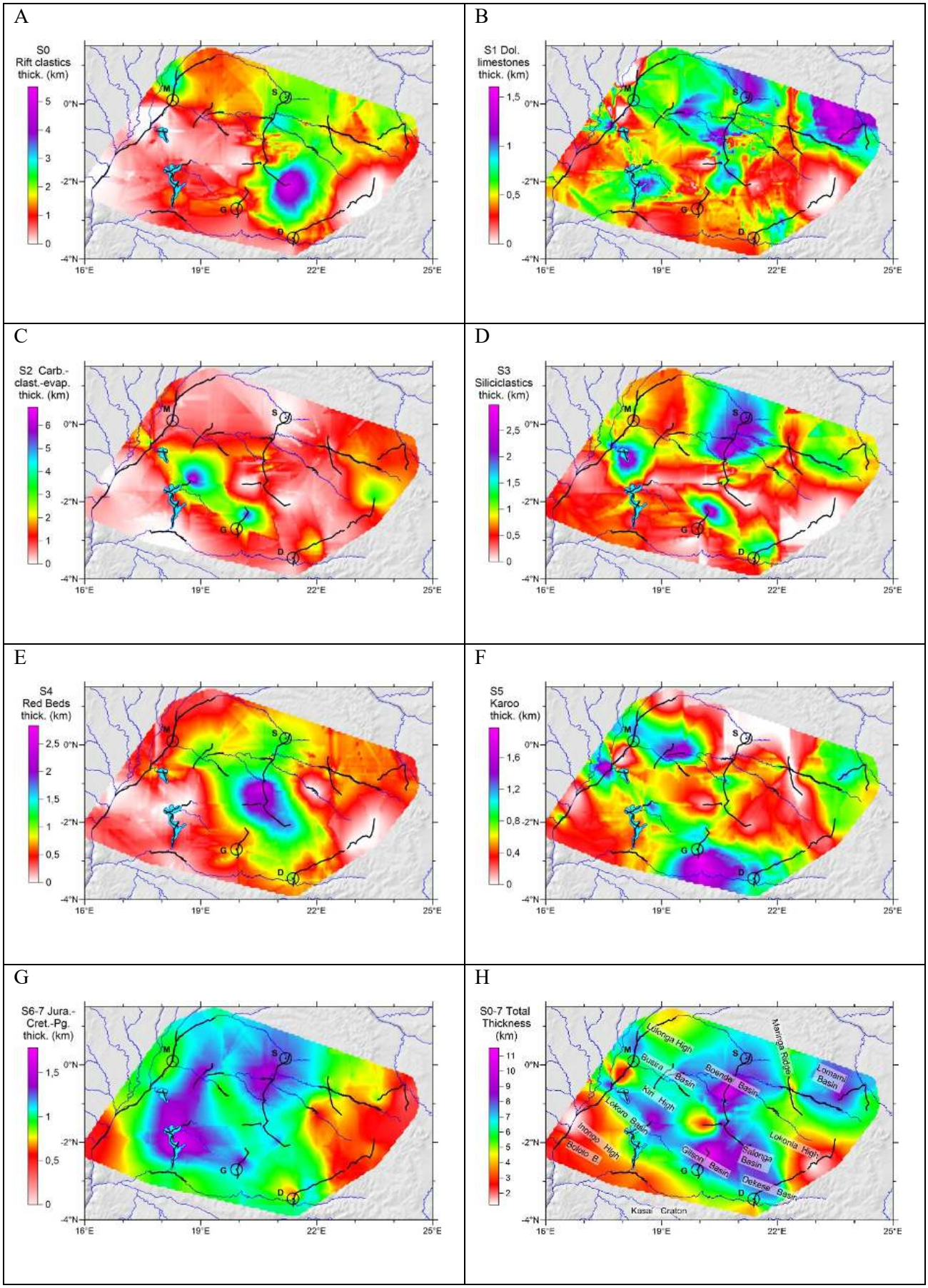

Figure 2.13. *Thickness maps (isopach) of the main stratigraphic sequences (**A-G**) and of the total sedimentary fill, with the names of the CB structures (**H**). Broken black lines show location of the seismic reflection profiles (Delvaux et al. 2021).*

2.5.3 Late Mesoproterozoic rifting (Sequences S0 and S1)

The sequences *S0* and *S1* (Fig. 2.13 a-b) have been proposed to correspond to the initial failed rift stage, of possible late Mesoproterozoic age. The Kiri High is devoid of late Mesoproterozoic sediments, as shown by the seismic line *R3* (Fig. 2.6 b) and the western half of line *L63* (Fig. 2.7 a). Between these two lines, I assume a similar situation, even if the interpolation suggests some sediment. As explained above, this might be an artefact of the interpolation. This indicates that the Kiri High appeared during the rifting stage of the *CB*. It separates the basin into two large depressions from the beginning of its history. Globally, the *CB* is asymmetric at this stage, with the northern depression shallower than the southern one. The Kiri High extends laterally to line *L63* in the center of the basin and forms a left-stepping relay with the Lokonia High (Fig. 2.11). The rift clastics (*S0*) are thicker in the northern part of the *CB*, immediately against the Kiri High, and become especially thick north of the Mbandaka well, in the Busira Basin. South of the Kiri High, the rift clastics are present as a blanket in the region of Lake Inongo (group of profiles *R21-25*). The over-thickening in the Salonga Basin appears to be caused by important subsidence at the time of deposition of the rift clastics, close to the relay zone between the Kiri and Lokonia Highs. The Dolomitic limestones (*S1*) are absent over the Kiri and Lokonia High and have a relatively constant thickness over the rest of the basin, fluctuating between 0.5 and 1 km. They have their greatest thickness in the northern part of the basin, where they reach up to 1.6 km.

2.5.4 Neoproterozoic post-rift evolution (sequences S2 and S3)

During the Neoproterozoic, the geography of the basin changed and new basins developed. Sequences 2 and 3 (Fig. 2.13 C-D) are the thickest in the southern depressions (Lokoro and Gilson basins), close to the Kiri High and also in the Boende Basin. The Lokoro Basin accumulated up to 6 km of carbonates-clastics (*S 2*) and the Gilson Basin, up to 5 km (Fig. 2.13 C). The Boende Basin started to develop during the deposition of the siliciclastics (*S3*), and the two others (Lokoro and Gilson) continued to accumulate sediments with about 2.5 km in all the tree basins, Fig. 2.13 D). The rest of the *CB* accommodated a much smaller thickness (about 2 km), with a maximum of 3.2 km in the Lomami Basin and a similar thickness over the Kiri High and the Busira Basin north of it (line R5, Fig. 2.6 c). Over the Kiri High, they cover directly the basement (Line *R3*, Fig. 2.6 b). The depocenter of the Lokoro Basin fluctuated in time, with the deepest part on the eastern side (line *R24*), during deposition of *S2* and then in the western side (Lake Tumba), during deposition of *S3* (Fig. 2.12 C-D). The post-rift sequences are locally not present over the eastern extremity of the Kiri High (Line *L63*; Fig. 2.7 a) and some parts of the Lokonia High (Line *L59*, Fig. 2.8 b) and the Salonga Basin (line *L63*, Fig. 2.7). They might have been deposited and removed after the Pan-African deformation, as the Pan-African unconformity truncates the entire Proterozoic sequences.

2.5.5 Paleozoic post-orogenic and deglacial sedimentation (sequences S4 and S5)

After the Pan-African orogenic period, the configuration of the CB changed drastically. During the deposition of the Red Beds (*S4*; Fig. 2.13 E), the depocenter, migrated towards a central *NW-SE* oriented depression, opens towards the north. This depression, centered on lines *L50*, *L60*, *L62*, and *L63* (Fig. 2.6-2.9) lies between the Boende and the Gilson basins, with a maximum of 2.8 km of sediments. During the Karoo period (*S5*; Fig. 2.13 F), depocenters developed between the Gilson and Dekese wells in the south (1.97 km deep), against the Kasaï Craton and in the Busira and Lokoro basins on both sides of the Kiri High. Little sediments were deposited in the area of the former depocenter of the Red Beds. No angular unconformity can be observed on the seismic profiles between the Red Beds and the Karoo sequences. Instead, as mentioned above, I observe a sedimentary hiatus with evidence of erosion in the Dekese well at 1677 m deep.

2.5.6 Jurassic-Cretaceous transgressive cover (sequences S6-S7)

The late Jurassic-Cretaceous-Paleogene sequences (*S6-S7*) form a transgressive cover over the Basal Jurassic unconformity (Fig. 2.13 G-H). Sedimentation was no more influenced by the initial rift structure. The depocenter of the *CB* now lies in the region of Lake May Ndombe with a maximum of 1.8 km of sediments (group of lines *L21-24*). It extends across the Kiri High towards the in the Busira Basin (lines *L64-65*). Another depocenter developed over the Boende Basin (lines *L51-52* and *R12*), with a maximum of 1.4 km of sediments.

2.6 Tectono-stratigraphic evolution of the Congo Basin

The *CB* had a long-lived evolution in an intracontinental setting at the center of the Congo Craton that stabilized during the Mesoproterozoic. Since then, it recorded a long geological history driven by global processes (plate tectonics and climate change) with several episodes of basin subsidence and sedimentation in intracontinental settings, interrupted by tectonic and erosional events (Pan-African near field, Gondwana far field). Sedimentation was also controlled by global climatic fluctuations and affected by several Ice House events. The stratigraphy of the *CB* is confirmed with the subdivision into three major units, representing the Proterozoic, Paleozoic-Triassic, and the Jurassic-Cretaceous sediments (Kadima et al., 2015). They are separated by two major tectonic unconformities at the Neoproterozoic-Paleozoic transition (related to the Pan-African deformation) and at the Triassic-Jurassic transition (related to far-field intraplate compression).

The initial rift and post-rift phases in the Meso- and Neoproterozoic produced significant subsidence of the basement in the northern part of the basin, where it currently reaches an average depth of 7-8 km (Fig. 2.11). In most of this area, the sedimentary sequences appear unaffected by successive tectonic events and the basement depth is sub-horizontal or shows small undulations, likely reflecting inherited heterogeneity. In the same area, the syn-rift clastics and carbonate ramp layers are well developed and they reach an average thickness of 3 km. The overlying Proterozoic sediments reach a thickness of 4-5 km (Fig. 2.12 C-D). The thickness maps of the main stratigraphic units show that the migration of the depocenters with time was clearly influenced by the *NW*-trending Kiri basement High, and to a lesser extent, the Lokonia High that are considered to be the axial magnetic zone of the paleo rift (Kadima et al., 2011b) that separates the *CB* into two parts (Fig. 2.13). The Kiri High had a strong control on the sedimentation and basin architecture during the late

Mesoproterozoic and Neoproterozoic. This control weakened during the Paleozoic and Mesozoic. The basin sedimentation and structure have been further influenced by global climate fluctuations (ice/greenhouse ages), the paleo-geographic position of the *CB* (South Pole to the Equator), as well as by tectonic phases (folding and thrusting) and local/regional denudation stages.

2.6.1 Late Mesoproterozoic basin initiation

The age of initiation of the *CB* remained controversial for a long time, but tends to get older with the increasing geological knowledge and data analyses. It was initially considered Carboniferous to recent (Veach, 1935; Cahen, 1954; Lepersonne, 1977), as these authors considered that the pre-Carboniferous sediments were part of the "Congo platform cover". After integration and synthesis of the results collected during the second exploration campaign and by correlation with the Lindian studied by Verbeek (1970), the *CB* was considered Neoproterozoic in age (Chorowicz et al., 1990; Daly et al., 1991, 1992). More recently, Delpomdor et al. (2013b) correlated the basal series of the *CB*, within the failed rift basin of Kadima et al. (2011a), with the Mbuji-Mayi Supergroup, which could represent its outcropping southeastern prolongation. The data that I analyzed also support this correlation, but Delpomdor et al. (2013b) puts the age of the of *BII* group of the Mbuji-Mayi Supergroup between 750 and 880 Ma, contemporaneous with the break-up of Rodinia and the initiation of the Katanga Basin (Cailteux and de Putter, 2019). However, François et al. (2017) dated the Mbuji-Mayi Supergroup between 1065 and 1000 Ma, (Stenian, Upper Mesoproterozoic), thus before the main collisional events at about 1000 Ma that led to the Rodinia supercontinent assembly (Li et al., 2008).

The initiation of the *CB* could therefore be contemporaneous with the Taoudeni Basin (Martin-Monge et al., 2016; Beghin et al., 2017a, b). It cannot be related to the initial Neoproterozoic divergence that occurred along the southern margin of the *CB*, recorded in the Zambezi and Lufilian basins belts between 880 and 820 Ma (first rift cycle of de Waele et al., 2008). Four main depocenters where the basement reaches very large depths between 9 and 11 km have been identified. The Lokoro Basin and the combined Gilson, Dekese and Salonga basins flank on the southern side the Kiri and the Lokonia Highs, while the Boende and Lomami basins flank these highs on their northern side. The latter two could have formed initially as a single large basin, now disrupted by the Maringa Ridge. This alternation of highs and deep basins, *NW-SE* oriented, is already known since the time of the first explorations in the *CB* (e.g., Cahen, 1956; Kadima et al., 2011a). However, in the frame of the study of which this thesis is one part, new basins were identified, such as the Dekese and Salonga basins with a total sedimentary infill of about 7 km.

The difference in the shape of the basins and thickness of the syn-rift sequences can be attributed to a non-uniform syn-rift extension, which affected more the northern than the southern part of the *CB*. Another hypothesis is that inherited heterogeneity of the basement, derived from different cratonic nuclei, influenced the shapes and sizes of the basins formed in response to uniform (or non-uniform) extension, as well as the thickness of syn-rift sediments (Chapter 3). This would explain the great thickness of syn-rift sediments in the Salonga Basin, relative to the Lokoro and Gilson basins, which are almost devoid of them. The basement heterogeneity is also considered as a major control for the subsidence of cratonic basins by Perron et al. (2018 and 2020). The paleo rift structure is represented by the Kiri and the Lokonia Highs, which act as basement uplifts between opposed diverging monoclines. They were not covered by the rift clastics (S0), nor by the

dolomitic limestones (*S1*), but by the post-rift sediments (*S2*-*S3*). They represent two offset highs, instead of a continuous rift structure, as proposed by Kadima et al. (2011a, b).

2.6.2 Neoproterozoic evolution (Rodinia to Gondwana)

New depocenters formed during the Neoproterozoic in the *CB* (Lokoro, Gilson and Boende basins), filled by *S2* and *S3* in a relatively continuous sedimentation. No regional unconformity can be seen between these two units, which are sometimes difficult to distinguish in the seismic profiles. The apparent continuity in sedimentation also suggests that no tectonic events disturbed the basin. The general geodynamic conditions of the *CB* were that of a relatively stable intracontinental setting, probably in a general extensional context. It is difficult to invoke post-rift subsidence for the entire period (nearly 500 Ma). During that time, complete Wilson-cycles occurred along the margins of the Congo Craton, in the West-Congo belt (Pedrosa-Soares et al., 2008), Damara (Gray et al., 2008), and Katanga (Lufilian) belts (Cailteux and De Putter, 2019), and possibly also along its south-eastern margin, in the Ubende belt (Boniface and Appel, 2017; Fig. 2.1).

2.6.3 Pan-African deformation and unconformity

Daly et al. (1991, 1992) already evidenced a distal effect of the late Paleozoic peri-Gondwana orogenies as major contraction deformation observed in the seismic profiles. The analysis of the profiles made in the frame of this project reveals that the Pan-African orogenies that developed around the Congo Craton at the end of the Neoproterozoic also caused locally intense far-field deformations in the *CB*. They are even better expressed than the late Paleozoic deformations in the center for the *CB*, as shown by profile *L50* (Fig. 2.7) and *L63*-*L62* (Fig. 2.6). The western extremity of profile *L63* (Fig. 2.6 a) shows that the entire Proterozoic succession has been eroded away before the deposition of the Paleozoic series over the Pan-African unconformity. In several profiles, such as *R5* (Fig. 2.6 c), R9 (Fig. 2.9), and *R22* (Fig. 2.10), the dolomitic limestones (*S1*), which is marked by strong parallel reflectors, is affected by reverse faults that disappear in the adjacent sequences below and above. Locally, in profiles *L51* (Fig. 2.6 a) and *L59* (Fig. 2.8 b), possible onlap during the deposition of *S3* (siliclastics) suggest that this sequence could have been deposited during the Pan-African deformation. This was related to the relatively long period of the final Gondwana assembly at the periphery of the Congo Craton during the Ediacaran (e.g. Fritz et al., 2013). At the periphery of the basin, the Mbuji-Maji series are folded and faulted at the contact with the Kibara belt in the Katanga region, in the area of the Lomami River (Cahen and Mortelmans, 1947). This deformation has been interpreted as a far-field effect of the Lufilian orogeny.

2.6.4 Karoo deglacial sequence

The CB was close to the South Pole in the earliest Carboniferous at the time of the Gondwana glaciation (Scotese et al., 1999; Torsvik and Cocks, 2011; 2013). Not much is left of this period in the *CB*, except for the depositional hiatus, which marks the transition between the Red Beds (*S4*) and Karoo (*S5*) in the Samba and Dekese wells (Cahen et al., 1959; 1960). The effect of this climatic event has been recorded in the Karoo deglacial sequence, from the periglacial Lukuga unit to the post-glacial Lueki unit. The paleogeography of the *CB* during the Permo-Triassic is clearly different from that of earlier stages. The marked *N-S* central depocenter of the Red Beds sequence is no more the dominant feature. There are no Karoo sediments in the Samba well and along the *L50-52 N-S* seismic lines (Fig. 2.6), while new depocenters appear on each side of the Kiri High, in the Busira and Dekese basins. The latter was probably part of a large intracontinental lake during the Permian deglacial period (Wopfner, 1999; Linol et al., 2015b), evolving into a warmer post-glacial basin in the Triassic. Recycled vitrinite in the sediments of the Lukuga Group (Permian) suggests their provenance from a sedimentary source, younger than the late Devonian (Sachse et al., 2012). In conclusion, I observe a major change in the depocenters and sediment source from the early Paleozoic (Seq. 4) to the late Paleozoic-Triassic (*S5*), even if no major unconformity is noticed between the two sequences (Fig. 2.13 E-F). There might have been a sedimentation hiatus with some reworking, likely driven by global climate change. A tectonic event at this stage cannot be excluded, but we do not observe a tectonic unconformity.

2.6.5 Late Permian-early Triassic deformation

In seismic line L50 (Fig. 2.6), the Paleozoic series and Pan-African unconformity are both deformed in continuity with the Pan-African structures that affect the Paleoproterozoic sequences underneath, suggesting their reactivation. In contrast, the Basal Jurassic unconformity and overlying sediments are not affected, constraining the deformation between the end of the Permian and the late Jurassic. The timing of the deformation relative to the Triassic Lueki Group is less clear. Some deformation could have occurred before and/or after it. Line 60 calibrated by the Gilson well (Fig. 2.6 a) would suggest that the Lueki was affected by the deformation in the Gilson Basin before deposition of the Kisangani Group (Fig. 2.6b). Another expression of this deformation is illustrated in lines R15-16 (Fig. 2.9), where the entire Paleozoic to Proterozoic sequences were deformed in an anticlinal folding (Maringa Ridge) with a 70 km-long wavelength. This falls within the range of upper crustal lithospheric folding that typically develops in a layered, lithosphere with an old thermo-tectonic age (> 500 Ma) submitted to horizontal compressional stresses (Cloetingh et al., 1999; Delvaux et al., 2013). The crest of the anticline has been completely eroded before the deposition of the Jurassic Kisangani series, which provide a clear age relationship. The rift clastics (*S1*) appear with a constant thickness across the Maringa Ridge anticline (Fig. 2.9, 14 A), while the dolomitic limestones (*S2*) and the carbonate-clastics are slightly thinned (Fig. 2.9, 14 B-C). This slight thinning could have located the anticlinal folding during the Late Paleozoic deformation.

2.6.6 Jurassic-Cretaceous

While the Permo-Triassic compressional event caused weaker and more localized deformation than the Pan-African deformation, it was still followed by important denudation. During the early Jurassic, up to 4000 m of sediments might have been removed, as constrained by vitrinite reflectance in the Mbandaka and Dekese wells (Lucazau et al., 2015), forming the Basal Jurassic Unconformity. The latter can be observed in-situ along the Lualaba segment of the Congo River, upstream of Kisangani (Caillaud et al., 2017), where sedimentation started in an anoxic lake, producing high quality lacustrine type II organic matter (Sachse et al, 2012). The overlying late Jurassic and Cretaceous to Paleogene seismic sequences (*S6* and *S7*) cover not only the *CB*, but also its margins as a transgressive blanket, thus enlarging the size of the basin. Towards the south, it covers a large part of the Kasaï Craton, locally over a thin layer of Karoo sediments (Roberts et al., 2015). It contains lacustrine, fluvial-lacustrine and aeolian sequences, deposited in the context of Gondwana breakup (Fig.1.1, Linol et al., 2015 c).

2.6.7 Late Cretaceous-Cenozoic

As stated earlier, the *CB* underwent since the Late Cretaceous a new stage of erosion and denudation (Sachse et al., 2012; Lucazeau et al., 2015) with the formation of the 'African Surface', the Kalahari Group and the modern landscape (Giresse, 2005; Guillocheau et al., 2015; Linol et al., 2015e).

2.7 Discussion

The long geological history of the *CB* recorded a series of tectonic and climatic events that, given the size of the basin, located centrally in the Gondwana Supercontinent, are likely of global scale. In the frame of this *PhD* project, the new findings from the seismic interpretation were integrated with the existing literature to update the knowledge on the evolution of the *CB*. In particular, I compared the stratigraphic model with the ones of Daly et al (1992) and Linol et al (2015b). The results of this study can first confirm the subdivision of the stratigraphy of the *CB* into three major units, belonging to the Proterozoic, Paleozoic-Triassic, and the Jurassic-Cretaceous phase (Kadima et al., 2015). They are separated by two major tectonic unconformities at the Neoproterozoic-Paleozoic transition (related to the Pan-African deformation) and at the Paleozoic-Jurassic transition (related to far-field intraplate compression). The novelty of this model is that the *CB* is here considered much older than in previous studies. According to Daly et al. (1992), the *CB* initiated in the Ediacaran with the Ituri Group and evolved as a cratonic basin during the entire Phanerozoic. Linol et al. (2015b) consider the cratonic evolution of the *CB* starting only from the late Paleozoic-Cenozoic and disconnect it from basement 'cover series', consisting in folded platform carbonates and Pan-African foreland red sandstones. The results of this study show that the *CB* initiated in late Mesoproterozoic and its evolution during the last one billion years is characterized by three cratonic basin cycles, separated by tectonic events. Each cycle began by an initial marked expansion of the deposition area, followed by a progressive centripetal restriction of the depocenter (offlap). Such offlap is a general characteristic of cratonic basins (Watts et al., 2018).

The initial rift and post-rift phases of the Meso- and Neoproterozoic age produced significant subsidence of the basement in the northern part of the basin, where it currently reaches an average depth of 7-8 km (Fig. 2.12). In most of this area, the sedimentary sequences appear unaffected by successive tectonic events and the basement depth is sub-horizontal or shows small undulations, likely reflecting inherited heterogeneity (Fig. 2.11). In the same area, the syn-rift clastics and carbonate ramp layers are well developed and they in total reach an average thickness of 3 km. The overlying Proterozoic post-rift sediments reach a thickness of 4-5 km. The difference in the shape of the basins and thickness of the syn-rift sequences can be attributed to a non-uniform syn-rift extension, which affected more the northern than the southern part of the *CB*. Another hypothesis is that inherited heterogeneity of the basement derived from different cratonic pieces, influenced shapes and sizes of the basins formed in response of uniform (or non-uniform) extension, as well as the thickness of syn-rift sediments. This would explain the anomalous great thickness of syn-rift sediments in the Salonga Basin, with respect to the Lokoro and Gilson basins, which are almost devoid. Furthermore, I should consider that a series of convergences and collisions of different continental blocks, which lead to the assembly of the Gondwana supercontinent (Pan-African deformation), between 550 and 530, Ma, caused a relative tectonic instability of the basin in response to intraplate stresses. Signs of these compressional deformations are clearly visible from seismic reflection profiles shot in the western and southern part of the Cuvette Centrale (Fig. 2.5 and 2.6). This compressional tectonics is expressed by both folding and faults of the Proterozoic sediments and underlying basement, which caused further subsidence and localized uplifts. In particular, in the southern and western parts of the Cuvette Central (Fig. 2.5 and 2.6) the crystalline basement in the main

depocenter of the Lokoro and Gilson basins reaches a depth greater than 9 km. Both basins are almost devoid of syn-rift clastics sediments, while the Neoproterozoic post-rift sequences are well developed and folded, indicating that the formation of these depocenters occurred later with respect to the basins located in the north (e.g., Boende, Busira, and Lomami basins).

Along the southern margin of the Cuvette Central, the sedimentation was reduced and only weakly disturbed by the successive compressional tectonics (Fig. 2.9). The convergence responsible for the Pan-African deformation produced also the amalgamation in the South American continent of the Sao Francisco and the 2.0–2.5 Ga Rio de la Plata Shields, partly underlying the Paraná Basin. Since the development of the *CB* and the Paraná Basin continued on the sutured southcentral African and South American Shields up to the break-up of the South Atlantic (about 200 Ma), the two basins show stratigraphic correlations between some of the Paleozoic sequences (Linol et al., 2015c). I can also speculate that the compressional tectonics, leading to the Gondwana formation, affected in similar way both the *CB* and Paraná Basin and may have produced in the latter further subsidence and formation of very deep basins, similar to the Lokoro and Gilson basins.

The compressional tectonics was followed by the post-orogenic extension and denudation (removal of several km of sediments) in the early Paleozoic, with consequent development of an unconformity (Lucazeau et al., 2015), and post-orogenic sedimentation, occurred during the general northwards movement of Gondwana since the Middle Paleozoic. The tectonic inversion, occurred during the Permo-Triassic age, was a far-field effect of the Gondwanides orogeny along the southern margin of Gondwana (Cape Fold Belt) (Lucazeau et al., 2015). This compressional event is expressed in the central part of the Cuvette Central by a dense pattern of faults affecting the sediments deposited above the Pan-African unconformity, and in some cases reaching the underlying Proterozoic sedimentary sequences, or even the basement (Fig. 2.7). However, this Permo-Triassic compressional event caused a weaker and more localized deformation of the basin, with respect to the Pan-African deformation.

The Gondwana break-up at 200 Myr was followed by continental to lacustrine sedimentation of Late Jurassic (Kimmeridgian) to Mid-Cretaceous (Albian - Cenomanian) age, with possible marine influence in Cenomanian (Lucazeau et al. 2015). The opening of the Central Atlantic produced uplift and erosion in several parts of the basin. The compression, exerted by the ridge-push and still active today, is expressed by thrust faults, observed in Samba well of the Late Cretaceous – Paleogene age and by the Quaternary deformation, consisting in *E-W* horizontal compression, low-angle thrust focal mechanisms, long-wavelength folding, and river incision (Lucazeau et al. 2015).

Sedimentation since the Late Cretaceous was also influenced by the global climatic variations, leading to intense weathering and deposition during the Cenozoic (Kalahari Group, Lucazeau et al. 2015). The tectono-stratigraphic history of the *CB* shows also similarities with the Taoudeni Basin of West-Africa (Trompette, 1973; Clauer, 1981; Deynoux et al., 2006; Beghin et al., 2017b). The latter has been initiated at about 1.1 Ga (Rooney et al., 2010) in a pericratonic to intracratonic unstable extensional tectonic context (Bronner et al., 1980; Beghin et al., 2017a). It recorded a discontinuous sedimentation history with four main groups of the Late Mesoproterozoic to Paleozoic units. As the *CB*, the Taoudeni Basin was deformed and uplifted by the Hercynian deformation and covered by thin Mesozoic–Cenozoic units in the basin center and Quaternary sand dunes (Trompette, 1973; Clauer, 1981; Deynoux et al., 2006; Balukiday et al., 2018).

2.8 Conclusions

In the frame of the *PhD* project, I investigated the long-term evolution of the *CB* trough analyzing all available geological and seismic data. This great amount of dataset let me the possibility to reconstruct in more detail than before the stratigraphic and tectonic history of this basin during the last 1200 Myr. After a review of the existing literature, I proposed a revised sismostratigraphic model of the *CB*, based on my interpretation of the seismic reflection profiles, integrated by well-log and outcrop data. I computed depth maps of the major seismic reflectors and thickness maps of the corresponding stratigraphic units. This allowed me to reconstruct a tectonic succession of events highlighting the three-dimensional evolution of the *CB* trough time.

The *CB* is a huge intracratonic basin, which initiated its formation through the end of Mesoproterozoic age. The extensional tectonic features let us to consider *CB* as a failed rift basin. The *CB* deposition history recorded Mesoproterozoic rift clastics (syn-rift depositions) and limestones (carbonate ramp) below Neoproterozoic carbonates/evaporites layers (post-rift depositions) and siliciclastics (signing the Rodinia breakup). These sequences are divided from those of the Phanerozoic by the Pan-African unconformity, characterized by compressional deformations related to Gondwana assembly, during which Gondwanides orogeny belts grew up.

During the post-orogenic phase, in the Paleozoic, occurred the deposition of red arkoses layers called Red Beds, observed at the base of the Samba and Dekese well cores. The end of Paleozoic (Late Devonian-Early Carboniferous) has been marked by the period of "Ice house" (ice age, during which one or two poles were covered by permanent ice), during which the *CB* was close to the South Pole and most part of the Gondwana was affected by glaciation. From late Carboniferous (Pennsylvanian) until Triassic, the *CB* recorded continental clastics above glacial-lacustrine sediments, referred to the deglacial phase of the Permian age. During the late Paleozoic to early Mesozoic evolution, sedimentation occurred in the context of the Gondwanide orogeny, along the southern margin of Gondwana. It induced locally intense tectonic reactivation and general vertical movements, leading to the development of a second basin-scale unconformity (Basal Jurassic). After the breakup of the Gondwana and the hiatus characterizing the stratigraphic unconformity of the Jurassic age (~200-157 Myr), we can observe a depositional environment until the Paleogene, composed by shallow lacustrine and fluvial ephemeral lakes. The *CB* might also have been locally influenced by distal tectonic events, but the current data available do not allow to precise that. Nowadays the *CB* is likely affected by a slow tectonic uplift, but I have not analyzed data supporting this hypothesis.

CHAPTER 3

- Potential field analysis -

3.0 Introduction of the chapter

In Chapter 2, I reconstructed the stratigraphy and tectonic evolution of the *CB*, using all available geological and seismic data (reflection and refraction seismic, borehole, and field data as outcrops). From the interpolation of the interpreted seismic profiles, I obtained the depth of the basement (seismic basement) and isobath maps of seven horizons corresponding to the main seismic reflectors and isopach maps of the sedimentary sequences overlying the basement. These maps revealed the existence of sedimentary depocenters of various sizes that originated from several rift phases and increased their depth during the compressional tectonics that accompanied the Gondwana assembly. These small basins belong to two large depressions that are separated by the Kiri High, which appeared during the initial stage of the *CB* (Fig. 3.1). However, the seismic data do not have a uniform distribution and their interpolation could have produced artefacts along the uncovered regions. Looking at Fig. 3.1, we observe that several specific features along the seismic profiles are extruded laterally. For example, we can observe a *NE*-extension of the Lomami Basin and *SE*-extension of the Lokonia High (Fig. 3.1).

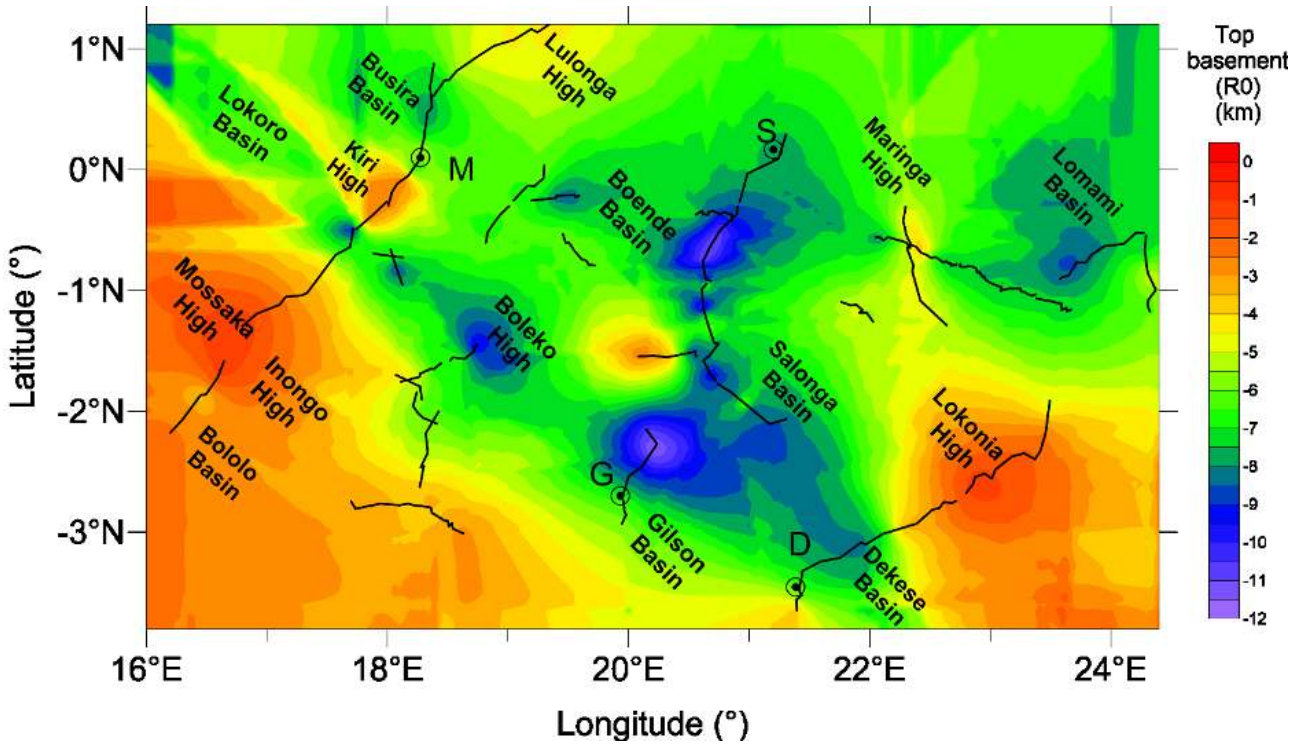

Figure 3.1 *- Main tectonic structures identified at the top of the seismic rock basement. Broken black lines show location of the seismic reflection profiles. Black circles show location of the four wells drilled in the study area: D= Dekese; G=Gilson-1; M=Mbandaka-1; S=Samba (Delvaux et al., 2021).*

In this chapter, I used the available aeromagnetic and gravity data to delineate the main structures of the basement and overlying sediments, as well as to investigate the shallow crustal structure of the *CB*. In this way, I had the chance to reconstruct the basement depth in areas between the seismic lines, where information on the seismic basement depth could have been only retrieved by interpolation (Chapter 2). Furthermore, I could extend the model laterally to the areas of the basin uncovered by the seismic data. I reconstructed the depth of the basement applying gravity analysis methods, which verify the agreement between the modelled and observed gravity field.

In Fig. 3.2, I display the main steps of the gravity method used in this study. To this aim, I used the isopach maps of the sedimentary sequences (Chapter 2, Delvaux et al., 2021) and their densities obtained from representative core and outcrop samples (stored at the *RMCA*, Belgium) to calculate the gravity effect of sediments (*G_SED*). The residuals of the regression analysis between the Bouguer anomalies and topography (*BG_RES1*) reflect the gravity effect cleared from the crustal thickness variations. An estimate of the sub-crustal, mantle contributions to the gravity field are estimated by fitting a low order polynomial surface (*PS*) to the gravity field corrected for the interpolated sediments (*BG_RES2 = BG_RES1 - G_SED*) and for the crustal thickness variations (*BG_RES3 = BG_RES1- PS*). Then, I inverted *BG_RES3* for the depth of the basement, using the seismic data as constraints and two different superficial density contrasts between sediments and crystalline rocks basement, according to the different thickness of sedimentary layers present in the CB, to test the reliability of the results.

The chapter is mostly based on Maddaloni et al. (2021a), already published on Global and Planetary Change.

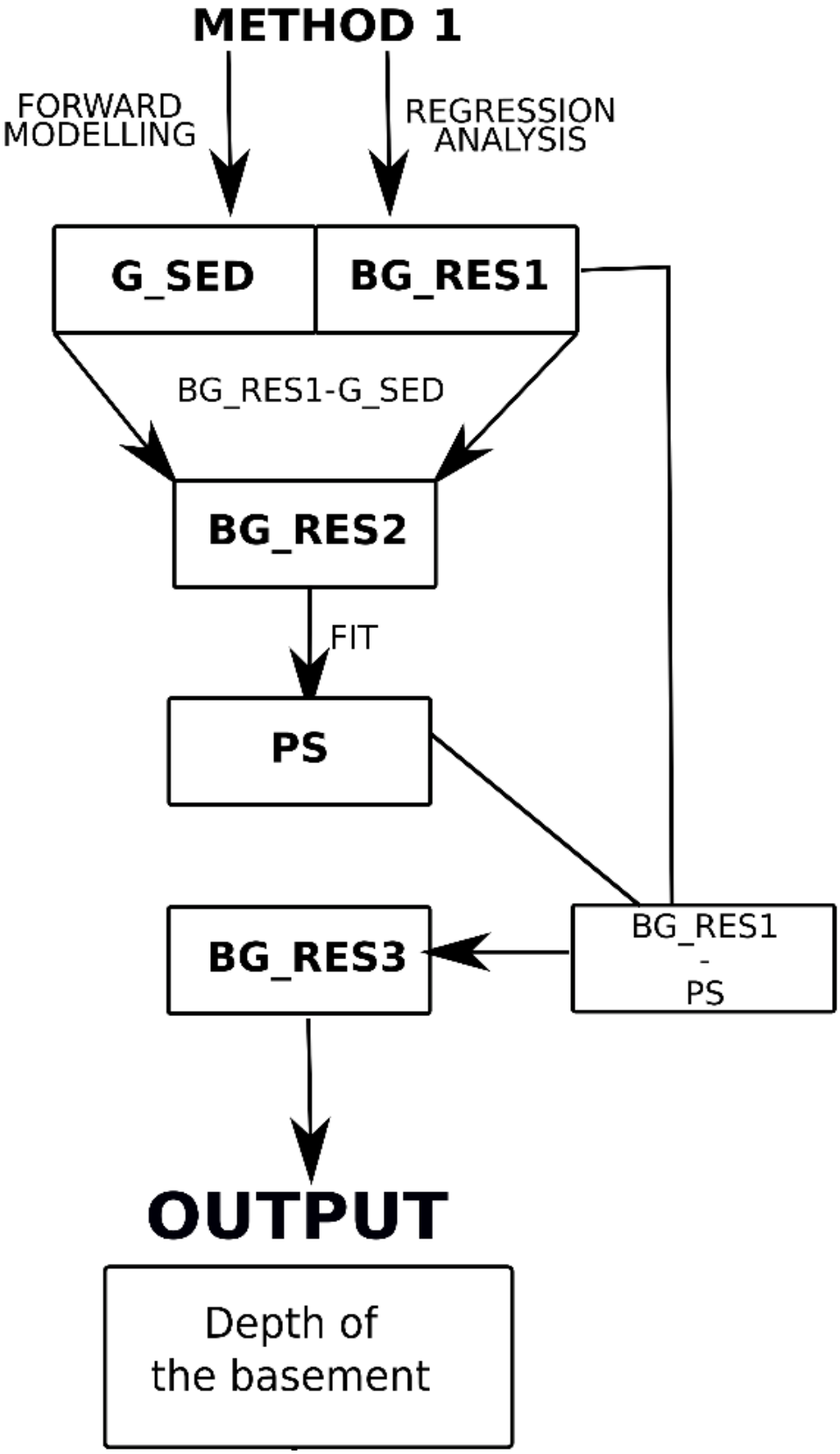

Figure 3.2 – *Flowchart illustrating the two main investigation methods used. Abbreviations are as follows: G_SED: gravity effect of sediments. BG_RES1: residuals from regression analysis. BG_RES2: residuals obtained subtracting G_SED to BG_RES1. PS: Polynomial surface. BG_RES3: residuals obtained subtracting PS to BG_RES1.*

3.1 Data presentation

Here, I present the main potential field data used for investigating the main crustal structures of the *CB*. The study has been mostly conducted between the second and the third year of my *PhD* project at the University of Trieste.

3.1.1 Aeromagnetic constraints on the structure of the Congo Basin

The aeromagnetic data set is composed of two surveys. The first one was flown in 1984 by the Japan National Oil Corporation (*JNOC*), with a line spacing of 18000 m, a cruising altitude of 750 m, and line direction of 0° respect to north. The two other surveys were made in 1987 and 1986 by the Companies Générale de Géophysique (*CGG*), with line spacing of 9000 m, a cruising altitude of respectively 915 m and 1332 m, and a line direction of 0° respect to north. The data covers large parts of the CB in the Democratic Republic of Congo (*DRC*) and an adjacent part in the Congo Republic. The release of magnetic data from *GETECH* (Geoscience data and geospatial technology for delivering the energy transition) group (Leeds, *UK*) has been done in the frame of a scientific collaboration between the *RMCA* and *GETECH*.

The total field magnetic data have been extracted from the GETECH 1 km x1 km grid compiled by the African Magnetic Mapping Project (*AMMP*) at Leeds University. The compilation is in the form of a unified grid of 1 km x1 km of total magnetic intensities (*TMI*). The original data have been merged, projected in an equatorial Mercator projection and interpolated on a regular grid of 1 km x 1 km (Barritt, 1983). Afterwards, the data have been reduced to the North Pole, in order to display the magnetic anomalies over the inducing bodies. The magnetic bodies are identified by positive anomalies and the magnetic lineaments correspond to sharp lateral change in the magnetic field. The resulting map (Fig. 3.3) shows a prominent highly magnetic zone *NW-SE* oriented, in the central part of the basin, indicated as 'axial magnetic zone'. It is interpreted as the signature of a failed rift, which is supposed to have initiated the *CB* (Daly et al, 1992; Kadima et al., 2011b). This zone currently corresponds to the Kiri High, a prominent structure that divides the *CB* into a *NE* (Busira, Boende, and Lomami basins) and a *SW* part (Lokoro, Gilson, and Dekese Basin). To the *NW*, the extension of the Kiri High into the Republic of the Congo on the *NW* side of the Congo River has been also observed in the aeromagnetic data (not available to us, but displayed in Master, 2010). The *SE* extension of this axial magnetic zone reaches the area where the interpretation of the seismic profiles and gravity data suggests the presence of a deep basin (Salonga Basin).

The positive anomaly in the *NE* corresponds to the Lindi Supergroup, covered by relatively thin sediments (Kadima et al., 2015a), and the positive anomaly around Lake Mai-Ndombe corresponds to the Inongo High (Fig. 3.3). In the extreme west, the positive anomaly marks the western limit of the *CB*. Towards the south, closely spaced and very short wavelength anomalies mark the signature of the highly magnetic Kasaï cratonic block under a thin sedimentary cover (e.g. Roberts et al., 2015). These anomalies do not show the typical signature of the deep Lokoro – Gilson – Dekese basins and trace the approximate southern limit of the *CB*. They are flanked by an alignment of strong negative anomalies that extend *SE* of the Dekese well site, which suggests an interaction between the Kasaï craton and the Dekese Basin. We draw the limit of the Kasaï craton, taking into account the interpolation of the refraction seismic data for both the 4200 ms and 5200 ms

refractors (Delvaux et al., 2021), and the outcropping field of the late Mesoproterozoic Mbuj-Maji Group (basal sequences Seq.0 and Seq.1 in Table 1). It shows a southward 'gulf' of the *CB* sediments between two lobes of the Kasaï Craton (Fig. 3.3). The aeromagnetic data show also a structural continuity between the *CB* and the Mbuji-Maji Basin towards the *SE*, confirming the assumption made (Delvaux et al., 2021) that the latter could represent the outcropping part of the basal series of the *CB*.

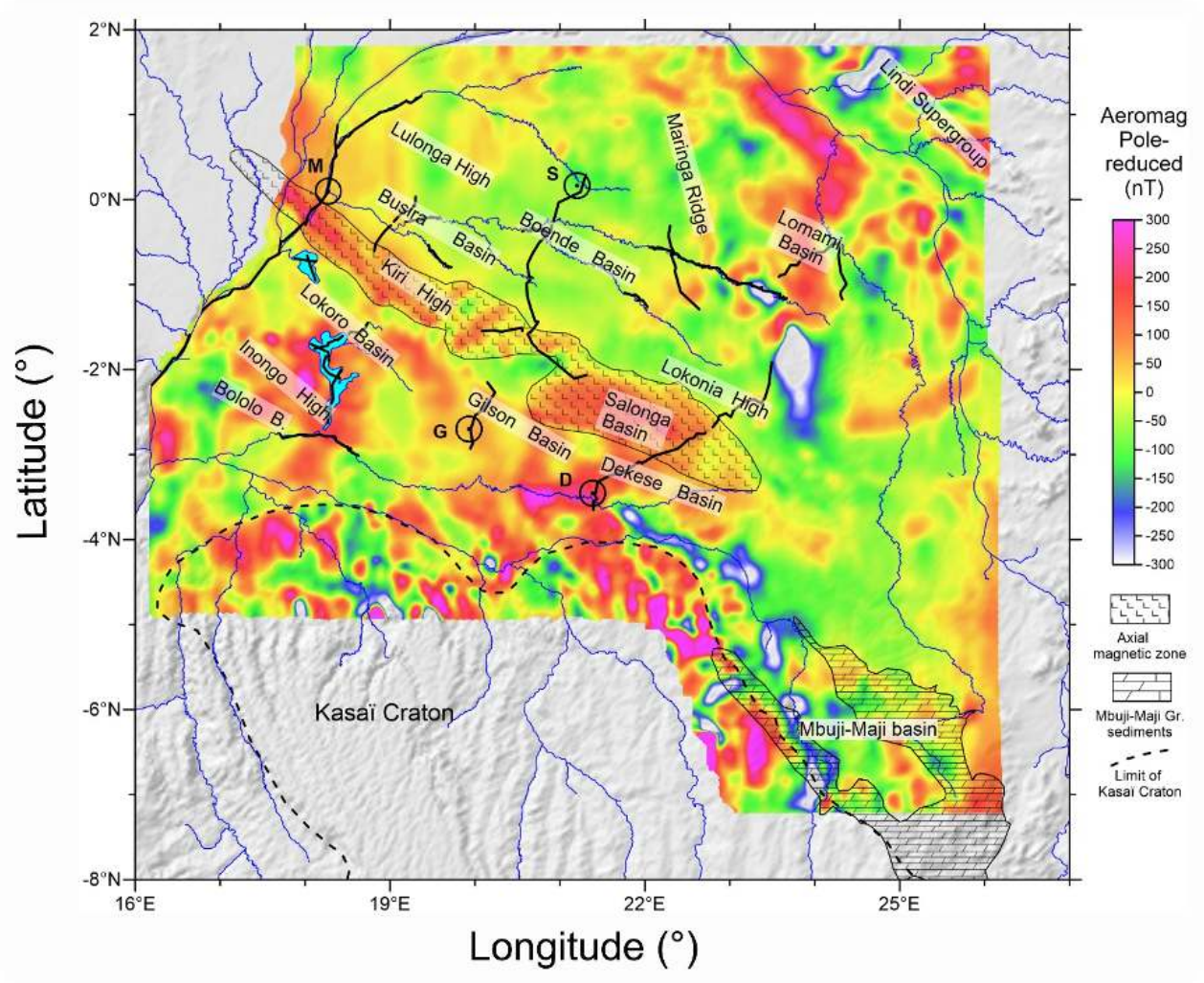

Figure 3.3 *- Aeromagnetic map reduced to the North Pole overlain by the axial magnetic zone. Thick dashed line shows the approximate northern limits of the Kasaï Craton interpreted from aeromagnetic data. Broken black lines show location of the seismic reflection profiles. Black circles show location of the four wells drilled in the study area: D=Dekese; G=Gilson-1; M=Mbandaka-1; S=Samba.*

3.1.2 Gravity data

The gravity field is derived from a gravity model (EIGEN-6C4, Förste et al., 2014) available in spherical harmonic expansion, obtained by combining satellite observations, from the satellites GOCE, LAGEOS, GRACE, and terrestrial data. The term EIGEN means European Improved Gravity model of the Earth by New techniques and Eigen-6c4 model is the latest release (year 2014) of the EIGEN-6 -Series. The field has been published with maximum degree/order 2190, which corresponds to a spatial resolution at the equator of 9 km. It is customary to obtain the Bouguer gravity field reducing the gravity field for the effect of topography. I adopt a global correction of topography, whose effect is published in terms of the spherical harmonical expansion, again to maximum degree and order 2190, to match the available gravity field. Essentially two groups have worked on this subject (Rexer et al., 2016; Grombein et al., 2016) and have published two models, which are very similar to each other and for our purpose can be used choosing either one of them. I have used the *REQ_TOPO_2015_plusGRS80,* which takes into account the rock topography (Fig.3.4), water and ice-cover, according to the terrain-model Earth2014 (Hirt and Rexer, 2015), discretizing and calculating the mass effect with tesseroids (Uieda et al., 2016). The gravity effect of the topography, obtained using the *REQ_TOPO_2015_plusGRS80* model, is negative and spans from -96 mGal to -50 mGal, with a general increase from west to east (Fig. 3.4).

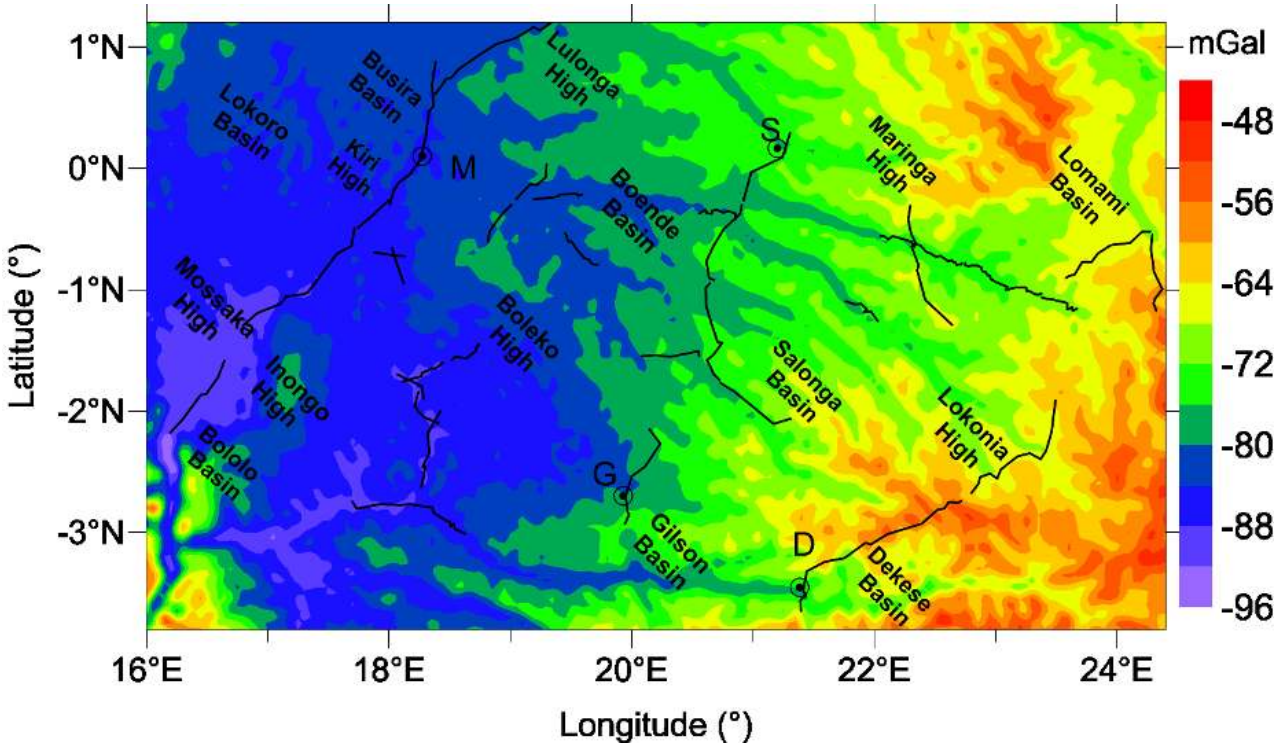

Figure 3.4 *- Gravity effect of Topography of the Congo Basin area, using the global model REQ_TOPO_2015_plusGRS80. Broken black lines show location of the seismic reflection profiles. Black circles show location of the four wells drilled in the study area: D= Dekese; G=Gilson-1; M=Mbandaka-1; S=Samba.*

The gravity disturbance (Fig. 3.5 A) spans from -105 mGal to +20 mGal. The Cuvette Centrale is mostly characterized by negative anomalies with average values around -80 mGal. I observe a series of *NW-SE* oriented negative and positive anomalies, corresponding to the alternation of highs and basins. The Bouguer anomalies (Fig. 3.5 B) have been calculated subtracting the gravity effect of the topography (*REQ* model, Fig.3.4), from the gravity disturbance. The anomalies range between -15 mGal to +115 mGal, with the minimum values forming small circular anomalies, which may be related to the sedimentary deposits and/or low-density bodies in the shallow crust. The maximum values are located in correspondence of the Kiri High and in the southern part of the Cuvette Centrale.

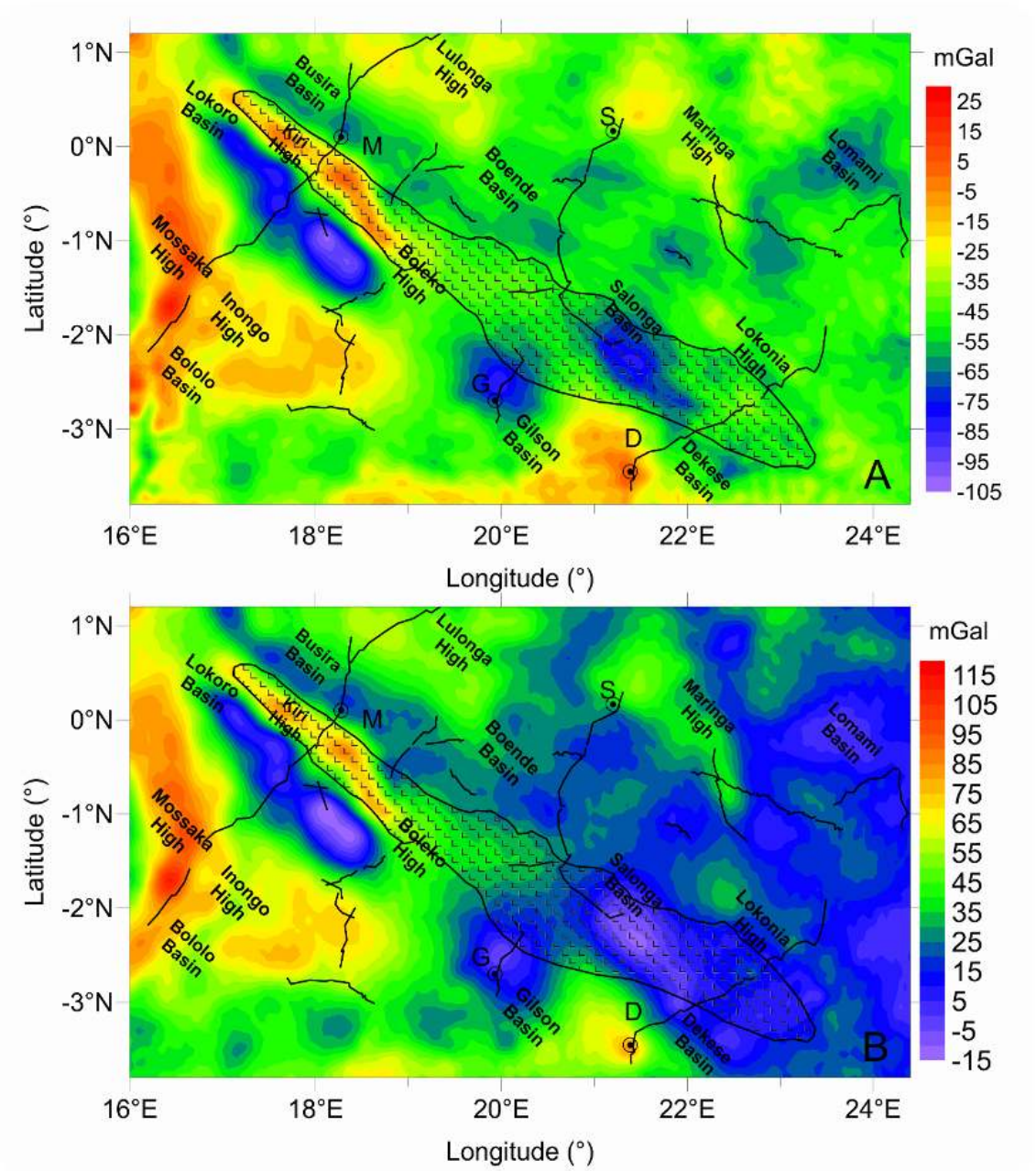

Figure 3.5 *- Gravity disturbance (**A**) and Bouguer gravity anomaly (**B**) maps obtained from Eigen-6c4 model, overlain by the axial magnetic zone. Broken black lines show location of the seismic reflection profiles. Black circles display location of the four wells (D= Dekese; G=Gilson-1; M=Mbandaka-1; S=Samba).*

3.2 Gravity effect of the sedimentary layers

In order to compute the gravity effect of sediments (*G_SED*), I discretized each sedimentary layer thickness (Table 3.1) obtained from the interpolation of seismic horizons (defined by seismic lines) and the 3D model of sediments (Chapter 2) into a grid of spherical tesseroids and calculated *G_SED*, with the *Tesseroids* software (Uieda et al., 2016). The density contrast of each tesseroid was computed as the difference between the standard reference density of crystalline basement equal to 2.67 g/cm^3, and the density of each sedimentary layer displayed in Figure 3.6.

Stratigraphy	Super-groups	Groups	Seq.	Age (Ma)		Dominant lithology	Density measurements		
				Max	Min		n	δ (g /cm^3)	1σ
Paleogene		Kalahari Gr.				Duricurst, eolian sandstones			
Cretaceous	Congo	Sankuru Sup.Gr. Kwango Gr. Bokungu Gr. Loia. Gr. Dekese Gr.	7	132	66	Shales and sandstones, calcareous	6	2.03	0.08
late Jurassic	Congo	Kisangani Gr.	6	157	132	Shales and sandstones	4	2.14	0.08
Base Jurassic unconcofmity		Gondwana breakup							
Triassic	Karoo	Lueki Gr. (ex-Haute-Lueki Gr.)	5	320	250	Red sandstones and mudstones	11	2.12	0.27
						Far-field Gondwanide orogeny			
Permian	Karoo	Lukuga Gr.	5	320	250	Shales and diamictites	5	2.25	0.12
Sed. Hiatus		Gondwana glaciation							
Paleozoic: Devonian	Aruwimi	Samba - Dekese Gr.	4	500	380	Red arkosic sandstones	5	2.39	0.07
Paleozoic: Silurian, Ordovician, Cambrian	Aruwimi	Inkisi - Banalia - Biano Gr., Nama Gr.	4	500	380	Micaceous sandstones	11	2.46	0.12
Pan-African unconformity		Final Gondwana assembly							
Neo-proterozoic: Ediacaran - Cryogenian	Lindi	Lokoma Gr.	3		580	Siliciclastics	11	2.45	0.17
Neo-proterozoic: Tonian	Lindi	Ituri Gr.	2	1000		Carbonates-clastics (evaporites)	20	2.61	0.15
Mesoproterozoic (Stenian)	Mbuji-Mayi	BII Gr. (1)	1	1040	1000	Dolomitic limestones, dolerite lava	19	2.75	0.12
	Mbuji-Mayi	BI Gr. (1)	0	1065	1065	Clastics & dol. Limest.	10	2.62	0.13
Top basement unconformity		Paleoproterozoic & Mesoproterozoic orogenies							
Mesoproterozoic - Archean		Crystalline basement	Metamorphic rocks, granites, quartzites				-	2.75	

Figure 3.6 *- Age and average density of the major stratigraphic horizons used for the calculation of density contrast, existing between each layer and the reference crustal density.*

The density of the Proterozoic sedimentary layers Seq.0-Seq.2 is close to that of the reference density of the crystalline basement and in particular, the density of layer Seq.1 (Dolomitic limestone and dolerite lava) is even higher (Fig. 3.6). Therefore, they give a small contribution to *G_SED*. In contrast, the layers Seq.3-Seq.5 show a progressively lower density upward and thus produce more pronounced density contrast with the crystalline basement.

Strati Sequences (N.)	Maximum Thickness (km)	Density (g/cm^3)
Seq.0	5.52	2.620
Seq.1	1.59	2.750
Seq.2	6.79	2.610
Seq.3	2.99	2.480
Seq.4	2.87	2.425
Seq.5	1.82	2.270
Seq.6	1.78	2.030

Table 3.1 – *Maximum thickness of the major stratigraphic sequences with associated their average density values (Chapter 2).*

The greatest negative values of *G_SED* (-115 mGal) correspond to the location of the deepest basins (Lokoro, Gilson, Boende and Busira basins), characterized by the greatest thickness of the low-density sequences *S3*-*S7* displayed in Chapter 2. On the other hand, the Lomami Basin, containing a greater thickness of the high-density layers (Seq.0-Seq.2), with respect to the low-density sequences, shows *G_SED* values around -75 mGal (Fig. 3.7). However, we should take into account that the *G_SED* field is reliable only along the seismic lines, whereas it is based on an interpolated basement depth between the lines, which we intend to verify through an inversion of the gravity field. This gravity field useful for the inversion of the basement must be cleared from the effects of crustal thickness and the sub-crustal contributions to the gravity field. We estimate the contribution of crustal thickness through a proxy method, which analyses the regression between the Bouguer field and the topography and has been tested and demonstrated in several contexts (Pivetta and Braitenberg, 2020; Maddaloni et al., 2021b).

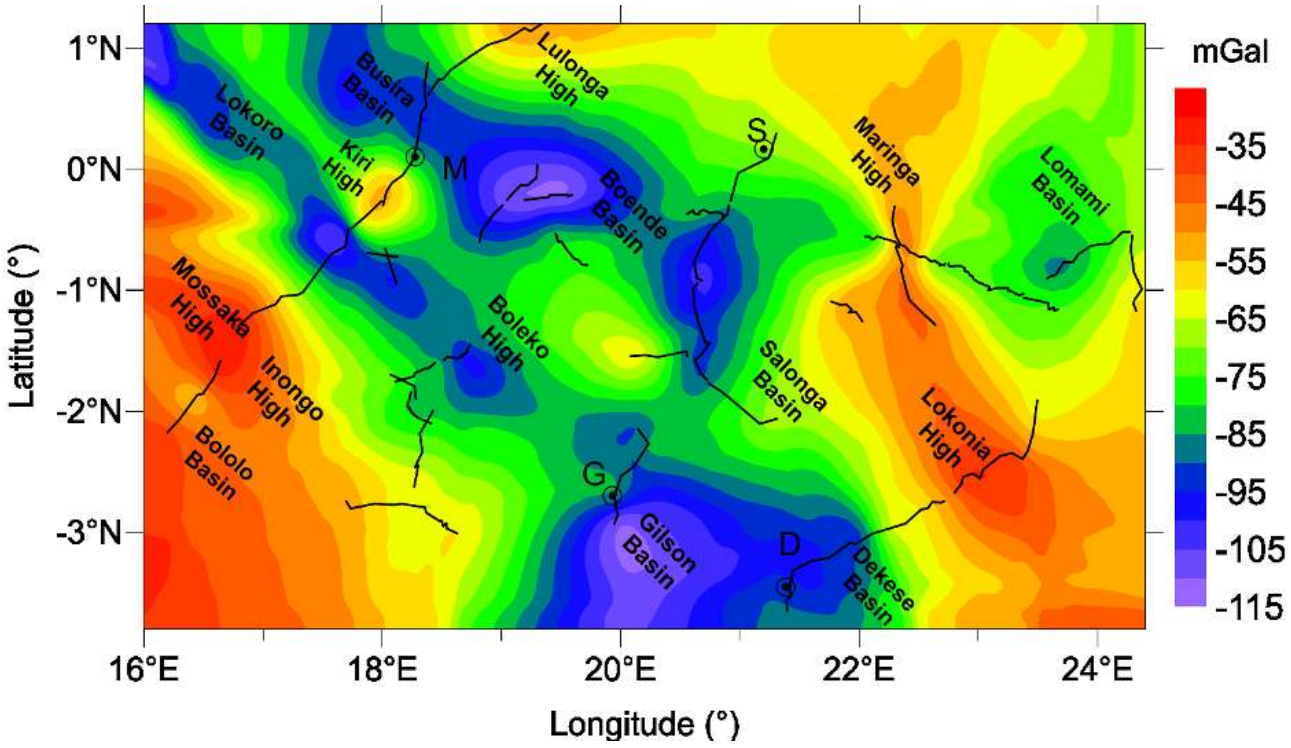

Figure 3.7 *- Gravity effect of sediments (G_SED) in the Cuvette Centrale, based on the interpolation of seismic lines. Broken black lines show location of the seismic reflection profiles. Black circles show location of the four wells drilled in the study area: D= Dekese; G=Gilson-1; M=Mbandaka-1; S=Samba.*

3.3 Regression analysis between topography and Bouguer gravity anomaly field

The regression analysis between the topography and Bouguer anomalies is a statistical method that allows reducing the gravity values from the effect of deep crustal layers, when a regional crustal model, based on seismic data, providing both Moho depth and velocity variations, is missing (Braitenberg, 2015; Pivetta and Braitenberg, 2020; Maddaloni et al., 2021b). Since this is the case of the *CB*, I applied the regression analysis method, which is based on the general observation that topography is anti-correlated with the Bouguer gravity field on a global scale (as a consequence of the isostatic theory). For the lithospheric flexure model, at increasing topography wavelengths and decreasing equivalent elastic thickness, the flexural response tends toward the Airy local isostatic compensation mechanism (e.g., Watts, 2001). According to the Airy hypothesis and in the approximation of the Bouguer plate, the expected relation between Bouguer field and topography is linear:

$$BG \approx -2\pi G\,(r - d)\,(\rho_m - \rho_c) = -2\pi G \rho_c h \qquad (1)$$

Where $(r - d)\,(\rho_m - \rho_c)$ is the gravimetric effect of the Airy isostatic root approximated to an infinite plate analogue to the Bouguer plate. *BG* is the Bouguer anomaly, *G* is the gravitational constant (6.67430 10^{-11} Nm^2/kg^2), *d* is the reference crustal thickness, *r* is the isostatic crustal thickness, ρ_m is the upper mantle density, and *h* is the topography over the sea level.

The regression line carries important information on the stress state of the lithosphere, since a negative slope demonstrates the existence of an isostatic compensation mechanism. The absolute value of the slope mainly depends on the density contrast between crust and mantle, although it is also influenced by the general isostatic state of the area (if the area is completely uncompensated, the regression slope between Bouguer anomaly field and topography should be zero). The regression analysis is usually made over extended areas and the resulting residual values could be considered as a type of isostatic residuals. The mathematical expression of residuals is given by:

$$BG\_REG\,(x, y) = m * topo\,(x, y) + q \qquad (2)$$

$$BG\_RES1\,(x.y) = BG\_obs\,(x, y) - BG\_REG\,(x, y) \qquad (3)$$

Where *BG_obs* is the observed gravity Bouguer anomaly (Fig. 3.5 B), *m* the angular coefficient of the regression line, *topo (x, y)* the low pass filtered topography, *q* the intercept, and *BG_REG* is the expected Bouguer from the regression relation.

The residuals (*BG_RES1*, Fig. 3.8) show the gravity signal induced by the crustal density variation, after the removal of the effect of topography and isostatic crustal thickening. With respect to the isostatic flexure analysis, the regression analysis has the advantage to be independent on any isostatic parameters. The method has been tested with different synthetic models in Pivetta and Braitenberg (2020) and successfully applied in areas characterized by both high and low topography, such as the Alps, South Atlantic, and parts of Africa and South America (Braitenberg, 2015, Pivetta and Braitenberg, 2020). In our case, the regression analysis between topography and gravity is used to determine the anomalies due to the upper crustal mass

inhomogeneity, reducing the Bouguer anomaly for the effect of crustal thickness variations. I performed the regression calculations for the entire *CB*, but we display the residual gravity field only for the Cuvette Centrale (Fig. 3.8). The Cuvette Centrale appears to have essentially negative residual gravity anomaly values, with a range from -90 mGal up to +55 mGal. I compared the gravity field with the basement depth obtained from the interpolated seismic deepest horizon, with the aim to verify the agreement between the two quantities. Qualitatively, it can be expected that gravity highs and basement highs are located in the same place and that gravity lows locate above the deepest depocenters. I observed that the basement highs are characterized by gravity residuals limited to the range of ±20 mGal, while the other areas of the Cuvette Centrale show values that are more negative. The *NW-SE* structure, formed by the Lokoro Basin, Kiri High, and Busira Basin, identified in the gravity disturbance map, are well visible by the alternation of negative and positive anomalies. The greatest positive anomaly (between +40 and +50 mGal) forms a curved basement high that limits the *CB* on its western side (the Mossaka High). The greatest negative anomaly (-90 mGal) is located in correspondence of the Lokoro Basin. However, the anomaly's peak is shifted to NW with respect to the maximum depocenter of the basin. Other two distinct main anomalies (-70 mGal) correspond to the Gilson Basin, slightly shifted to the south with respect to the maximum interpolated sedimentary infill, and the Salonga Basin. In contrast, Lomami and Boende basins show weaker negative anomalies (-40 mGal). Therefore, there is not a strict correspondence between the basement depth and negative values of the residuals. This deviation could be due to interpolation-problems in the areas uncovered by seismic data or density variations in the sediments or shallow crystalline crust.

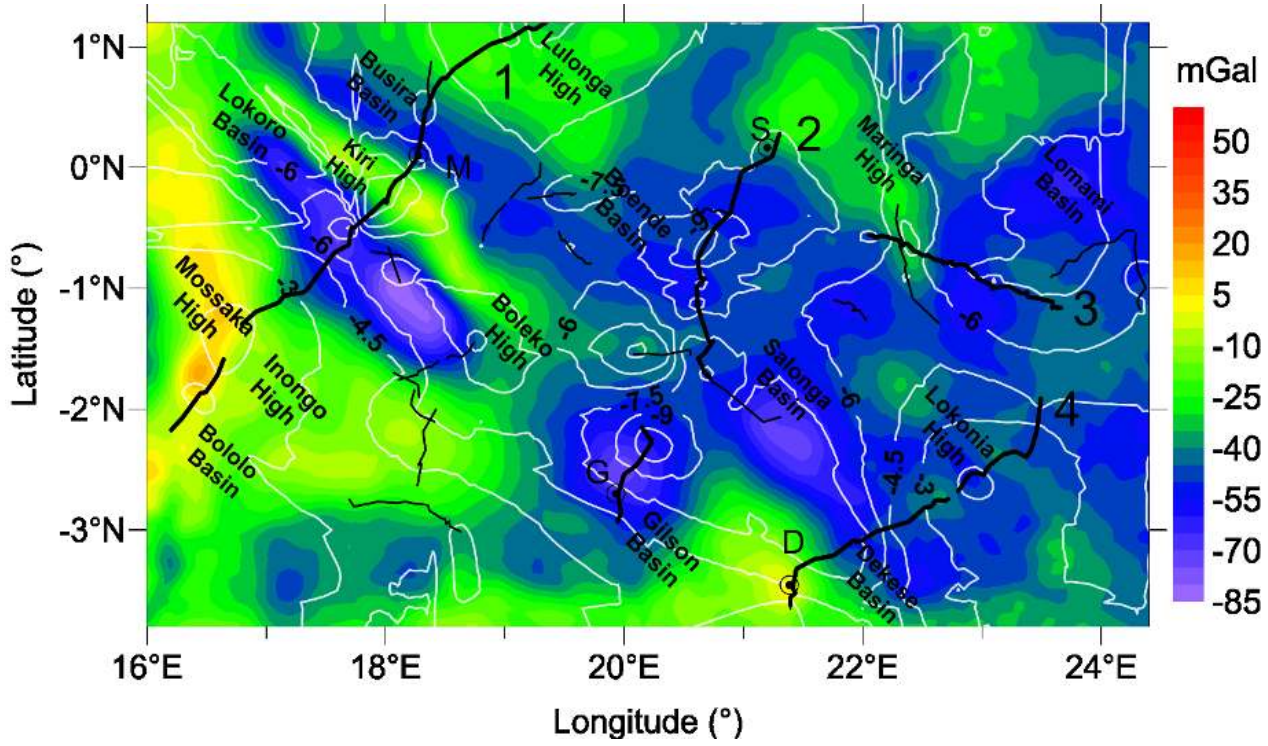

Fig. 3.8 *- Gravity residuals derived from the regression analysis between topography and Bouguer gravity anomaly field (BG_RES1). Thin broken thin black lines show the location of the seismic reflection profiles. Thick broken black lines labelled by black numbers (placed at the end of each line) are the chosen profiles used for the gravity analysis. White curves show the crystalline rock basement depth, reconstructed from the interpolation of the seismic reflection surveys. Black circles show location of the four wells drilled in the study area: D= Dekese; G=Gilson-1; M=Mbandaka-1; S=Samba.*

We plot the values of the residuals of the regression analysis against the depth of the two deepest seismic horizons related to top of the basement and the base of dolostones (R0 and R1, Chapter 2), along four profiles shown in Fig. 3.8. We can observe a good general correspondence between the lateral variations of the basement depth and residuals trend (Fig. 3.9-3.12, panels A and B). In particular, the deepest sedimentary depocenters match the most pronounced negative residuals. The direct correlation between the basement and dolomitic limestone depths with residuals is observed in the accompanying scatter plots (Fig. 3.9-3.12, panels C and D). We define a linear model in which the coefficients have 95% of confidence bounds:

$$Line(x) = p_1 * x + p_2 \qquad (4)$$

Where *p1* is the slope and *p2,* the intercept of the regression lines for the rock basement and the base of the dolomitic limestones along the profiles 1, 2, 3, and 4 (Fig. 3.9-3.12, panels C and D). The vaues of correlation coefficient, slope, and intercept are displayed in Table 3.

Profile 1 corresponds to the seismic combined lines R7-6-3-5-19 along the Congo River. Profile 2 corresponds to the seismic profile R60-50-51-52 across the central part of the basin, from the Gilson to the Samba well. Profile 3 corresponds to the seismic combined lines R15-9-10-16 crossing the Maringa High and the Lomami Basin. Profile 4 corresponds to the seismic profile L59 calibrated by the Dekese well and L58 (not interpreted due to the poor quality). All profiles have been interpreted and displayed in Chapter 2.

The high correlation coefficients for profiles 1 and 3 (Table 3.2) demonstrate the good fit between the gravity field and the deepest horizons, with a slightly better correlation with the base of dolomitic limestones compared to the top basement. This could be because the layer just above the basement contributes little to the entire mass-reduction of the sediments package. In addition, the base of the dolomitic limestone layer is better defined in the seismic profiles than the top of the basement, so the latter could be determined with less accuracy during the seismic interpretation. The greatest values of the correlation coefficients for profile 3 could be probably due to the sedimentary sequences not significantly affected by the tectonic deformation (Chapter 2). I find a much lower correlation coefficient for the profile 2, likely due to the lack of resolution in parts of the raw seismic data, a large gap in the seismic data, and presence of faults. Furthermore, the residuals along profile 4 show a weak correlation with both seismic horizons (Table 3.2). However, I initially calculated a single linear trend as for the previous profiles, whose correlation coefficient was 0.145 and 0.165 for R1 and R0, respectively. Then, according to the two main different trends followed by the samples (Fig. 3.12 A-C), I divided them into two groups and fitted them separately by two linear equations (Figs. 3.12 B-D). The steeper line (a, Fig. 12) refers to the first ~100 km along the profile: here I observed a high correlation between gravity signals and seismic basement depth. On the other hand, the less steep line (b, Fig. 12) indicates a very weak correlation between these parameters. This suggests that in this area, between Dekese Basin and Lokonia High (Profile R59, Chapter 2), the gravity is not sensitive to the shallow basement and/or base dolostones depth variations. The systematic negative gravity anomaly is likely caused by the shallowest sedimentary sequences, which are characterized by a low density and an almost constant thickness of about 3 km all over the southeastern regions (Chapter 2).

	Profile 1	Profile 2	Profile 3	Profile 4
Correlation Coefficient R0	0.723	0.297	0.832	0.916 (a) 0.237 (b)
Correlation Coefficient R1	0.785	0.423	0.906	0.909 (a) 0.241 (b)

Table 3.2 - *Values of the correlation coefficients between the isostatically corrected Bouguer gravity anomalies (residuals of the topography-Bouguer field regression analysis) and depths of the crystalline basement (R0) and base of dolomitic limestones (R1), respectively, along the four profiles displayed in Fig. 8. In Profile 4, (a) and (b) values refer to the two different groups of samples showed in Fig. 12.*

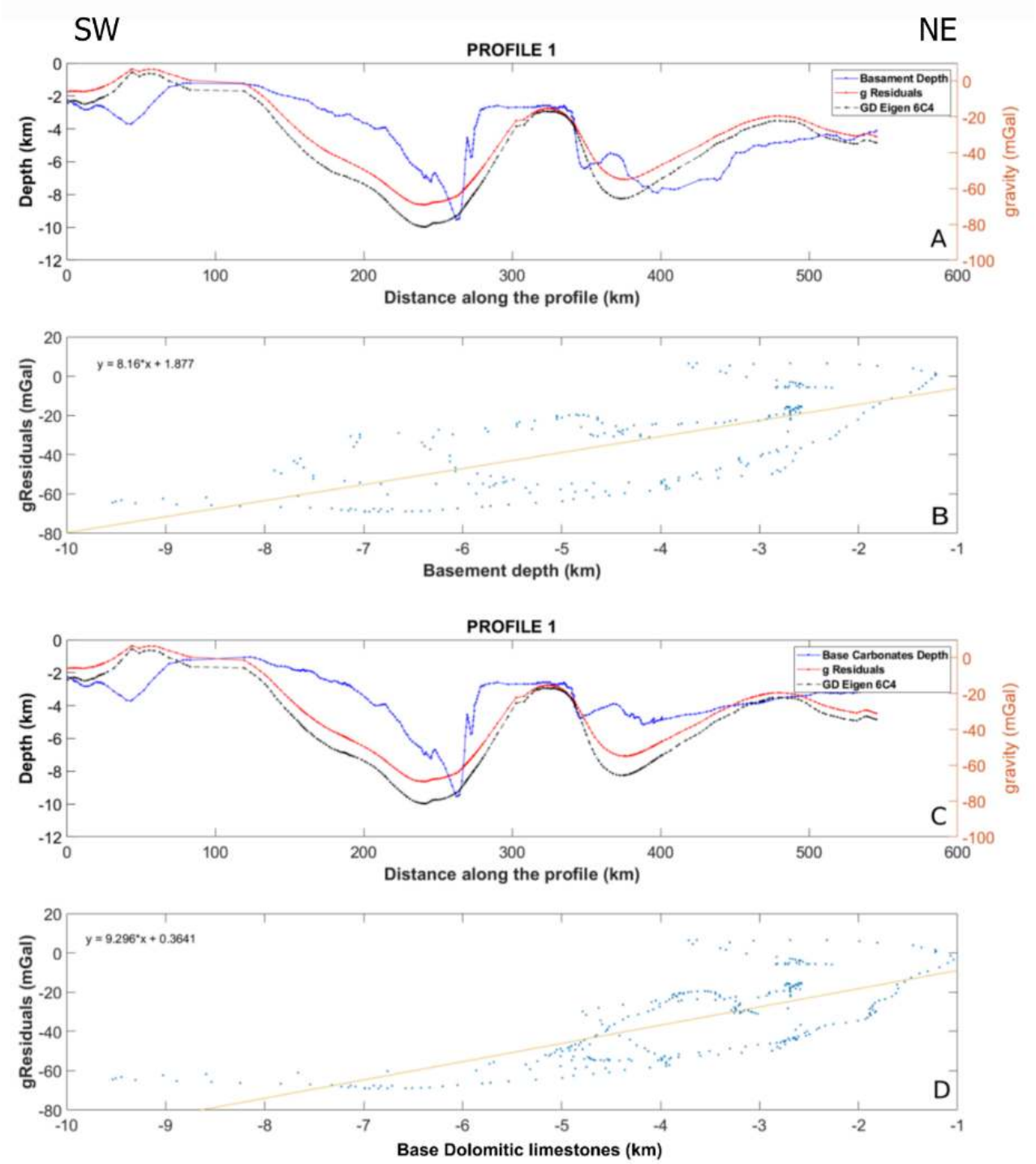

Fig. 3.9 *- (A-C) Relationship between BG_RES1, gravity disturbance, and depth of the seismic reflection horizons. (B-D) Scatter plot of the residuals of BG_RES1 versus the depth of the seismic reflection horizons along profile 1, displayed in Fig.3.8.*

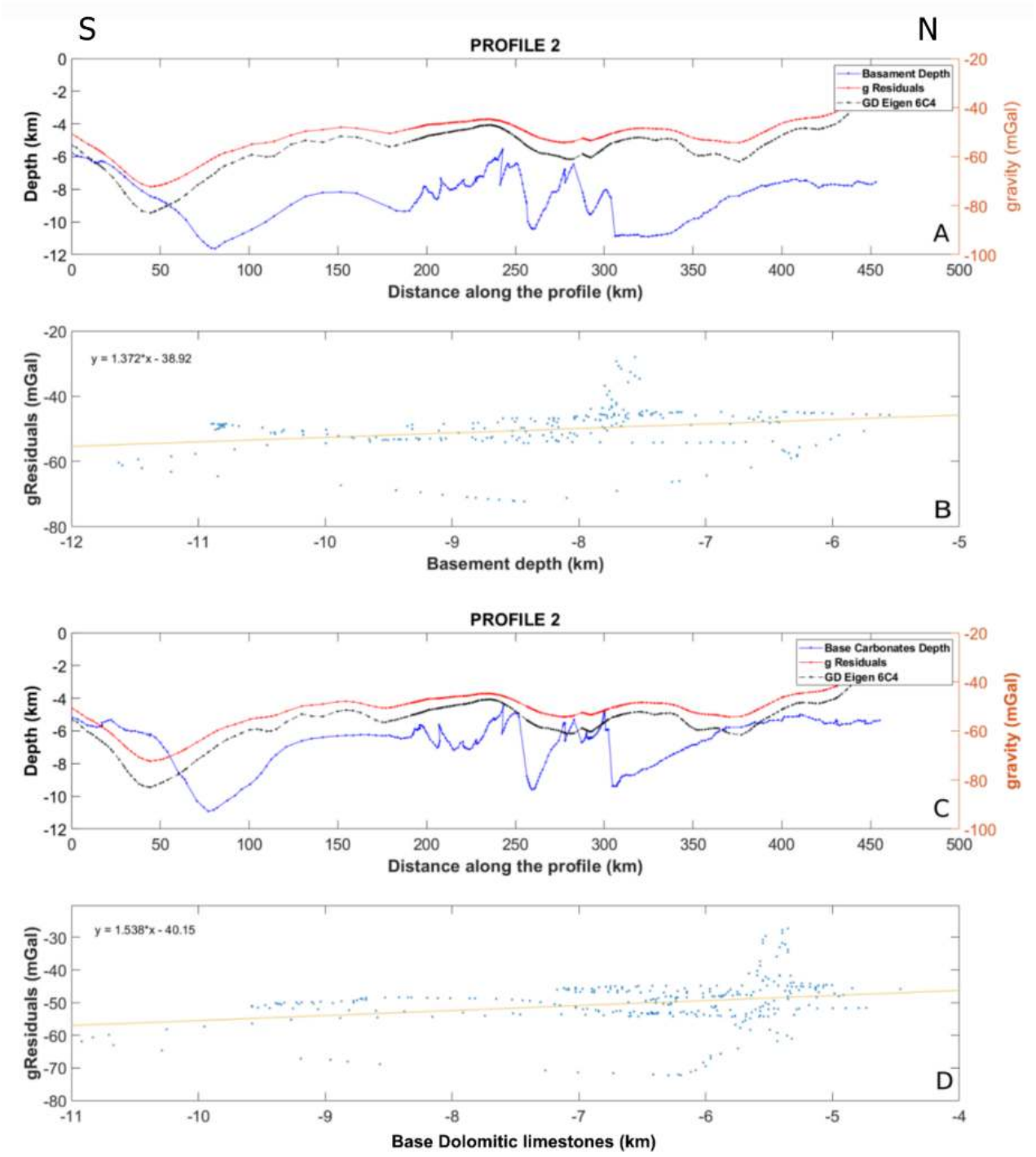

Fig. 3.10 *- (A-C) Relationship between BG_RES1, gravity disturbance, and depth of the seismic reflection horizons. (B-D) Scatter plot of the BG_RES1 versus the depth of the seismic reflection horizons along profile 2, displayed in Fig.3.8.*

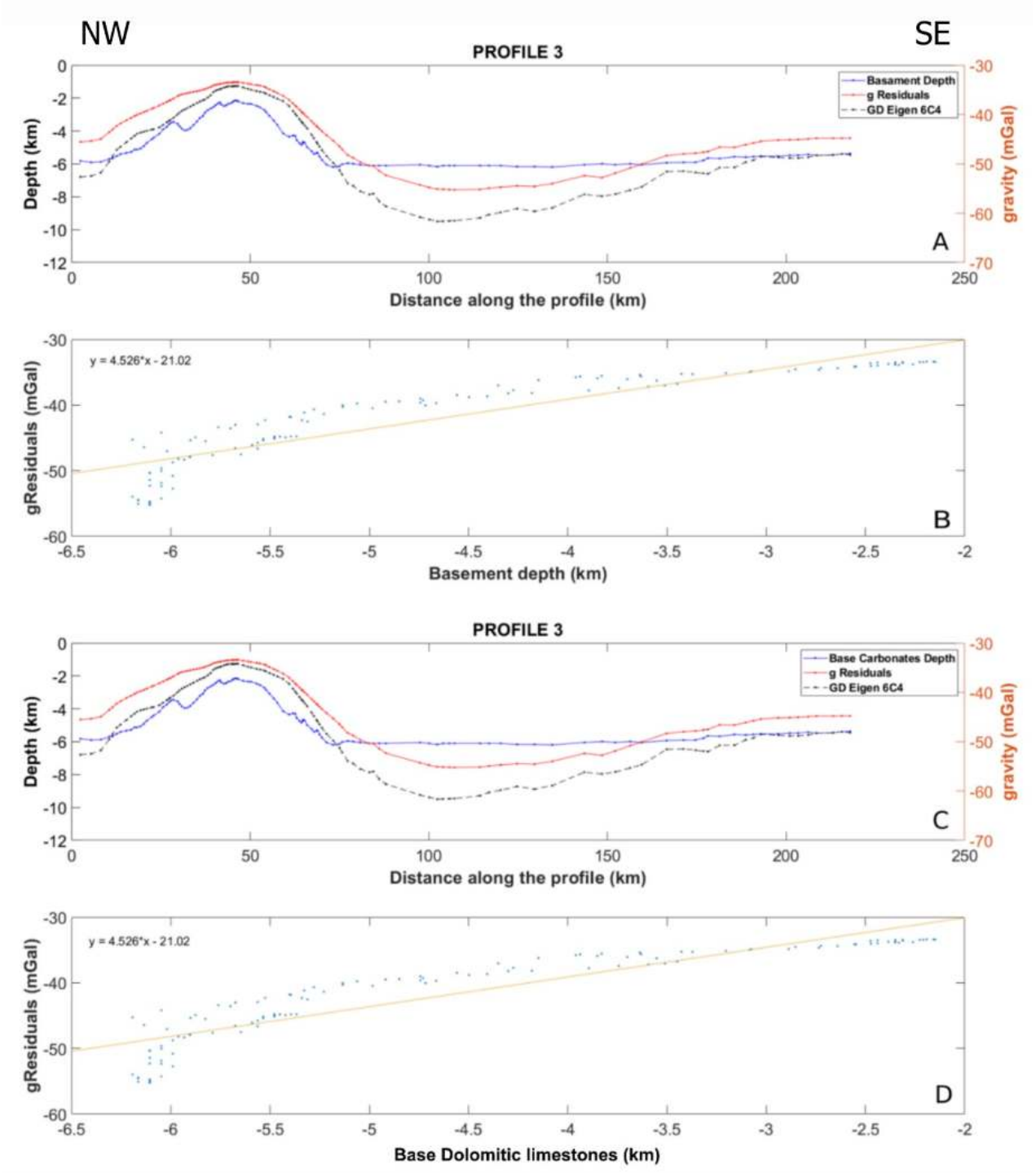

Fig. 3.11 - ***(****A-C) Relationship between BG_RES1, gravity disturbance, and depth of the seismic reflection horizons. (B-D) Scatter plot of the BG_RES1 versus the depth of the seismic reflection horizons along profile 3, displayed in Fig.3.8.*

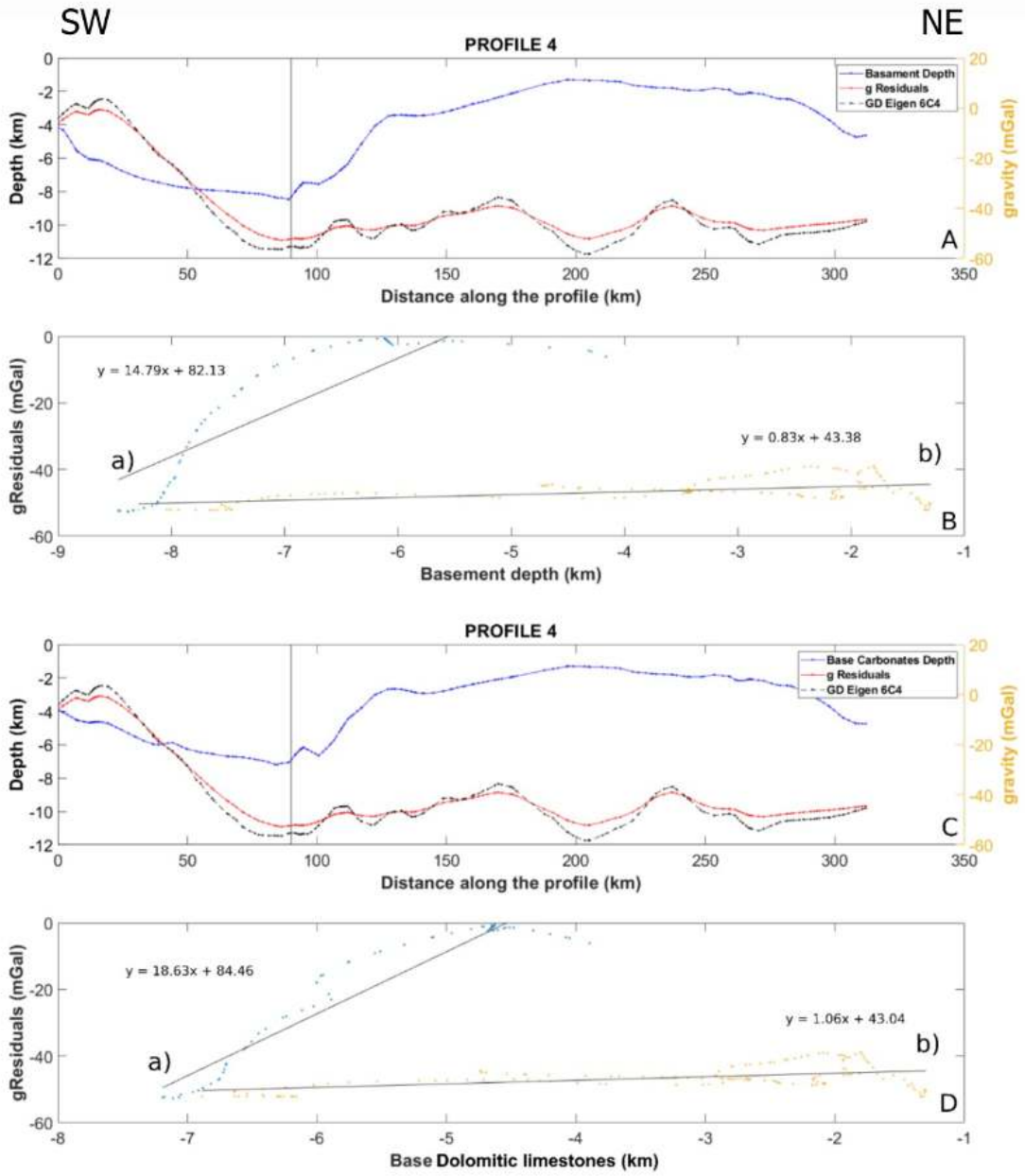

Fig. 3.12 *- (A-C) Relationship between BG_RES1, gravity disturbance, and depth of the seismic reflection horizons. (B-D) Scatter plot of the BG_RES1 versus the depth of the seismic reflection horizons along profile 4, displayed in Fig.3.8. The vertical line shown in panels A and C represents the location, along the profile, in which the gravity data points (B and D) change their behavior. a) and b) labels refer to the two different lines interpolating samples along the profile 4. Line a) describes the behavior of samples around the Dekese Basin, while line b) around the Lokonia High.*

3.4 Field residualization

As a first test to verify the amount of signal reduction through the gravity effect of the interpolated sediments layers, I subtracted the sedimentary gravity effect *G_SED* from the residuals of the Bouguer-topography regression analysis (*BG_RES1*). The results are the field *BG_RES2* (Fig. 3.13), in which the small-scale features due to the basement architecture variations and overlying sediments are expected to be reduced, and the average level of the residuals to oscillate around zero. If this is not the case, for instance, if the field has a systematic positive upward shift, it represents the gravity effect of increased density variations at some depth level in the crustal and sub-crustal lithosphere. The short wavelength part of the field can also represent flaws in the basement depth, and consequently in the sediment layer thickness, due to interpolation between the seismic lines.

The new residuals *BG_RES2* have reduced short wavelength signal, but values span between -20 and +110 mGal and are systematically positive in most of the Cuvette Centrale. These results are in agreement with the gravity anomalies obtained by Watts et al. (2018) after the removal of the calculated gravity effect of sediments from the Bouguer anomaly, with the assumption of a density contrast with the crystalline basement of 2.7 g/cm^3 and applying a high-pass filter to the gravity field, to remove the very long wavelength contributions. In particular, the results agree in the central area of the *CB*, where Watts et al. (2018) show a gravity anomaly high between +40 and +60 mGal and negative anomalies along the edge of the basin. Some differences are present across the Kiri High and Lokoro Basin, where the values of *BG_RES2* span from +70 mGal to +10 mGal, respectively, while the gravity anomalies of Watts et al. (2018) are weakly negative. Furthermore, the Lokonia High shows a well distinct positive anomaly in Watts et al (2018) and weak negative values of *BG_RES2* (Fig. 3.13).

The strong linear positive-negative gravity field of the Kiri High and adjacent basins is very much reduced, although larger scale positive values located in the Kiri, Inongo, and Mossaka highs (between +40 and +70 mGal) are present. They might be related to an increase of crustal density, due to the intrusion of mafic bodies (2.8-3.0 g/cm^3), which likely occurred during the rift phase that initiated the subsidence of the *CB*. High positive values, likely of similar origin, are also observed in the southern part of the Dekese Basin (+96 mGal). The most negative values cover the eastern part of the Cuvette Centrale, between the Salonga and Lomami basins and in the Lokonia High (-12 mGal), suggesting the presence of a different crustal type (e.g., a more sialic crust). Other sedimentary depocenters show weak positive residuals (< 35 mGal), such as the deepest part of the Lokoro, Boende and Lomami basins. This indicates that the gravity effect of sediments obtained from the interpolated seismic lines correctly reduced small-scale anomalies at the scale of the basins. However, there is an effect of compensation of the density of the sediments by an increased density in the underlying crust.

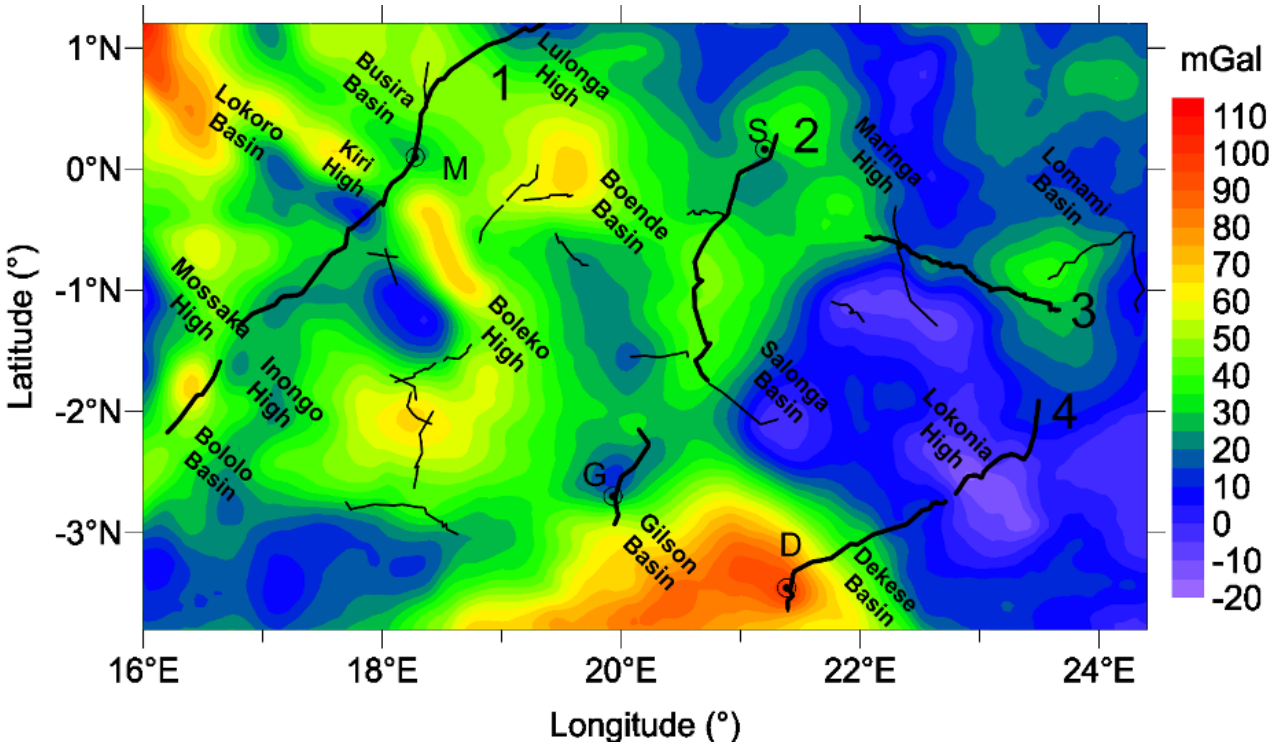

Figure 3.13 *- Gravity residuals BG_RES2, obtained by subtracting the gravity effect of the sediments (G_SED) from the Bouguer residual values BG_RES1. Thin broken black lines show location of the seismic reflection profiles. Thick broken black lines labelled by black numbers (placed at the end of each line) are the chosen profiles used for the gravity analysis. Black circles show location of the four wells drilled in the study area: D= Dekese; G=Gilson-1; M=Mbandaka-1; S=Samba.*

3.5 Basement depth from gravity inversion modelling

I estimated the depth of the basement from a preliminary gravity inversion modelling of the entire Cuvette Centrale, using as input the gravity field *BG_RES1* (the residuals of the regression analysis between Bouguer field and topography), the seismic basement depth along the seismic lines, and the superficial density contrast between the shallowest sedimentary layer and the crystalline crust. The top of the model is represented by the topography, while the bottom by the top basement. The density of the basin is assumed to increase with depth, following an analytical parabolic function, which mimics the well-known exponential depth decay of rock porosity. The parabolic function represents the interpolation of the observed density increase as shown in Fig. 3.6. I performed the calculation imposing the maximum depth of the basement equal to 15 km, which is close to the maximum value obtained from the interpolation of the seismic profiles (Chapter 2, Fig. 2.12 A).

In particular, the density variation with depth of the basin (Martins et al., 2010) is obtained using an analytic function that approximates the exponential compaction law. The function is the following:

$$\Delta\rho(z) = \frac{{\Delta\rho_0}^3}{(\Delta\rho_0 - \alpha z)^2} \qquad (3.5)$$

With $\Delta\rho_0$ the superficial density contrast, and α, the function parameter that governs the increase of density with depth (3.7). The increasing density is due to compaction and is expressed by an exponential function:

$$\Delta\rho(z) = \Delta\rho_0 e^{-\beta z} \qquad (3.6)$$

Where $\Delta\rho_0$ is the superficial density contrast and β the porosity decay parameter, assumed equal to 0.27 km^{-1}, an appropriate value for sandstone (Allen and Allen, 2005), which is the most representative lithology of the sediments of the basin (Table 3.1). Given a reference depth (*z_ref*), chosen as maximum depth of the basement (15 km), I can calculate the parabolic parameter α from equation:

$$\alpha = \frac{1}{z}\Delta\rho_0\left(1 - e^{\frac{1}{2}\beta z\_ref}\right) \qquad (3.7)$$

In order to define the parameters of the parabolic density, we also fit the parabolic function to the observed density values as a function of depth. In this way, I calculated the best approximation of the parabolic function to the exponential function fitting the porosity decay with depth. The results obtained by these first tests, using different superficial density contrasts and both including and excluding the seismic constraints, show a basement depth shallower by several km (Fig. 3.14), compared to the seismic basement (Fig. 3.1). This can be the effect of high-density bodies at crustal level below the basin, which partly compensate the gravity field of the low-density sediments, and are the reason for the systematically positive gravity residuals of *BG_RES2* (Fig. 3.13).

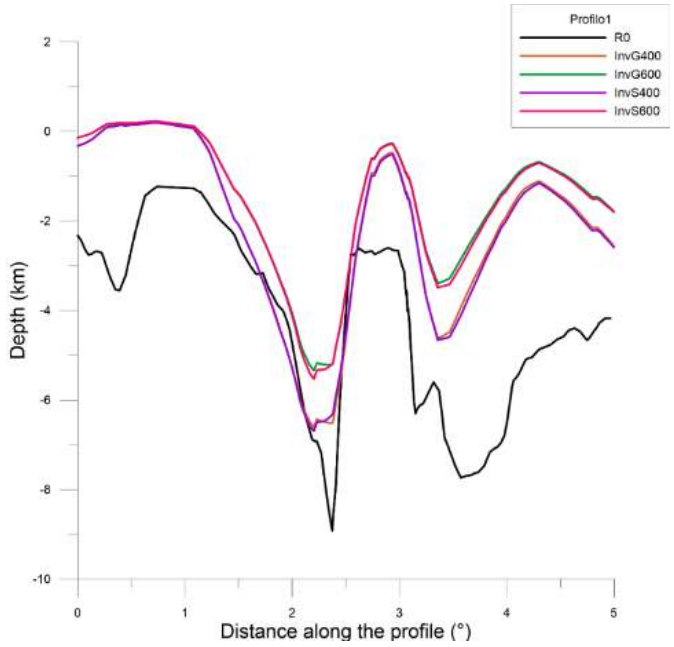

Figure 3.14 *– Example of the basement depth retrieved along seismic reflection profile 1, using superficial density contrast of -0.400 g/cm³ and -0.600 g/cm³ and resulting from the preliminary inversion-modelling test based on the inversion of BG_RES1. R0: seismic basement. InvG400: basement depth obtained using gravity input and density contrast of -0.400 g/cm³. InvG600: basement depth obtained using density contrast of -0.600 g/cm³. InvS400: basement depth obtained for inversion of the BG_RES1 constrained by seismic reflection with a density contrast of -0.400 g/cm³. InvS600: basement depth obtained for inversion of the BG_RES1 by seismic reflection lines with a density contrast of -0.600 g/cm³.*

To improve the consistency of the results obtained from the gravity inversion and the seismic interpretation, I first interpolated the residuals *BG_RES2* (Fig. 3.13) with polynomial regression surfaces (*PS*, linear, quadratic, and cubic, Fig. 3.15), using the same grid size and resolution of the other data (Lat: 1.2°N-3.8°S, Lon: 16°E 24.5°E and resolution 0.025°). For the interpolation, I used SURFER, Golden Software package. In the case of cubic fitting, the long period of anomaly correction amounts up to -35 mGal, while for the linear and quadratic one the effect is lower. Afterwards, I subtracted *PS* from the residuals of the regression analysis *BG_RES1* (Fig. 3.8), and obtained *BG_RES3*, representing the sediments contribution. Indeed, although the interpolated basement has short-wavelengths flaws, it is a valid means to define the long-wavelength gravity field generated by the mantle and that remains after correcting the observed gravity field for crustal thickness and interpolated sediments. If this step would not be done, the gravity residuals corrected for the crustal thickness only, would still have a long wavelength signal, similar to an almost static shift that does not represent the sediment layers or intra-crustal anomalies, which in turn produce shorter wavelengths.

The new residuals (*BG_RES3*, Fig. 3.15 A-C) are thus obtained subtracting the polynomial regression surfaces of first, second and third order. They show a similar distribution: the greatest negative values (< -80 mGal) coincide with the deep basins, while the weak negative or positive values correspond to the highs. I observed that significant negative values are present also in regions uncovered by seismic data (such as those southwest to the Gilson Basin), which may identify other sedimentary depocenters along the margin of the Kasaï craton. I also noticed that the increase of the polynomial degree causes an increase of the residuals range (Fig. 3.15 A-C). I inverted *BG_RES3*, for the depth of the basement initially using a superficial density contrast of sediments against the crystalline rock basement of -0.400 g/cm^3 and the above-mentioned parabolic density-

depth curve (Fig. 3.20). I then analyzed the results along the four profiles used in the previous analyses and noticed that they do not change significantly by varying the polynomial degree of the surface (on average few hundred meters). However, the residuals obtained using the cubic surface (Fig. 3.15 C) produce a basement depth slightly more consistent with the seismic basement.

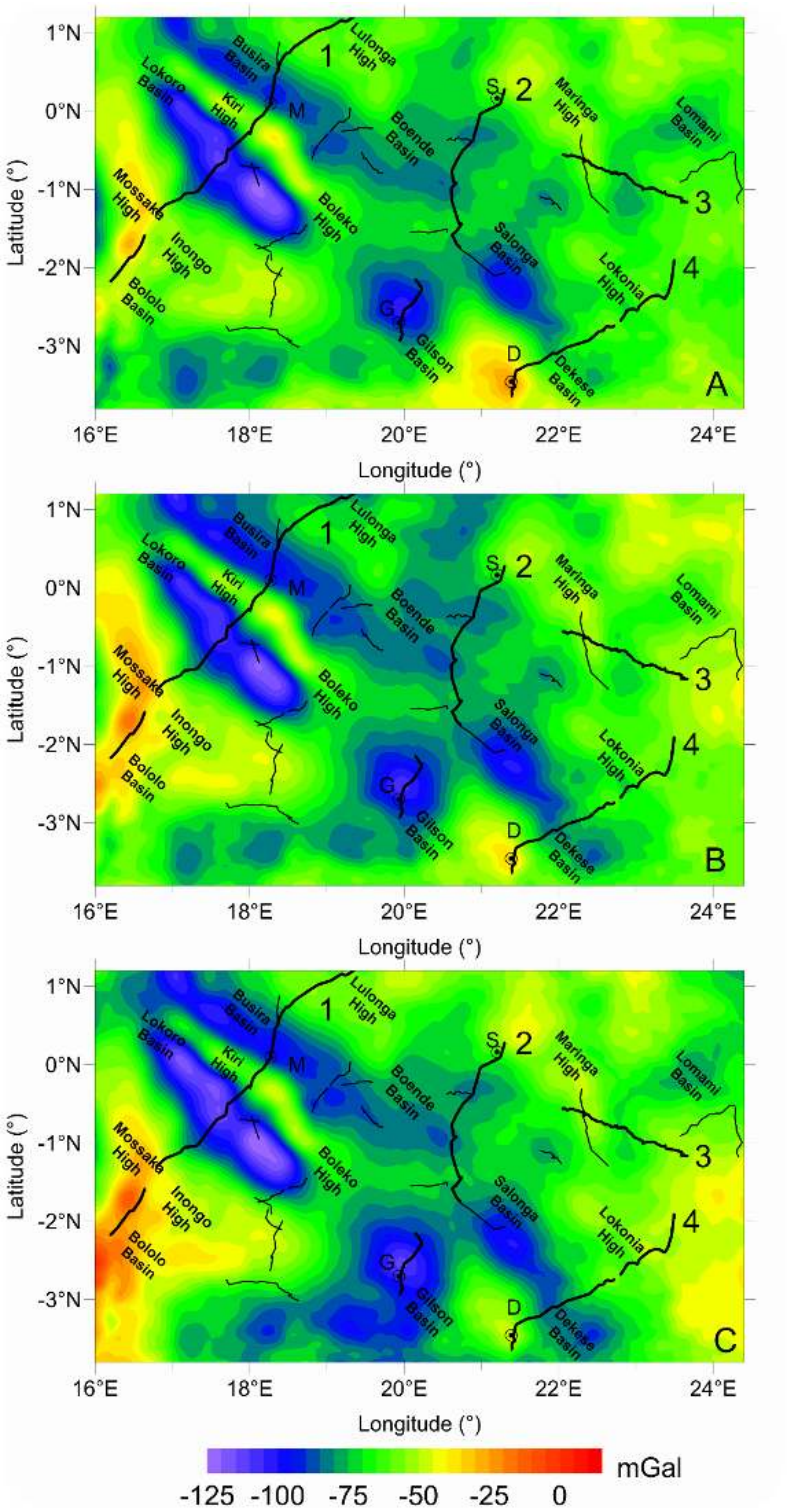

Figure 3.15 - *Residuals (BG_RES3) obtained subtracting the polynomial regression surfaces: (**A**) Simple planar, (**B**) quadratic, and (**C**) cubic from the residuals (BG_RES1, Fig. 3.8). Thin broken black lines show location of the seismic profiles. Thick broken black lines identified by numbers (placed at the end of each line) are the chosen profiles used for the gravity analysis. Black circles show location of the four wells drilled in the study area: D= Dekese; G=Gilson-1; M=Mbandaka-1; S=Samba.*

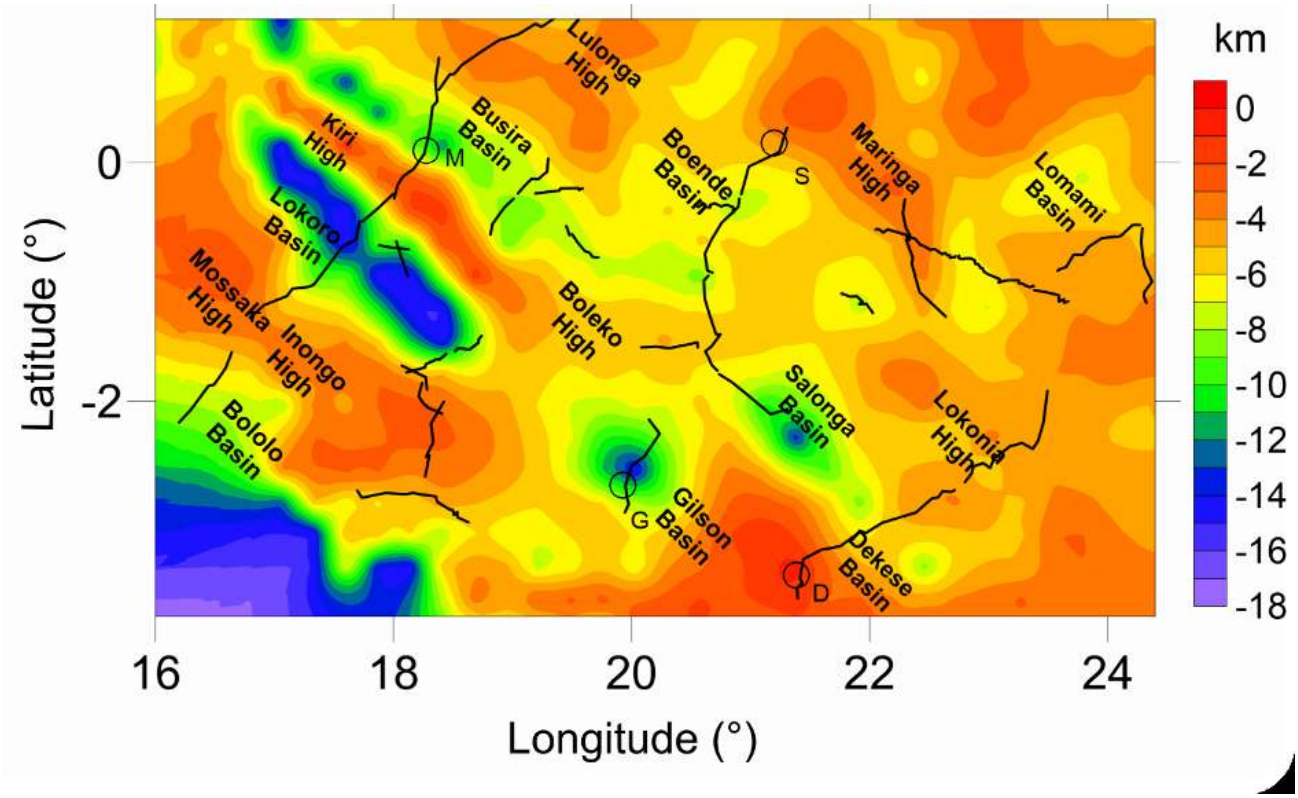

Figure 3.16 – *Basement depth obtained from gravity inversion modelling using a simple planar regression surface. The model is constrained by basement depth values obtained from the interpretation of the seismic reflection profiles, displayed as broken black lines, and a density contrast of -0.400g/cm³. Black circles show location of the four wells drilled in the study area: D= Dekese; G=Gilson-1; M=Mbandaka-1; S=Samba.*

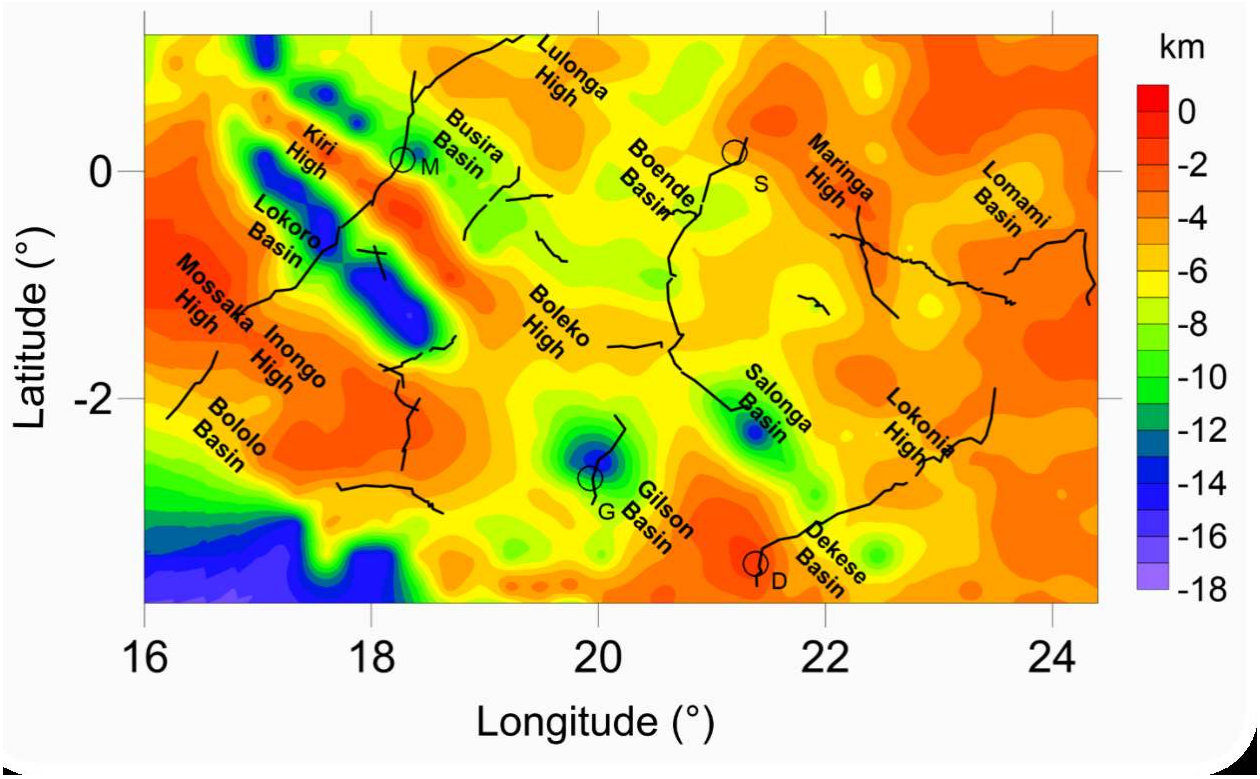

Figure 3.17 *– Basement depth obtained from inversion modelling using a quadratic regression surface. The model is constrained by basement depth values obtained from the interpretation of the seismic reflection profiles, displayed as broken black lines, and a density contrast of -0.400g/cm³. Black circles show location o he four wells drilled in the study area: D= Dekese; G=Gilson-1; M=Mbandaka-1; S=Samba.*

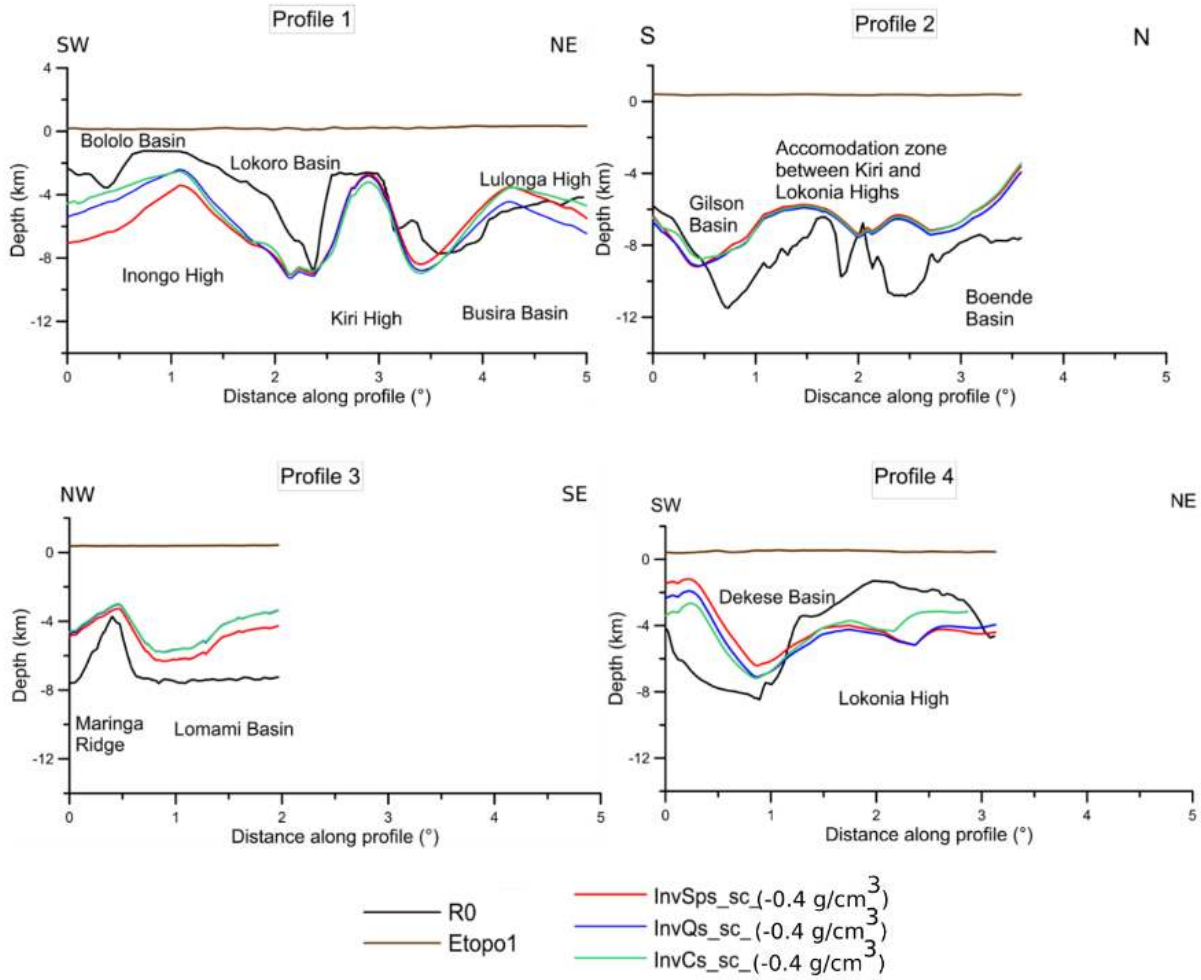

Figure 3.18 - *Basement depth obtained from the inversion of the residuals displayed in Fig. 3.15, using seismic data as constraints and a superficial density contrast crystalline rock basement and sediments of -0.400 g/cm³. Abbreviations in the legend are as follows: R0 = seismic basement. Etopo1 = topography. InvSps_sc_ (-0.4 g/cm³) = basement depth obtained from inversion of the residuals BG_RES3 displayed in Fig. 3.15 A. InvQs_sc_ (-0.4 g/cm³): basement depth obtained from inversion of the residuals displayed in Fig. 3.15 B. InvCs_sc_ (-0.4 g/cm³): basement depth obtained from inversion of the residuals displayed in Fig. 3.15 C.*

The comparison of the values of *G_SED* (Fig. 3.7), *BG_RES1* (Fig. 3.8), and the residuals *BG_RES3*, (Fig. 3.15 C) along the same four profiles (Fig. 3.19), shows that the first two fields have very similar trends, but only the last one is in the same range of *G_SED*. This means that the residuals *BG_RES3* reflect only the effect of sediments. Furthermore, there is a significant lateral variation of *G_SED* and *BG_RES3*, linked to the basement depth heterogeneites (high correlation between the negative anomalies and deep basins). Therefore, I considered for discussion only the results obtained from the inversion of the residuals *BG_RES3*, derived from the subtraction of the cubic *PS* (Fig. 3.15 C). I inverted these residuals also using a superficial density contrast of -0.800 g/cm³ (Fig. 16 B). The choice of two different density contrasts was made, considering that the sedimentary layers have a different density and thickness in the study area (Delvaux et al., 2021). A very high density contrast (-0.800 g/cm³) is justified, considering the very low density of the shallowest sediments (Table 1) and that of the rock basement in case its composition becomes more mafic for the intrusion of volcanic bodies (2.8 to 3.0 g/cm³).

In defining the parabolic density increase, I find that in the range between -0.400 and -0.800 g/cm^3, the values of the density cotrast obtained from samples can be fitted by the parabolic curve. However, using the higher superficial density contrast, I observed a faster reduction of density contrast with depth (Fig. 3.20). More precisely, from the top to the depth of 3 km, the density curve referring to the lower density contrast (Lower Density Curve, LDC), Fig. 3.20, shows a smaller density contrast associated to the basement depth, with respect to the other curve (Higher Density Curve, HDC). The opposite is true for depths greater than 3 km. The greatest density contrast produces a significant deepening of the basement depth in the basin areas, while in other parts this deepening is less evident. The results of the inversions using the two superficial density contrasts are displayed in Fig 3.21 A-B.

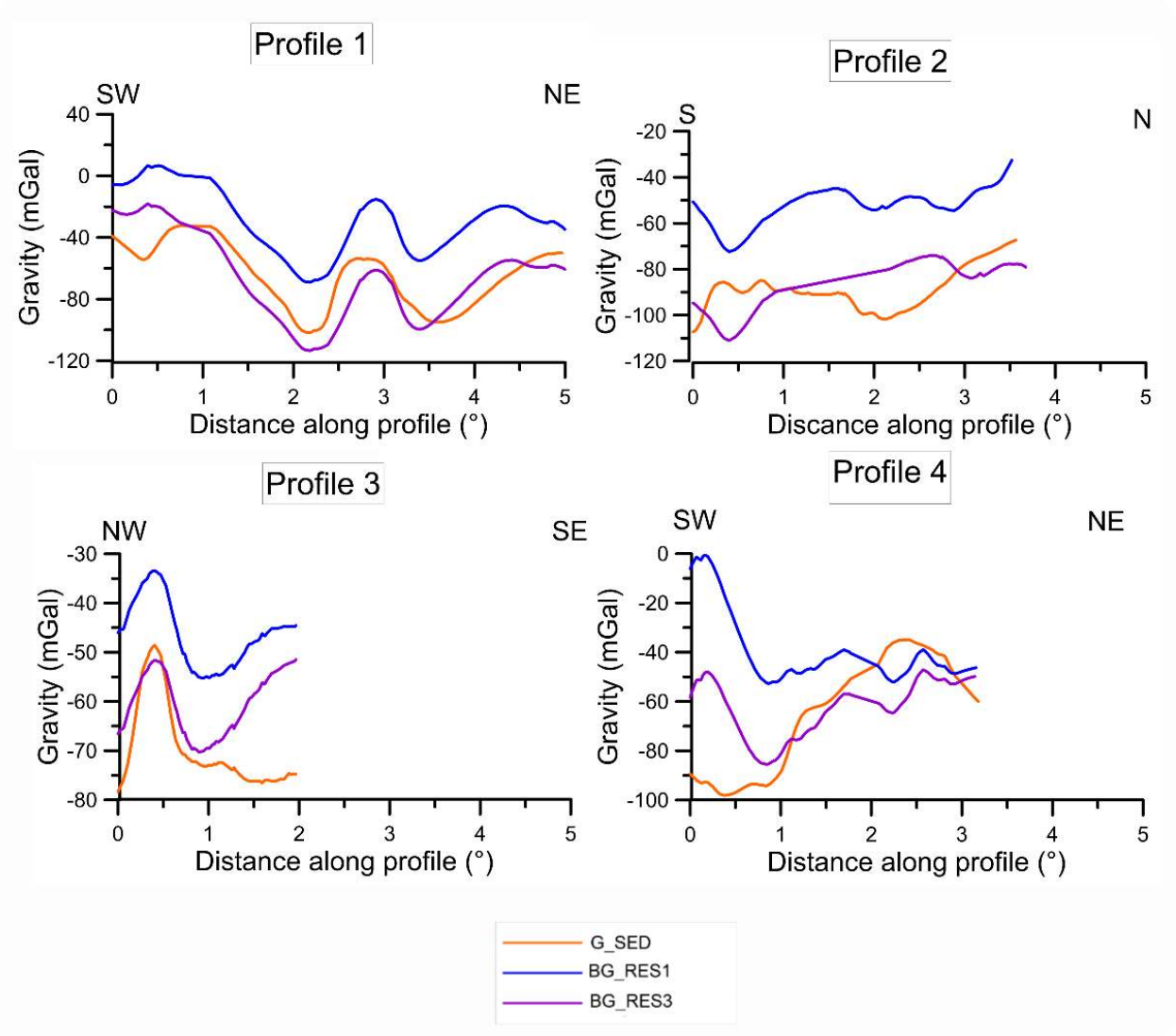

Figure 3.19 – *Gravity fields and basement depths derived along four profiles located in the Cuvette Centrale. Black line: basement depths obtained from interpolation of seismic lines G_SED: Gravity effect of the sediments; BG_RES1: residuals obtained from regression analysis; BG_RES3: difference between residuals from the regression analysis and the polynomial (Cubic) regression surface.*

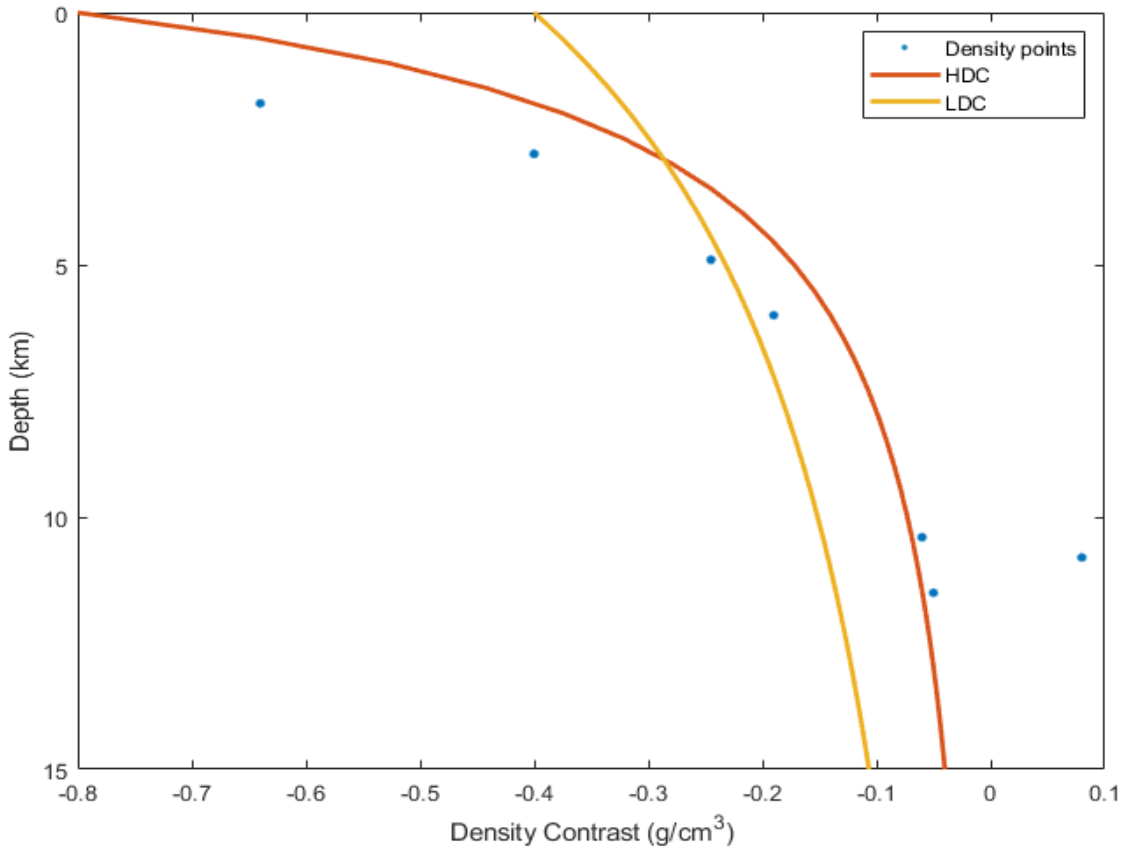

Figure 3.20 *– Depth variation of density contrast. Blue points show the density contrast of sediments belonging to the different sedimentary sequences at their average depth (Delvaux et al., 2021) with the density of the crystalline crust (2.67 g/cm^3). HDC stands for High Density Curve and represents the parabolic curve implemented, using superficial density contrast equal to -0.800 g/cm^3. LDC stands for Low Density Curve and represents the parabolic curve implemented, using superficial density contrast equal to -0.400 g/cm^3*

The results show the alternation of small basins and highs, *NW-SE* trending (Fig. 3.21 A-B), already observed in the magnetic anomalies (Fig. 3.3). In particular, the continuity of the Kiri High, masked by the effect of the interpolation of the seismic profiles (Fig. 3.1), is now clearly visible and the sharp variation with the surrounding small basins is enhanced when we use the top density contrast of -0.800 g/cm^3 (Fig. 3.21 B). Both maps show the possible extension of the Lokoro Basin (10.5 km deep), trending *NW-SE*, in areas uncovered by seismic profiles. On the other hand, the maximum depocenter of the Lomami Basin (~11 km deep) appears *NW* shifted with respect to that obtained from the interpretation of seismic profiles. When I use a density contrast of -0.800 g/cm^3, the depth of the basement becomes deeper in the basins and shallower in the areas outside the basins, compared to the seismic basement (Fig. 3.1). In particular, I can notice the extension of the Busira Basin (7-9 km deep) in *NW* direction and the presence of other possible small basins south to Gilson Basin (Fig. 3.21 B).

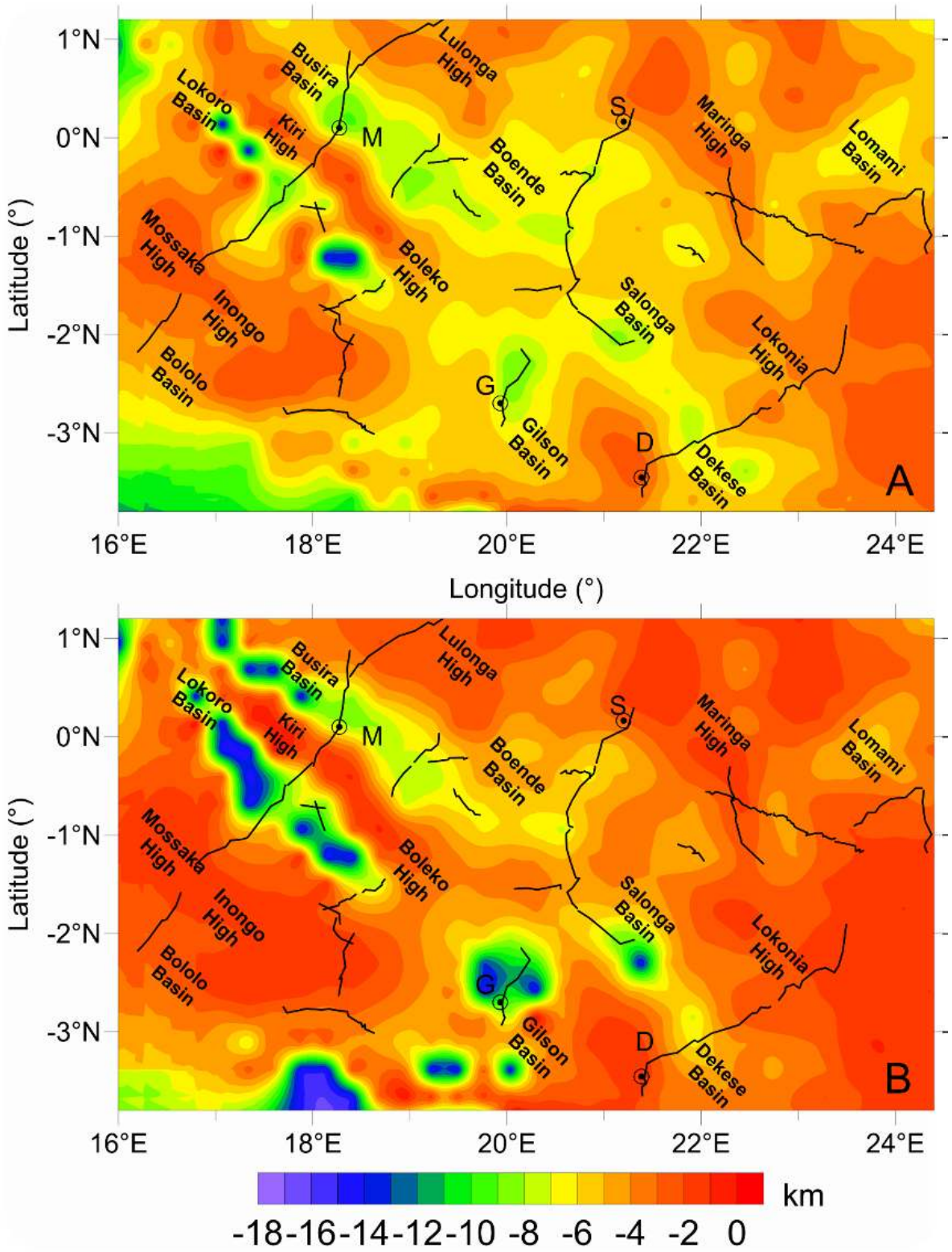

Figure 3.21 - *Basement depth obtained from the inversion of the residuals displayed in Fig. 3.15C and constrained by seismic data. The shallow density contrast (Δρ) used is (**A**): -0.400 g/cm³ and (**B**): -0.800 g/cm³, with contrast decaying with depth according to the parabolic function. Broken black lines show location of the seismic profiles. Black circles show location of the four wells drilled in the study area: D= Dekese; G=Gilson-1; M=Mbandaka-1; S=Samba.*

3.6 Discussion

The investigation of the shallow structures of the *CB*, using potential field data and seismic constraints, revealed the existence of *NW-SE* structural highs, matching the axial magnetic zone (Fig. 3.3), dividing the Cuvette Centrale into two parts. In particular, the Kiri High matches the high axial magnetic zone, which is marked by the general absence of Dolomitic limestones, while further to the West the magnetic zone coincides partly with the Lokonia High, but also with the Salonga Basin. These results are consistent with the series of positive and negative Bouguer and free-air gravity anomalies *NW-SE* oriented, which identify an alternation of highs and sedimentary depocenters (Fig. 3.5). The comparison between the seismic basement depth (Fig. 3.1), reconstructed form the interpolation of seismic data and that of the different basements, obtained using gravity data, shows the existence of common features. In particular, it is possible to identify three main depocenters, where the basement reaches very large depths between 7 and 18 km, the Lokoro Basin in the SW and two basins, such as the Gilson and Boende, *NE-SW* oriented. The Lokoro Basin, formed by two main *NW-SE* trending depocenters, is separated from the Busira Basin (maximum basement depth about 7.5 km), and located in the northern part, by the Kiri High. This alternation of highs and deep basins, *NW-SE* oriented, is already known since the time of the first explorations in the *CB* (e.g., Cahen, 1954; Kadima et al., 2011a). This feature is also well visible as a negative-positive *NW-SE* trending structures in the gravity disturbance (Fig. 3.3a) and a recent reconstruction of the basement depth, obtained using gravity data (Kaban et al., 2021). On the other hand, the basement depths reconstructed from gravity modelling (Fig. 3.5) reveal in most of cases the continuity of the Kiri and Boleko High, while that obtained from seismic data shows the presence of a sedimentary cover in the areas between the two highs (Fig. 3.1). Therefore, I consider this feature as an artefact due to the interpolation of the seismic reflection profiles, in a zone uncovered by data. Another artefact of the seismic interpolation is the merging of the Gilson, Salonga, and Dekese basins in one single large sedimentary depocenter (Fig. 3.1), while they clearly appear as separate basins in the other basement maps (Fig. 3.21).

On the other hand, there are features that I could identify only by the basement depths reconstructed from gravity inversion modelling. Among the others, there is the Salonga Basin, having a peculiar position in the alignment of the Kiri High and evidenced by a positive magnetic anomaly (Fig. 3.21). The correlation coefficient between the two gravity basement maps (Table 3.3), as expected, reveal a significant consistency, while it is much lower with the seismic basement. To compare the results in more detail, I derived the seismic (Fig. 3.1) and gravity basement depths (Fig. 3.21) along the four seismic lines (Fig. 3.22) used in the previous analysis.

	R0	Inv400	Inv800
R0	1.000	0.242	0.254
Inv400	0.242	1.000	0.698
Inv800	0.254	0.698	1.000

Table 3.3 – *Correlation coefficient (CC) between the different basement depths. R0: seismic basement. Inv400 and Inv800: basement depth obtained from the inversion of the gravity residuals BG_RES3 and using a density contrast value of -0.400g/cm^3 and -0.800g/cm^3, respectively.*

	R0	Inv400	Inv800
R0	1.000	0.737	0.728
Inv400	0.737	1.000	0.972
Inv800	0.728	0.972	1.000

Table 3.4 – *Correlation coefficient (CC) between the different basement depths along profile 1. Labels are as in table 3.3.*

	R0	Inv400	Inv800
R0	1.000	0.367	0.311
Inv400	0.367	1.000	0.925
Inv800	0.311	0.925	1.000

Table 3.5 – *Correlation coefficient (CC) between the different basement depths along profile 2. Labels are as in table 3.3.*

	R0	Inv400	Inv800
R0	1.000	0.537	0.491
Inv400	0.537	1.000	0.997
Inv800	0.490	0.997	1.000

Table 3.6 – *Correlation coefficient (CC) between the different basement depths along profile 3. Labels are as in table 3.3.*

	R0	Inv400	Inv800
R0	1.000	0.616	0.657
Inv400	0.616	1.000	0.994
Inv800	0.658	0.994	1.000

Table 3.7 – *Correlation coefficient (CC) between basement depths along profile 4. Labels are as in table 3.3.*

Along profile 1, the basement depths obtained from the gravity data show similar trends and reproduce more smoothly the seismic basement depth variations and thus they do not identify sharp transitions between local sedimentary deeps and highs (Fig. 3.22). The maximum misfit of all gravity basement depths with respect to the seismic one is about 2-3 kilometers. This indicates that the different methods produce consistent results and supports the interpretations of the seismic reflection profiles. The correlation coefficients (*CC*) between the seismic and gravity basement depths along the profile are high, reaching values between 0.737, 0.728, and even higher between the different gravity basement depths (*CC* = 0.972, Table 3.4). The maximum depth of the Busira Basin, reconstructed from the gravity inversion, is southwestward shifted by some tens of kilometers with respect to that obtained from seismic interpolation. On the other hand, the shallow Bololo Basin and Inongo High are not clearly distinguished by the trend of the gravity basement depths. The last one are 2-3 km shallower than the seismic basement in the Lulonga High. This feature likely indicates that the density of sediments has been locally underestimated or can be related to the crustal effect not completely removed, considering that the residuals reflecting the crustal density variations (Fig. 12) are strongly positive (~70 mGal).

Along profile 2, all the gravity basements are poorly correlated with the seismic basement (*CC* < 0.5), but the correlation is much higher when we compare the results obtained from the different gravity basement depths (*CC* = 0.925; Table 3.5). The discrepancy between the results obtained with different gravity and seismic basement depth, in the area representing the accommodation zone between the Kiri and Lokonia High, can be partly ascribed to the strong lateral heterogeneity of the seismic basement, which is highly faulted (Chapter 2). The basement depths obtained from the gravity inversion (Fig. 3.22) clearly identify the Gilson Basin, but its maximum depth is southward shifted, with respect to the results based on seismic data. This part of the seismic profile is also very faulted and heterogeneous, with many gaps that make the interpretation more difficult (Delvaux et al., 2021). We can further notice that the higher density contrast (-0.800 g/cm^3) produces a basement depth more consistent with the seismic basement in the areas where the intermediate and low-density sediments have a thickness significantly greater (6-8 km) than that of the underlying carbonate sequences (1-2 km). This mostly occurs in the basins located in the southern part of the Cuvette Centrale (e.g., Bololo and Gilson Basin, profile 1 and 2).

Along profile 3, the relatively high correlation coefficients between the seismic basement depth and that obtained from gravity data (max *CC* = 0.537, Table 3.6), indicates their good consistency. As in the previous cases, the correlation coefficients are even higher when we compared the two gravity basement depths. Indeed, the trends of the basement depths obtained from gravity data are very similar, but the values are quite different (Fig. 3.22). In particular, we can observe that the basement depths obtained from the two inversion modelling, are shallower than the seismic basement up to 4-5 km. Along this profile, a smaller density contrast (-0.200 g/cm^3) in the gravity inversion would improve the consistency with the seismic basement depth. The reasons could be that the thickness of Proterozoic clastics and Dolomitic limestones (Table 3.1) is particularly high in the Lomami Basin (Delvaux et al. 2021). In that area, the seismic basement is sub-horizontal, while the gravity basements show trends that are more variable. This can be ascribed to lateral density variations of the sediments and/or shallow crust, whose effect can be still present.

Along profile 4, the correlation coefficient between the seismic basement depth and the results obtained from the inversion gravity modelling is relatively high (*CC* >0.600), indicating the good consistency between the trends (Table 3.7). The inversion models identify the Dekese Basin, with the maximum depth approximately coincident with that obtained from seismic data. However, in the south westernmost part of the profile the basement depths show a reverse trend with the respect to that of the seismic basement (Fig. 3.22). This can be explained by the effect of an anomalous high-density crust not completely removed. The presence of a high-density mass in this area (southernmost part from Dekese well) has been also postulated by the study of Watts et al. (2018), which observed sediment-corrected Bouguer gravity anomalies of about +50 mGal. This hypothesis is based on the presence of a strong positive anomaly of *BG_RES2* (~ 90 mGal, Fig. 3.13). In the Lokonia High, all the gravity basement depths show a trend very similar to that of the seismic basement (Fig. 3.22).

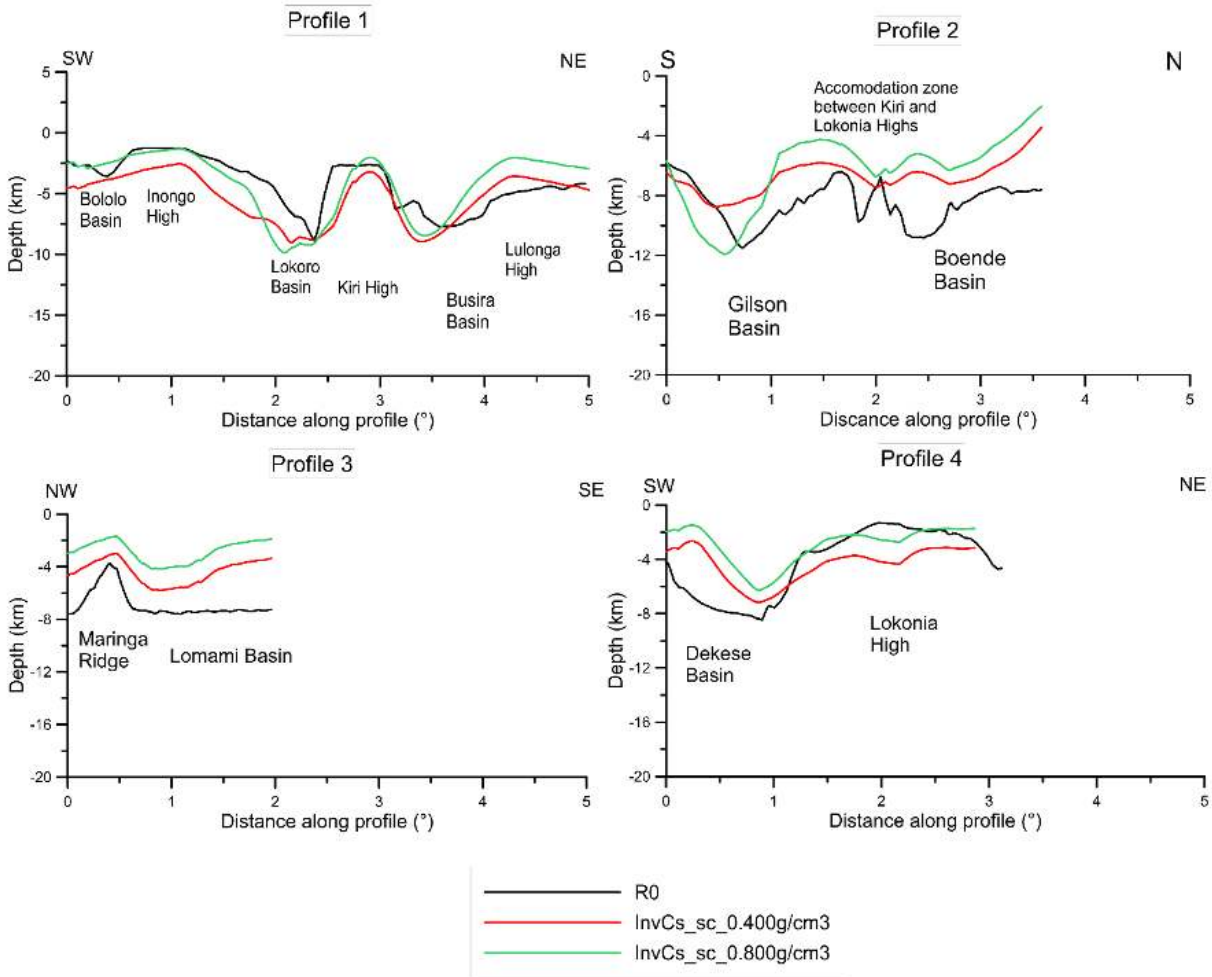

Figure 3.22. - *Comparison between inversion modelling and seismic reflection basement for the investigation of the basement depth. R0: basement depth obtained from interpretation of seismic reflection profiles; InvCs_sc_0.400g/cm^3: basement depth obtained from gravity inversion, using a density contrast of -0.400 g/cm^3; InvCs_sc_0.800g/cm^3: basement depth obtained from gravity inversion, using a density contrast of -0.800 g/cm^3.*

Potential uncertainties of the basement depths obtained from the inversion of the residuals *BG_RES3* arise from two major sources. First, we should consider that the depth of the seismic basement and the other horizons, to constrain my gravity calculations, could be affected by uncertainties, related to the seismic data acquisition, processing, and interpretation. Since a complete uncertainty analysis would only be possible with a Montecarlo simulation approach, which is out of the scope of this study, I decided to test the influence on the *G_SED* and basement depth of the uncertainty of the total sedimentary thickness. To this purpose, I introduced in the calculations a variation of ±10% (Fig. 3.23 A-B) of each sedimentary layer thickness. Such a thickness variation produces a change of the *G_SED* values of about ±22 mGal (Fig. 3.23 C), which translated in an uncertainty of the basement depth obtained from gravity inversion of about ±1.5 km (Fig. 3.24).

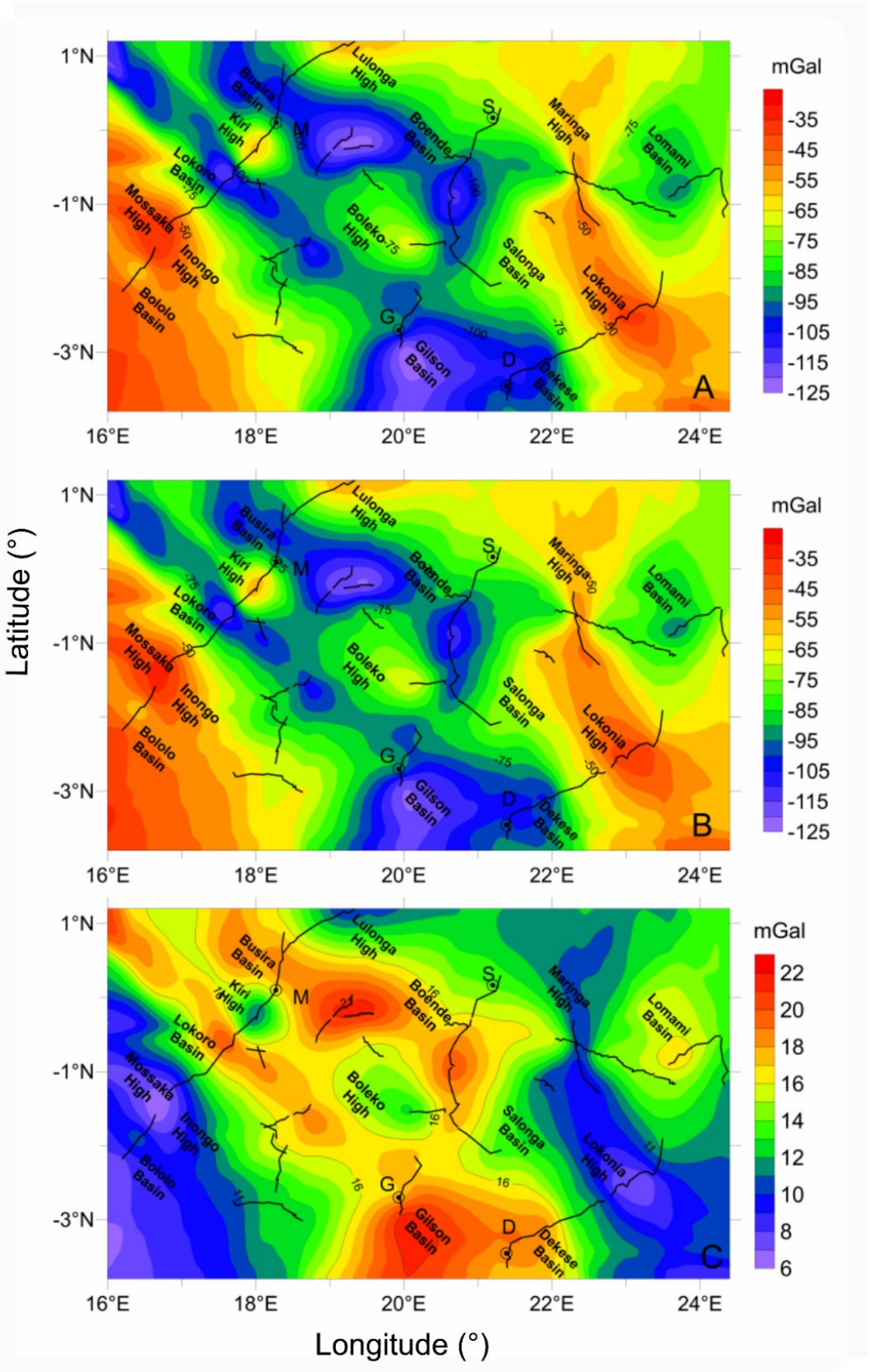

Figure 3.23 – Estimates of the uncertainties on the gravity effect of sediments, introducing an error in the thickness of each sedimentary layer of (A) +10%; (B) -10%; (C) Difference between the gravity effect estimated introducing an error in the thickness of each sedimentary layer of +10% and –10%, respectively. Broken black lines show location of the seismic profiles. Black circles show location of the four wells drilled in the study area: D= Dekese; G=Gilson-1; M=Mbandaka-1; S=Samba.

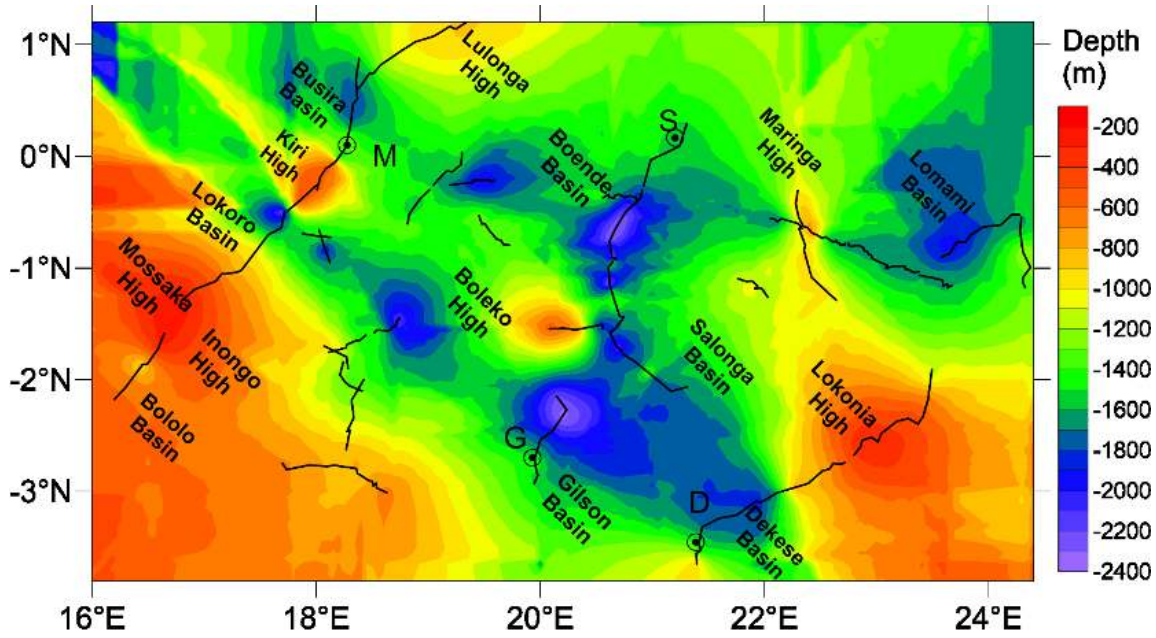

Figure 3.24 –Difference between the basement depths obtained introducing an error in the thickness of each sedimentary layer of -10% and + 10%, respectively. Broken black lines show location of the seismic profiles. Black circles show location of the four wells drilled in the study area: D= Dekese; G=Gilson-1; M=Mbandaka-1; S=Samba.

3.7 Conclusions

The gravimetric methodology proposed in this thesis to estimate the *CB* basement depth is essentially based on a forward modelling for calculating the gravity effect of sediments, an estimation of gravity residuals, to isolate the long wavelength period associated to isostatic effects of deeper crust, and few inversion-modelling tests for the definition of the basement depth above the *CB*. In particular, the methodology proposed retrieves the basement depth from inversion of gravity residuals (*BG_RES3*), obtained from the regression analysis between the surface topography and Bouguer gravity anomalies (*BG_RES1*), to which I subtracted a cubic *PS*, related to the crustal or sub-crustal gravity effect (*BG_RES2*).

This gravity method has been applied using two different superficial density contrast between the sediments and the crystalline crust (-0.400 and -0.800 g/cm^3, respectively). The gravity analysis confirms the strong heterogeneity of the basement depths, as a consequence of long geodynamic history of the *CB*, which started with a rift phase that caused its initial subsidence accompanied by the formation of a series of highs (i.e. Kiri High and Inongo High) and depressions (e.g., Busira and Lokoro Basin), aligned *NW-SE*. This alignment, already observed in previous studies, is consistent with the distribution of the aeromagnetic anomalies. The basement depths reconstructed are quite consistent with that derived from the interpretation of the seismic profiles. The discrepancies can be ascribed to the gravity resolution, not sufficient to detect the sharp lateral variations of the basement depth, when is segmented by a series of faults, or to the effect of the crystalline crust not completely removed from the inverted gravity residuals. The basement depth retrieved from gravity could eliminate the artefacts produced by the interpolation of the seismic profiles. Indeed, it could identify the continuity of the Kiri and Boleko High that appeared in the reconstructed seismic basement separated by a sedimentary cover. Furthermore, the results from gravity analysis clearly distinguishe the Busira, Lokoro, Gilson, and Salonga basins, which as effect of seismic data interpolation, form a single large sedimentary depocenter. I could also identify other basins in areas uncovered by seismic data, such as the Lomami Basin in the northeastern sector of the Cuvette Centrale. Other possible basins, identified only from gravity inversion using a superficial density contrast of -0.800 g/cm^3, are located southeast to the Gilson Basin. Furthermore, the maximum depocenter of the Lokoro Basin appears northwest shifted with respect to that identified from the interpretation of the seismic reflection profiles.

Furthermore, I noticed that the gravity effect of sediments (*G_SED*) is strong in the basins where the Mesoproterozoic syn-rift sediments are thinner than those of the overlying sequences having a low density (Lokoro, Gilson, and Boende basins). In contrast, in other basins (Salonga and Lomami basins) the gravity effect is reduced because of the large thickness of the high-density sequences, composed of carbonates and clastics sediments. The analysis of the gravity anomalies mainly related to the crystalline crust (*BG_RES2*) supposes the presence of high-density bodies, likely intruded into the crust during the extensional phase affecting the CB along the southern part of the Cuvette Centrale (in the surrounding of the Dekese Basin), where the values are strongly positive, as well as along the Kiri High. In contrast, another study hypothesizes the existence of mafic bodies in the Lokonia High on the base of gravity anomalies, removing the calculated gravity effect of sediments from the Bouguer anomaly field.

CHAPTER 4

- 3D Numerical Modelling -

4.0 Introduction of the chapter

As introduced in Chapter 1, the *CB* lies on several amalgamated Archean cratonic blocks (Ntem, Bouca-Mboumou-Uganda, Tanzanian-Kibaran, and Cuango-Kasai blocks, according to the studies of De Wit and Linol, 2015; Fernandez-Alonso et al., 2012; Boniface and Schenk, 2012, surrounded by Paleo- and Meso-Proterozoic mobile belts. Several seismic tomography models (e.g., Sebai et al., 2006; Pasyanos and Nyblade, 2007; Begg et al., 2009; Fishwick, 2010; Raveloson, 2015) revealed the huge size of the Congo Craton, which appears as a single lithospheric block about 250-300 km thick. On the other hand, according to the seismic tomography model of Celli et al. (2019), the Congo Craton is composed of at least three cratonic pieces (Ntem, Mboumou-Uganda, and Kasai blocks, respectively), having a roots' thickness between 200 and 250 km. The most recent regional seismic tomography model of Ojo et al. (2020) reveals that the Congo Craton is characterized by a homogeneous crustal thickness of about ~45 km and lithospheric roots between 100 and 200 km.

Looking at these results and the past geodynamic history, we can speculate that the cratonic amalgamation left a weak zone in the suture areas, corresponding to the Cuvette Centrale. Such a zone, under the influence of extensional tectonics, could have been more easily deformed than the other parts of the Congo Craton (Figure 4.1).

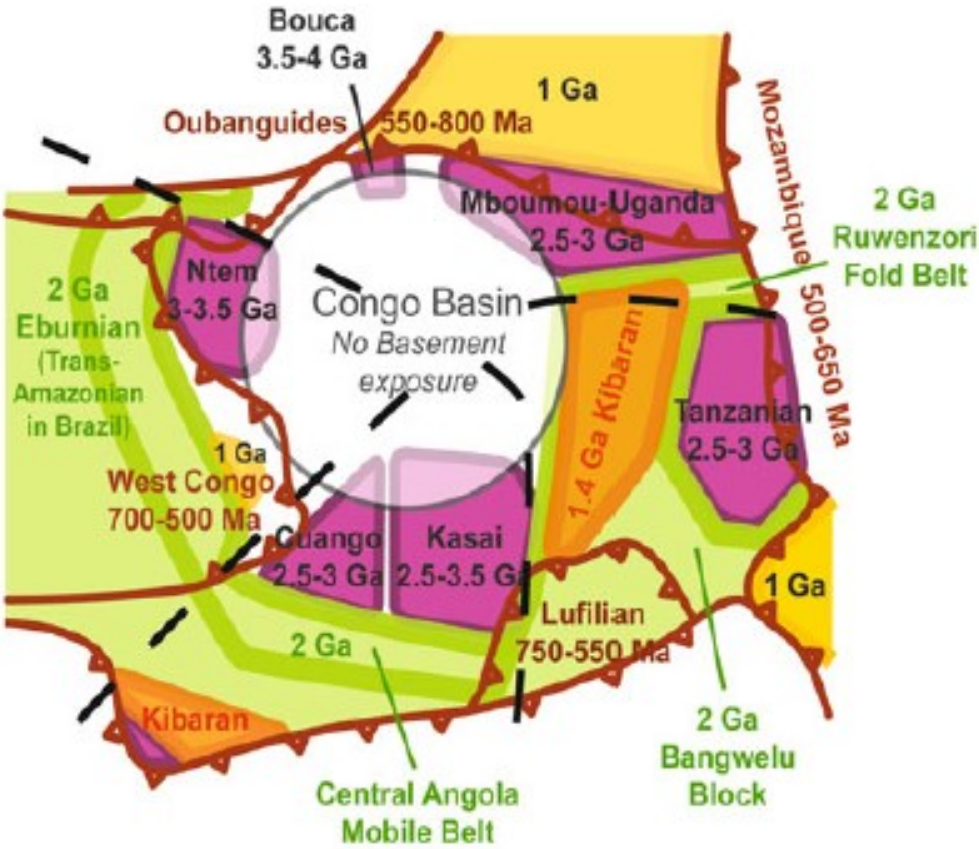

Figure 4.1 *- Sketch map of the Precambrian basement underlying and surrounding the CB, showing the Archean cratonic blocks (purple); Eburnean (green) and Kibaran terrains (orange and yellow). Brown curves represent the tectonic fronts of Pan African fold-and-thrust belts (brown). Dashed black lines show the possible suture zones of the amalgamated cratonic pieces (De Wit and Linol., 2015).*

Although the dynamic processes that shaped the *CB* remain partly unknown, geological and geophysical data interpreted in previous studies (e.g., Kadima 2011a, b) and in this *PhD* study (Chapter 1 and 2), demonstrated that the basin has been subjected to extensional tectonics during the initial stages of its formation. This extension likely acted from more than one direction, producing a strongly heterogeneous basement depth, characterized by several small basins and structural highs *NW-SE* aligned (Chapter 2). Other *ICBs* could have formed in similar conditions, considering the complexity of their tectonic structure. This is likely for the case of the Parnaiba basin, the Neoproterozoic Centralia Super basin of Australia, and the basins of north-central Africa, whose subsidence initiated from rift phases (De Wit and Linol, 2015; Lindsay et al., 2002; Burke and Gunnel, 2008). This is not surprising, considering that the heating of a convecting mantle, accumulated at the base of a thick plate, can induce tensional stress, leading to asthenospheric mantle updoming and consequent basin formation (e.g., Gurnis, 1988; Phillips and Bunge, 2007).

The hypothesis that multi-divergent velocities caused rift formation have been recently tested by Gerya and Burov (2018) to explain the generation of quadruple *rift-rift-rift-rift* junctions, transient features, evolving in the more stable triple *rift-rift-rift* junctions in few tens of Myr. However, multi-divergent velocities could have acted also on cratonic areas and the geometric and kinematic characteristics of the lithosphere involved in the formation of triple/quadruple junctions could have been similar to that of the lithosphere underlying intracratonic basins, such as the *CB*. Koptev et al. (2015) modelled in 3D tensional far-field stress induced by the rise of a mantle plume beneath a cratonic area and monitored the surface topography evolution. The results showed the formation of a series of topographic highs and lows, forming parallel rift structures, due to the interaction of the plume with a lithosphere having a variable thickness and rigidity. These features are the effect of a unidirectional extension exerted by the mantle plume. In a more recent study, Koptev et al. (2018a) simulated the formation of a triple junction in Central Afar, as effect of a mantle plume upwelling under variable far-field stress conditions. They demonstrated that a complex pattern of triple junctions form in response of a bi-directional extension.

Starting from these considerations, in the frame of my *PhD* study, I implemented 3D geodynamic models to test the hypothesis that the complex structures of the *CB* basement are the product of a multi-divergent velocity, acting on a cratonic area. The numerical simulations carried out have in common the kinematic boundary conditions, represented by orthogonal velocity vectors, which cause a slow multi-extensional tectonics, leading to lithospheric stretching and surface topography variations. In this chapter, I present the results of these 3D numerical models, taking into account the early geodynamic history of the basin and the results obtained from the first part of this thesis project (Chapter 2 and 3). To this purpose, I used the thermomechanical *I3ELVIS* code developed by Prof. T. Gerya, at *ETH-Zurich*, where I spent 4 months of the *PhD* project. In that period, I also attended the course "Numerical Modeling I and II: Theory and Applications" held by Prof. T. Gerya, who introduced me to the theory of the numerical geodynamic modelling.

The results of the numerical models are used to implement forward gravity models to estimate the temporal variations of the gravity effect of the tectonic structures formed during the simulation. Finally, I compared the forward gravity models with the present-day gravity field, in order to check the consistency between the modelled and observed main structures of the *CB* (Chapter 2 and 3).

4.1 Numerical modelling method

The 3D thermomechanical numerical code *I3ELVIS* (Gerya and Yuen, 2007; Gerya, 2013) is a parallel 3D thermomechanical modeling code, which solves the momentum, mass and energy conservation equations. It solves partial differential equations at several types of nodal points to which Cartesian coordinates and values of thermo-physical parameters are associated. These nodal points compose 1D, 2D, and 3D Eulerian or Lagrangian grids (Gerya, 2019). The employed numerical methodology (Gerya, 2010a; 2010b; 2013) is based on a combination of a finite difference method combined with marker-in-cell technique (Gerya, 2019), which consists in the use of Lagrangian advective points (markers) with a fixed Eulerian grid (e.g., Schmeling, 1987; Weinberg and Schmeling, 1992). With this technique, properties are initially distributed on a large amount of Lagrangian points that are advected according to a computed velocity field. The advected material properties (e.g., viscosity, plastic strain, temperature, density) are then interpolated from the displaced Lagrangian points to the Eulerian grid (Fig. 4.2), by using a weighted-distance averaging, such as the following linear interpolation formula:

$$\rho_i^{t+\Delta t} = \frac{\sum_m \rho_m w_{m(i)}}{\sum_m w_{m(i)}}$$
$$w_{m(i)} = 1 - \frac{\Delta x_{m(i)}}{\Delta x} \qquad (4.1a)$$

translated in 3D

$$\rho_{(i,j,k)}^{t+\Delta t} = \frac{\sum_m \rho_m w_{m(i,j,k)}}{\sum_m w_{m(i,j,k)}}$$
$$w_{m(i,j,k)} = \left(1 - \frac{\Delta x_m}{\Delta x_{i-1/2}}\right) \times \left(1 - \frac{\Delta y_m}{\Delta y_{j-1/2}}\right) \times \left(1 - \frac{\Delta z_m}{\Delta z_{k-1/2}}\right) \qquad (4.1b)$$

Where $w_{m(i)}$ represents the weight of the m_{th} marker for the ith node and $\Delta x_{m(i)}$ denotes the distance from the m_{th} marker to the ith node and Δx represents the distance between the nodes. In 1D (Fig. 4.2), the density at an Eulerian node is interpolated only with markers found in the two surrounding cells (i.e. within one grid step distance from the node). For a local interpolation, a shorter limiting distance from the node (i.e. within half grid distance) with fewer markers can be used.

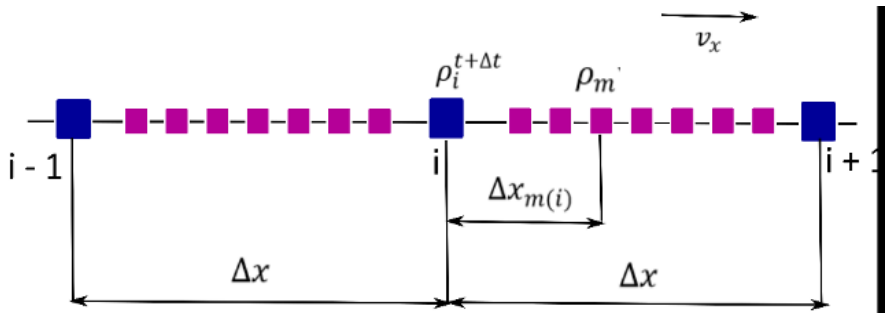

Figure 4.2 *– Stencil of a 1D Eulerian-Lagrangian grid used with the marker in cell technique. Mobile Lagrangian markers (violet squares) move with a prescribed velocity v_x and carry information on material density (ρ). At every time step, the density at the Eulerian nodes (blue squares) is interpolated from markers found within two grid cells around the nodes (modified after Gerya, 2019).*

The numerical modelling consists of solving partial differential equations, in particular, the continuity equation that describes the conservation of mass during the displacement of a continuous geological media in geodynamics approach (Gerya, 2010). The mass conservation equation (as many other time-dependent conservation equations), can be either written in Eulerian or Lagrangian style, it depends by the nature of the geometrical point for which the equation is referred. For example, the Eulerian continuity equation is written for fixed point in space with the form:

$$\frac{\partial \rho}{\partial t} + div\,(\rho \vec{v}) = 0 \qquad (4.2)$$

Where $\partial/\partial t$ is the Eulerian time derivative, ρ is the local density, which characterizes the amount of mass per unit volume (kg/m^3), $\vec{v}$ is local velocity (m/s), and div () denotes the divergence operator.

The divergence that has to be equal to zero to satisfy the condition of mass conservation, in three dimensions is a scalar function of a vector field:

$$div\,(\vec{v}) = \frac{\partial v_x}{\partial x} + \frac{\partial v_y}{\partial y} + \frac{\partial v_z}{\partial z} = 0 \qquad (4.3)$$

Where *x, y, z* are Cartesian coordinates, with *x* and *z* that denote the horizontal direction and y the vertical one. They subscript the components parallel to the respective coordinate axes of the velocity vector $\vec{v}$.

Starting from the concept that the deformation of continuous media always results from the balance of several forces (internal and external) that act on these media, the relation between forces-deformation is expressed by momentum equations. It is possible to solve partial differential equations of motion by using numerical modelling, which describes the conservation of momentum for a continuous medium in the gravity field:

Eulerian form
$$\frac{\partial \sigma_{ij}}{\partial x_j} + \rho g_i = \rho \left(\frac{\partial v_i}{\partial t} + v_j + \frac{\partial v_i}{\partial x_j} \right) \qquad (4.4\ a)$$

Lagrangian form
$$\frac{\partial \sigma_{ij}}{\partial x_j} + \rho g_i = \rho \frac{Dv_i}{Dt} \qquad (4.4\ b)$$

Where in three dimension: *x-momentum (i = x; j = y, z); y-momentum (i = y; j = x, z); z-momentum (i = z; j = x, y)*. In addition, *g* is the gravity acceleration (m/s^2); σ_{ij} are the components of the stress tensor, and ρ is the density (kg/m^3), dependent on rock composition (*C*), temperature (*T*), and pressure (*P*) as:

$$\rho = f\,(P + T + C\,) \qquad (4.5\ a)$$

or
$$\rho = \rho_r[1 + \beta(P - P_r)] \times [1 - \alpha(T - T_r)] \qquad (4.5\ b)$$

Where ρ_r is the density of a given material at reference pressure P_r (typically 10^5 Pa = 1 bar) and reference temperature T_r (typically 298.5 K = 25°C). In addition, variation in the density of minerals and rocks with *T* and *P* are characterized by the thermal expansion (α) and compressibility (β), expressed respectively as:

$$\alpha = -\frac{1}{\rho}\frac{\partial \rho}{\partial T} \quad (4.5\text{ c})$$

and

$$\beta = \frac{1}{\rho}\frac{\partial \rho}{\partial P} \quad (4.5\text{ d})$$

Using the momentum equation written in Lagrangian form (4.4 b), and the relationship between the total (σ_{ij}) and deviatoric stresses (σ'_{ij}), it is possible to present the form of Naiver flow approximation, which describes the conservation of momentum for a fluid in the gravity field:

$$\frac{\partial \sigma'_{ij}}{\partial x_j} + \frac{\partial P}{\partial x_i} + \rho g_i = \rho \left(\frac{Dv_i}{Dt}\right) \quad (4.6)$$

Where *j* and *i* are coordinate indexes; x_i x_j are spatial coordinates; g_i is the *i*th component of the gravity vector $\overrightarrow{g} = (g_x, g_y, g_z)$. Dv_i/Dt is the substantive time derivative of the *i*th component of the velocity vector.

Under some cases, the deformation of highly viscous flows can be accurately described by the Stokes equation of slow flow:

$$\frac{\partial \sigma'_{ij}}{\partial x_j} + \frac{\partial P}{\partial x_i} + \rho g_i = 0 \quad (4.7\text{ a})$$

That is translated in 3D as:

X-Stokes equation $$\frac{\partial \sigma'_{xx}}{\partial x} + \frac{\partial \sigma'_{xy}}{\partial y} + \frac{\partial \sigma'_{xz}}{\partial z} + \frac{\partial P}{\partial x} + \rho g_x = 0 \quad (4.7\text{ b})$$

Y-Stokes equation $$\frac{\partial \sigma'_{yy}}{\partial y} + \frac{\partial \sigma'_{yx}}{\partial y} + \frac{\partial \sigma'_{yz}}{\partial z} + \frac{\partial P}{\partial x} + \rho g_y = 0 \quad (4.7\text{ c})$$

Z-Stokes equation $$\frac{\partial \sigma'_{zz}}{\partial z} + \frac{\partial \sigma'_{zx}}{\partial y} + \frac{\partial \sigma'_{zy}}{\partial z} + \frac{\partial P}{\partial x} + \rho g_z = 0 \quad (4.7\text{ d})$$

Where *P* is the pressure (Pa), σ'_{ij} are the components of the viscous deviatoric stress tensor. The equations (4.7a-d) are valid for the laminar flow of highly viscous materials, such as crustal and mantle rocks, when the inertial forces $\rho\left(\frac{Dv_i}{Dt}\right)$ are negligible with respect to viscous resistance and gravitational forces.

The numerical modelling let us solve also the partial differential temperature equation that describes the conservation of energy (heat). In order to predict temperature variations due to heat transport, the heat temperature equation (also called temperature equation) describes the balance of heat with temperature changes in terms of heat generation, advection, and conduction.
The Eulerian/Lagrangian temperature equation is:

(Eulerian) $$\rho C_P\left(\frac{\partial T}{\partial t} + \vec{v} \cdot grad\,(T)\right) = -\frac{\partial q_i}{\partial x_i} + H \quad (4.8\text{ a})$$

$$\rho C_P \left(\frac{\partial T}{\partial t} + v_x \frac{\partial T}{\partial x} + v_y \frac{\partial T}{\partial y} + v_z \frac{\partial T}{\partial z}\right)$$

or in 3D, $$= -\frac{\partial q_x}{\partial x} - \frac{\partial q_y}{\partial y} - \frac{\partial q_z}{\partial z} + H \quad (4.8\text{ b})$$

(Lagrangian) $$\rho C_P \frac{DT}{Dt} = -\frac{\partial q_i}{\partial x_i} + H \quad (4.8\text{ c})$$

or in 3D, $$\rho C_P \frac{DT}{Dt} = -\frac{\partial q_x}{\partial x} - \frac{\partial q_y}{\partial y} - \frac{\partial q_z}{\partial z} + H \quad (4.8\text{ d})$$

Where the index *i* means a summation of derivatives (i.e. divergence) of heat flux components by respective coordinates (*x*, *y*, *z*), ρ is the density (kg/m^3), C_P heat capacity at constant pressure (isobaric heat capacity, J/kgK), and *H* is the volumetric heat production/consumption (W/m^3).

In 4.8, the parameter *H* is the sum of 1) the radioactive heat production (H_r), which is due to the decay of radioactive elements that are present into the rocks, 2) shear heat production (H_s), related to the dissipation of mechanical energy during viscous/plastic deformations, 3) adiabatic heat production/consumption (adiabatic heating/cooling) (H_a), depending on changes in pressure and thermal expansion (α), and 4) latent heat production/consumption (latent heating/cooling) (H_L), related to phase transformations in rocks subjected to changes in pressure and temperature (Gerya, 2019). In particular, in the Lagrangian case:

$$\rho C_P \frac{DT}{Dt} = -\frac{\partial q_i}{\partial x_i} + H_r + H_s + H_a + H_L \quad (4.9)$$

with $$H_s = \sigma'_{xx}\dot{\varepsilon}'_{xx} + \sigma'_{yy}\dot{\varepsilon}'_{yy} + \sigma'_{zz}\dot{\varepsilon}'_{zz} + 2\left(\sigma'_{xy}\dot{\varepsilon}'_{xy} + \sigma'_{xz}\dot{\varepsilon}'_{xz} + \sigma'_{yz}\dot{\varepsilon}'_{yz}\right) \quad (4.10)$$

and $$H_a = T\alpha\left(\frac{DP}{Dt}\right) \quad (4.11)$$

In numerical modeling, as in nature, rocks often behave on geological time scales as highly viscous fluids. For this reason, the viscous rheological relationship between stress (σ'_{ij}) and deviatoric strain rate $\dot{\varepsilon'}_{ij}$ is used (it is also known as Newtonian law of viscous friction). Viscosity changes with different materials and may depend on some parameters, like pressure (*P*) and temperature (*T*). In 3D, the law of viscous friction is formulated in this way:

$$\sigma'_{ij} = 2\eta\dot{\varepsilon'}_{ij} \quad (4.12\text{ a})$$

or, $$\sigma'_{ij} = 2\eta(\dot{\varepsilon'}_{ij} - \tfrac{1}{3}\delta_{ij}\dot{\varepsilon}'_{kk}) \quad (4.12\text{ b})$$

Where η is the shear viscosity, $\dot{\varepsilon}'_{kk}$ is the isotropic strain rate responsible for material volume changes, *i*, *j* are coordinates indexes (*x*, *y*, *z*), while δ_{ij} is the Kronecker delta that is equal to 1 when *i* =*j* and 0 when $i \neq j$

In general, the behavior of rocks is considered visco-elastic-plastic, which can be formulated by decomposing the bulk deviatoric strain rate $\dot{\varepsilon'}_{ij}$ into three main components:

$$\dot{\varepsilon}'_{ij} = \dot{\varepsilon}'_{ij(viscous)} + \dot{\varepsilon}'_{ij(elastic)} + \dot{\varepsilon}'_{ij(plastic)} \quad (4.13a)$$

where

$$\dot{\varepsilon}'_{ij(viscous)} = \frac{1}{2\eta}\sigma'_{ij}$$

$$\dot{\varepsilon}'_{ij(elastic)} = \frac{1}{2\mu}\frac{D\sigma'_{ij}}{Dt} \quad (4.13\ b)$$

$$\dot{\varepsilon}'_{ij(plastic)} = 0\ for\ \sigma_{II} < \sigma_{yield}$$

Where $\frac{D\sigma'_{ij}}{Dt}$ is the time derivative of the deviatoric stress component (σ'_{ij}), σ_{yield} is the plastic yield strength for a given rock, and σ_{II} is the second invariant of the deviatoric stress tensor. The code accounts for the visco-plastic deformation, an effective viscosity formulation that includes diffusion (η_{diff}) and dislocation creep (η_{disl}). For this aim, the ductile creep viscosity $\eta_{ductile}$ is calculated as following:

$$\frac{1}{\eta_{ductile}} = \frac{1}{\eta_{diff}} + \frac{1}{\eta_{disl}} \quad (4.14a)$$

with

$$\eta_{diff} = \frac{A_D}{2\sigma_{cr}^{n-1}}\exp\left(\frac{E+PV}{RT}\right) \quad (4.14\ b)$$

$$\eta_{disl} = \frac{A_D^{1/n}}{2}\exp\left(\frac{E+PV}{RT}\right)\dot{\varepsilon}_{II}^{\frac{1}{n}-1}$$

Where $A_D, E, V,$ experimentally determined and considered as a constant, are the pre-exponential factor, activation energy, and volume, respectively. R is the gas constant, P pressure, T temperature, ε_{II} second invariant of the deviatoric strain rate tensor, and σ_{cr} diffusion-dislocation transition stress (named critical stress in Table 4.1). The plastic strength(σ_{yield}) of a rock generally depends on the mean stress of the solid (P_{solid} = P) and on the pore fluid pressure (P_{fluid}) such that:

$$\sigma_{yield} = C + \sin(\varphi)P \quad (4.15a)$$

with

$$\sin(\varphi) = \sin(\varphi_{dry})(1-\lambda)$$

$$\lambda = \frac{P_{fluid}}{P_{solid}} \quad (4.15\ b)$$

Where C is the cohesion (residual strength at P=0), φ effective internal friction angle (φ_{dry} stands for dry rocks), and λ pore fluid pressure factor for dry fractured crystalline rocks. For dry fractured crystalline rocks, *sin (φ)* is independent on composition and varies from 0.85 at P<200 MPa to 0.60 at higher pressure (Byerlee, 1978; Brace and Kohlstedt, 1980). In order to obtain a numerical solution, boundary conditions have to be defined. In this study, the velocity boundary conditions used for solving Stokes and continuity equations are typically composite, combining Dirichlet and Neumann mathematical conditions (Gerya 2010). In particular, the "free-slip" condition has been chosen, because it requires that the normal velocity component on the boundary is zero and the two order components do not change across the boundary. This condition implies zero shear strain rates and shear stresses along the boundary, favoring the divergence equal to zero.

The boundary conditions are also time-dependent and this could imply that the physical location of the boundary conditions may be function of time. To allow surface deformation, the "free-surface" boundary condition at the top of the crust is applied, implementing a 20 km thick of *sticky air* with low density (1 kg m^{-3}) and reduced viscosity (10^{18} Pa s). The sticky air approach is used for simplifying the implementation of the free surface condition, using the marker-in-cell method (Gerya and Yuen 2003b; Schmeling et al., 2008; Crameri et al., 2012a). With this method, a low density and low viscosity fluid layer is introduced at the top of the model, producing any noticeable resistance to the deformation of the air-crust interface, disadvantaging the formation of the "drunken sailor instability" (Kaus et al., 2010; Gerya, 2019), which geodynamic models could produce. This peculiar free surface behavior depends on inaccurate time integration of the moving free surface position, which does not take into account changes in material velocity during the time steps (Kaus et al., 2010). In the case of "sticky air" approach, the problem of "drunken sailor instability" can be solved considering implicitly advection-related density changes at Eulerian nodes (Kaus et al., 2010; Duretz et al., 2011a; Gerya, 2019). The temperature changes from 273 K in the sticky air layer to 1973K at the bottom of the lithosphere. No external forces are applied and the evolution of the model is due to its internal dynamics.

4.2 3D Numerical modelling setup

In order to model the *CB* formation, I performed several numerical simulations testing different geometry designs, continental geotherm, and kinematic boundary conditions. In all the simulations, the study area is 4050 km x 4050 km wide in both horizontal directions and extends up to a depth of 392 km, to include the upper mantle. The lateral and vertical resolution is 10 km and 2 km, respectively. We should keep in mind that the sizes of the study area, as well as of the modelled tectonic features, are larger than in the reality. However, the aim of these numerical simulations is to understand the tectonic conditions that lead to the formation of a heterogeneous basement depth, characterizing the *CB* (Chapter 2 and 3), without performing a quantitative comparison with the real case. Since there is a lot of uncertainty about the initial shape of the Congo Craton, I implemented several models, in which the study area is composed of cratonic lithosphere divided by (or containing) 'weak zones', having different values of the thermophysical properties. More precisely, in the first two numerical experiments, I assumed that the amalgamation of cratonic pieces resulted in four cratonic blocks divided by weak zones crossing each other in the central part. In all the other simulations, I assumed that the collision of the cratonic pieces simply left a weak zone in the center. The transition between the lithosphere of cratons and weak zones occurs smoothly through "transition zones" (*TZs*). To design the different tectonic features, I used cubic and trapezoidal prisms geometries, each of them composed of eight nodes characterized by Cartesian coordinates and values of the thermophysical parameters. Every node (Fig. 4.3) is identified by a number (from 0 to 7) that represents the Cartesian coordinates. The even (0, 2, 4, and 6) and odd numbers (1, 3, 5, and 7) represent the nodes limiting the top and bottom of the features, respectively. The cubes (squares in 2D, Fig. 4.3) represent the cratonic blocks or weak zones (this depends on the simulation that I performed). They are drawn surrounded by four trapezoidal prisms (trapezoids in 2D, Fig. 4.3), two parallel to the *X*-axis and the other two parallel to the *Z*-axis respectively, simulating the TZs between a cratonic (or stiff zone) and off-cratonic (or weak zone) lithosphere.

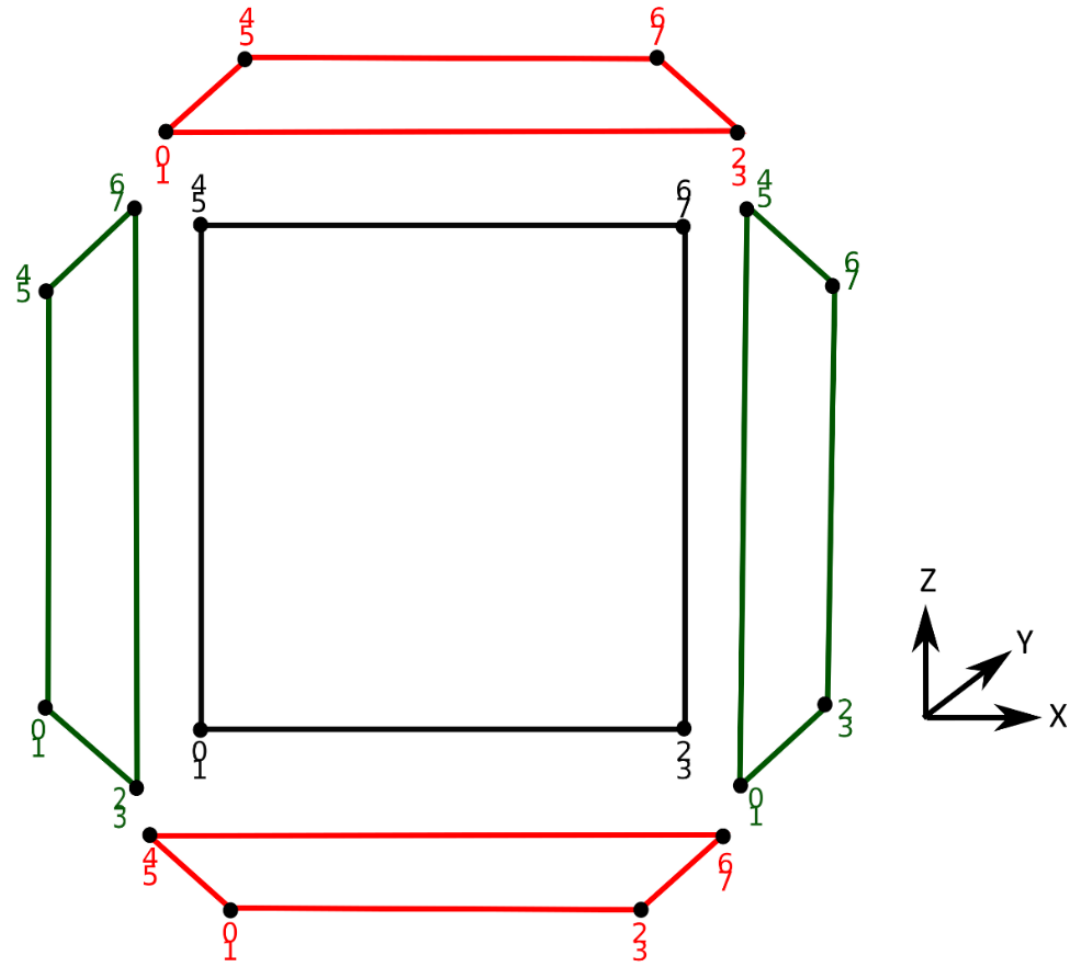

Figure 4.3 *– 2D geometry design of the tectonic features implemented in the numerical simulations. The black square represents cratonic and weak zones areas (depending on the numerical simulation performed), while trapezoids (in green and red) that are parallel to X and Z-axis, respectively, represent TZs. Each figure is composed of eight nodes (black points), four in plane, to which are assigned Cartesian coordinates and values of the thermophysical parameters. Every node has an associated number (from 0 to 7), with the even defining the top and the odds the bottom (in 3D) of the features.*

I considered a fixed initial crustal thickness equal to 35 km, divided in an upper and lower crust of 20 km and 15 km, respectively, and a fixed lithospheric thickness in the cratonic areas equal to 230 km, in agreement with the estimates derived from seismic tomography data (e.g., Celli et al. 2020). Depth temperature variation in the cratonic areas is defined by a linear gradient between 273 K at the surface topography and 1698 K at the bottom of the lithosphere (Appendix C, Fig. C1). The areas off-cratons (or weak zones) and the TZs have a different depth of the lithosphere and thermal gradient for each numerical simulation (Appendix C, Fig. C1). The temperature increases according to an adiabatic gradient (~ 0.5 K/km) below the lithosphere, reaching 1973 K at the bottom of the model (Appendix C, Fig. C1). In order to simulate a slow multi-extensional tectonics, I applied divergent velocity boundary conditions (2.5 mm/yr) in *N-S* (v_{z2} ,v_{z1}) and E-W direction (v_{x2} ,v_{x1}), along the nodes of the lateral boundaries of the model. The velocities applied at the top (v_{top}) and bottom (v_{bottom}) of the model (0.05 and -0.85 mm/yr, respectively) have been obtained considering that $div\ (\vec{v})$ has to be zero to satisfy the condition of the mass conservation (4.3).

For this purpose, these velocities have been calculated, based on the size of the model (4050 km (x_{size}) x 4050 km (z_{size}) x 392 km (y_{size})), velocity applied along the *x*- and *z*-axis, and thickness of the sticky air (y_{air}) equal to 20 km, as follows:

$$v_{ytop} = \left(\frac{v_{x2} - v_{x1}}{x_{size}} + \frac{v_{z2} - v_{z1}}{z_{size}}\right) y_{air} \tag{4.16a}$$

$$v_{ybottom} = \left(\frac{v_{x1} - v_{x2}}{x_{size}} + \frac{v_{z2} - v_{z1}}{z_{size}}\right) (-1\ (y_{size} - y_{air})) \tag{4.16 b}$$

The initial density of the cratonic lithosphere is assumed lower (3250 kg/m^3) than that of the off-cratonic areas and asthenosphere (3300 kg/m^3), since the depletion in iron components characterizing the Archean rocks makes them more buoyant (McDonoug and Sun, 1995; Poudjom et al., 2001). This assumption prevented the subsidence of the cratons, during the simulations, induced by the applied extension.

As previously introduced, the rheological model assumes visco-plastic rheology for the lithospheric plates, with a realistic temperature and strain rate dependent viscosity, computed according to experimentally determined flow laws. I used the rheology of the dry olivine for both lithospheric and sub lithospheric mantle and felsic and mafic granulite for the upper and lower crust (Ranalli, 1995). Solving the heat conduction equation, combined with a temperature-dependent viscosity for the mantle, allows conductive cooling of asthenospheric mantle, which becomes rheologically strong and accretes spontaneously to the bottom of the lithosphere. Cutoff limits of 10^{18} Pa s and 10^{26} Pa s were applied to limit minimal and maximal crustal and mantle rock viscosity, respectively. The rheological and thermo-physical parameters with the values assumed in the numerical simulations are displayed in Table 4.1:

	Air	Upper Crust	Lower Crust	Lithosphere	Asthenosphere
Pre-Expo. Factor (A_D) ($Pa^{MM}s$)	1.00E+18	1.97E+17	4.80E+22	3.98E+16	3.98E+16
Activation Energy (E) (J)	0.00 E+05	1.54E+05	2.38E+05	5.32E+05	5.32E+05
Stress Exponent (n) (MM)	1.00E+00	2.30E+00	2.30E+00	3.50E+00	3.50E+00
Density (ρ) (kg/m^3)	1.00E+00	2.75E+03	2.95E+03	3.25E+03	3.30E+03
Thermal Conductivity (k) (W/(m*K))	2.00E+01	0.64E+00	1.18E+00	0.73E+00	0.73E+00
Isobaric Heat Capacity (C_P) (J/kgK)	0.00 E+02	8.07E+02	4.74E+02	12.93e+02	12.93e+02
Radiogenic Heat (H_r) (W/kg)	0.00 E-08	1.00E-08	0.50E-08	2.00E-08	2.20E-08
Viscosity (η) (Pa*s)	1.00E+18	1.00E+26	1.00E+26	1.00E+26	1.00E+26
Stress max Value (σ_{ij}) (Pa)	5.00E+04	5.00E+29	5.00E+29	5.00E+29	5.00E+29
Activation Vol. (E) (J/bar)	0.00E+00	0.00E+00	0.00 E+00	1.20E+00	1.20E+00
Critical Stress (σ_{cr}) (Pa)	0. 00E+04	3.00E+04	3.00E+04	3.00E+04	3.00E+04
Cohesion (C) (Pa)	0. 00E+05	3.00E+05	3.00E+05	3.00E+05	3.00E+05
Shear Strength (σ) (Pa)	0. 00E+05	3.00E+05	3.00E+05	3.00E+05	3.00E+05
Thermal Expansion (α) (1/K)	0. 00E-05	3.00E-05	3.00E-05	3.00E-05	3.00E-05
Compressibility (β) (1/Pa)	0. 00E-03	1.00E-03	1.00E-03	1.00E-03	1.00E-03

Table 4.1 – *Values of the thermo-physical parameters used in the numerical simulations.*

4.3 Results of the 3D numerical simulations

The models run for different time intervals, from a minimum of 50 Myr to a maximum of 200 Myr. The upper limit was chosen considering that the rift duration is supposed to have lasted maximum 200 Myr (Delvaux et al., 2021). I stopped the run before this time, when the results obtained were not consistent with the geological/geophysical observations or when the purpose of the simulations was to check the sensitivity of some parameters and a shorter running time was enough for this aim. A summary of the main characteristics of the 3D numerical simulations performed with different geometry designs and thermal gradient of the off-cratonic areas (weak zones) are displayed in Table 4.2.

In the next sections, I display the results of the different simulations, in terms of temporal lateral variations of topography and viscosity at the depths of the main lithospheric discontinuities. To this aim, I traced the surface topography in correspondence of the depth of the isodensity 2200kg/m^3 (a value between the density of the sticky air and that of the upper crust). The base of the lithosphere and crust corresponds to the depth of the isotherm 1573 K and of the isodensity 3000 kg/m^3, respectively. In addition, I displayed the viscosity variations at a depth inside the mantle lithosphere, corresponding to that of the isotherm 1073 K. I also displayed depth-temperature variations, along one cross-section *N-S* oriented and depth-viscosity variations, along three cross-section *N-S*, *NW-SE*, and *NE-SW* oriented.

Models	**Design (km)**	**Depth Litho (off-craton) (km)**	**T. Moho (off-craton) (K)**	**T. Litho (off-craton) (K)**	**Age reached (Myr.)**
1_Congo_cratons	1000x1000 (Cratonic Blocks)	200	773	1673	95
2_Congo_cratons	1900x1900 (Cratonic Blocks)	200	773	1673	95
3_Congo_weak1	405x405 (Weak Zone)	200	773	1673	200
4_Congo_weak2	810x810 (Weak Zone)	100	873	1623	200
5_Congo_weak3	810x810 (Weak Zone)	100	873	1623	50
6_ Congo_weak4	405x405 (Weak Zone)	100	873	1623	200
7_ Congo_cratons+weak	1402x1402 (Cratonic Block) 623x623 (Weak Zone)	100	873	1623	100

Table 4.2 *– Main thermo-physical characteristics of the 3D numerical simulations carried out in this study.*

4.3.1 First model: 1_Congo_cratons

Numerical model design: In the first 3D numerical model (*1_Congo_cratons*, Fig. 4.4), I assumed that the Congo Craton is composed of four equal cratonic blocks of size 1000 km x 1000 km. The thickness of the lithosphere in the areas external to the cratons is 180 km. The distance between one craton to another is 500 km, while from a craton to the edge of the model is 775 km. The TZs surrounding the cratonic areas are large about 100 km. This geometry design produces an off-cratonic area or weak zone in the center about 500 km wide (Fig.4.4 A).

Initial Temperature Conditions: According to this geometry, in the areas external to cratonic blocks, I associated a temperature at the base of the crust and mantle lithosphere of 773 K and 1673 K (Table 4.2), respectively. I chose these values, in order to obtain a crustal gradient, which is more than double (~14 K/km) that of the mantle lithosphere (~6 K/km). This setup favors decoupling of the crust from the mantle lithosphere, during the applied multi-divergent velocities, and thus a more distributed deformation. In contrast, in the cratons, where a constant gradient is applied in the entire lithosphere (~6 K/km), coupling conditions of the lithospheric layers are expected.

Results: We observe a progressive decrease of viscosity at the base of the lithosphere and subsidence in the areas surrounding the cratonic blocks, while the opposite occurs in the peripheral part of the cratons, in particular at the corners (Fig. 4.5-4.7). On the other hand, in the central part of the model, ideally representing the Cuvette Centrale, the topography variations are very modest, while the major topography variations occur along the cratonic edges (Fig 4.7). The progressive topography changes are accompanied by viscosity variations: in the areas that subside, the viscosity at the base of the lithosphere decreases and vice versa. Looking at the different time steps, we can notice that the thermal anomaly does not change significantly its shape, but the temperature variations along the *TZs* become smoother with time (Fig. 4.6). Since these kinds of features are quite different from those observed from geological and geophysical data, I decided to stop the running at 95 Myr and modify the model geometry in the next simulation.

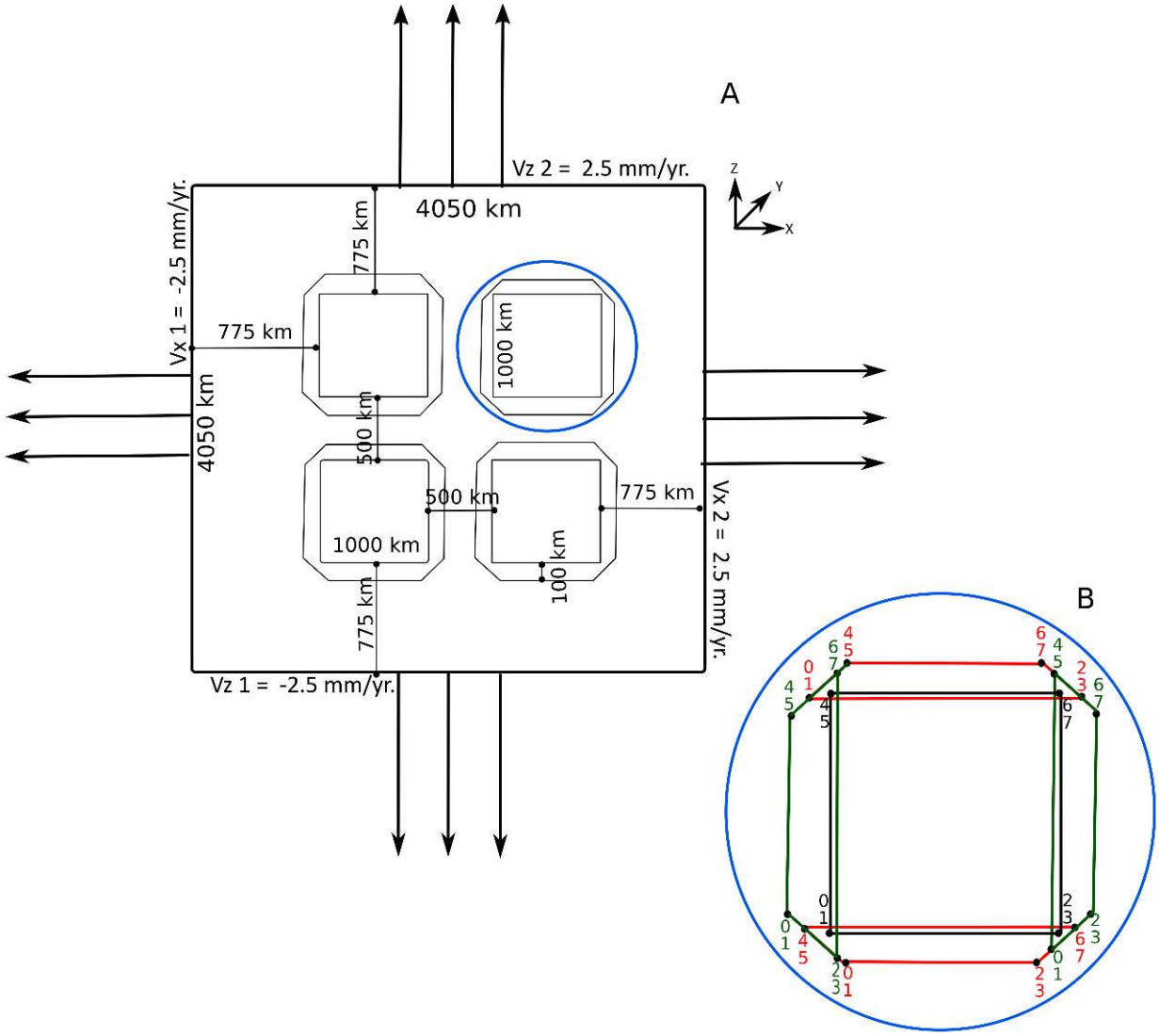

Figure 4.4 *– Geometry design of the model 1_Congo_cratons.* ***A****: Horizontal plane visualization of the model. Black arrows show velocity directions.* ***B****: Zoom in plane on one cratonic block (black square), represented in staggered grid-mark-in cell technique. The nodes are represented by black points and the associated couple of numbers, having the same colors of the referred geometry, denotes the two nodes having the same planar coordinates (x and z) and different vertical coordinate (y). In green and red are the trapezoids, representing the TZs from cratonic to off-cratonic lithosphere, parallel to x and z-axis, respectively.*

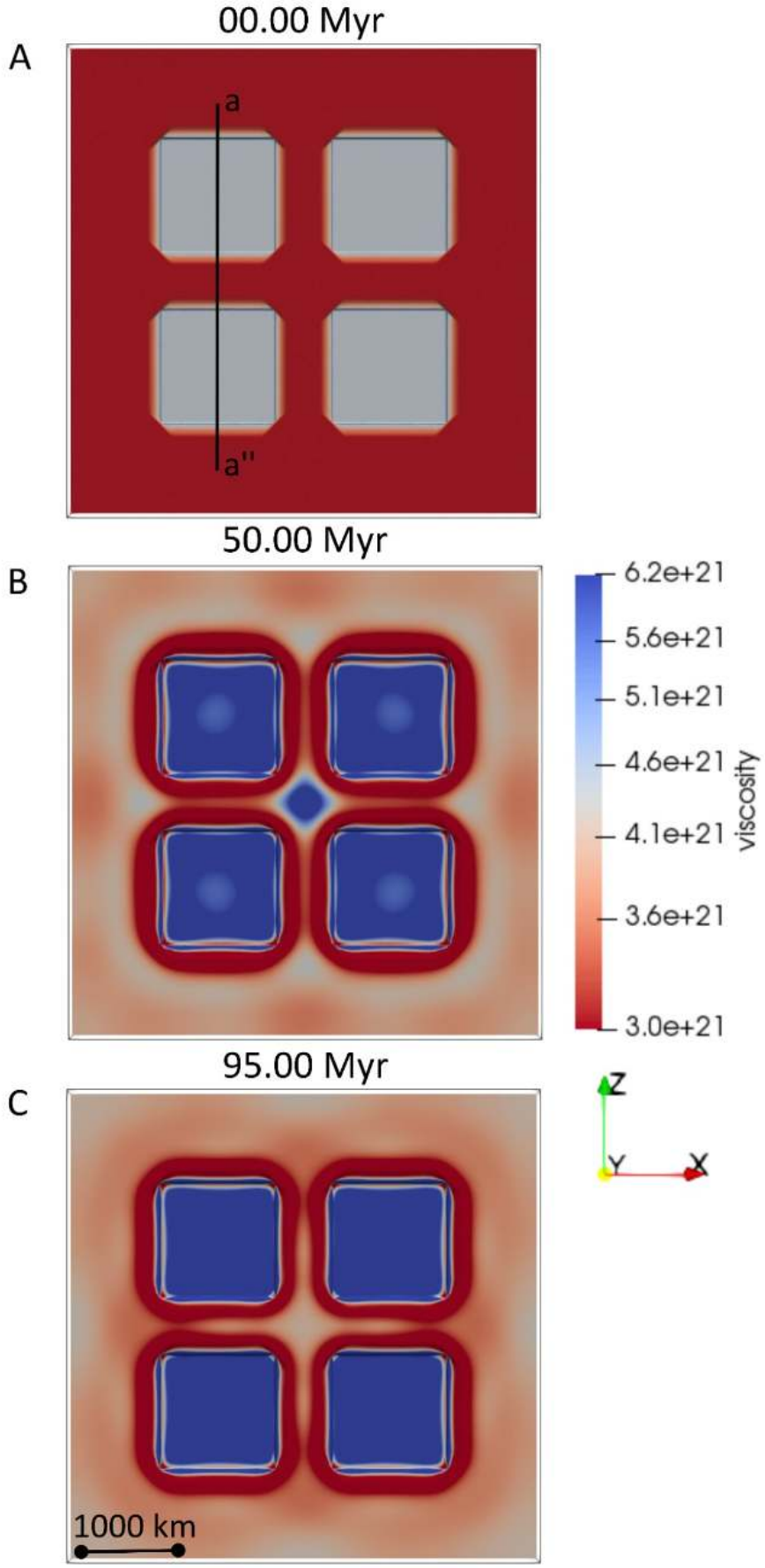

Figure 4.5 *– Model 1_Congo_cratons. Lateral variation of viscosity (Pa s) at the base of the lithosphere, defined as depth of the isotherm 1573 K, at (**A**) 0 Myr (**B**) 50 Myr, and (**C**) 95 Myr. Black line delimited by labels a-a"shows the location of the cross-setion of temperatures (Fig. 4.6), density (Figs. 4.52-4.53), and viscosity (Figs. C2-C6).*

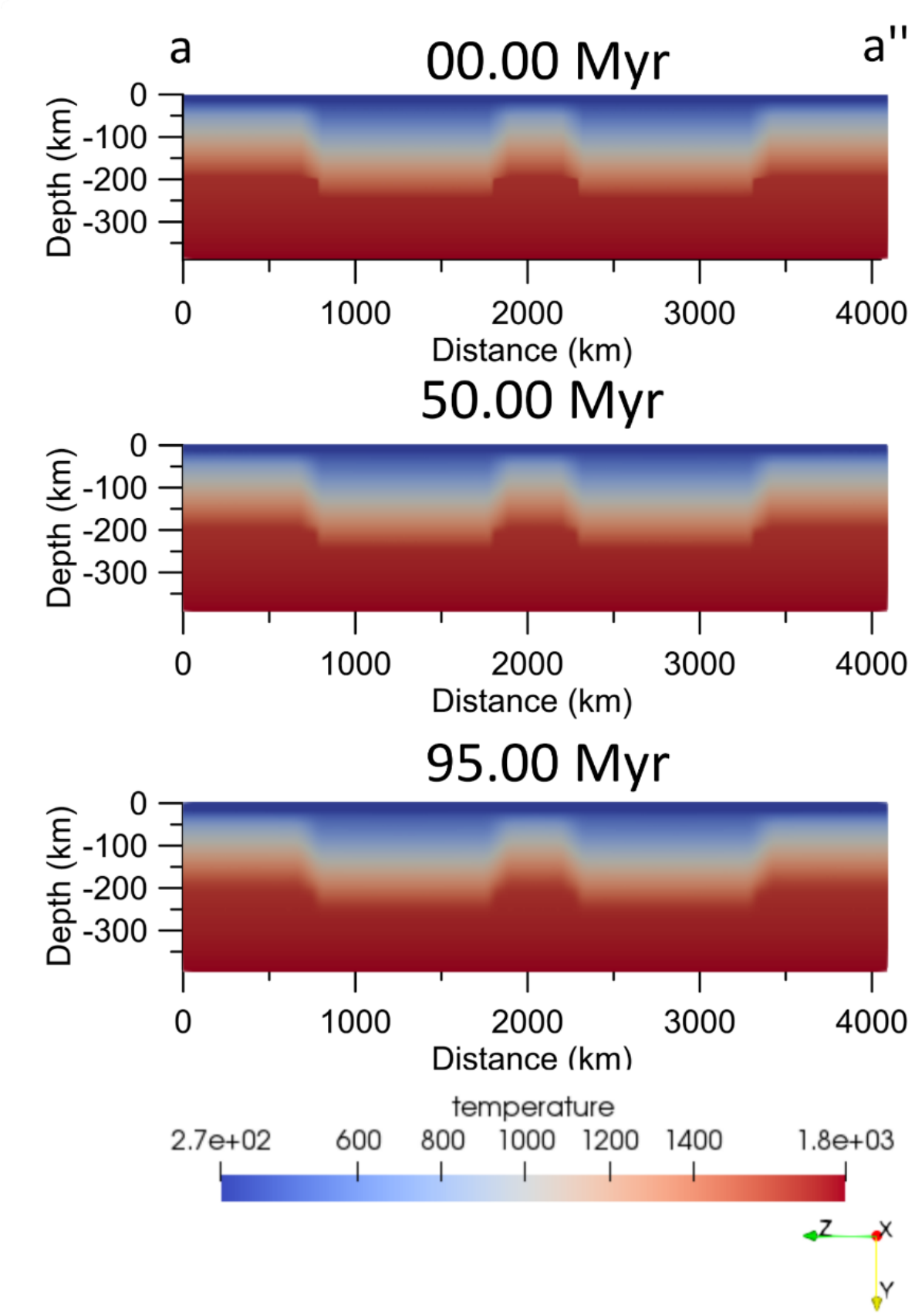

***Figure 4.6**- Model 1_Congo_cratons. Depth-temperature variation (K) at (**A**) 0 Myr, (**B**) 50 Myr, and 95 Myr (**C**), along the cross-section displayed in Fig. 4.5A. Vertical scale increased by 15% with respect to horizontal axis.*

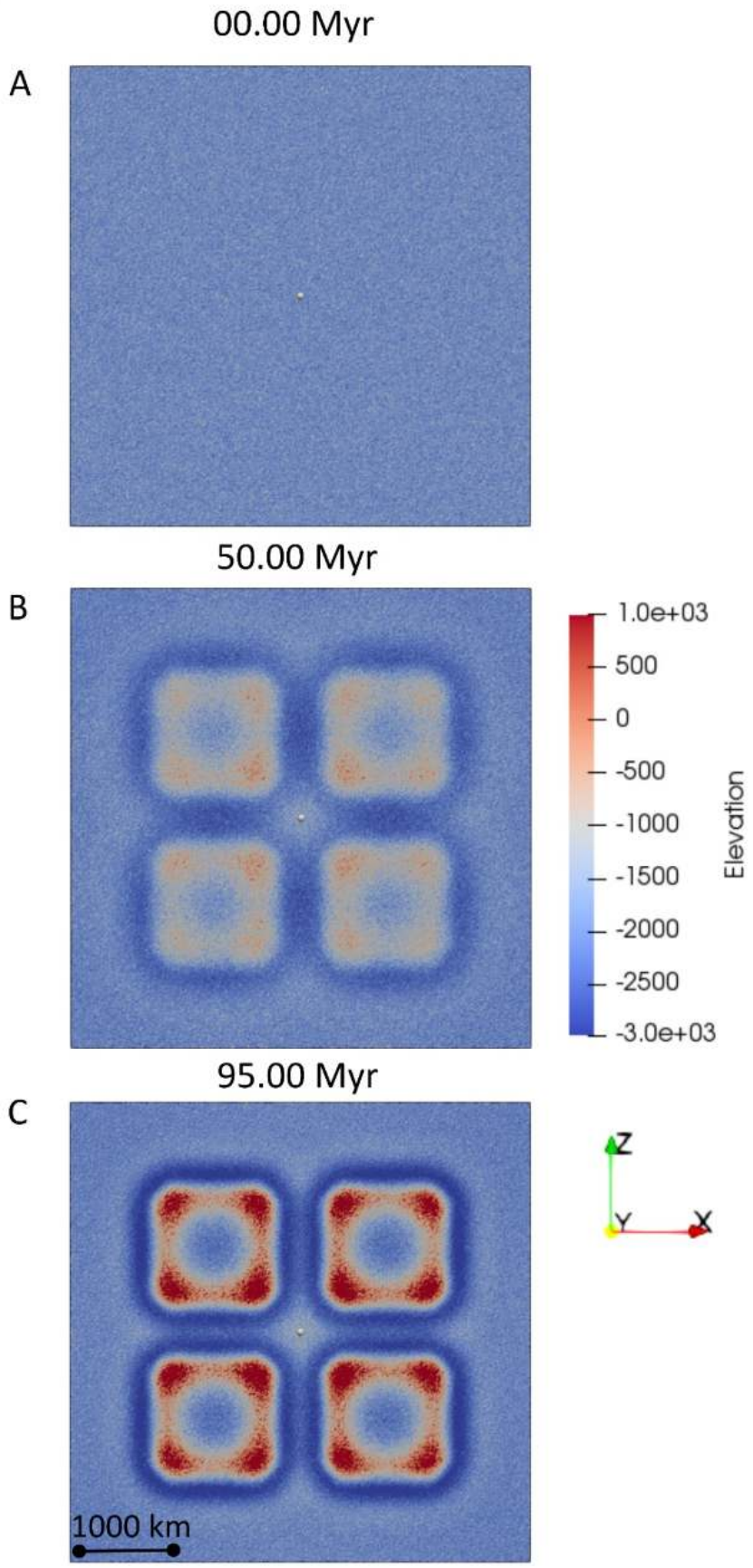

Figure 4.7 *- Model 1_Congo_cratons. Lateral variation of surface topography (m) at 0 Myr (**A**), 50Myr (**B**) and 95 Myr (**C**).*

4.3.2 Second model: 2_Congo_cratons

Numerical model design: As in the previous numerical simulation, I assumed in this model (2_Congo_cratons, Fig. 4.8) that the study area is divided into four equal cratonic blocks, which have a larger size (1900 km x 1900 km) and the external boundaries coincident with those of the box model. Therefore, the distance between the cratons decreases to 250 km, with respect to the first simulation, and the *TZs* surrounding the cratonic areas are more extended (about 1869 km x 62 km). The thickness of the lithosphere in the areas external to the cratons remains equal to 180 km. This geometry configuration, as in the previous simulation, leaves a weak zone in the center, but in this case large only about 150 km.

Initial Temperature Conditions: The thermal gradients are the same as those of the first simulation, according to the same crustal and lithospheric thickness assumed.

Results: Temporal lateral viscosity variations at the base of the lithosphere (Fig. 4.9) show a progressive reduction of this parameter, from the central weak zone towards the inner part of the cratons. The formation of a low-viscosity zone in the central part of the area and between the cratonic areas is consistent with the upwelling of the asthenosphere, in response to the multi-extensional stresses. Compared to the results of the previous simulation, the narrowing of the weak zones dividing the cratonic blocks causes a reduction of the area of asthenospheric upwelling (Fig. 4.10), which significantly localizes the deformation. This promotes a progressive subsidence in the central parts of the weak zones and uplift along their edges (Fig. 4.11). The subsidence is more pronounced between the cratonic areas than in the central part of the model. On the other hand, the cratonic blocks are progressively uplifted from their external parts towards the inner parts. Therefore, the simulation does not reproduce the formation of a broad subsiding central area with a heterogeneous surface topography. Because of the inconsistency of the results obtained with the geological/geophysical observations, I stopped the running at 105 Myr and changed the geometry designs in the next simulations.

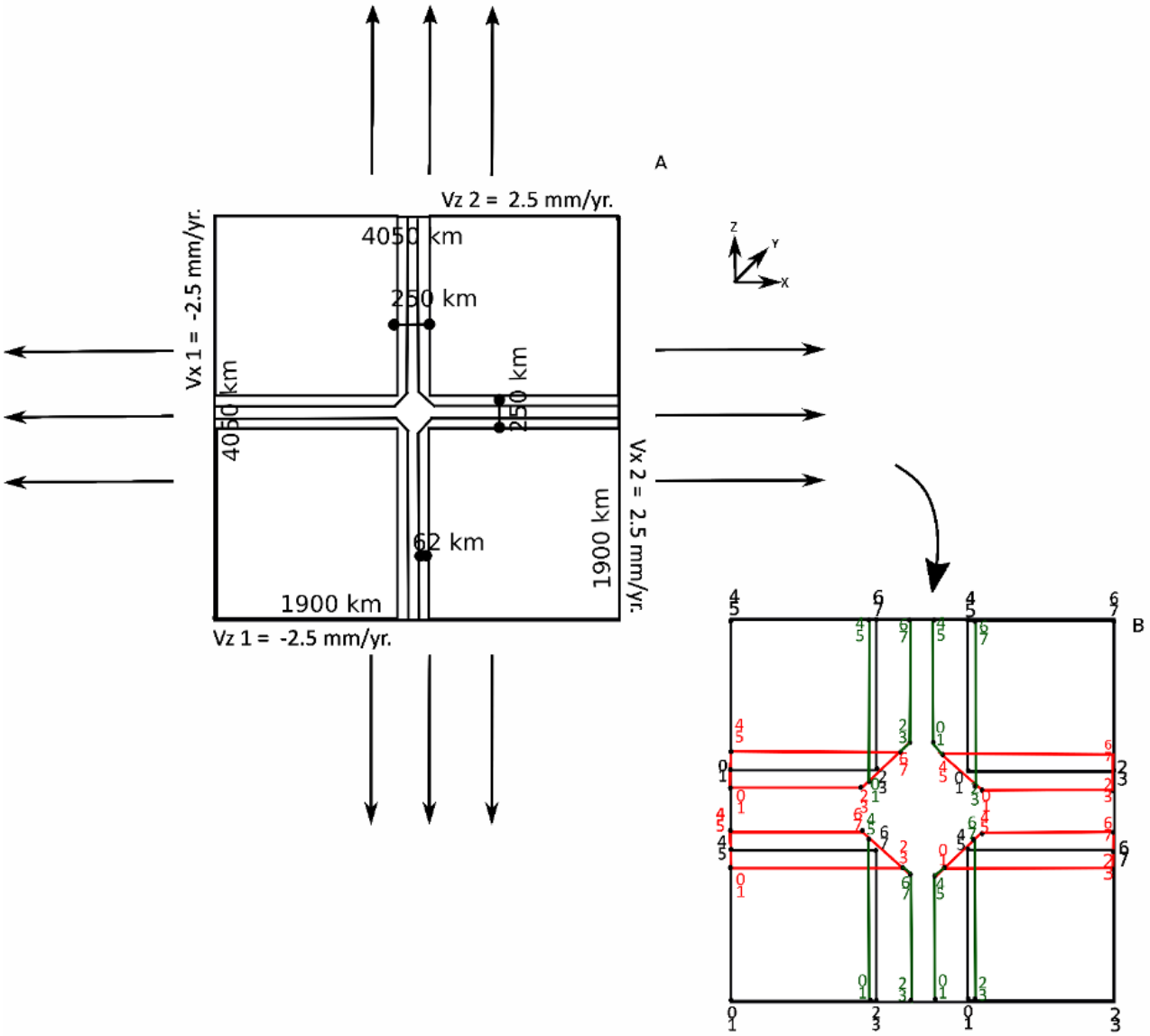

Figure 4.8 *– Geometry design of the model 2_Congo_cratons.* ***A****: Horizontal plane visualization of the model. Black arrows show velocity directions.* ***B****: Representation of the model (A) in staggered grid-in cell marker technique. The black square represents the cratonic blocks. Red and green features represent the TZs and numbers are as in Fig. 4.4.*

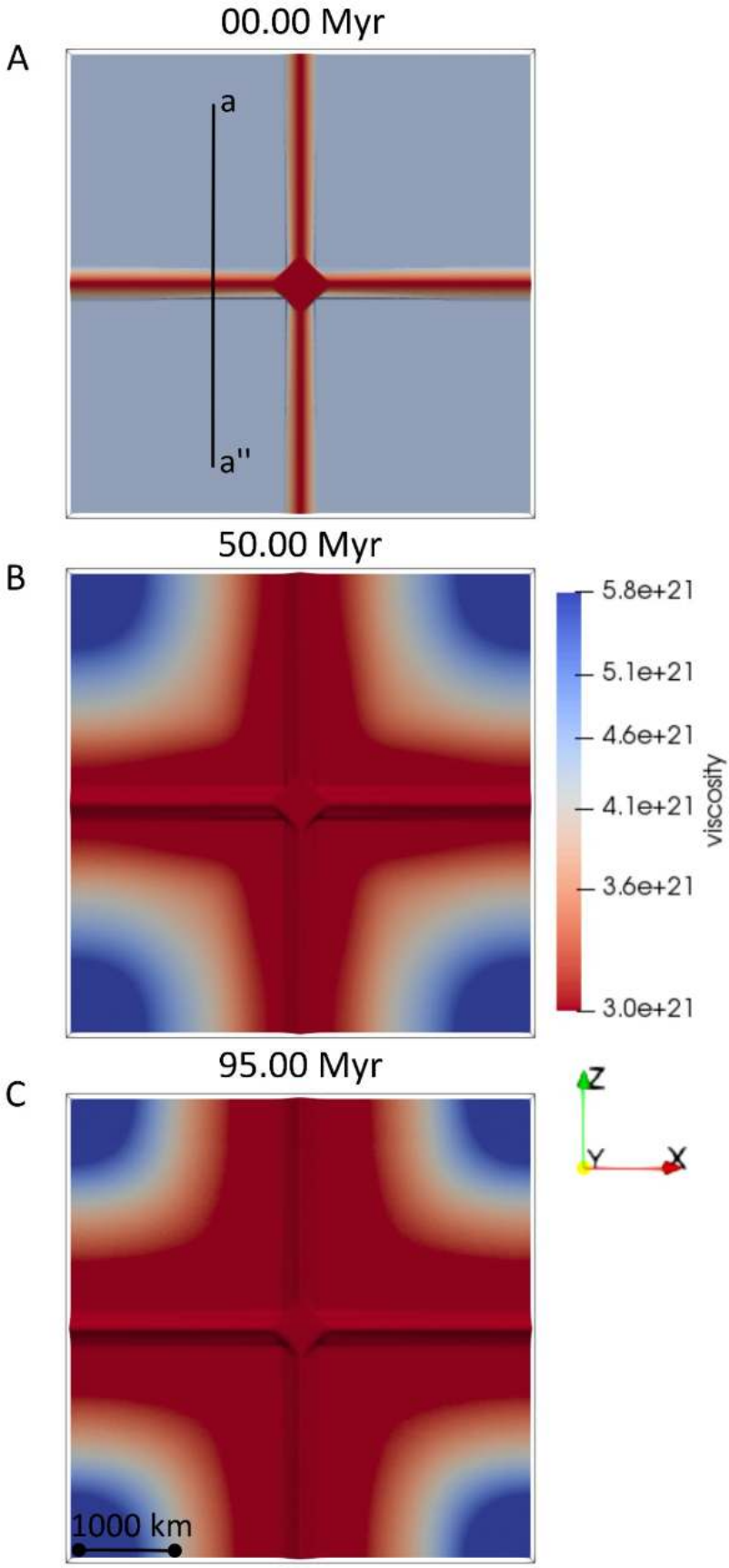

Figure 4.9 *– Model 2_Congo_cratons. Lateral variation of viscosity (Pa s) at the base of the thermal lithosphere, defined as depth of the isotherm 1573 K, at 0 Myr (**A**), 50 Myr (**B**) and 95 Myr (**C**). Black line delimited by labels a-a"shows the location of the cross-setion of temperatures (Fig. 4.10), density (Figs. 4.52-4.53), and viscosity (Figs. C2-C6).*

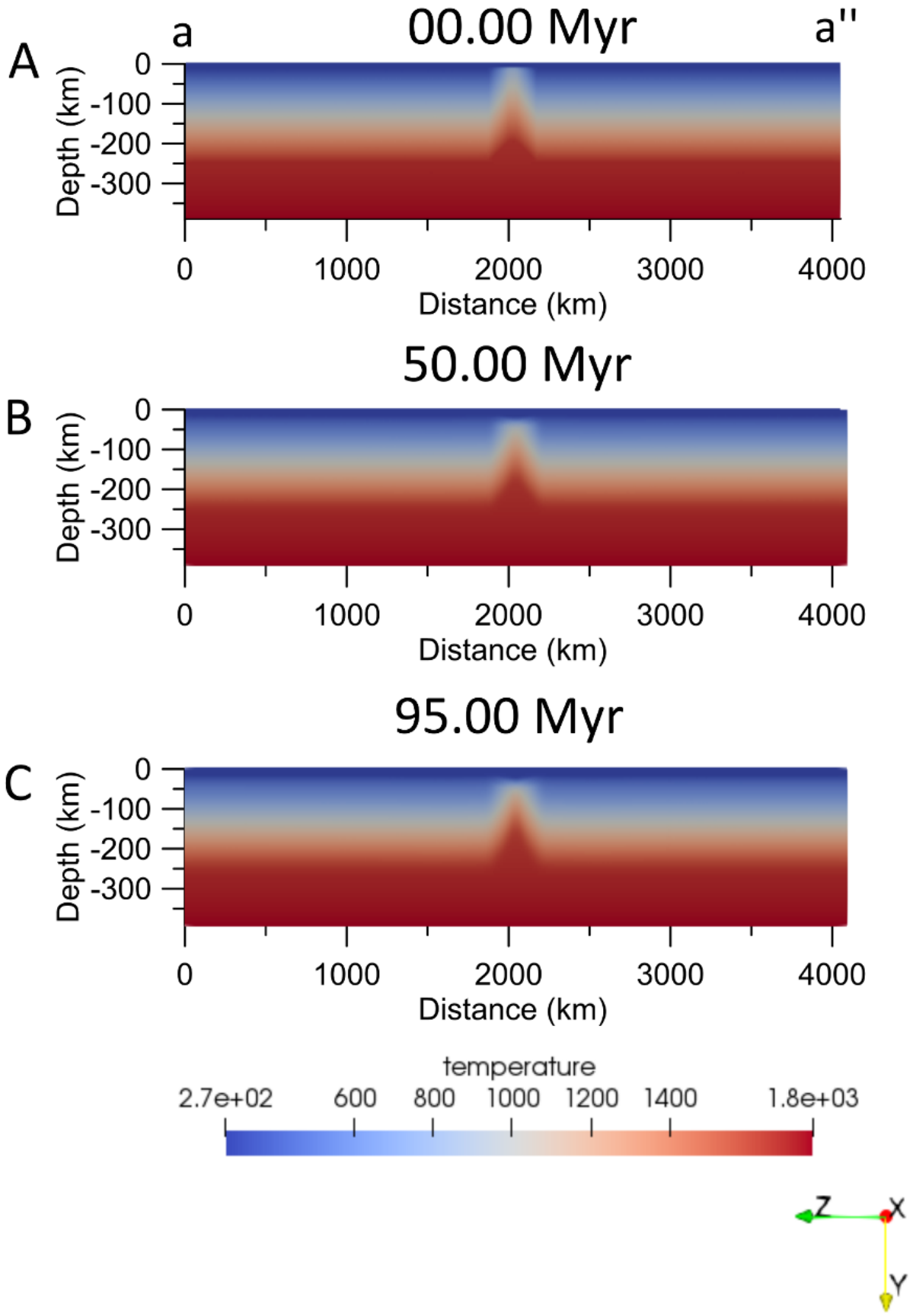

Figure 4.10 *- Model 2_Congo_cratons. Depth-temperature variations (K) at 0 Myr (**A**) to 50 Myr (**B**) and 95 Myr (**C**), along the cross-section displayed in Fig. 4.9A. Vertical scale increased by 15% with respect to horizontal axis.*

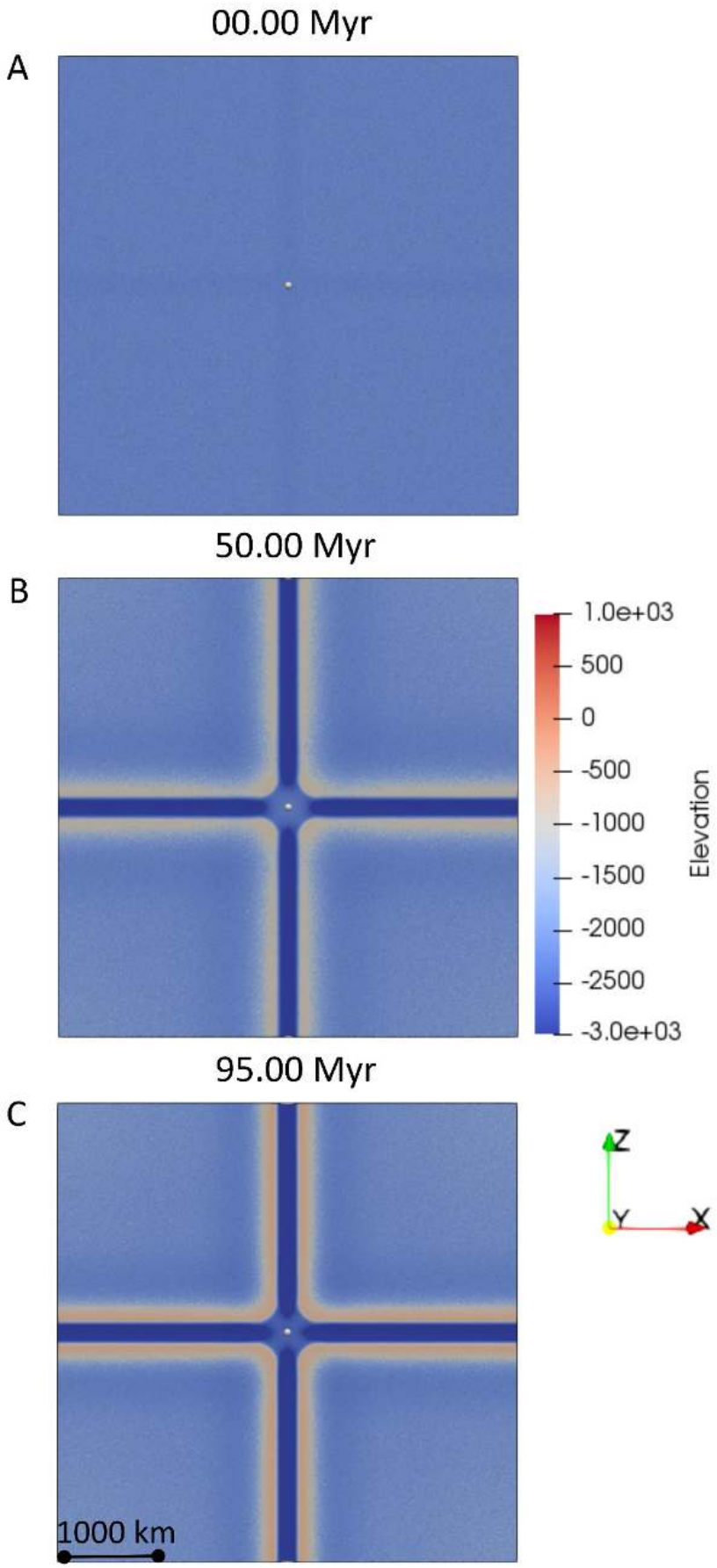

Figure 4.11 *- Model 2_Congo_cratons. Lateral variation of surface topography (m) at 0 Myr (**A**), 50 Myr (**B**), and 95 Myr (**C**).*

4.3.3 Third model: 3_Congo_weak1

Numerical model design: The numerical simulation has been conducted considering the existence of a weak zone of size 405 km x 405 km (*3_Congo_weak1*, Fig. 4.12), located in the central part of a single cratonic block, surrounded by a *TZ* of size equal to 101 km. The depth of the lithosphere in the weak zone is of 180 km and the distance between the weak zone and cratonic borders is 1822 km.

Initial Temperature Conditions: The thermal gradients in the weak zone are the same as those of the previous simulations, according to the same crustal and lithospheric thickness assumed.

Results: Temporal lateral variations of viscosity at the base of the crust, within the lithosphere, and at the base of the lithosphere are displayed in Figs. 4.13-4.15. We can notice a viscosity decrease at the base of the lithosphere (Fig. 4.15 B) during the first 50 Myr of simulation, in the central area (Figs. 4.13 B-4.15 B), consistent with the upwelling of the asthenosphere (Fig. 4.16 B). After longer time (100 Myr), the further asthenosphere updoming increases the size of the thermal anomaly and enhances lateral contrast in temperature (Fig. 4.16 C-D). Consequently, the central weak zone becomes larger, but at the same time, there is the formation of two elongated zones, orthogonal each other, characterized by very low viscosity (Fig. 4.15 B, 4.15 C), also at shallower depths (4.13 C-D and 4.14 C-D). However, at 200 Myr the viscosity increases in the areas surrounding the orthogonal weak zones (4.13 D-4.15 D) and within them at the Moho depth (Fig. 4.13 D). This is even more visible looking at the cross-sections that display the temporal depth-viscosity variations, where I could observe a low vicosity zone, which reaches the surface at 200 Myr, due to a time-increasing mantle upwelling (Appendix C, Fig. C2). The formation of these structures is mainly due to the sharper lateral temperature and lithospheric thickness variations (Fig. 4.16 D). In particular, the replacement of the lower crust with mantle material can produce local viscosity increases, due to its stiffer rheology (4.13 D) and decrease of the surface topography in the central part of the model and along the two orthogonal structures. The last one occurs between 0.010 Myr and 100 Myr (4.17 A-C). At last time step displayed, we observe the uplift of the edges of these structures (4.17 D). Therefore, the geometry design used in this simulation produces a heterogeneous basement depth, characterized by an alternation of highs and depressions in a central subsided circular zone (Chapter 2). On the other hand, there is a progressive updoming of the Moho in the central part of the model (Fig. 4.18) and of the lithospheric boundary along the two orthogonal structures that become well defined at 200 Myr (Fig. 4.19).

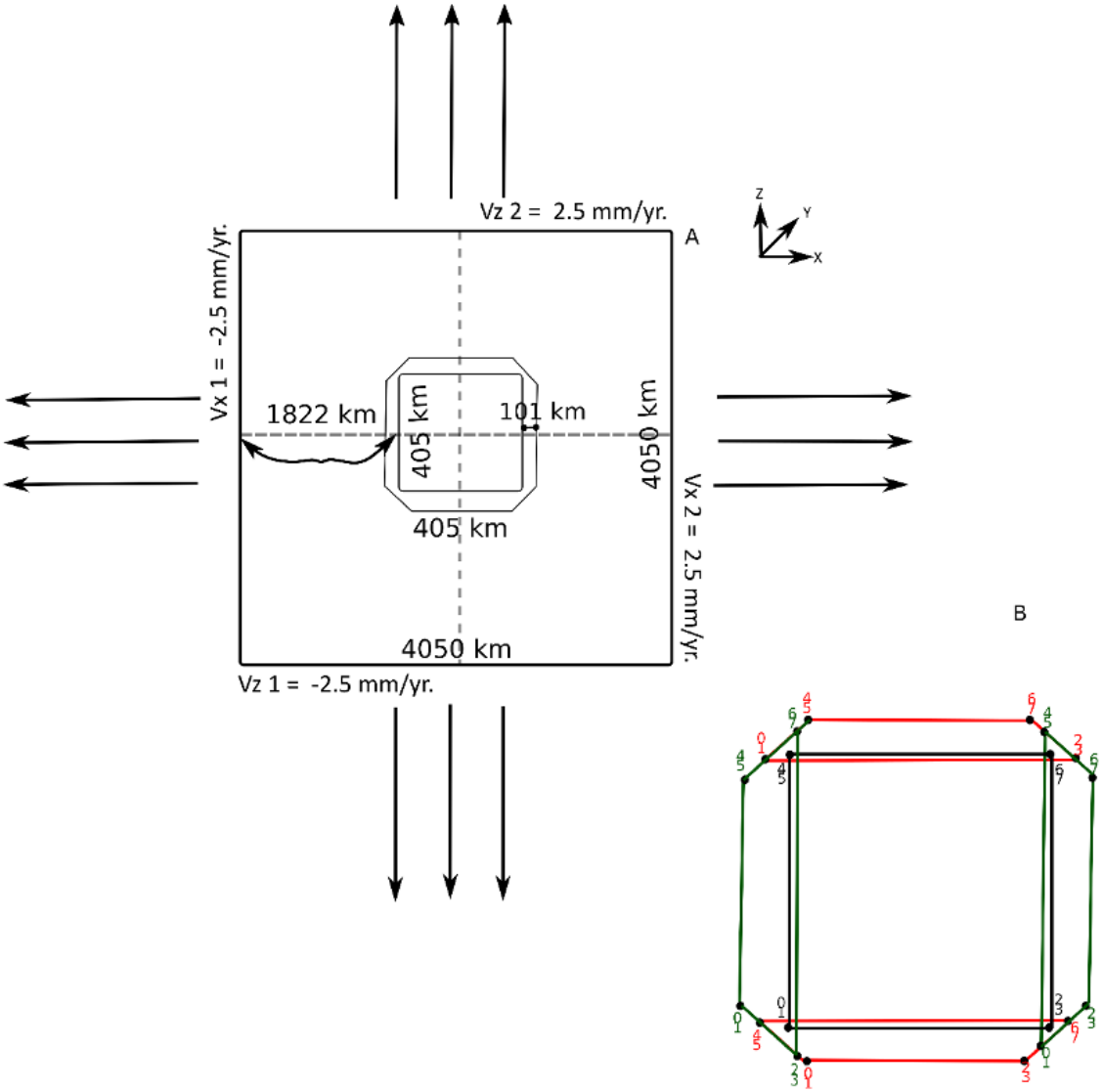

Figure 4.12 *– Geometry design of the model 3_Congo_weak1.* ***A****: Horizontal plane visualization of the model. Black arrows show velocity directions.* ***B****: Zoom in plane on the weak zone (black square), represented in staggered-in cell marker technique. Red and green features represent the TZs and numbers are as in Fig. 4.4.*

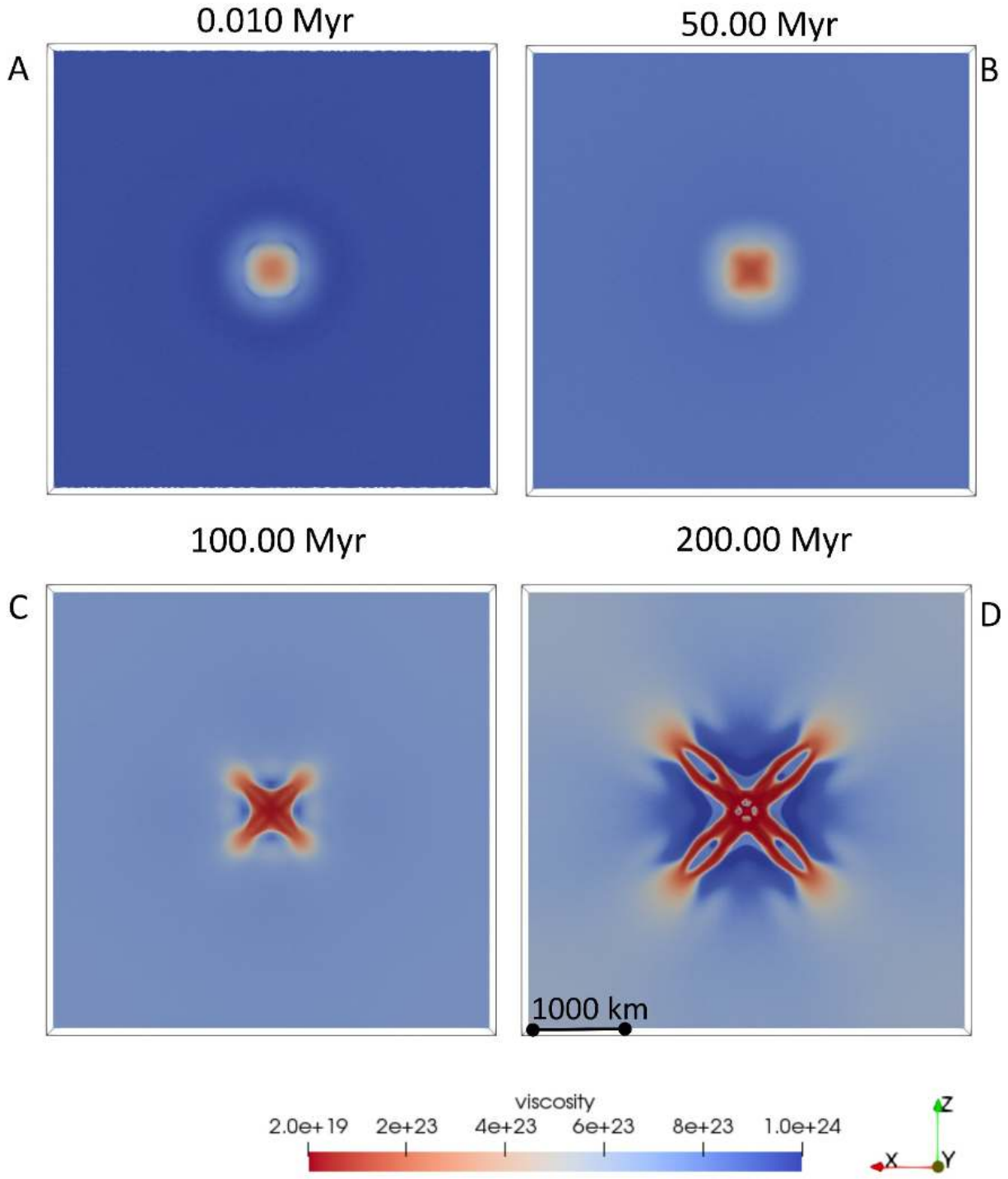

Figure 4.13 *- Model 3_Congo_weak1. Lateral variation of viscosity (Pa s) at the base of the crust, defined by the depth of the isodensity 3000 kg/m³, at 0.010Myr (**A**), 50Myr (**B**), 100 Myr (**C**), and 200Myr (**D**).*

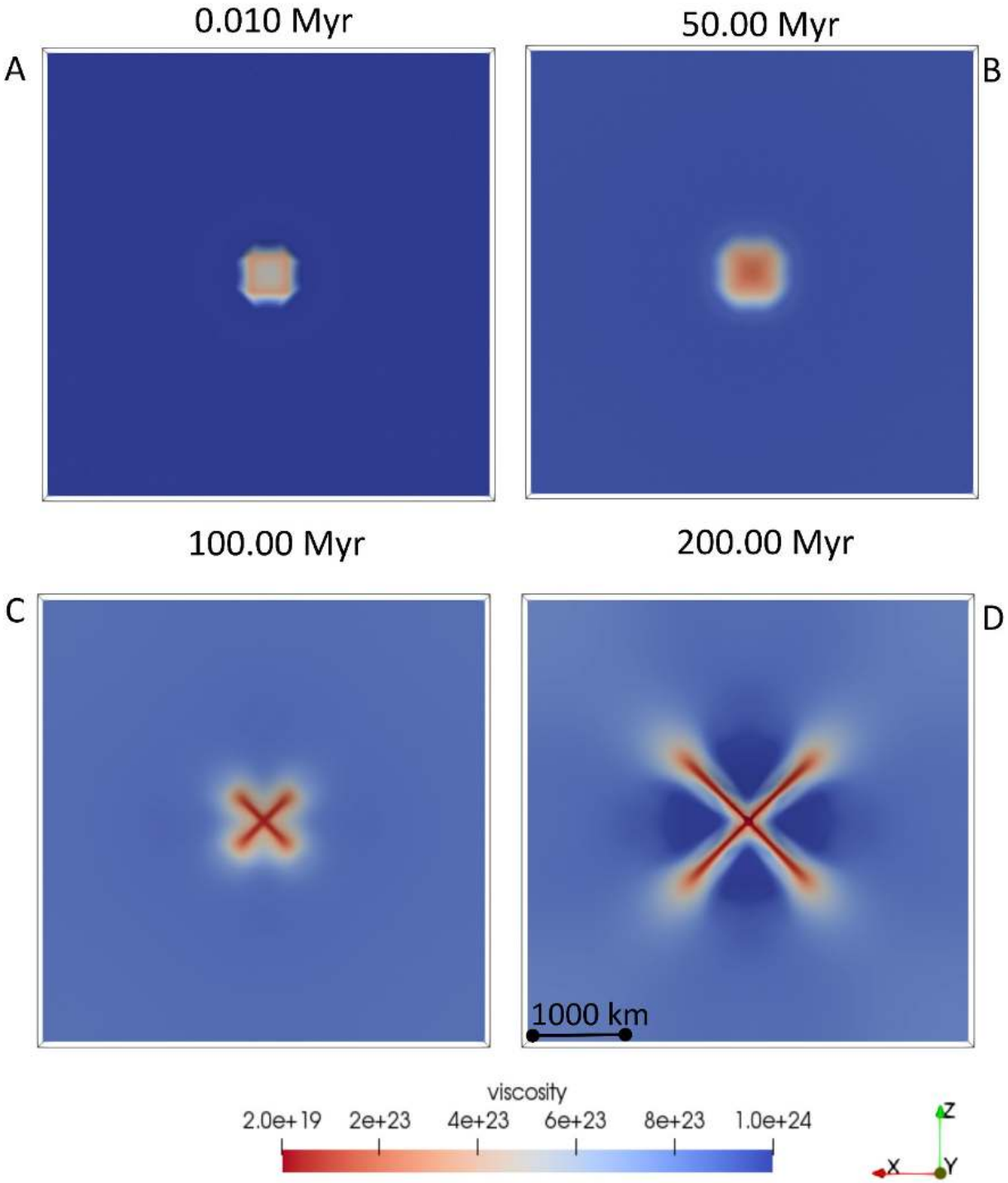

Figure 4.14 *- Model 3_Congo_weak1. Lateral variation of viscosity (Pa s) within the lithosphere, at a depth defined by the isotherm 1073K, at 0.010Myr (**A**), 50Myr (**B**), 100 Myr (**C**), and 200Myr (**D**).*

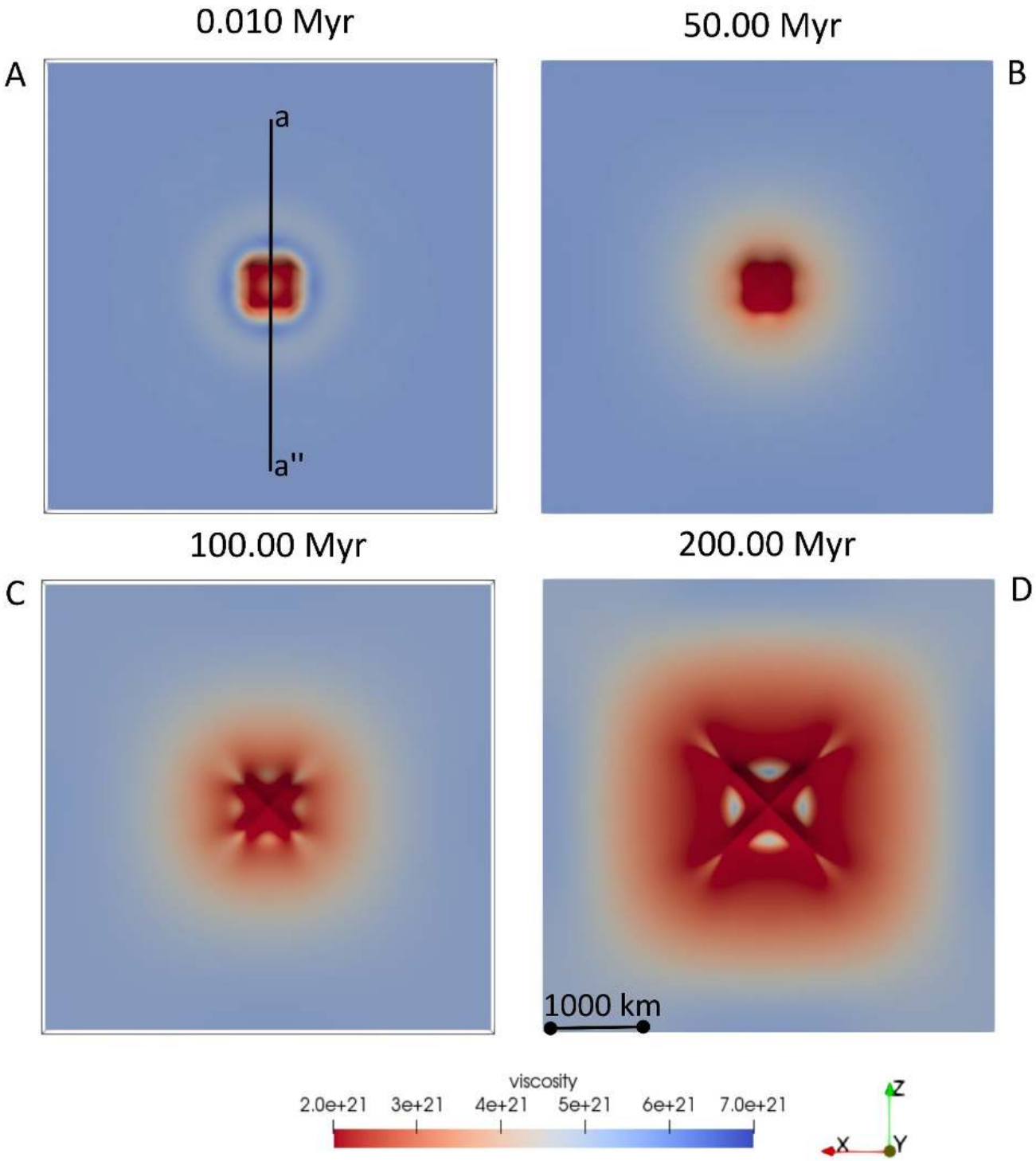

Figure 4.15 *- Model 3_Congo_weak1. Lateral variation of viscosity (Pa s) at the base of the lithosphere, defined as depth of the isotherm 1573 K, at 0.010Myr (**A**), 50Myr (**B**), 100 Myr (**C**), and 200Myr (**D**). Black line delimited by labels a-a"shows the location of the cross-setion of temperatures (Fig. 4.16), density (Fig. 4.52), and viscosity (Fig. C2 A).*

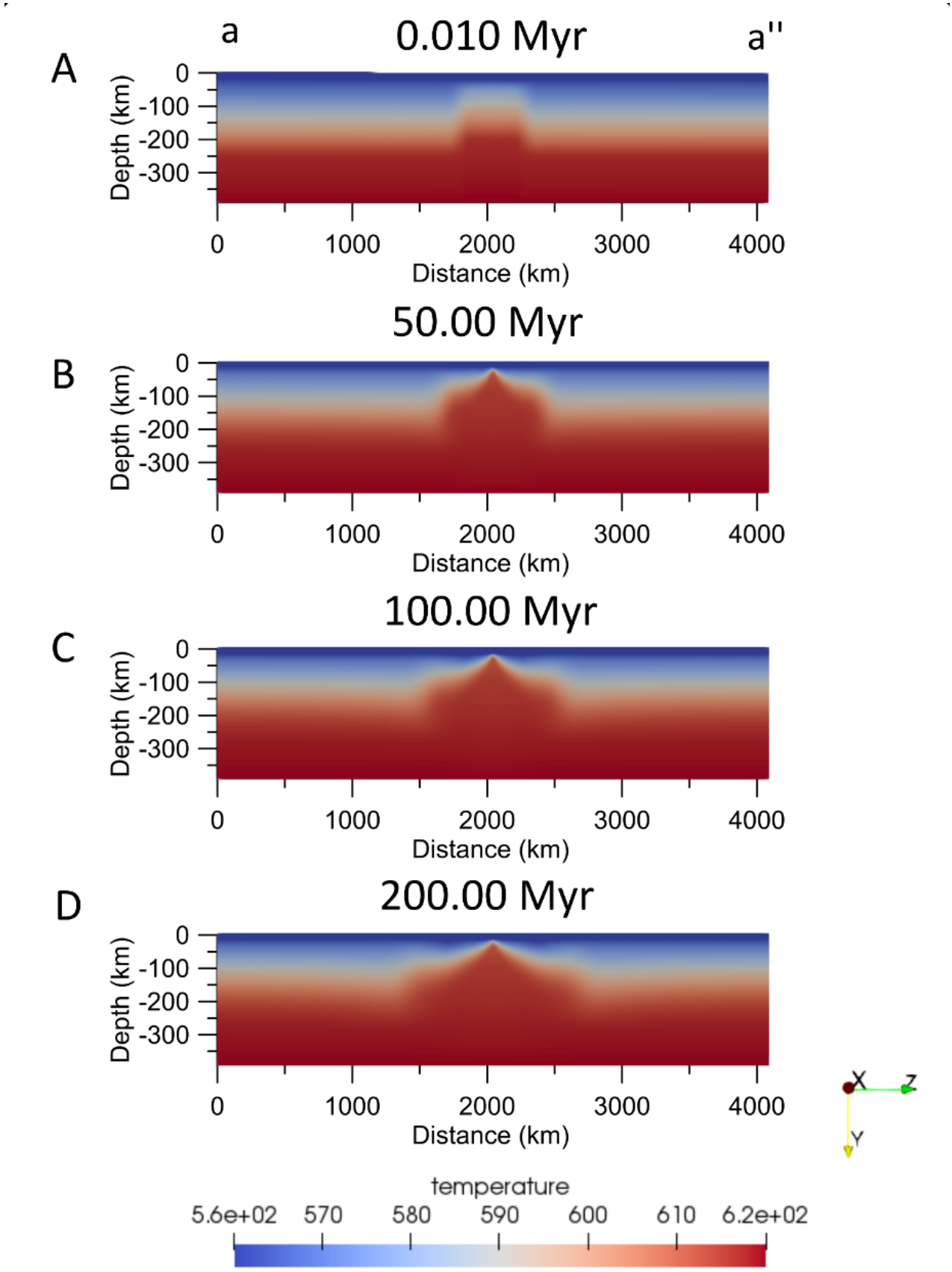

Figure 4.16 *- Model 3_Congo_weak1. Depth-temperature variations (K) at 0.010 Myr (**A**), 50 Myr (**B**), 100 Myr (**C**), and 200 Myr (**D**), along the cross-section displayed in Fig. 4.15 A. Vertical scale increased by 15% with respect to horizontal axis.*

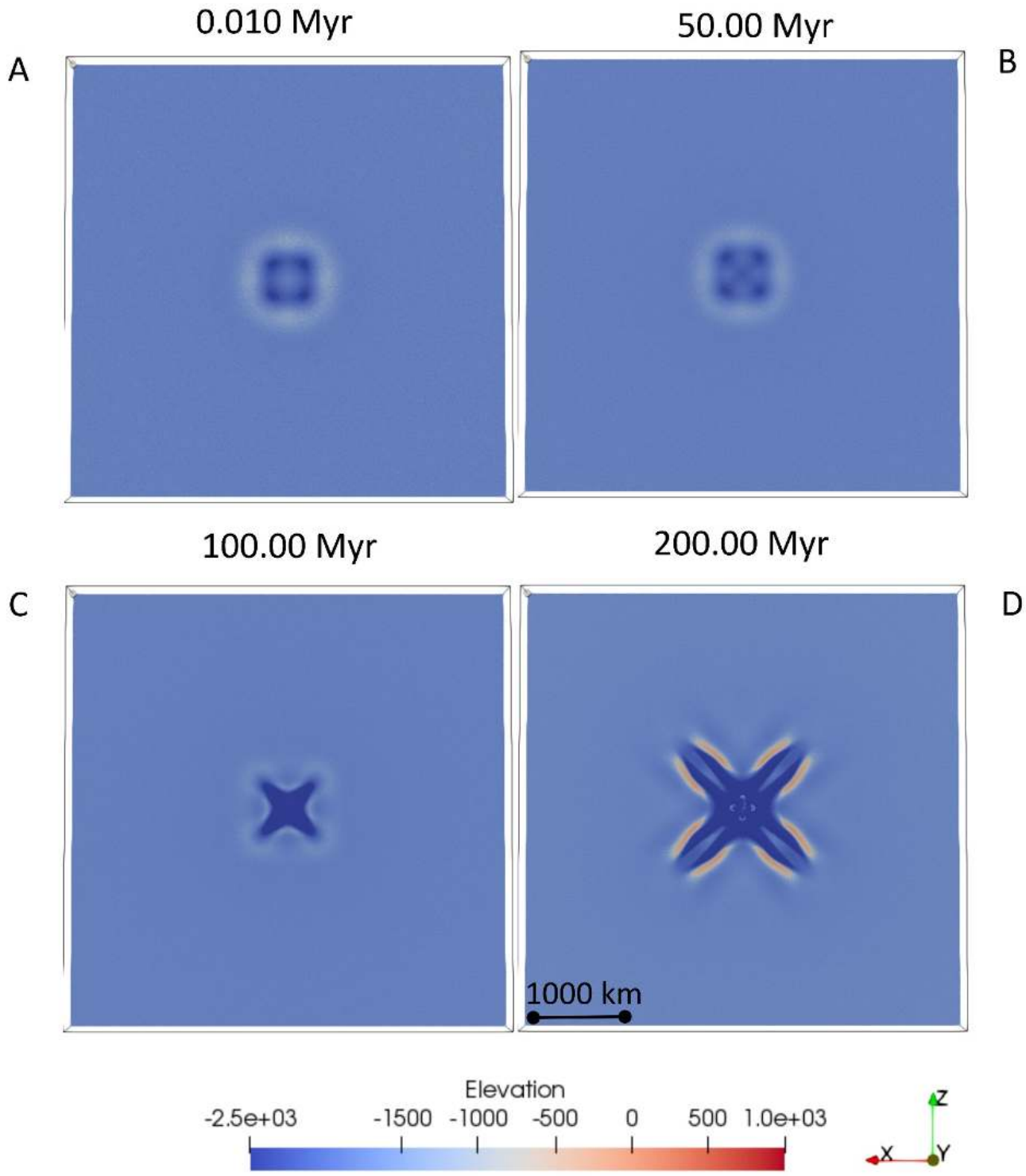

Figure 4.17 *- Model 3_Congo_weak1. Lateral variation of surface topography (m) at 0.010Myr (**A**), 50Myr (**B**), 100 Myr (**C**), and 200Myr (**D**).*

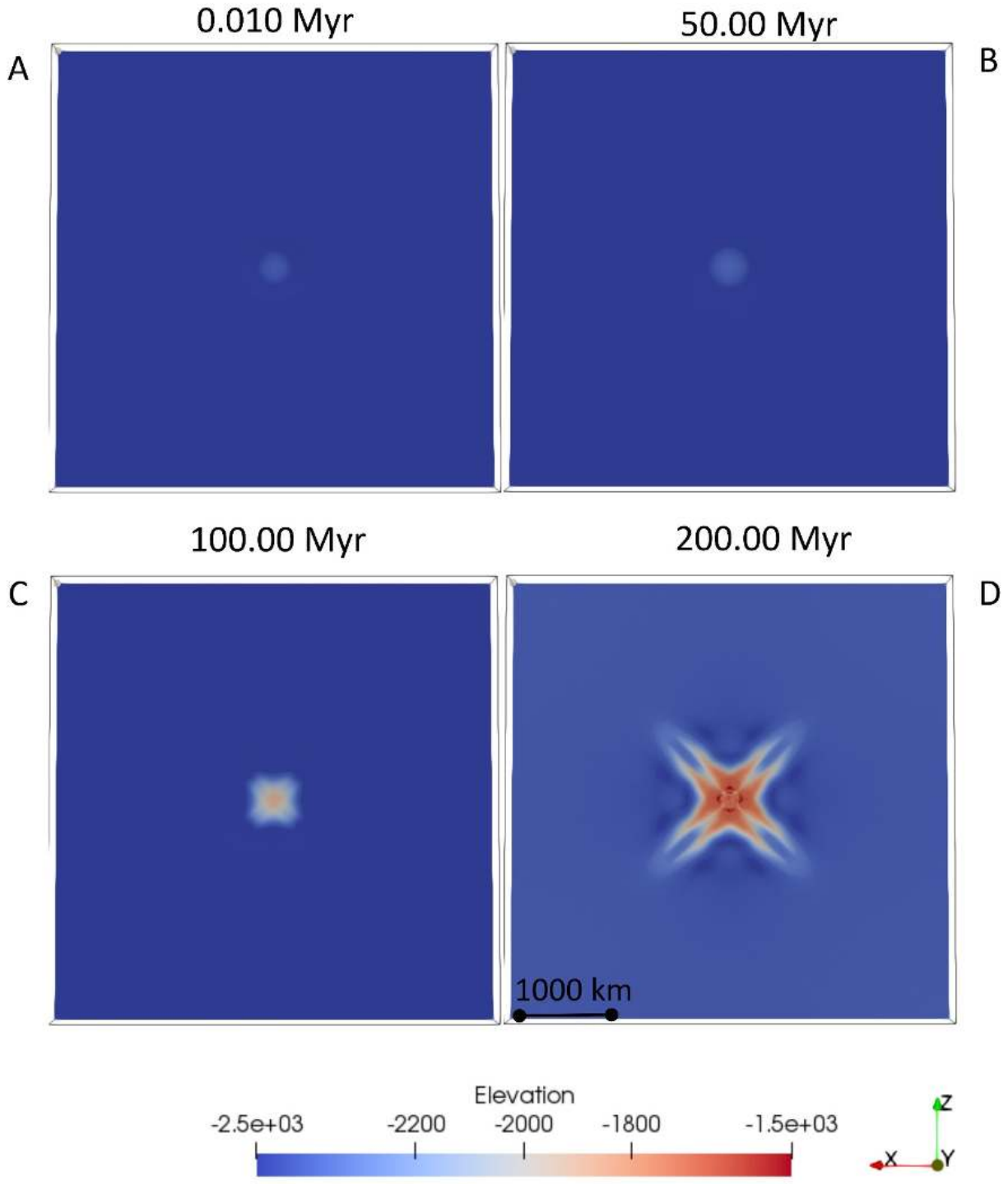

Figure 4.18 *- Model 3_Congo_weak1. Lateral variation of topography (m) at the base of the crust, defined by the depth of the isodensity 3000 kg/m³, at 0.010Myr (**A**), 50Myr (**B**), 100 Myr (**C**), and 200Myr (**D**).*

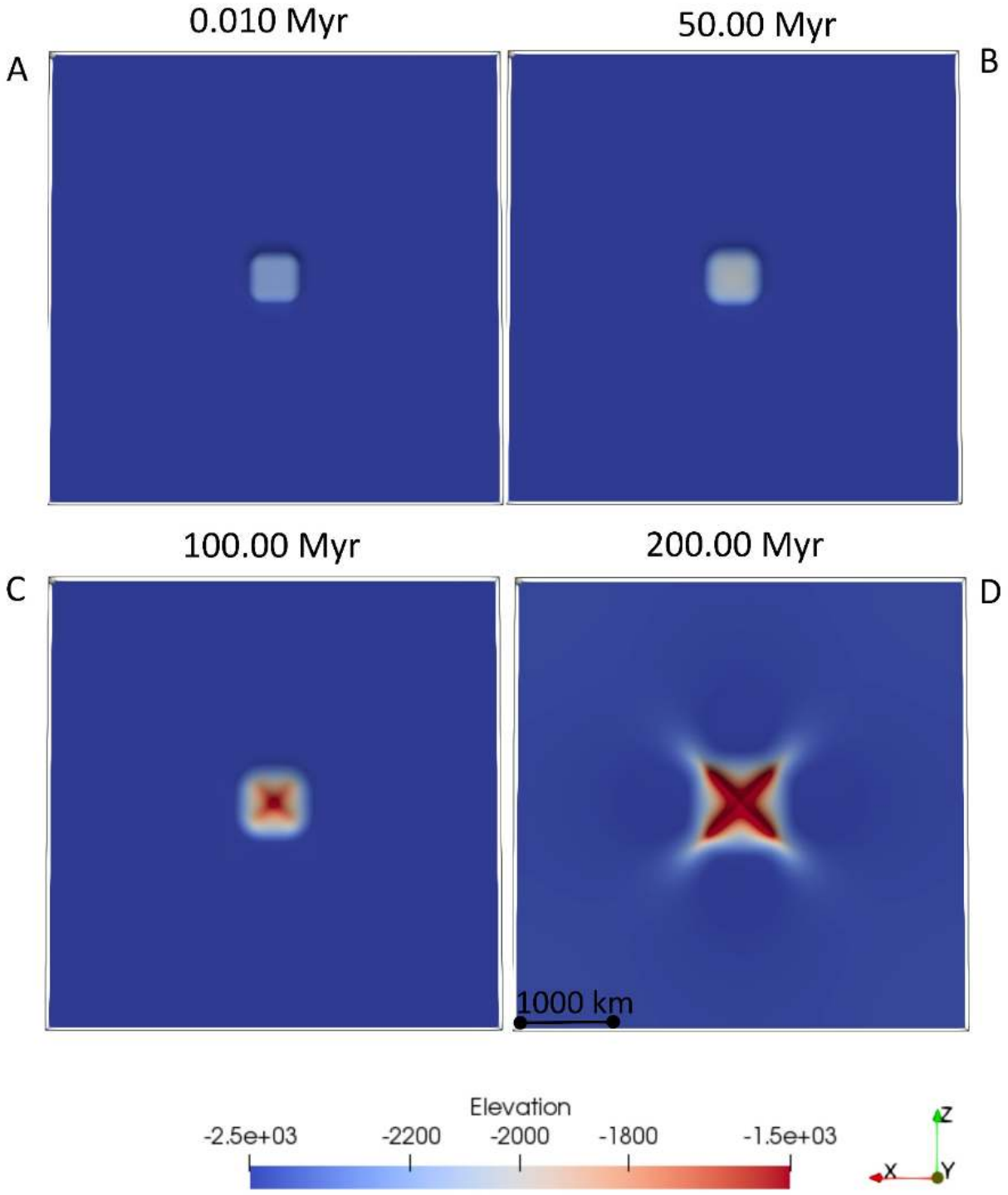

Figure 4.19 *- Model 3_Congo_weak1. Lateral variation of topography (m) at the base of the lithosphere, defined as depth of the isotherm 1573K, at 0.010Myr (**A**), 50Myr (**B**), 100 Myr (**C**), and 200Myr (**D**).*

4.3.4 Fourth model: 4_Congo_weak2

Numerical model design: As in the previous numerical simulation (*3_Congo_weak1*), I considered the existence of a weak zone in the central part of a single cratonic block, but in this case twice extended (810 km x 810 km) and having a lithospheric thickness of 80 km. The *TZ*s have the size of 202 km, and the distance between the weak zone and the craton borders is 1620 km (*4_Congo_weak2*, Fig. 4.20).

Initial Temperature Conditions: Since I assumed that the lithosphere of the weak zone is twice thinner than in the model 3_Congo_weak1, I increased the thermal gradient both in the crust and mantle lithosphere to ~17K/km, associating a temperature at the bottom of the crust and lithosphere of 873 K and 1623 K, respectively (Table 4.2). This higher thermal gradient is more consistent with the hypothesis of the stretched lithosphere produced by extensional tectonics.

Results: The results are similar to those observed in the previous simulation (3_Congo_weak1). However, the increase of the size of the weak zone and the decrease of its lithospheric thickness produces a larger depressed central zone and promotes an earlier formation of the two elongated low-viscosity zones (Fig. 4.23). These structures become very pronounced, already at 100 Myr, and at 200 Myr, the two weak orthogonal zones are greater and thinner than in the previous simulation, while the areas of high viscosity within and surrounding them become more extended (Figs. 4.21 and 4.22). As for the previous model (3_Congo_weak2), these features are also observable looking at temporal depth-viscosity variations at different time steps (Appendix C, Fig. C3). In addition, the topography variations at all the considered depths (Figs. 4.25-4.27) are very similar to those of the previous simulation. In particular, a large surface topography depression is formed, with an alternation of highs and lows characterizing the two elongated structures (Fig. 4.25). The formation of these features is the direct effect of the asthenospheric upwelling in a larger area. We can also observe a change in the shape of the thermal anomaly, with a gradual increase of its size with time (Fig. 4.24).

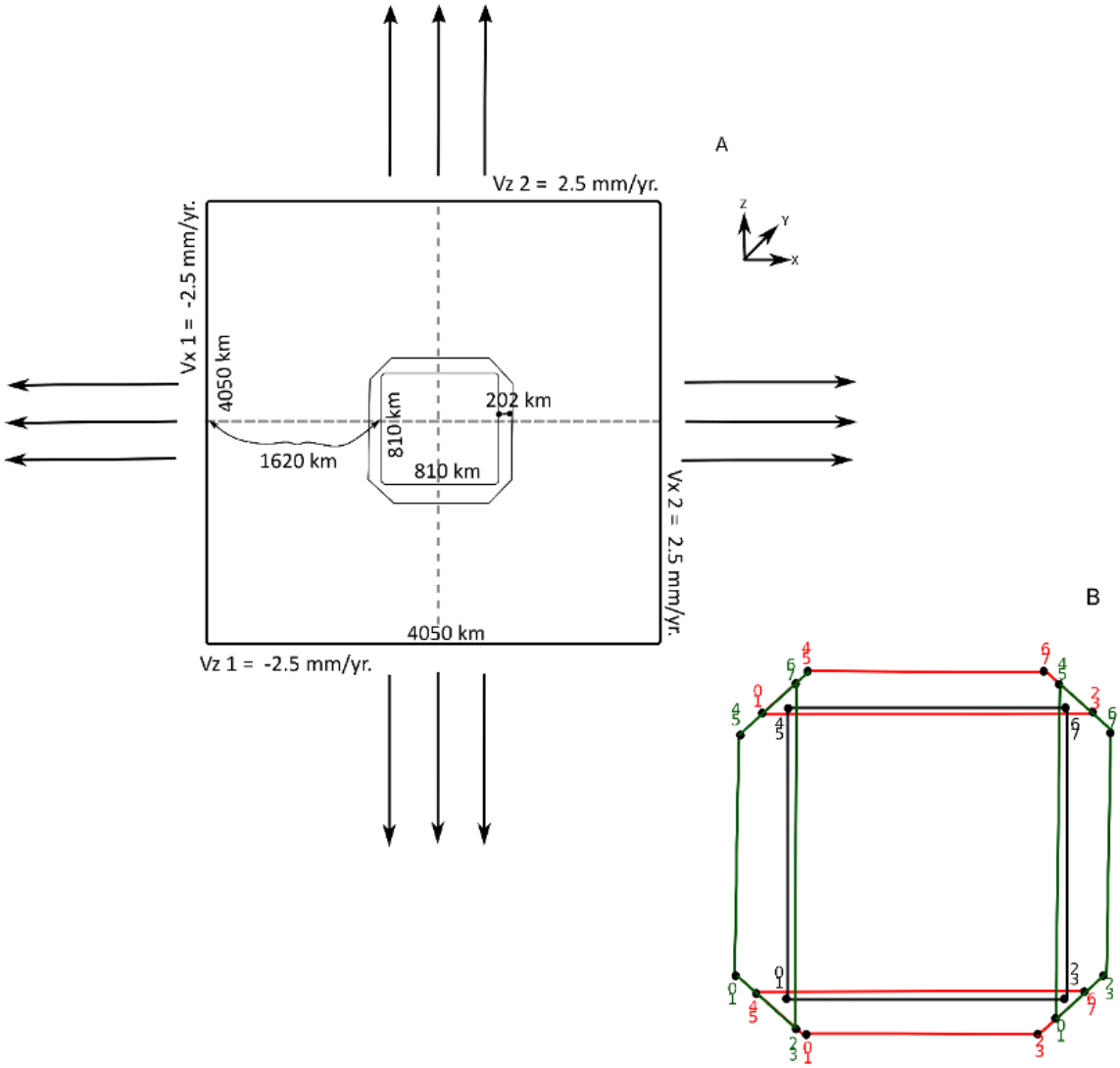

Figure 4.20 *- Geometry design of the model 4_Congo_weak2.* ***A****: Horizontal plane visualization of the model. Black arrows show velocity directions.* ***B****: Zoom in plane on the weak zone (black square), represented in staggered grid-in cell marker technique. Red and green features represent the TZs and numbers are the same as in Fig. 4.4.*

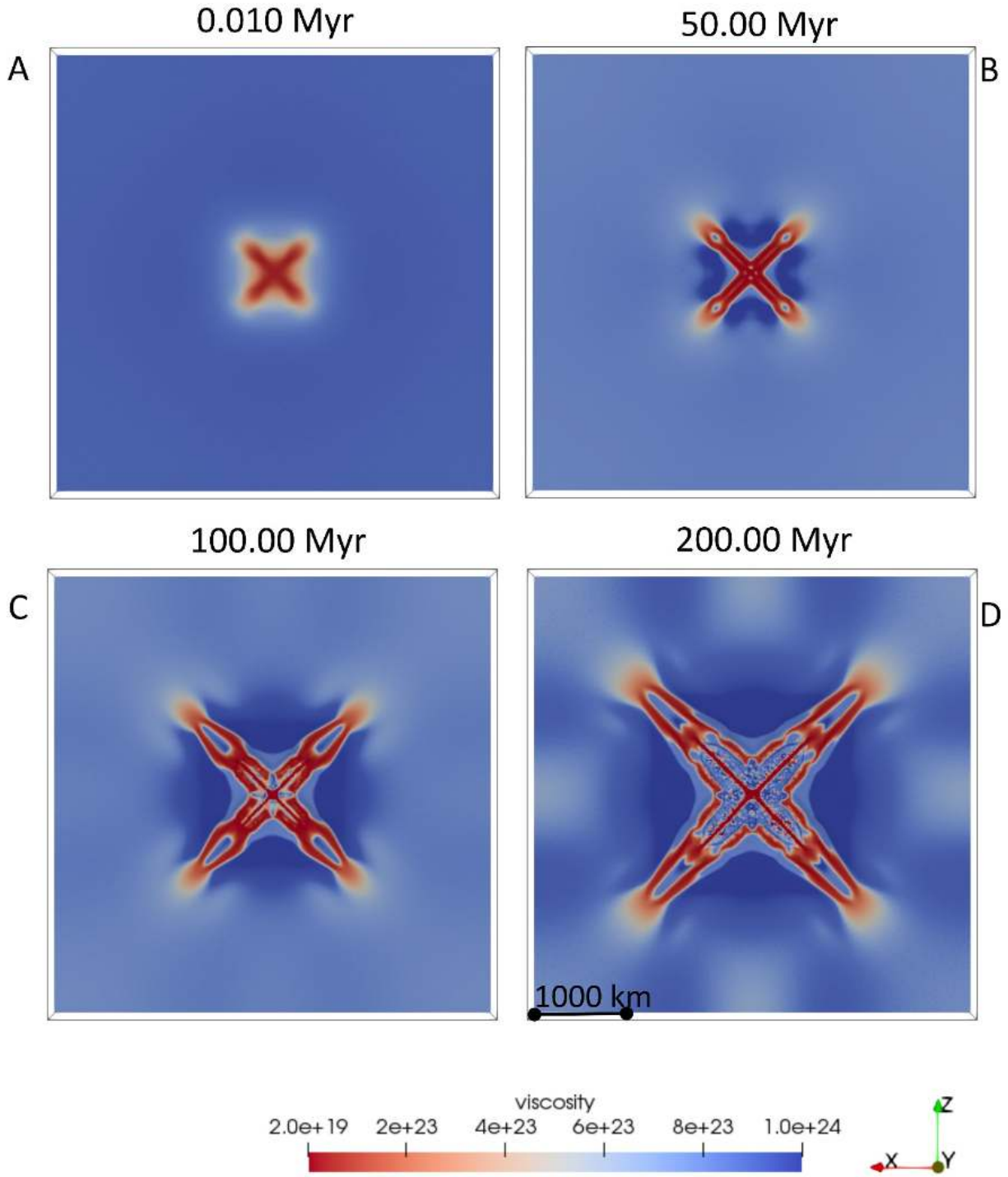

Figure 4.21 - *Model 4_Congo_weak2. Lateral variation of viscosity (Pa s) at the base of the crust, defined by the depth of the isodensity 3000 kg/m³, at 0.010Myr (**A**), 50Myr (**B**), 100 Myr (**C**), and 200Myr (**D**).*

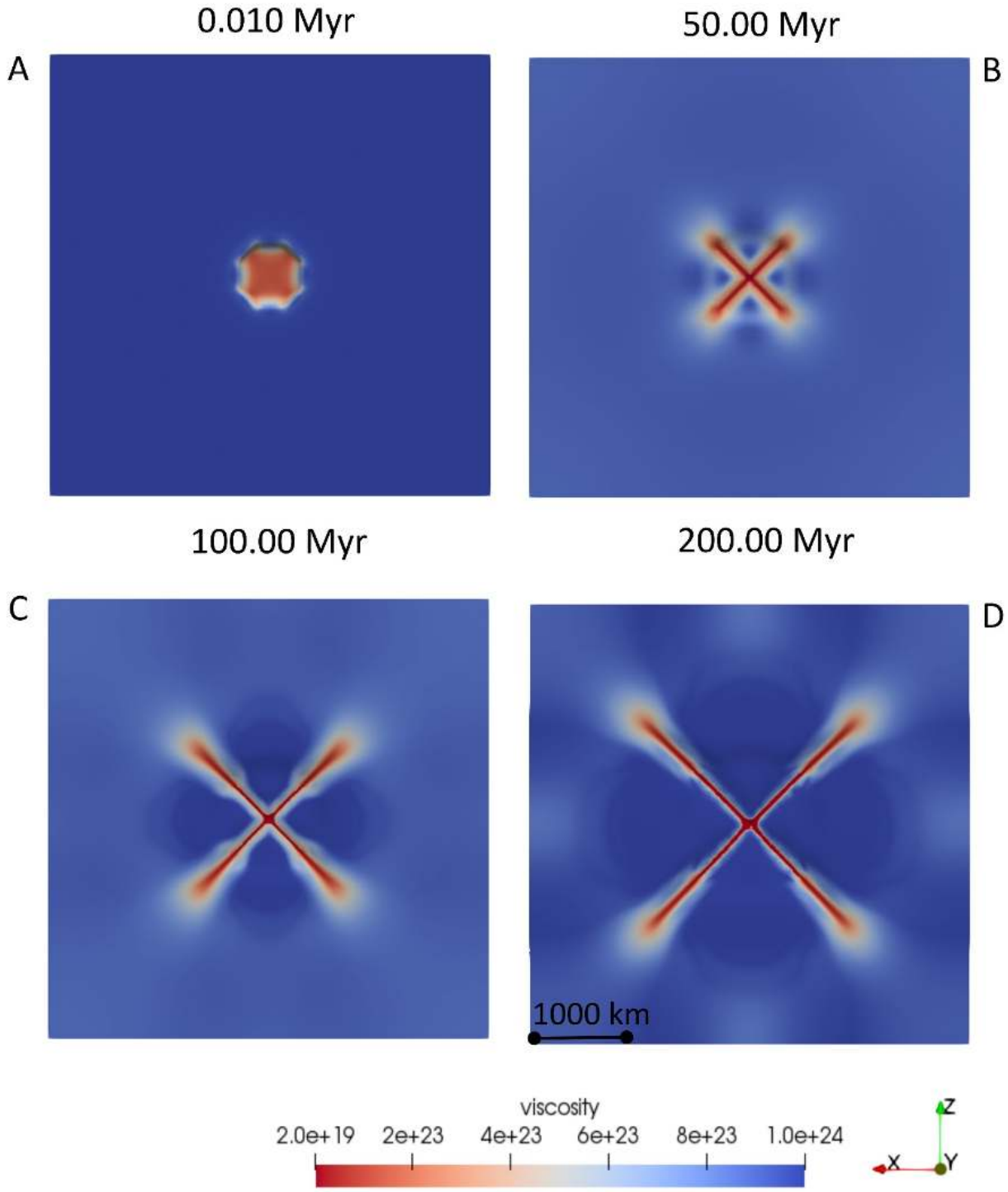

Figure 4.22 - *Model 4_Congo_weak2. Lateral variation of viscosity (Pa s) within the lithosphere, at a depth defined by the 1073 K isotherm, at 0.010Myr (**A**), 50Myr (**B**), 100 Myr (**C**), and 200Myr (**D**).*

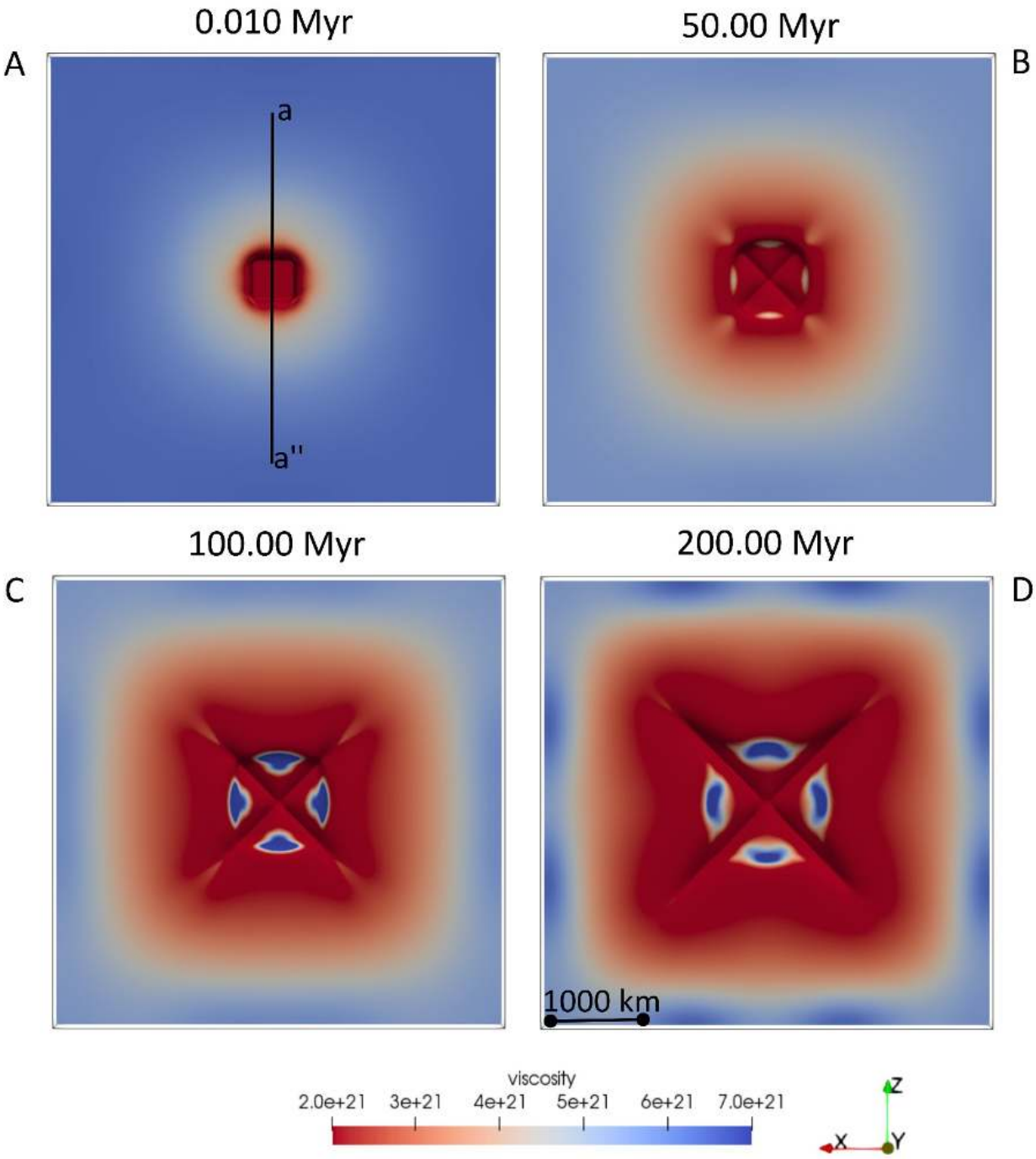

Figure 4.23 *- Model 4_Congo_weak2. Lateral variation of viscosity (Pa s) at the base of the lithosphere, defined as depth of the isotherm 1573 K, at 0.010Myr (**A**), 50Myr (**B**), 100 Myr (**C**), and 200Myr (**D**). Black line delimited by labels a-a"shows the location of the cross-setion of temperatures (Fig. 4.24), density (Fig. 4.53), and viscosity (Fig. C.3 A).*

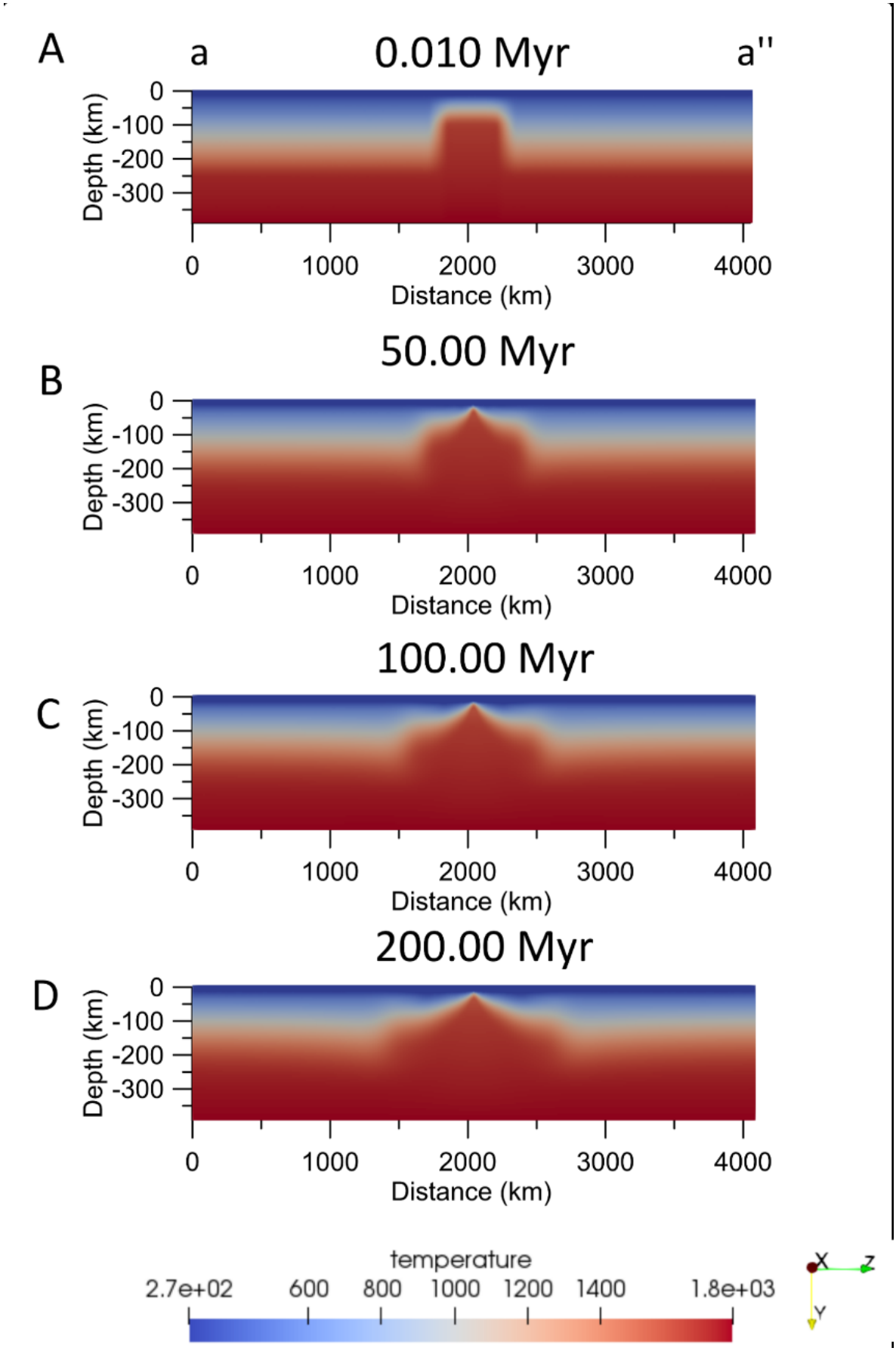

Figure 4.24 *- Model 4_Congo_weak2. Depth-temperature (K) variation, along the cross-section displayed in Fig. 4.23 A, at 0.010 Myr (**A**), 50 Myr (**B**), 100 Myr (**C**), and 200Myr (**D**). Vertical scale increased by 15% with respect to horizontal axis.*

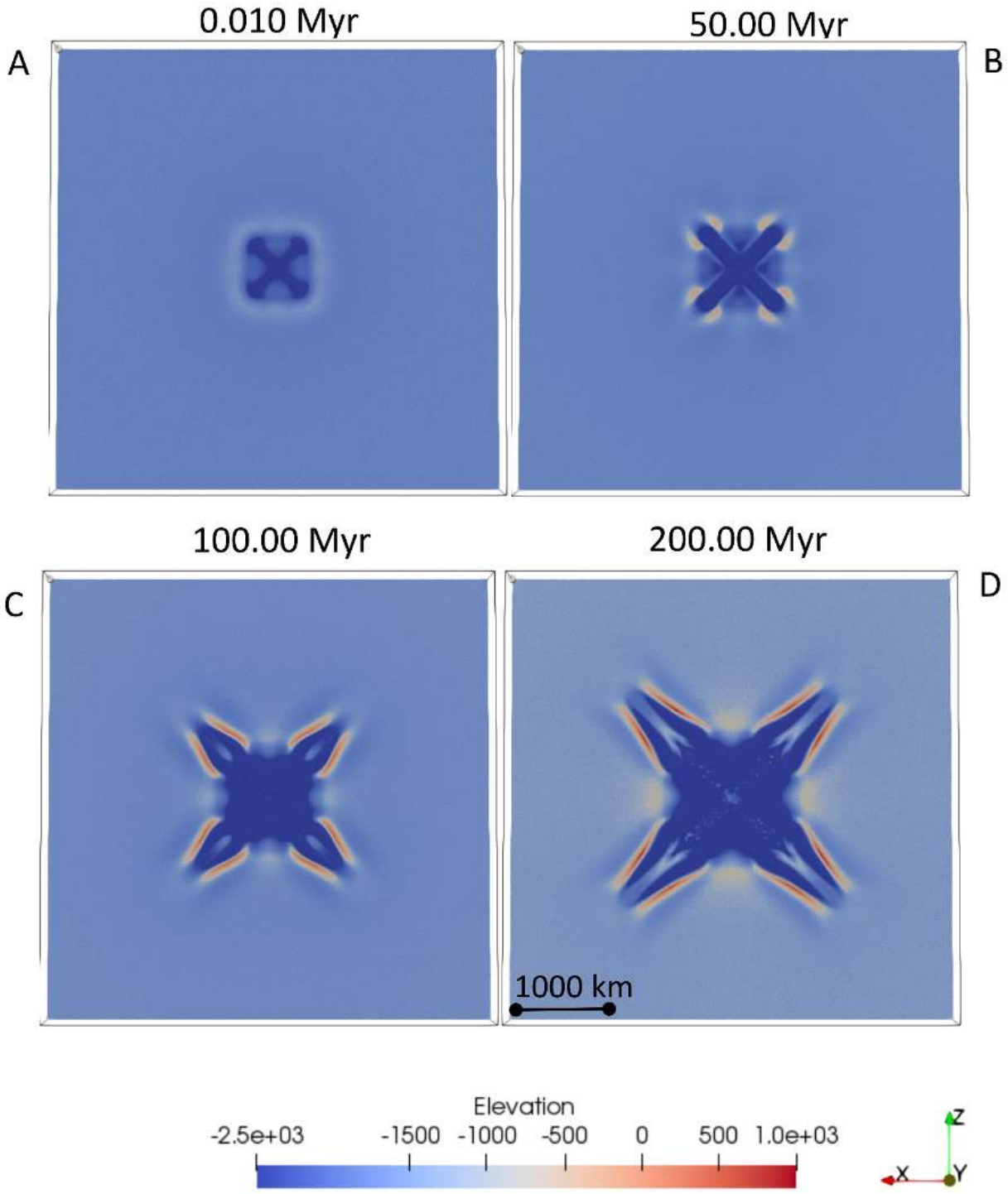

Figure 4.25 *- Model 4_Congo_weak2. Lateral variation of surface topography (m) at 0.010Myr (**A**), 50Myr (**B**), (**C**) 100 Myr, and 200Myr (**D**).*

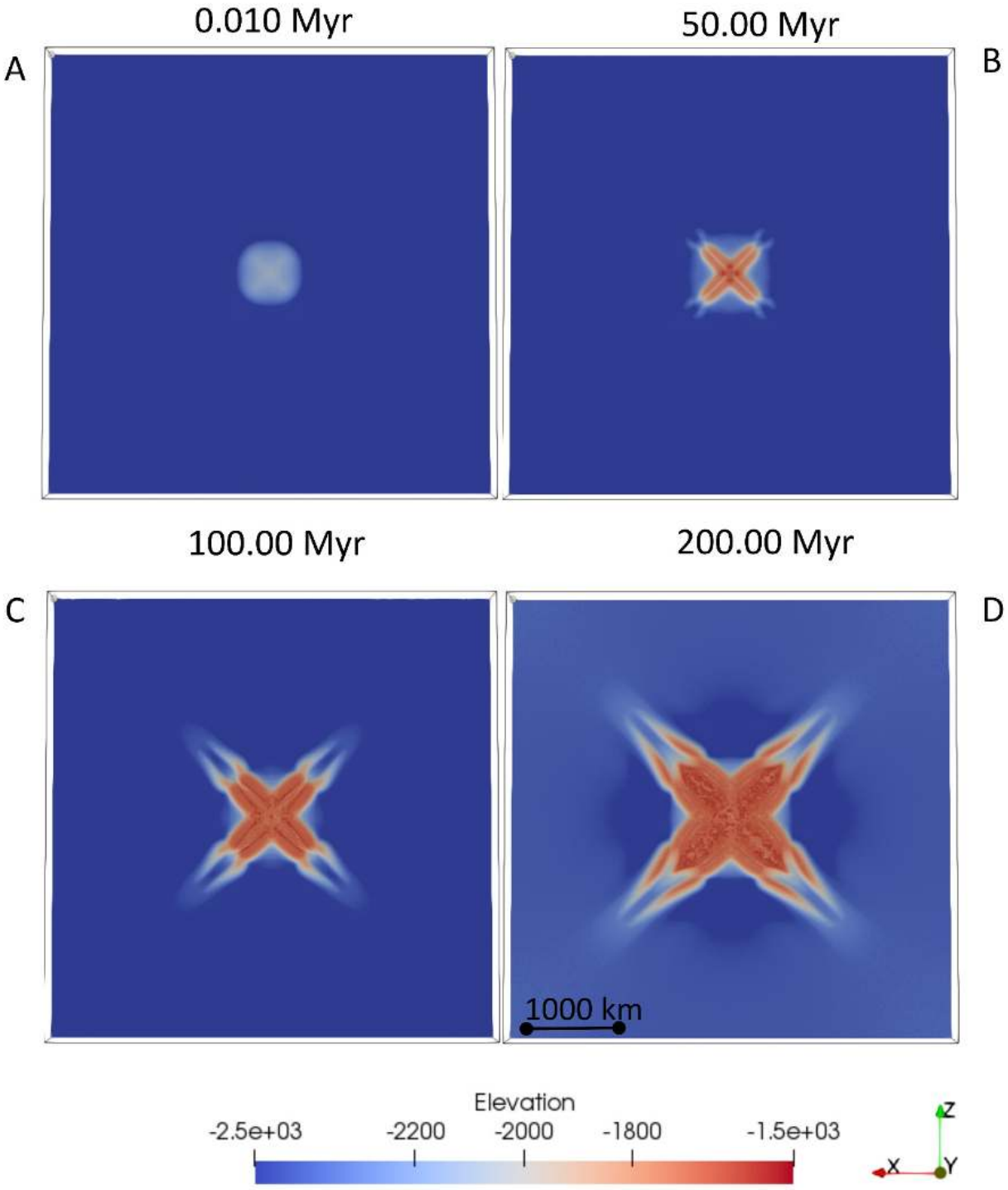

Figure 4.26- *Model 4_Congo_weak2. Lateral variation of topography (m) at the base of the crust, defined by the depth of the isodensity 3000 kg/m³, at 0.010Myr (**A**), 50Myr (**B**), 100 Myr (**C**), and 200Myr (**D**).*

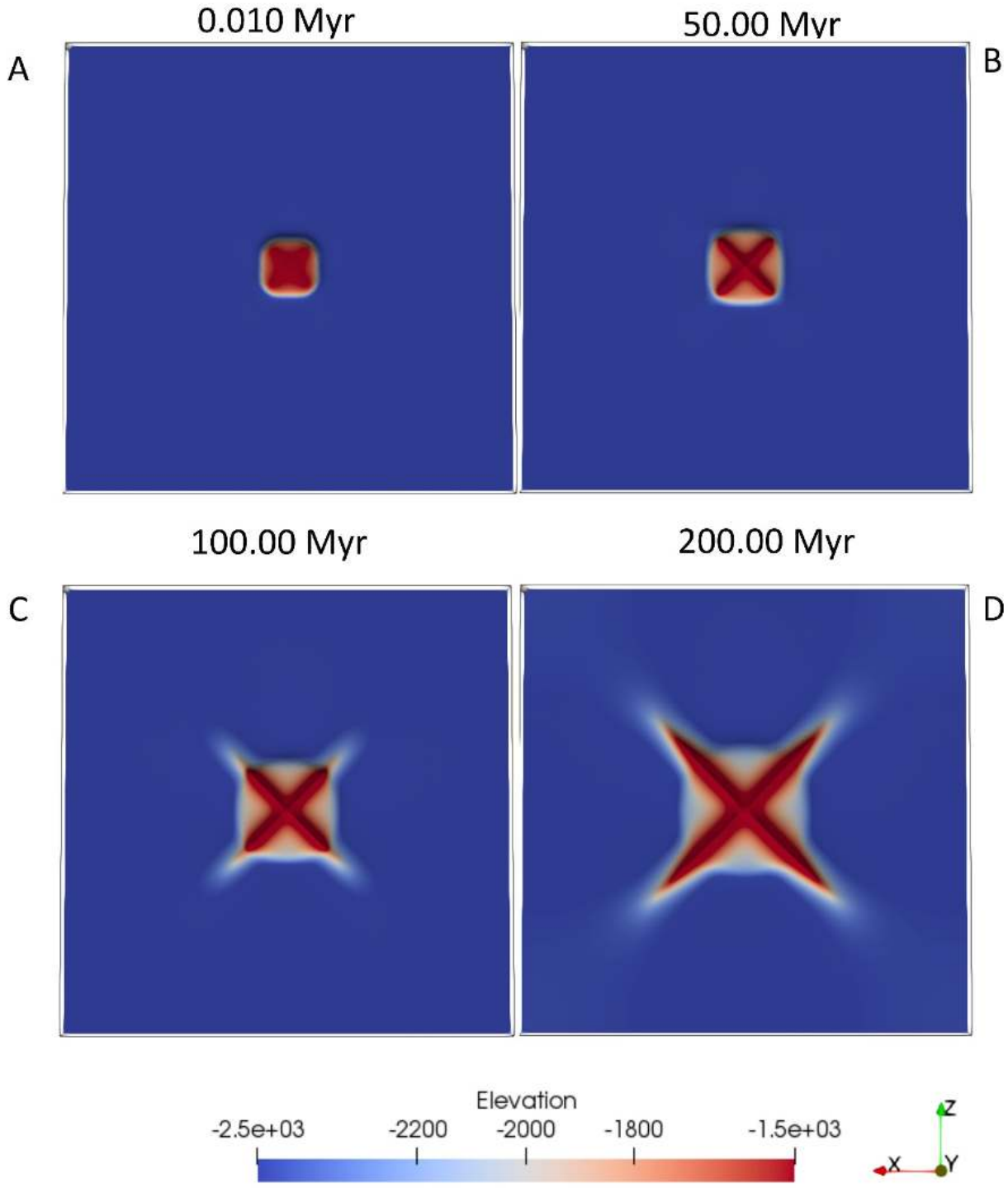

Figure 4.27- *Model 4_Congo_weak2. Lateral variation of topography (m) at the base of the lithosphere, defined as depth of the isotherm 1573 K, at 0.010Myr (**A**), 50Myr (**B**), 100 Myr (**C**), and 200Myr (**D**).*

4.3.5 Fifth model 5_Congo_weak3

Numerical model design: With this numerical simulation, I wanted to test the effect of the orientation of the central weak zone and of the *TZ*s on the deformation produced during the multi-extensional tectonics. To this aim, the simulation was performed considering the existence of a weak zone of size 810 km x 810 km, in the central part of the single cratonic block (*5_Congo_weak3*, Fig. 4.28). The vertices are rotated by 45° respect to the weak zones designed in the two previous models (3_Congo_weak1 and 4_Congo_weak2) and the *TZ* between the cratonic and off-cratonic lithosphere is removed. The thickness of the lithosphere in the weak zone is 80 km, and the distance between the weak zone and the cratonic borders is 1620 km.

Initial Temperature Conditions: The thermal gradients are the same as those of the previous simulation (4_Congo_weak2), and the same crustal and lithospheric thickness assumed.

Results: The temporal lateral variations of viscosity and topography are very similar to those of the previous simulations (section 4.3.3). In particular, the two elongated structures are already well defined at 50 Myr, as in model 4_Congo_weak2, just rotated by 45° (Fig. 4.29). On account of the similarity of the results with those of the previous two simulations, I stopped the run at 50 Myr. The effect of the absence of the *TZ* is negligible on the lateral viscosity and topography variations (Figs. 4.29-4.32), while it produces a sharp change in the thermal and viscosity anomaly (Appendix C, Fig. C4), which assumes a tabular shape and remains localized in the central part of the area. This is due to the sharper temperature variations at the edges of the weak zones (Fig. 4.32). Therefore, the presence of the *TZ*s produces a deformation distributed on a larger area, increasing the consistency between the modeling results and the basement structure of the *CB* (Figs. 4.33-4.35).

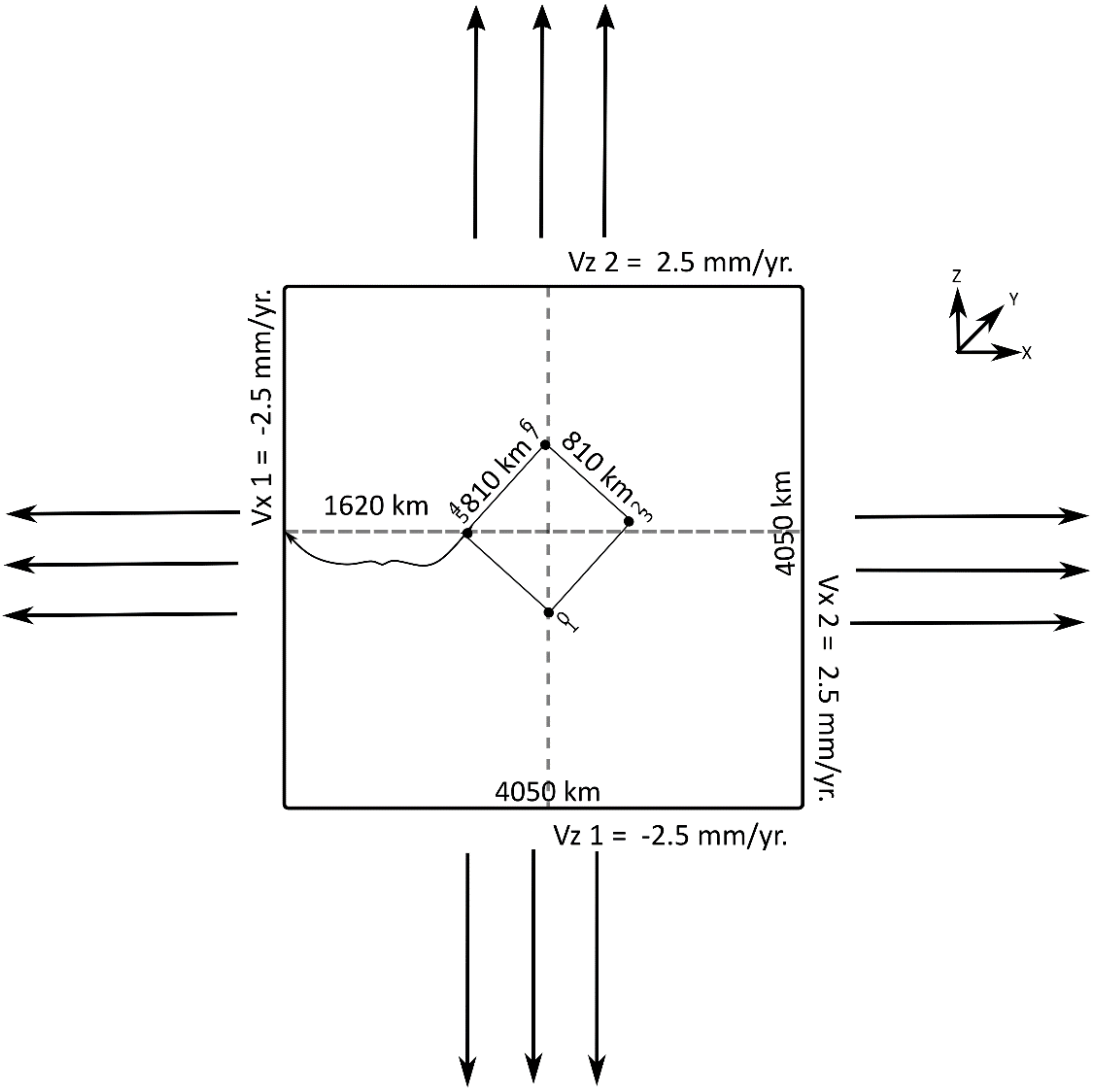

Figure 4.28 *- Geometry design of the model 5_Congo_weak3. Horizontal plane visualization of the model, with the weak zone (small black square) in the central part of the Congo Craton rotated of 45°. Black arrows show velocity directions. Black points and numbers are as in Fig. 4.4.*

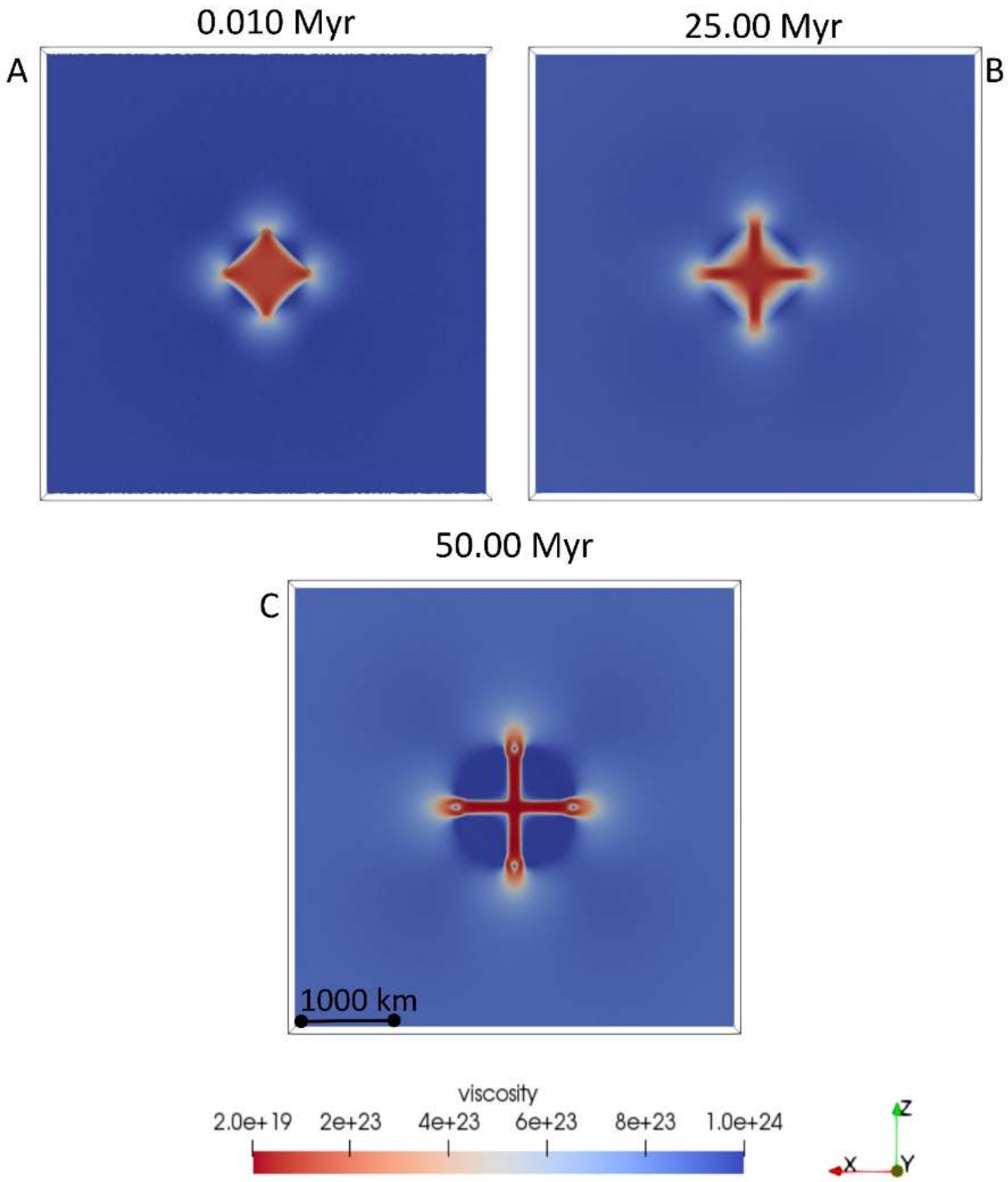

Figure 4.29 - *Model 5_Congo_weak3. Lateral variation of viscosity (Pa s) at the base of the crust, defined by the depth of the isodensity 3000 kg/m³, at 0.010Myr (**A**), 50Myr (**B**), 100 Myr (**C**), and 200Myr (**D**).*

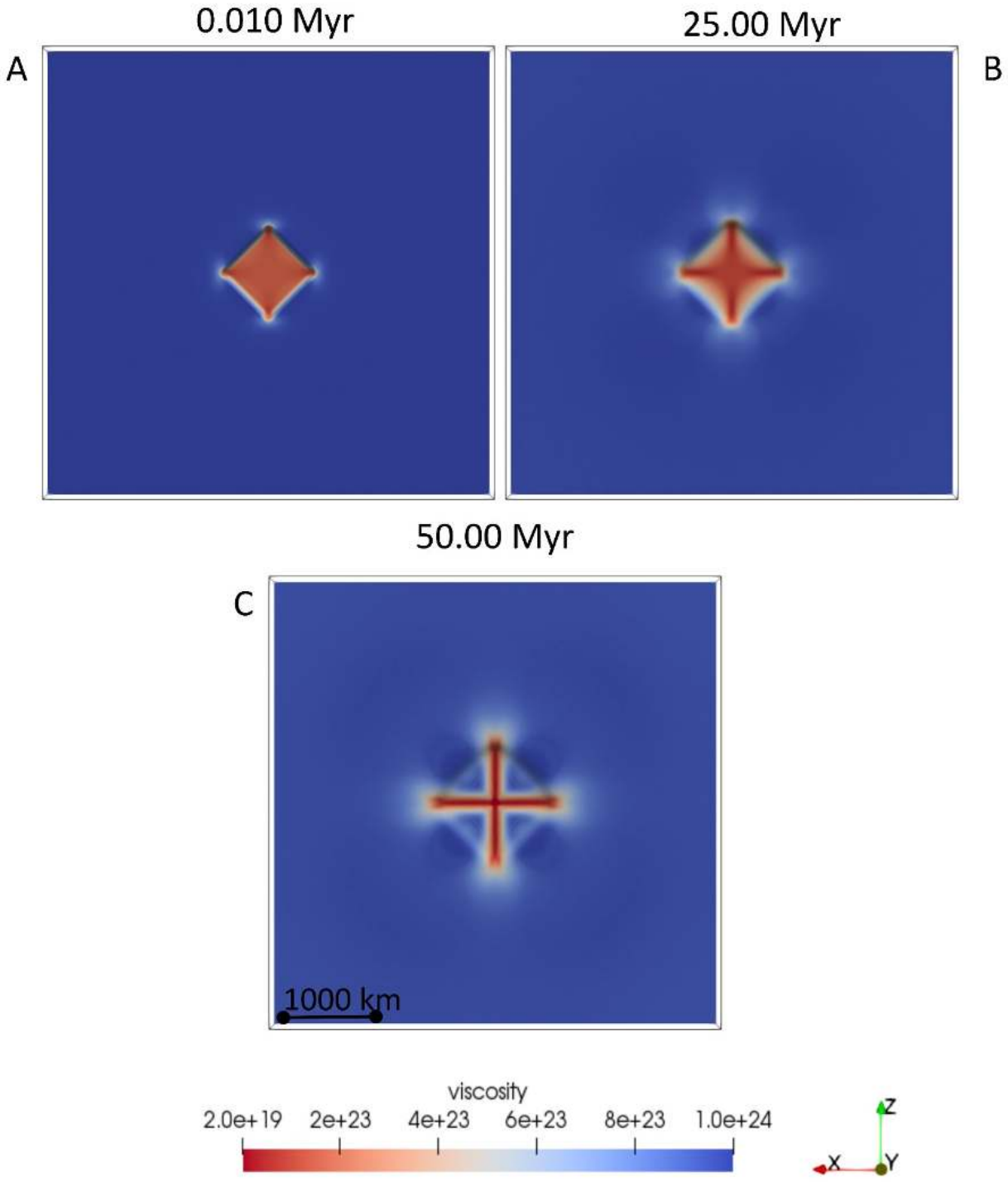

Figure 4.30- *Model 5_Congo_weak3. Lateral variation of viscosity (Pa s) within the lithosphere, at a depth defined by the isotherm 1073K, at 0.010Myr (**A**), 25Myr (**B**), 50 Myr (**C**).*

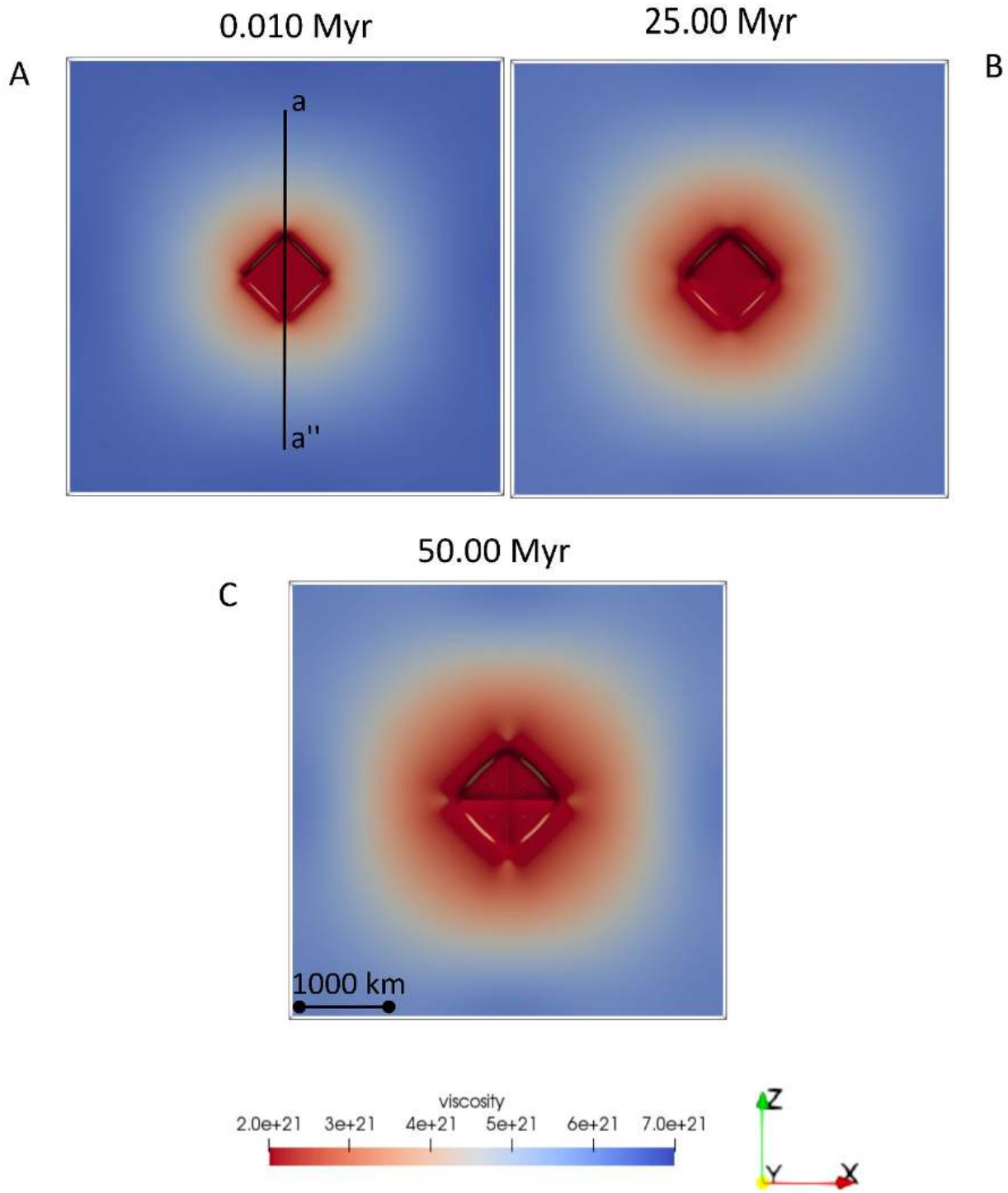

Figure 4.31 *- Model 5_Congo_weak3. Lateral variation of viscosity (Pa s) at the base of the lithosphere, defined as depth of the isotherm 1573 K, at 0.010Myr (**A**), 25Myr (**B**), and 50Myr (**C**). Black line delimited by labels a-a"shows the location of the cross-setion of temperatures (Fig. 4.32), density (Figs. 4.52-4.53), and viscosity (Fig. C4 A).*

.

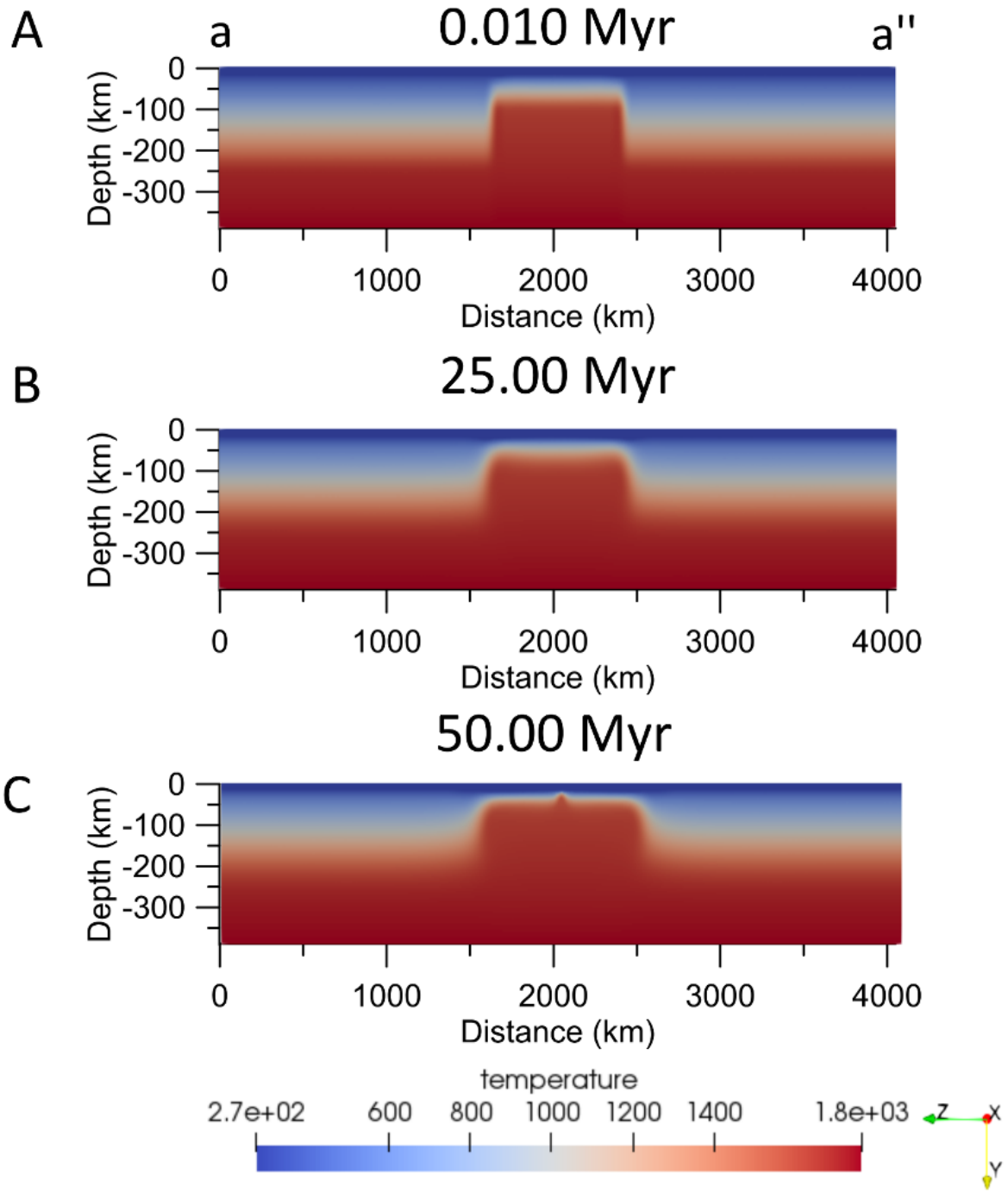

Figure 4.32 *- Model 5_Congo_weak3. Depth-temperature (K) variation, along the cross-section displayed in Fig. 4.31 A at 0.010 Myr (**A**), 25Myr (**B**), and 50Myr (**C**). Vertical scale increased by 15% with respect to horizontal axis.*

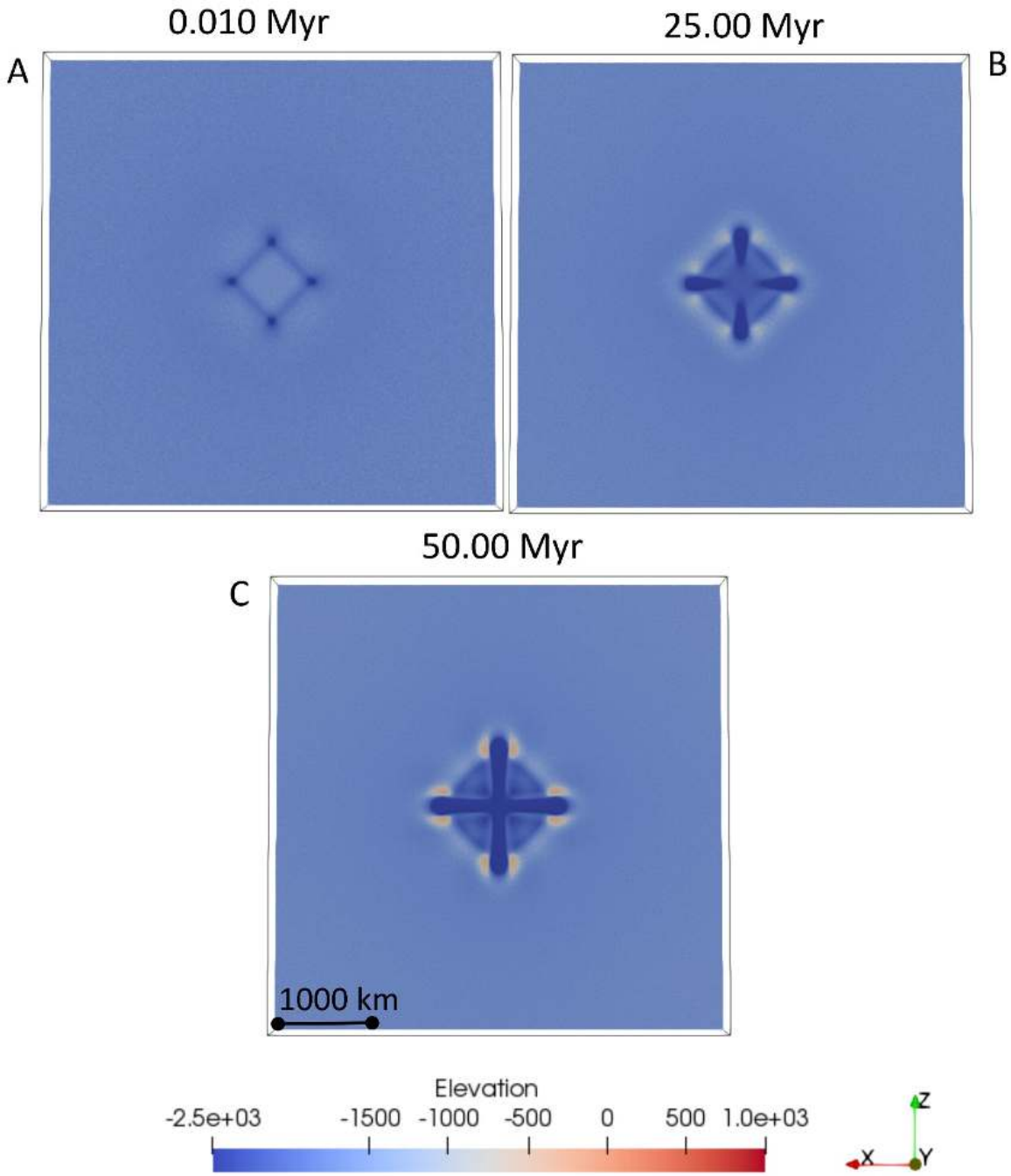

Figure 4.33 *- Model 5_Congo_weak3. Lateral variation of surface topography (m) at 0.010Myr (**A**), 25Myr (**B**), and 50Myr (**C**).*

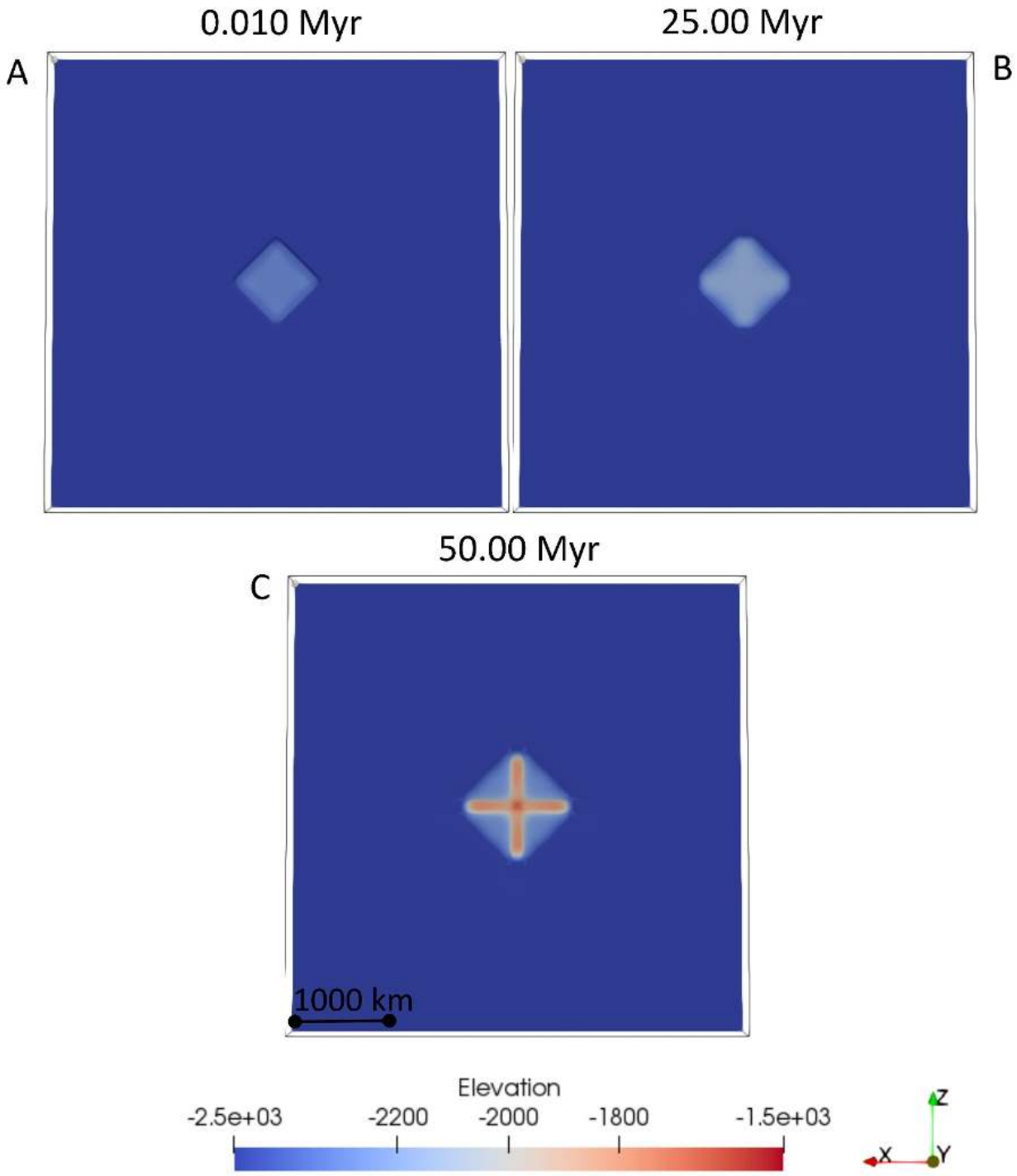

Figure 4.34- *Model 5_Congo_weak3. Lateral variation of topography (m) at the base of the crust, defined by the depth of the isodensity 3000 kg/m³, at 0.010Myr (**A**), 25Myr (**B**), 50 Myr (**C**).*

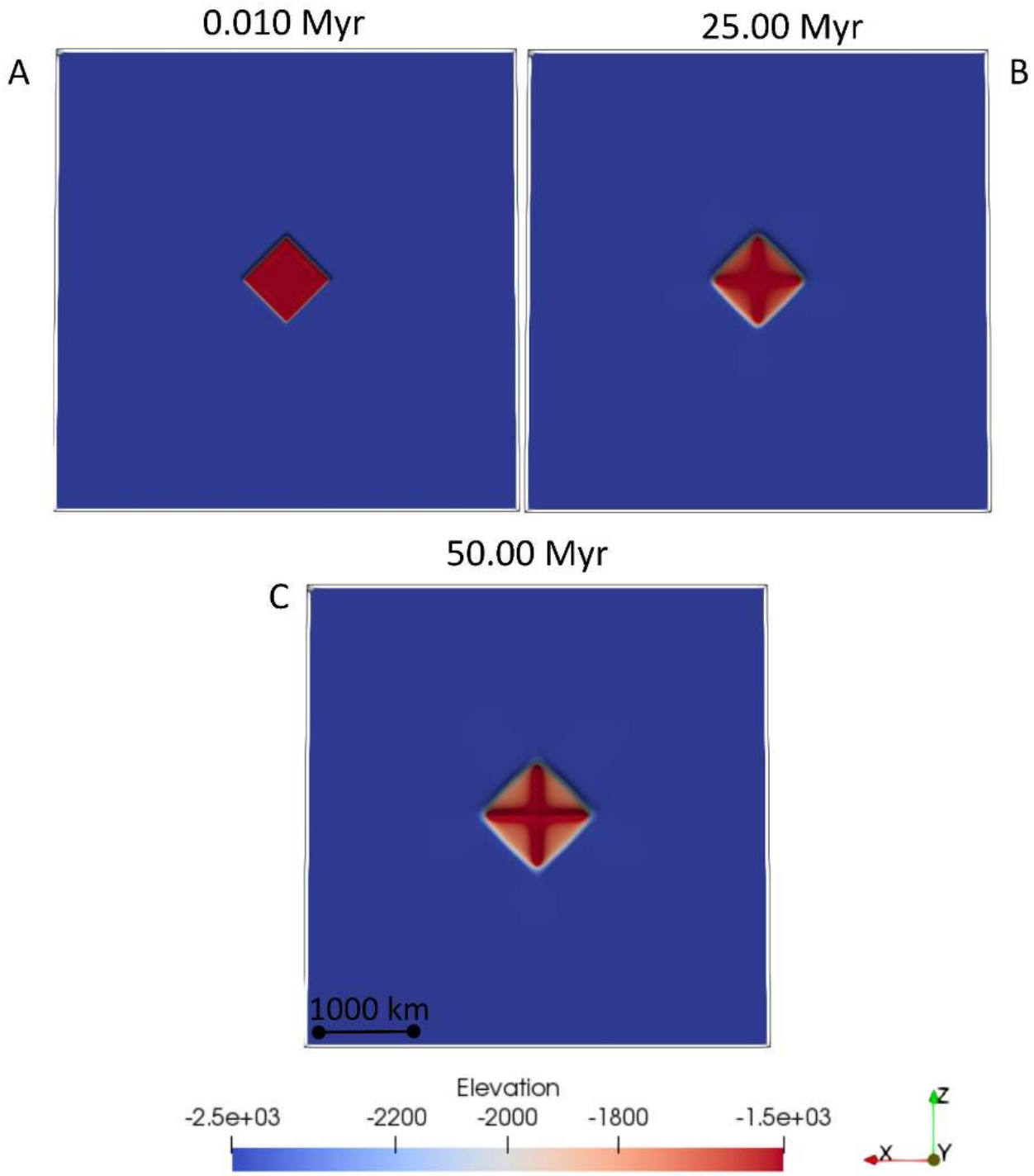

Figure 4.35- *Model 5_Congo_weak3. Lateral variation of topography (m) at the base of the lithosphere, defined as depth of the isotherm 1573 K, at 0.010Myr (**A**), 25Myr (**B**), 50 Myr (**C**).*

4.3.6 Sixth model 6_Congo_weak4

Numerical model design: In this model simulation (*6_Congo_weak4*, Fig. 4.36), I considered the existence of a weak zone in the central part of a single cratonic block, having a size equal to 3_Congo_weak1, but with a lithospheric thickness of 80 km. Differently from the previous simulations, the *TZs* have a lithosphere thinner (205 km) than that of the cratonic areas (Fig. 4.36).

Initial Temperature Conditions: The thermal gradients in the weak zone are the same as those of the two previous simulations (4_Congo_weak2 and 5_Congo_weak2), according to the same crustal and lithospheric thickness assumed.

Results: The structures formed (Figs. 4.37-4.43, Appendix C, and Fig. C5 A-B) are very similar to those observed in the simulation 4_Congo_weak2, but delayed of about 50 Myr, according to the smaller size of the weak zone. Therefore, the thermal geotherm, equal to that of the simulation 4_Congo_weak2, determines the shape of the structures, while the size of the weak zone controls the size and speed of the deformation. The thinning of the lithosphere of the *TZs* does not have any influence on the structures formed.

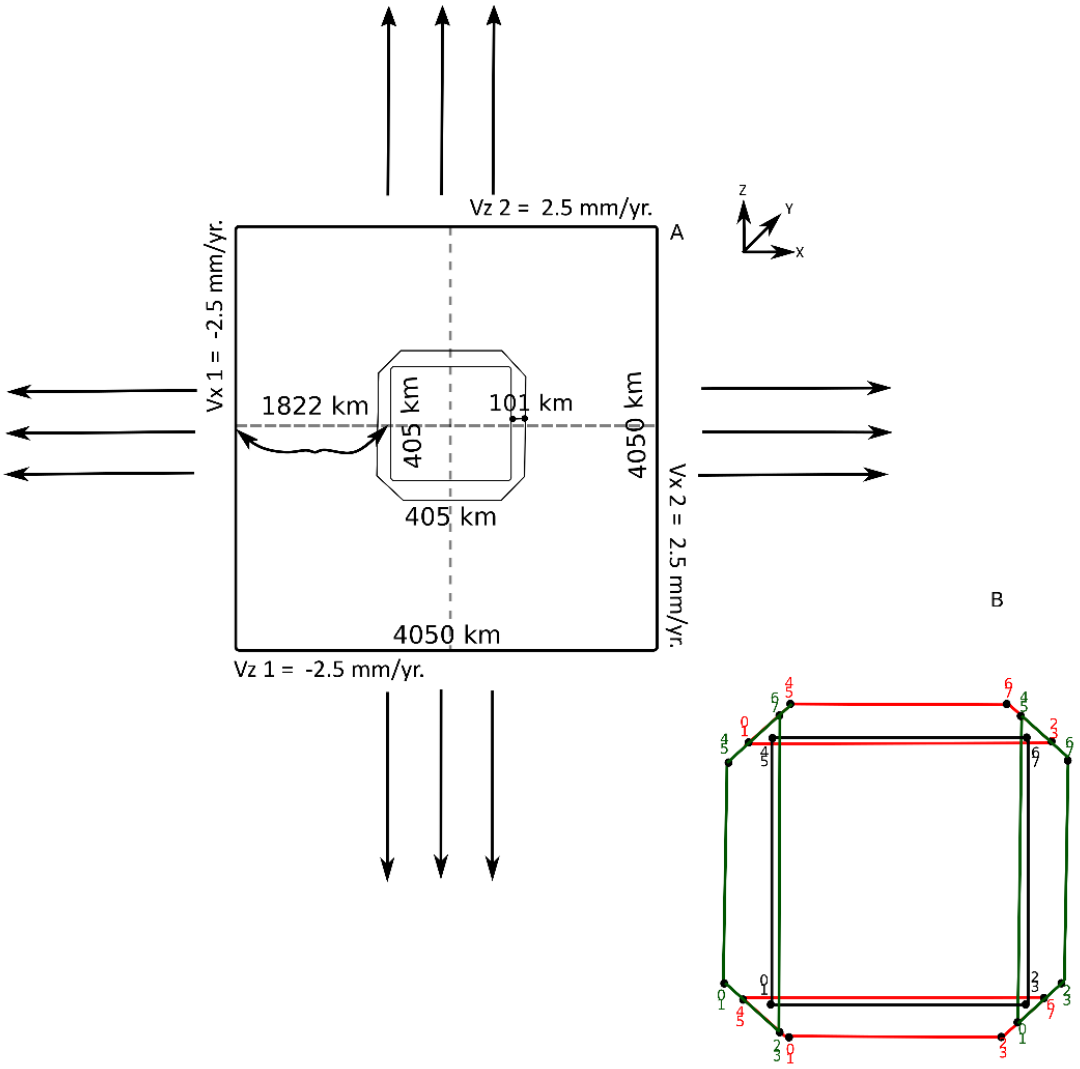

Figure 4.36 - *Geometry design of the model 6_Congo_weak4.* ***A****: Horizontal plane visualization of the model. Black arrows show velocity directions.* ***B****: Zoom in plane on the weak zone (black square), represented in staggered grid-mark-in cell technique. Red and green features represent the TZs and numbers are as in Fig. 4.4.*

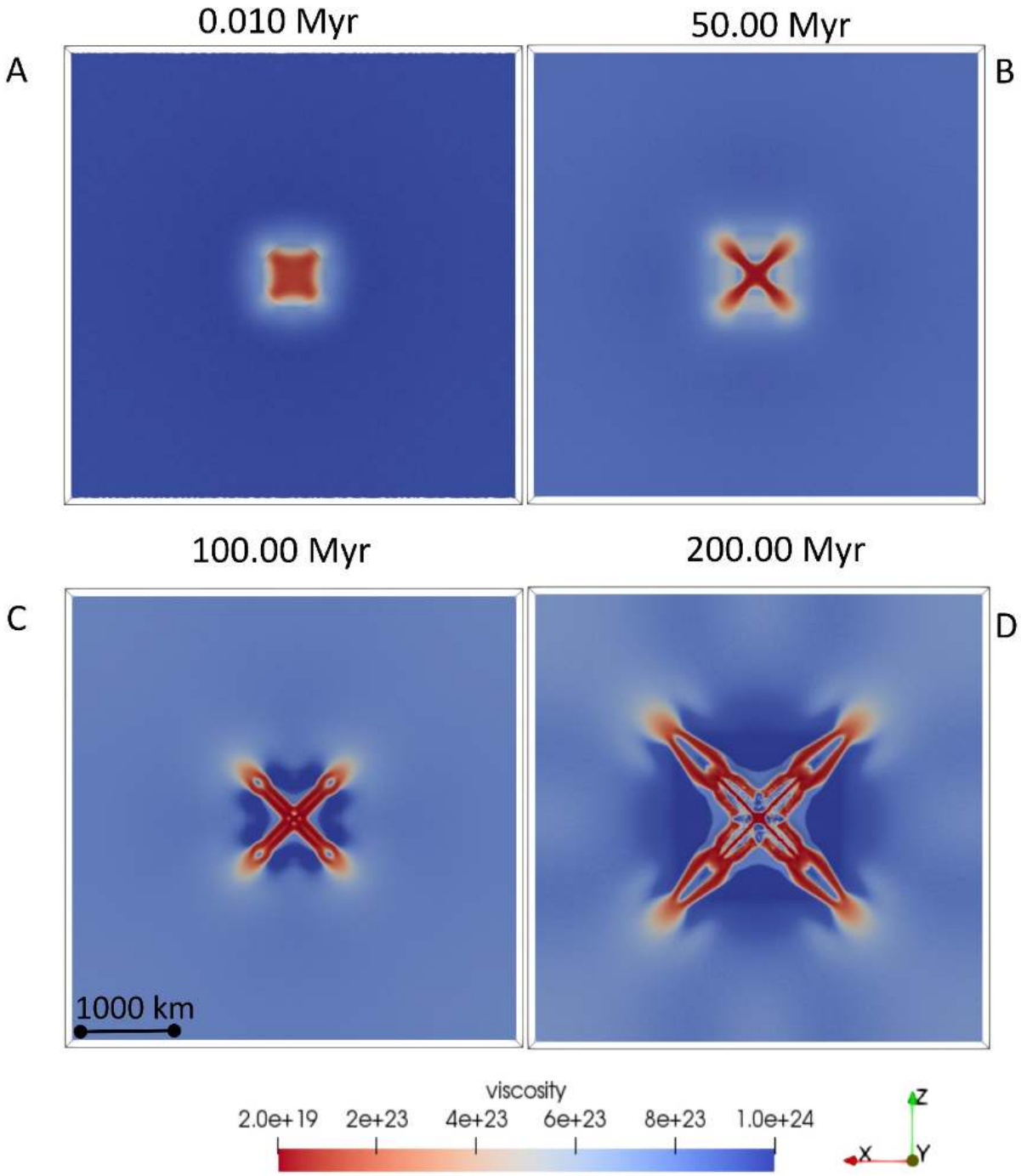

Figure 4.37 - *Model 6_Congo_weak4. Lateral variation of viscosity (Pa s) at the base of the crust, defined by the depth of the isodensity 3000 kg/m³, at 0.010Myr (**A**), 50Myr (**B**), 100 Myr (**C**) and 200Myr (**D**).*

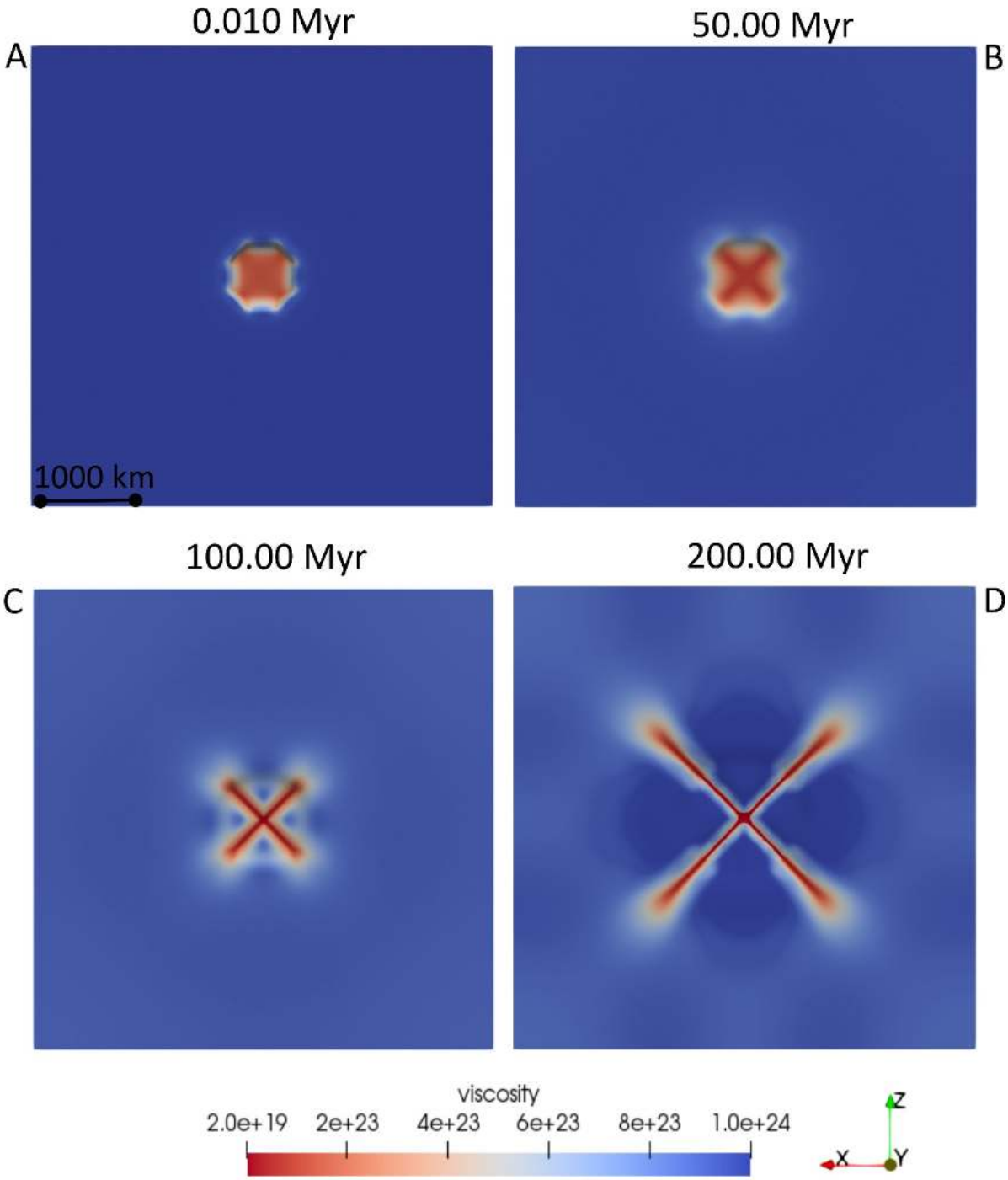

Figure 4.38 - *Model 6_Congo_weak4. Lateral variation of viscosity (Pa s) within the lithosphere, at a depth defined by the 1073 K isotherm, at 0.010Myr (**A**), 50Myr (**B**), 100 Myr (**C**) and 200Myr (**D**).*

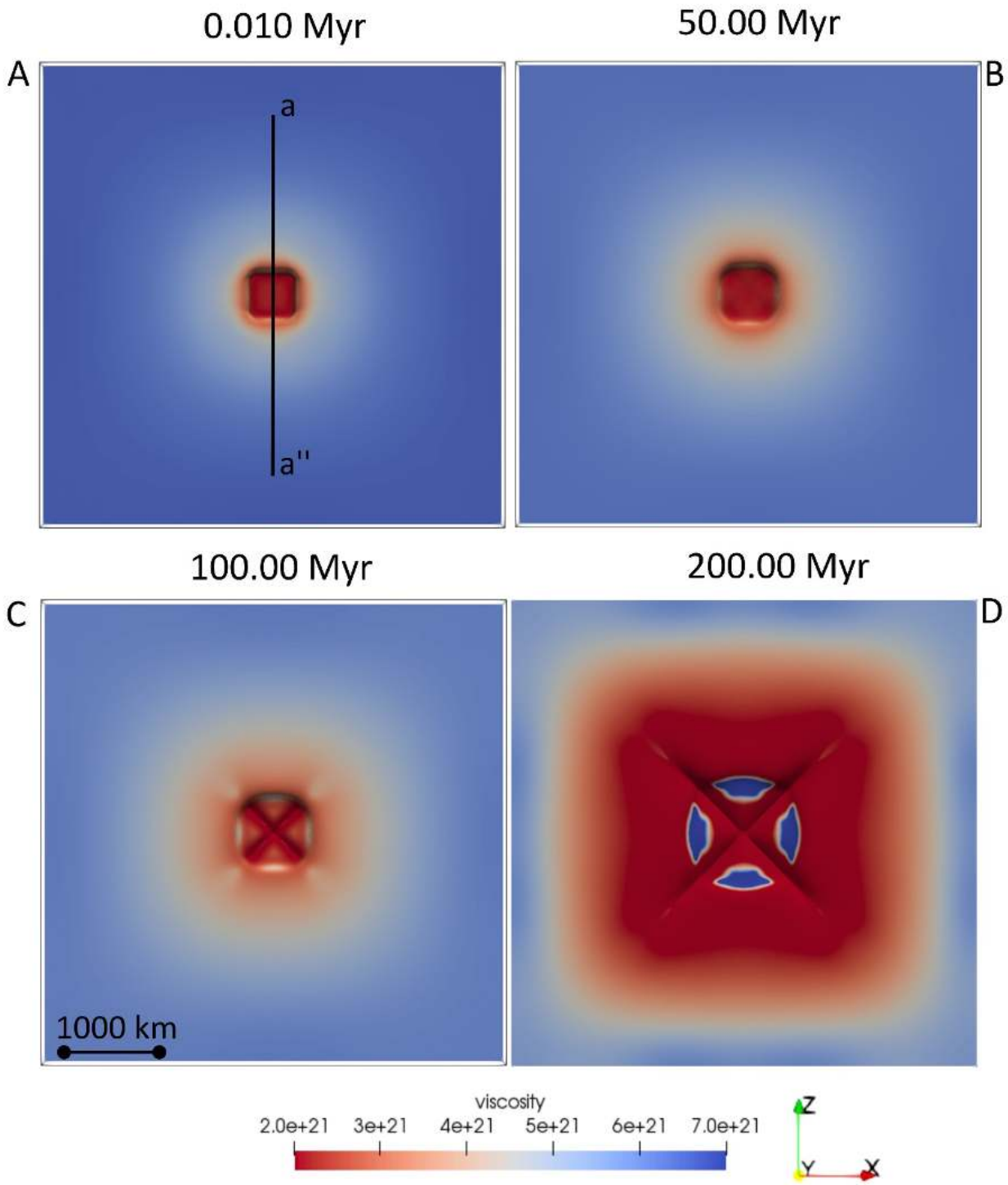

Figure 4.39 - *Model 6_Congo_weak4. Lateral variation of viscosity (Pa s) at the base of the lithosphere, defined as depth of the isotherm 1573 K, at 0.010Myr (**A**), 50Myr (**B**), 100 Myr (**C**) and 200Myr (**D**). Black line delimited by labels a-a"shows the location of the cross-setion of temperatures (Fig. 4.40), density (Figs. 4.52-4.53), and viscosity (Fig. C5 A).*

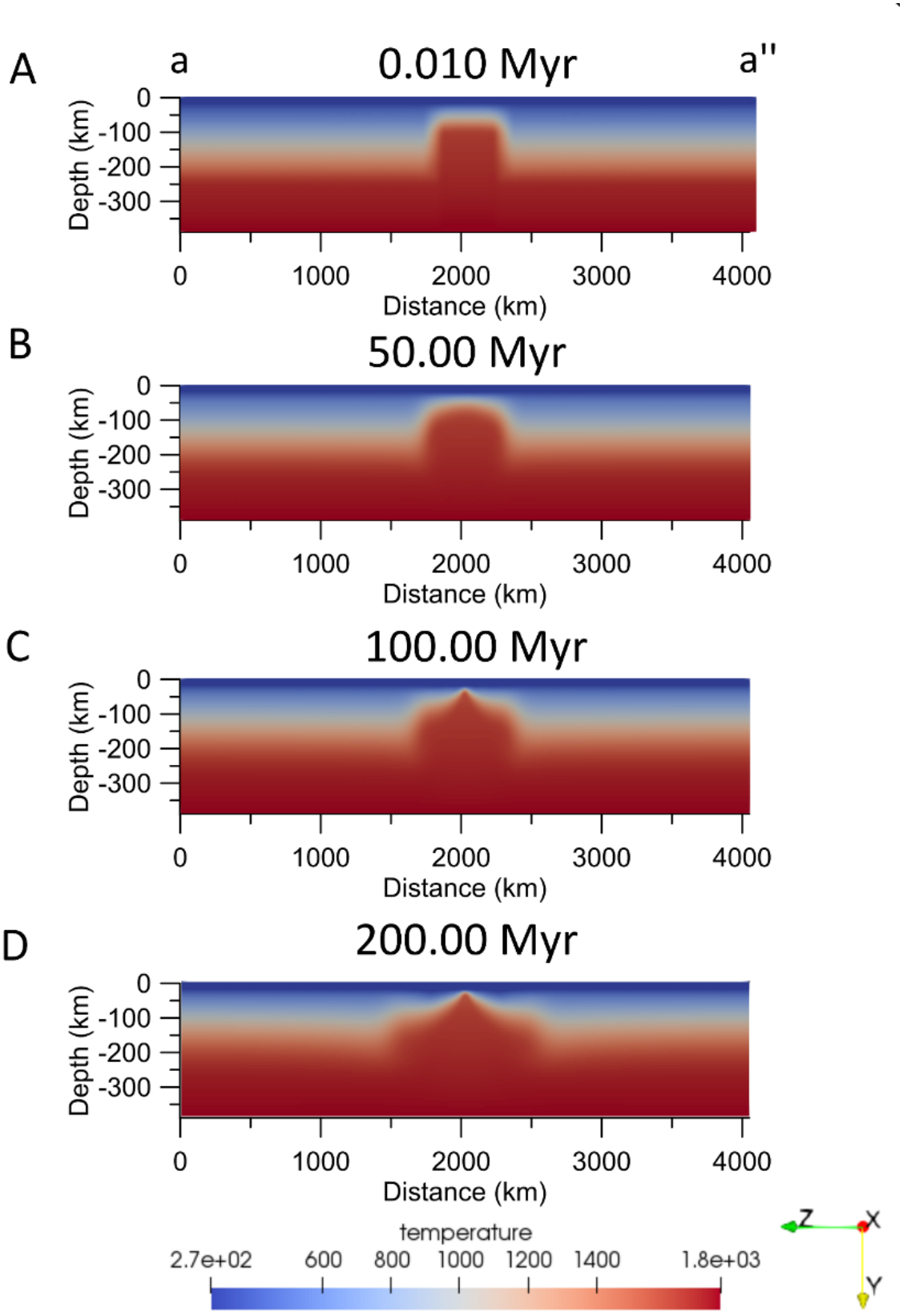

Figure 4.40 - *Model 6_Congo_weak4. Depth-temperature (K) variation, along the cross-section displayed in Fig. 4.39 A, at 0.010Myr (**A**), 50Myr (**B**), 100 Myr (**C**), 200 Myr (**D**). Vertical scale increased by 15% with respect to horizontal axis.*

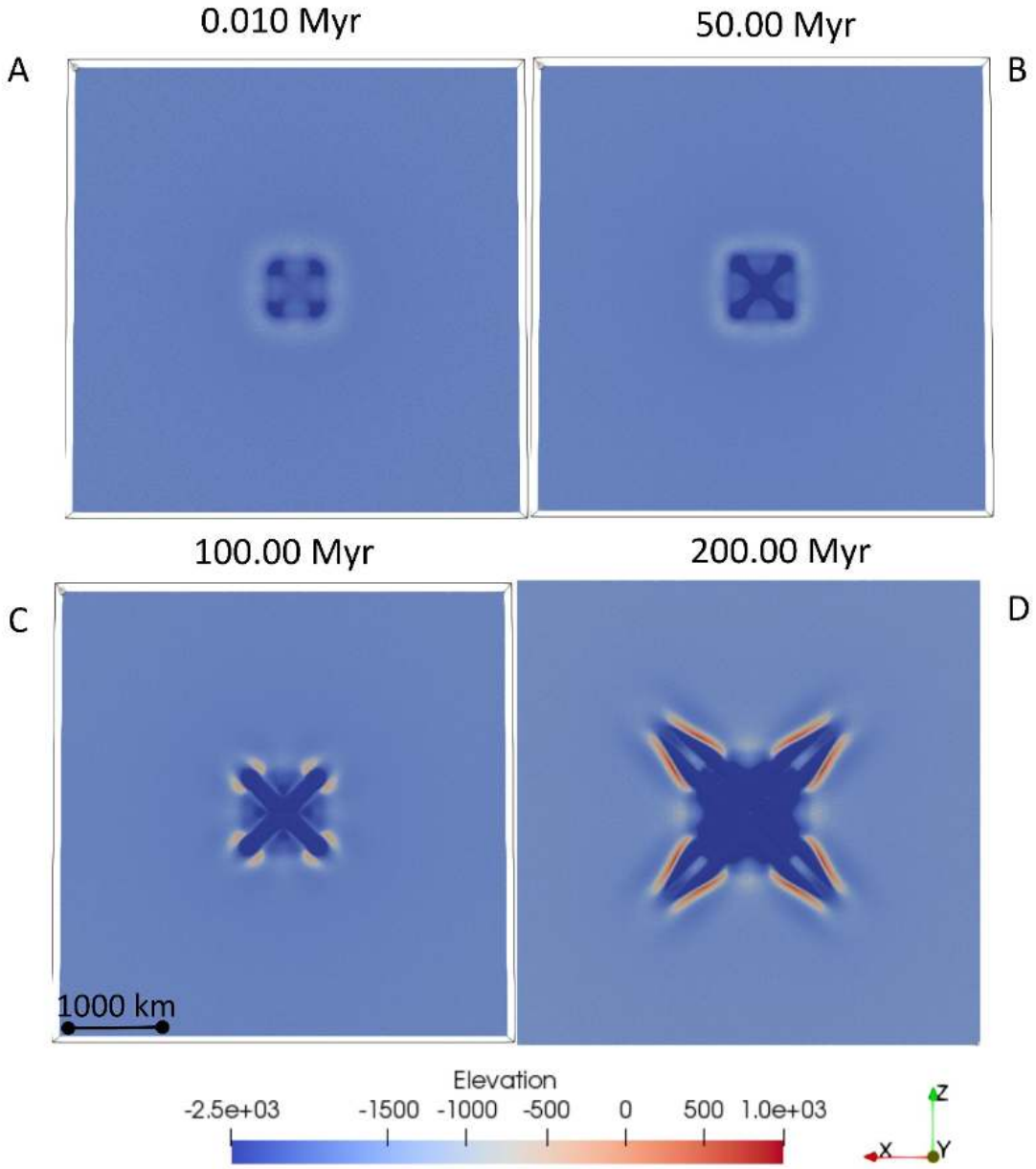

Figure 4.41 - *Model 6_Congo_weak4. Lateral variation of surface topography (m), at 0.010Myr (**A**), 50Myr (**B**), 100 Myr (**C**) and 200Myr (**D**).*

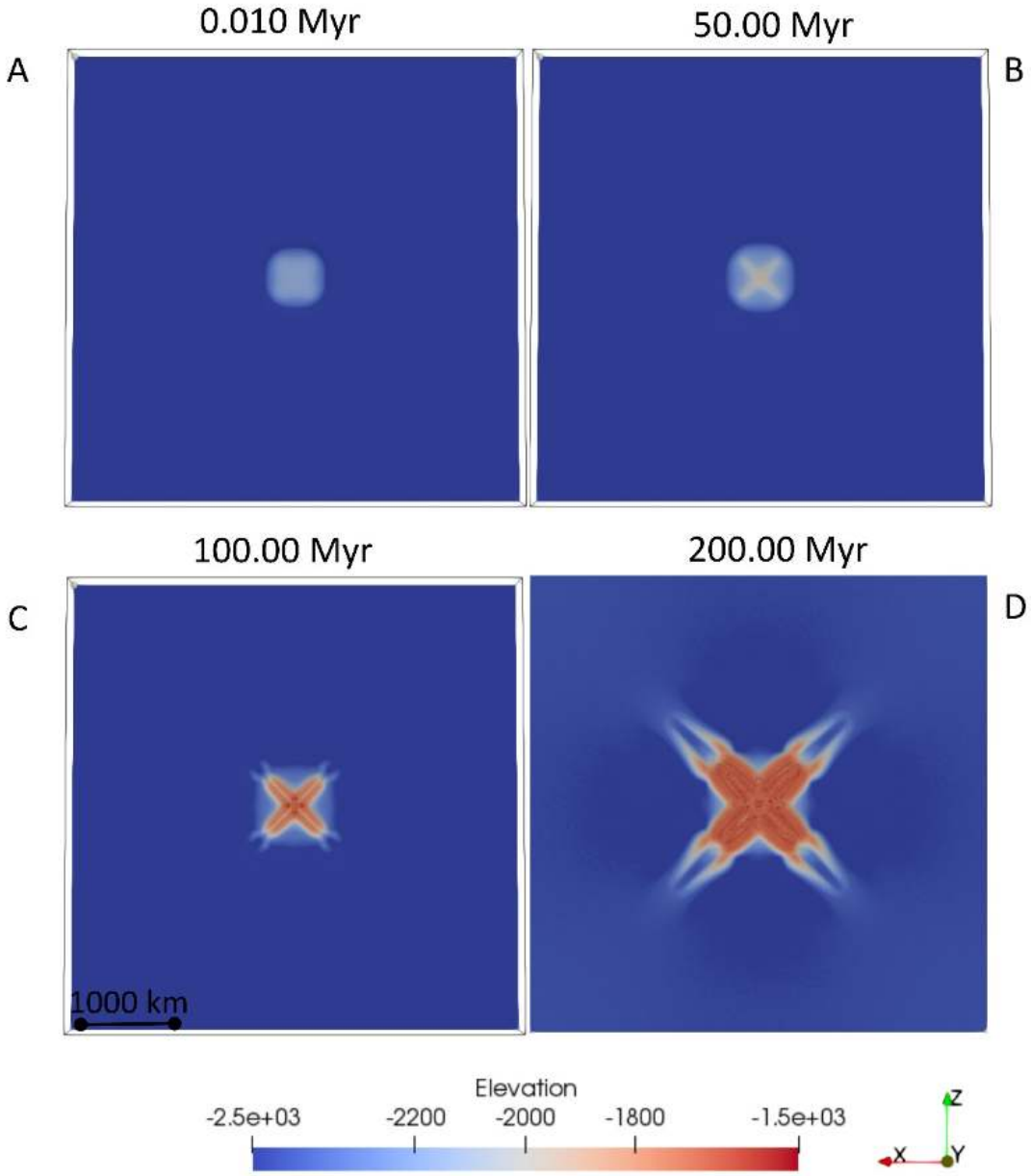

Figure 4.42 - *Model 6_Congo_weak4. Lateral variation of topography (m) at the base of the crust, defined by the depth of the isodensity 3000 kg/m^3, at 0.010Myr (**A**), 50Myr (**B**), 100 Myr (**C**) and 200Myr (**D**).*

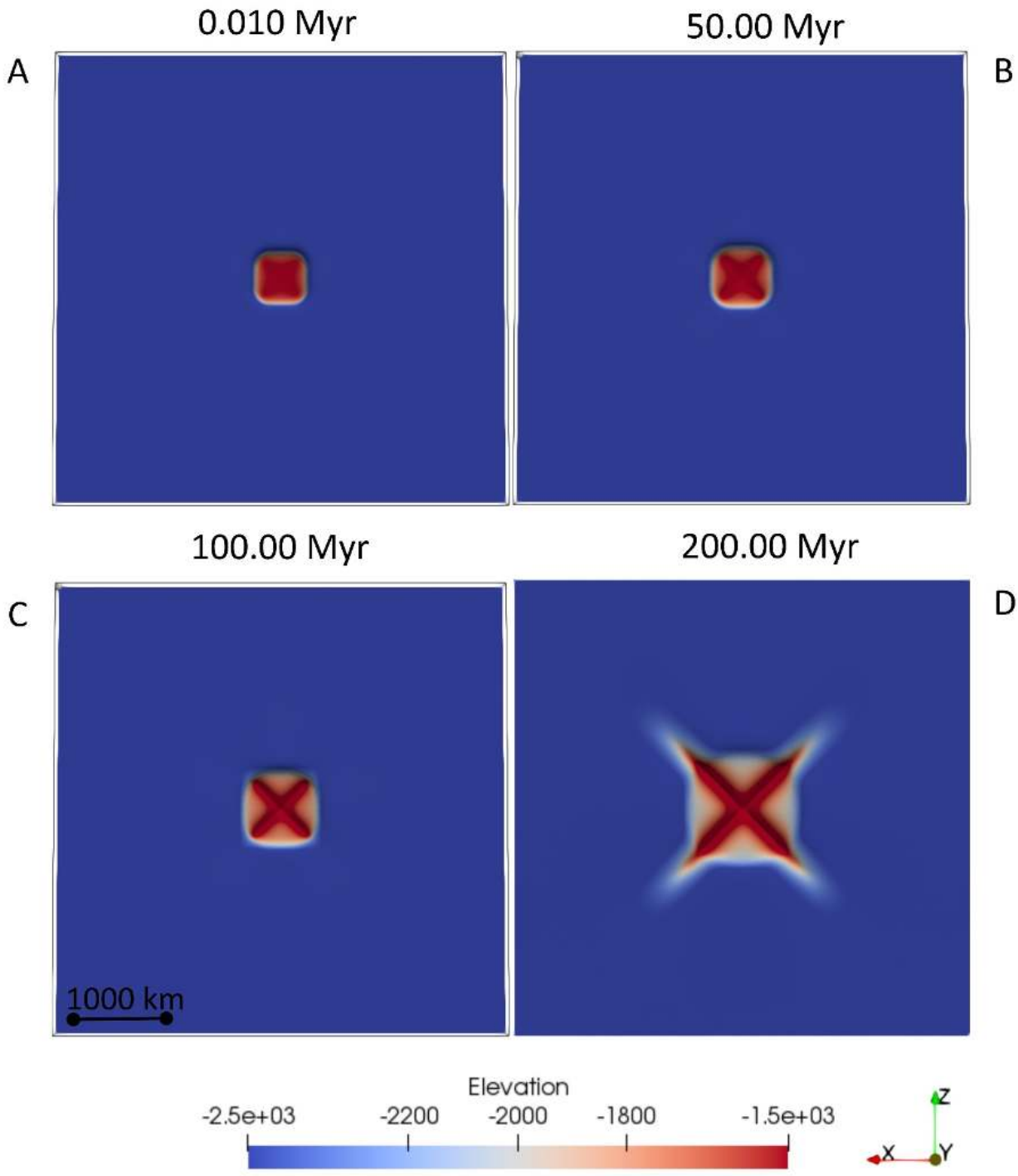

Figure 4.43 - *Model 6_Congo_weak4. Lateral variation of topography (m) at the base of the lithosphere, defined as depth of the isotherm 1573 K, at 0.010Myr (**A**), 50Myr (**B**), 100 Myr (**C**) and 200Myr (**D**).*

4.3.7 Seventh model 7_Congo_cratons+weak

Numerical model design: In this model simulation (*7_ Congo_cratons+weak,* Fig. 4.44), I considered the existence of a weak zone having a size of 623 km x 623 km and a lithospheric thickness of 80 km located in the central part of the model. It is divided into four cratonic blocks (as in the second simulation 2_Congo_cratons), having a size of 1402 km x 1402 km, surrounded by *TZs* having a width of 311 km. Among the weak zone and the cratonic blocks, there is an area having a lithospheric thickness intermediate between the two (155 km). Therefore, this model is a hybrid model between those already implemented. It was carried out, in order to test the effect on the deformation of this new geometry design.

Initial Temperature Conditions: The thermal gradients in the weak zone are the same as those of the three previous simulations (4_Congo_weak2, 5_Congo_weak3, and 6_Congo_weak4), according to the same crustal and lithospheric thickness assumed. In the areas between the cratonic blocks and the weak zone, the thermal gradient in the crust is the same of that of the weak zone, while in the mantle lithosphere it is about 6.5 K/km, according to the temperature assumed at the base of the lithosphere (1660 K).

Results: The results of the first 50 Myr of simulation are similar to those obtained in the previous models, while they become quite different later on, reflecting a more complex geometry design. In particular, we can observe at the time step 50 Myr, the formation of the two elongated low-viscosity zones at the Moho depth and deeper (Figs. 4.45 B-4.47 B). At the time step 100 Myr, at the Moho depth, we can observe a viscosity increase within the two elongated structures, effect of the lateral extension of the thermal anomaly (Fig. 4.48). The last one shows a peculiar shape, with two close peaks at the time step 50 and 100 Myr, depending on the initial lithospheric thickness assumed for the different parts of the model. These results are consistent with the time evolution of the depth-viscosity variations (Appendix C, Fig. C6).

The two elongated structures are characterized by the deepest subsidence of the surface topography (Fig. 4.49 B) and uplift of the Moho and lithosphere-asthenosphere boundary depths (Figs. 4.50 B-4.51 B). Furthermore, the edges of these structures show elevation of the surface topography (Fig. 4.49 B). These features are very similar to those formed in the previous simulations at the time step 50 Myr (Fig. 4.25 B) and 100 Myr (Fig. 4.41 C), respectively. However, at the time step 100 Myr, the topographic variations are mostly concentrated along the two elongated structures that become wider and go beyond the edges of the circular depressed central zone (Fig. 4.49 C). These differences are due to the presence of a lithospheric thickness intermediate between that of the cratons and central weak zone. This ‘intermediate’ zone also smoothies the lateral topography variations, occurring between the mostly deformed and undeformed part of the model, both at the surface, as well as at the depth of the Moho and base of the lithosphere. On the other hand, the edges of the cratonic blocks appear uplifted at all the time steps, as in 2_Congo_cratons model (Fig. 4.11), despite the assumed more complex geometry design (Figs. 4.49-4.51).

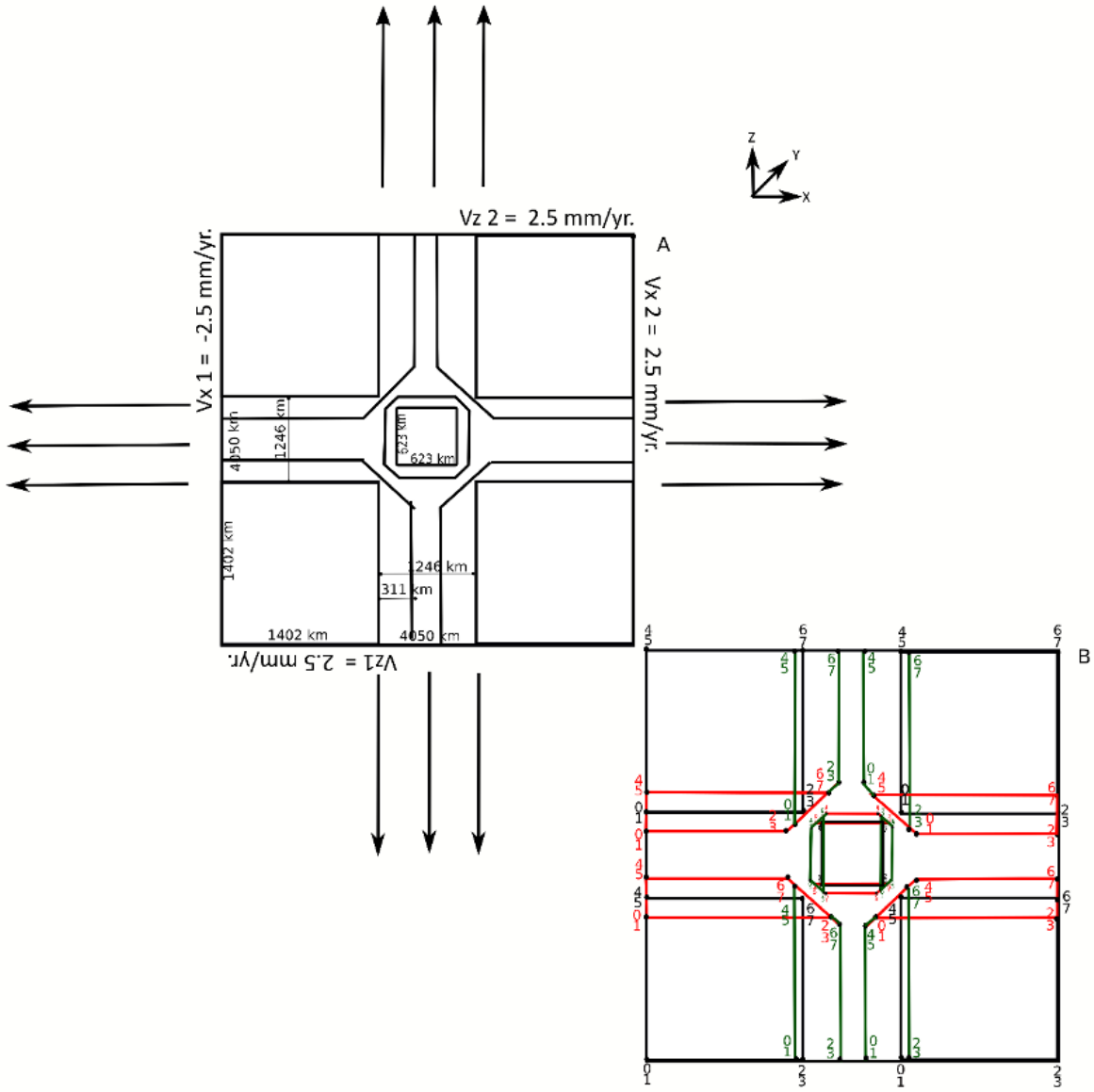

Figure 4.44 - *Geometry design of the model 7_Congo_cratons+weak.* ***A****: Horizontal plane visualization of the model. Black arrows show velocity directions.* ***B****: Representation of the model (A) in staggered grid-mark-in cell technique. The black squares represent the four-cratonic blocks and the weak zone in the center. Red and green features represent the TZs and numbers are as in Fig. 4.4.*

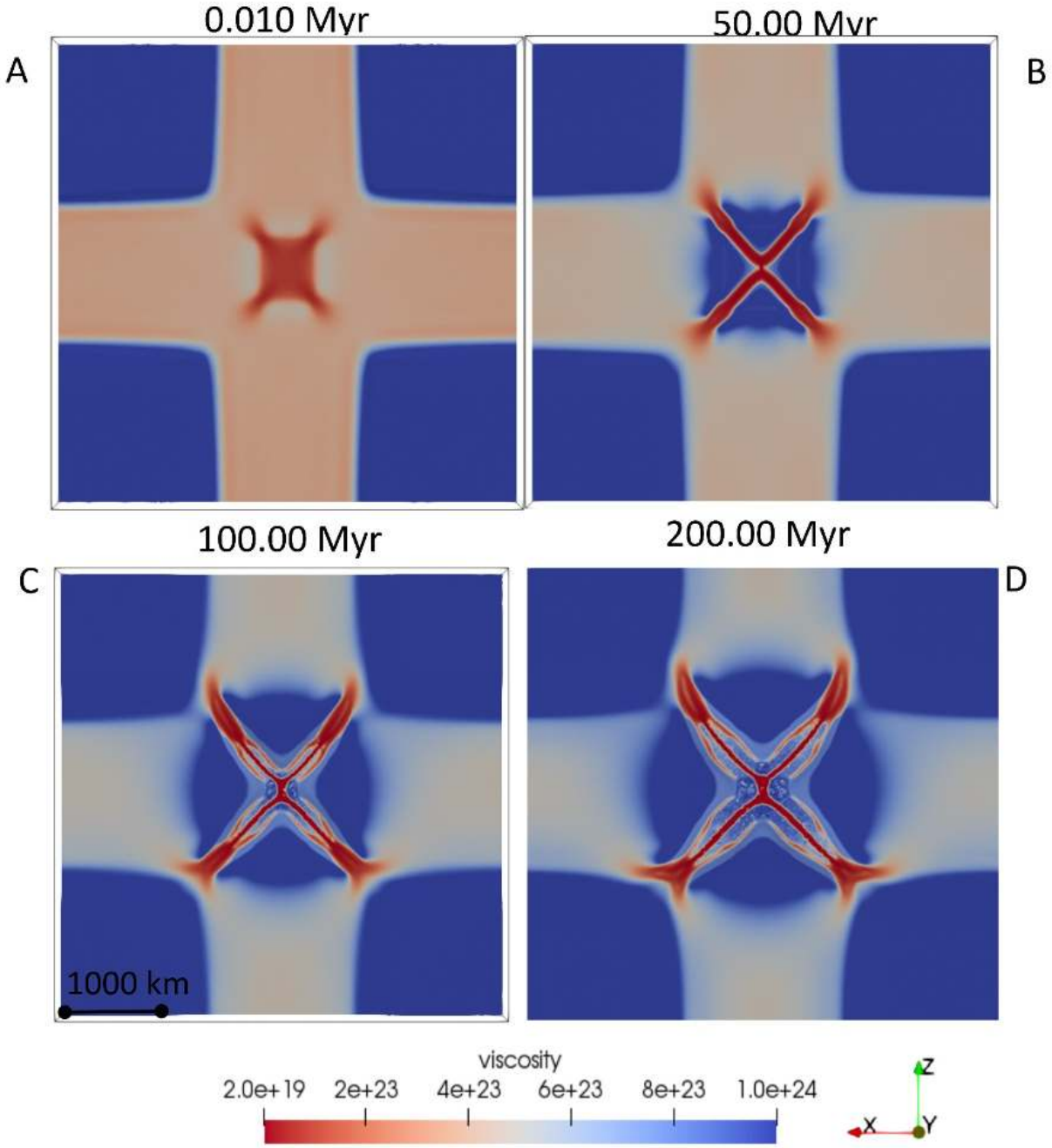

Figure 4. 45 - *Model 7_ Congo_cratons+weak. Lateral variation of viscosity (Pa s) at the base of the crust, defined by the depth of the isodensity 3000 kg/m³, at 0.010Myr (**A**), 50Myr (**B**), 100 Myr (**C**), 200 Myr (**D**).*

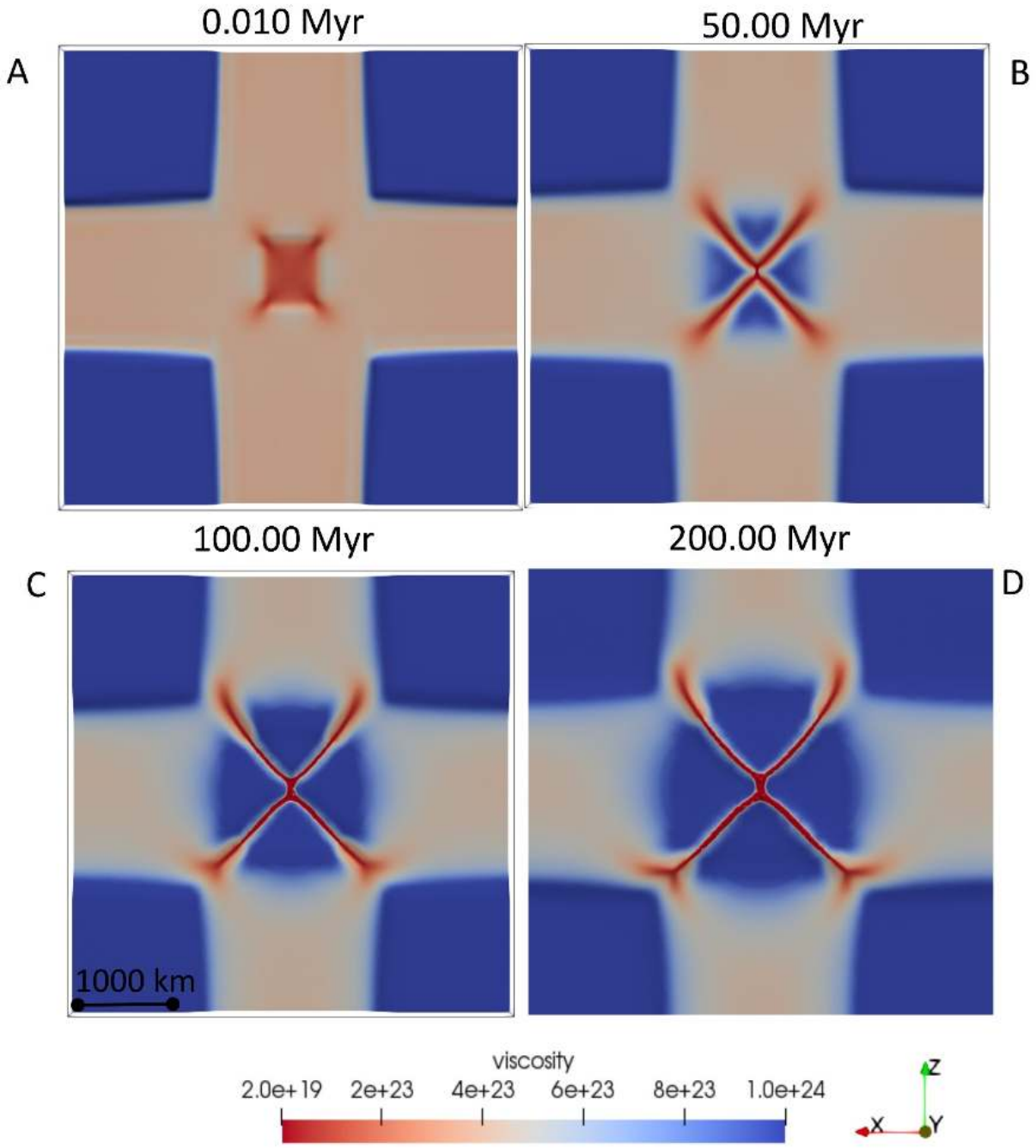

Figure 4.46 - *Model 7_ Congo_cratons+weak. Lateral variation of viscosity (Pa s) within the lithosphere, at a depth defined by the 1073 K isotherm, at 0.010Myr (**A**), 50Myr (**B**), 100 Myr (**C**), 200 Myr (**D**).*

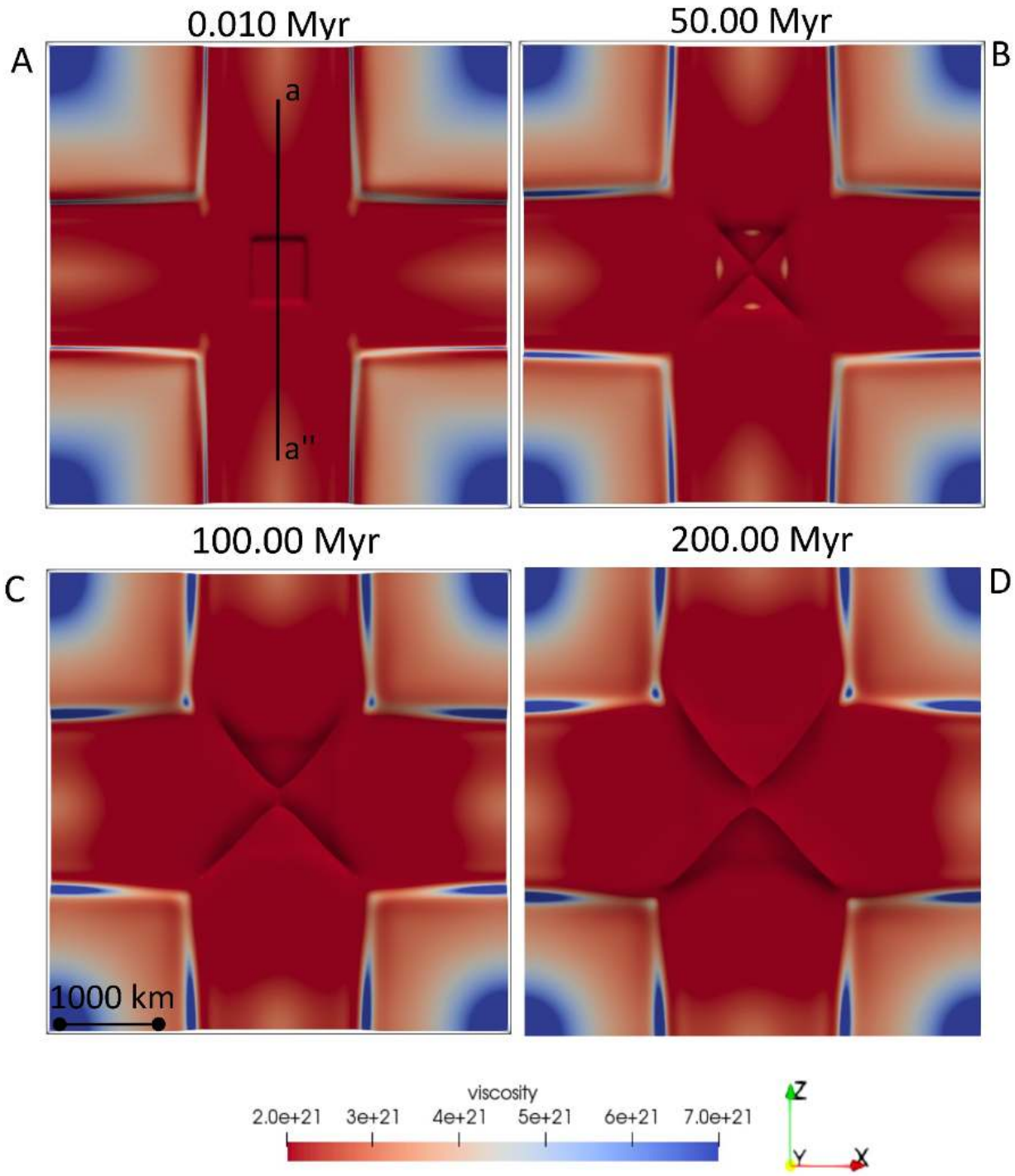

Figure 4.47 - *Model 7_ Congo_cratons+weak. Lateral variation of viscosity (Pa s) at the base of the lithosphere, defined as depth of the isotherm 1573 K, at 0.010Myr (**A**), 50Myr (**B**), 100 Myr (**C**), 200 Myr (**D**). Black line delimited by labels a-a"shows the location of the cross-setion of temperatures (Fig. 4.48), density (Figs. 4.52-4.53), and viscosity (Fig. C6 A).*

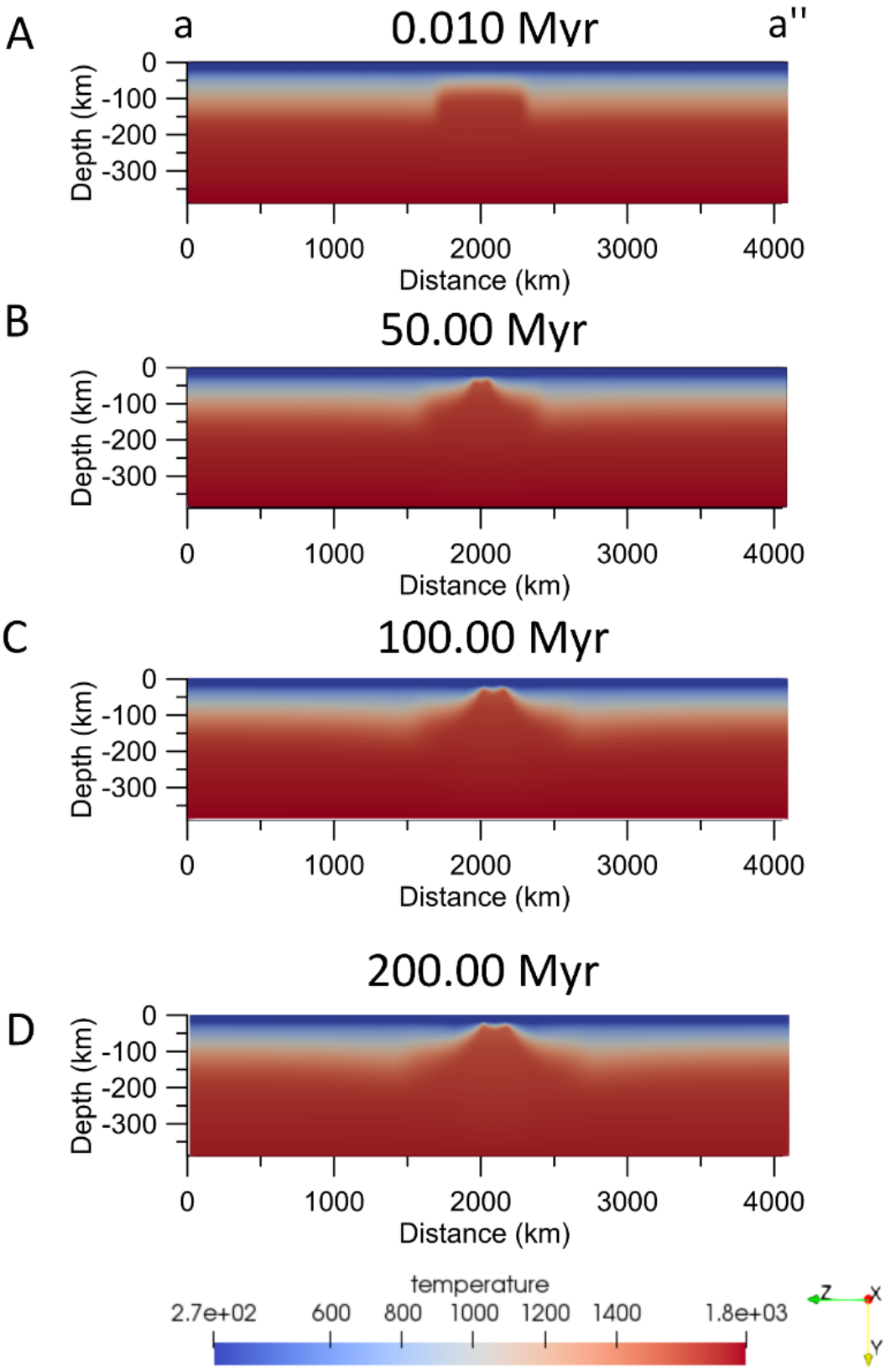

Figure 4.48 - *Model 7_ Congo_cratons+weak. Depth-temperature (K) variation, along the cross-section displayed in Fig. 4.39 A, at 0.010Myr (**A**), 50Myr (**B**), 100 Myr (**C**), 200 Myr (**D**). Vertical scale increased by 15% with respect to horizontal axis.*

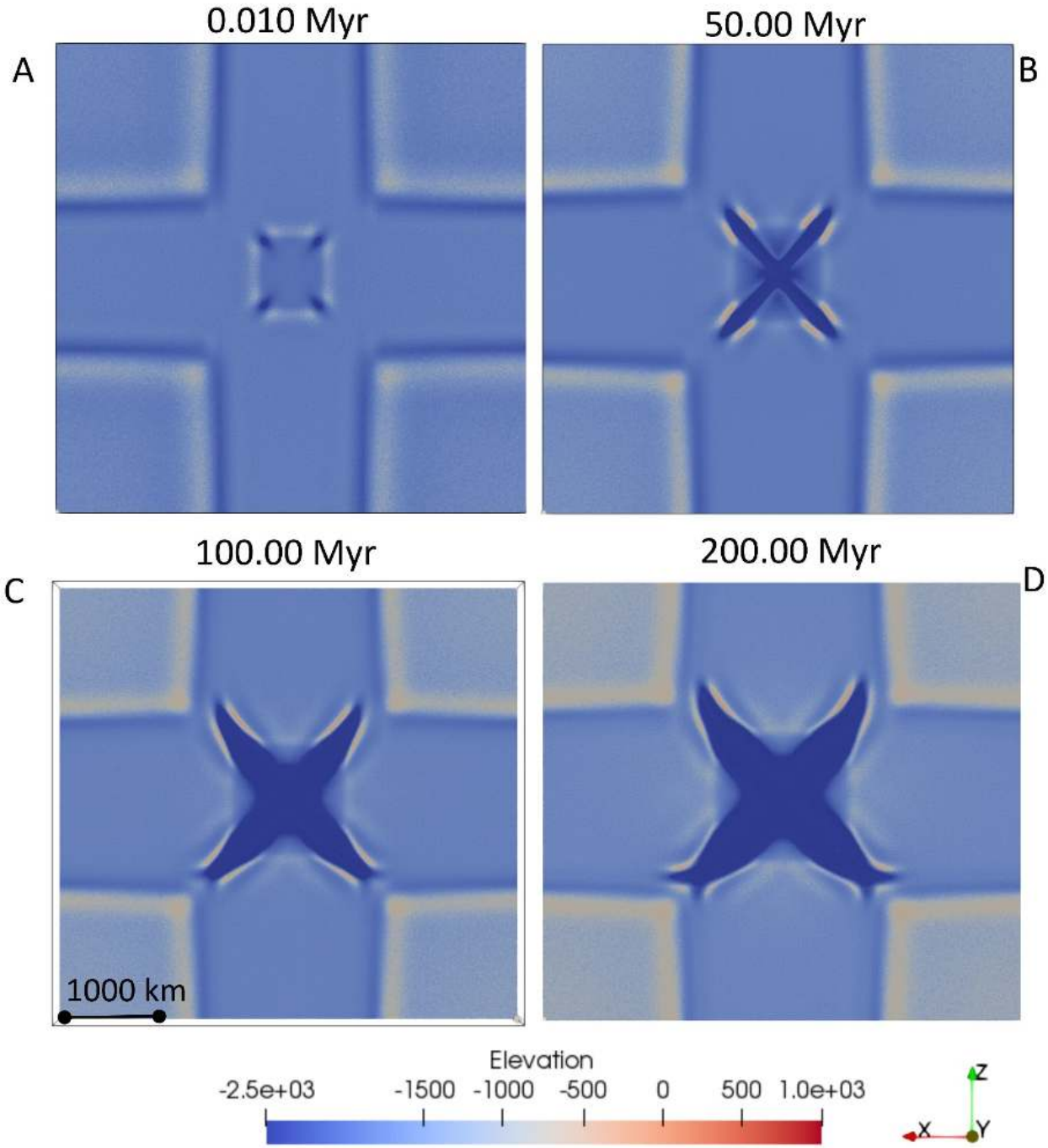

Figure 4.49 - *Model 7_ Congo_cratons+weak. Lateral variation of surface topography (m), at 0.010Myr (**A**), 50Myr (**B**), 100 Myr (**C**), 200 Myr (**D**).*

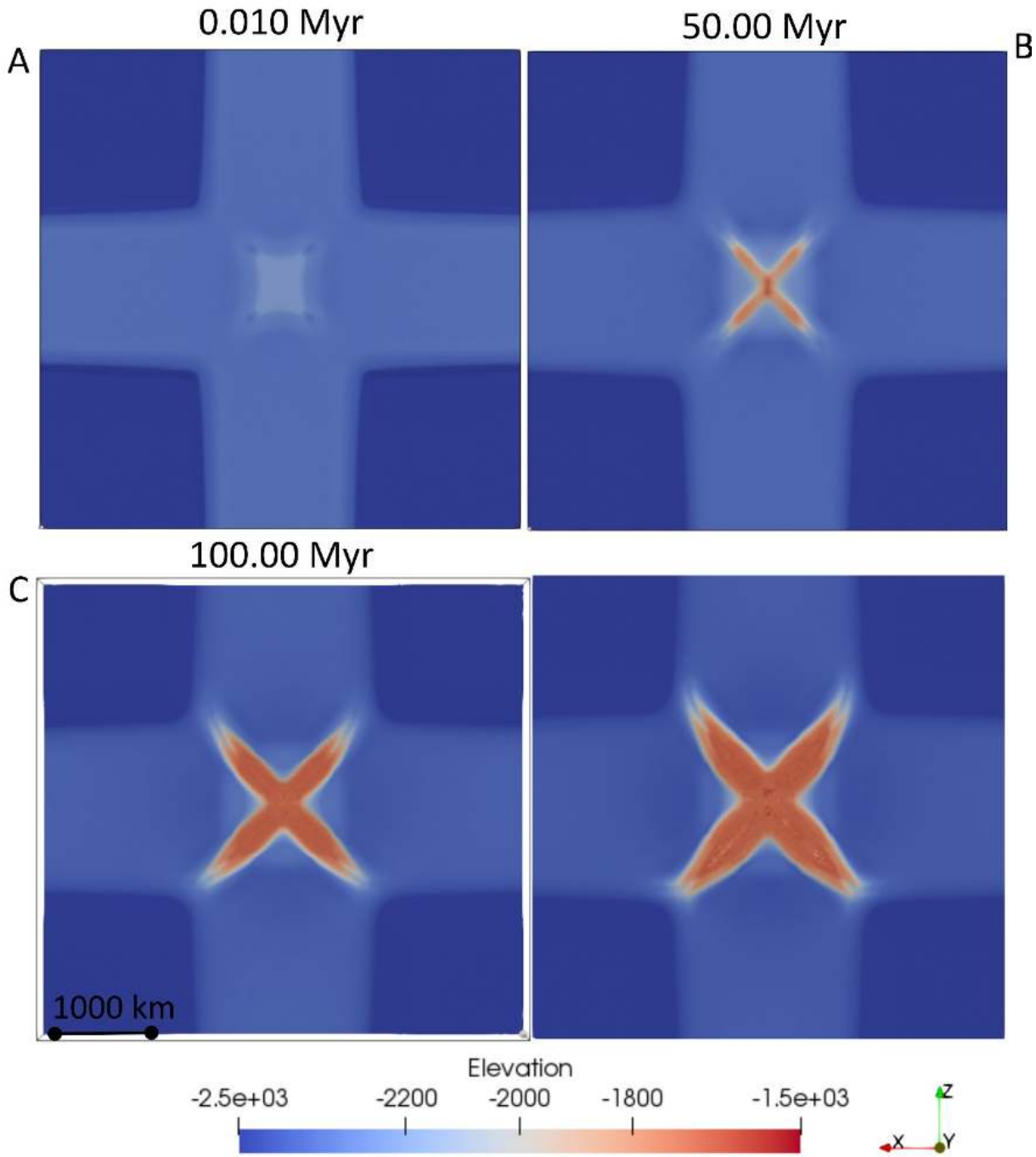

Figure 4.50 - *Model 7_ Congo_cratons+weak. Lateral variation of topography (m) at the base of the crust, defined by the depth of the isodensity 3000 kg/m³, at 0.010Myr (**A**), 50Myr (**B**), 100 Myr (**C**), 200 Myr (**D**).*

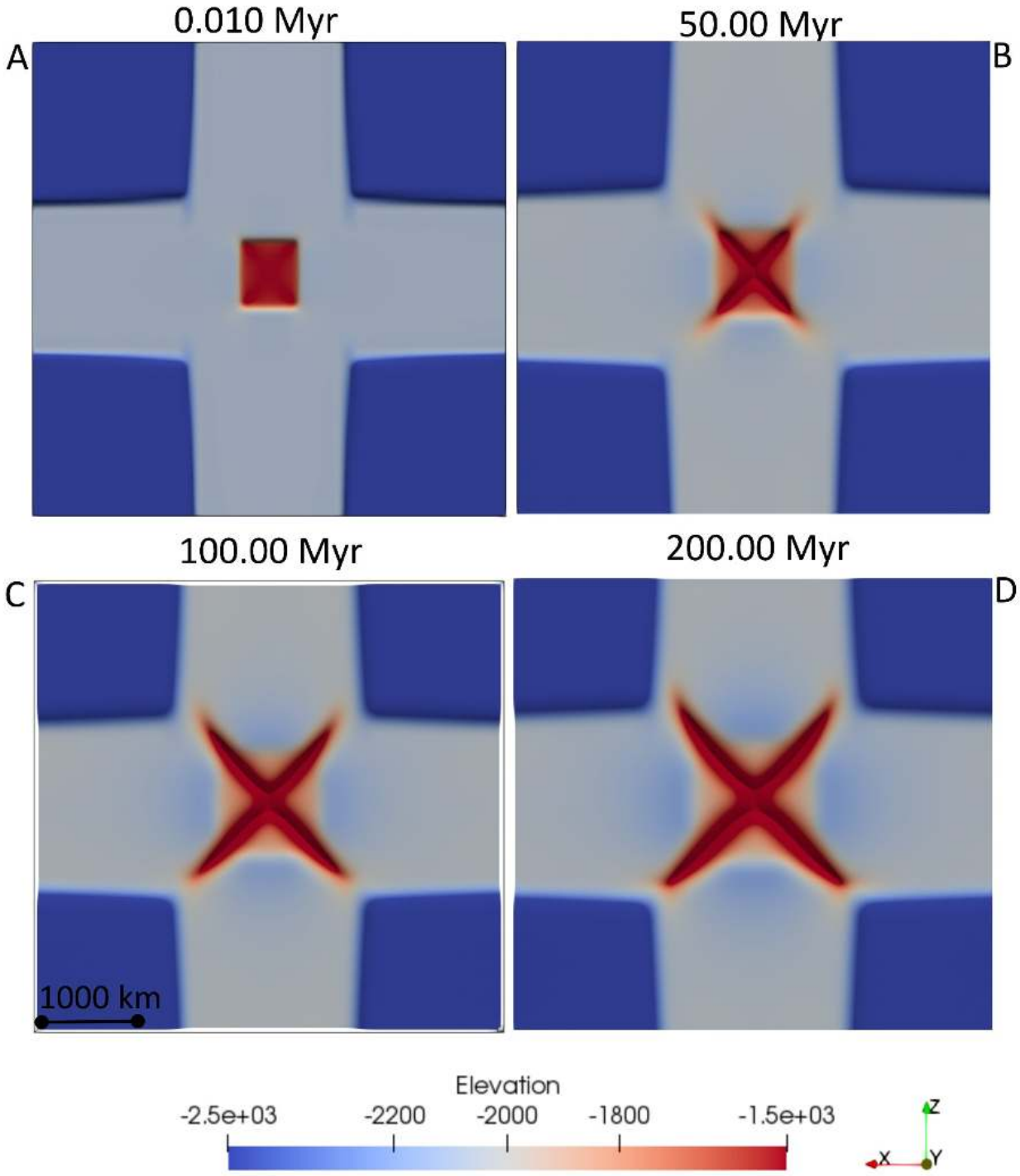

Figure 4.51 - *Model 7_ Congo_cratons+weak. Lateral variation of topography (m) at the base of the lithosphere, defined as depth of the isotherm 1573 K, at 0.010Myr (**A**), 50Myr (**B**), 100 Myr (**C**), 200 Myr (**D**).*

4.4 Forward gravity modelling of the 3D numerical simulation results

After performing the 3D simulations to test the hypothesis of the *CB* formation as a multi-extensional rift within a cratonic area (section 4.3), I calculated their gravity fields and compared them with the gravity observations (Fig. 3.5 A). To this aim, I performed static and dynamic forward gravity modelling (*SFGM* and *DFGM*, respectively) using the 3D numerical simulations 3_Congo_weak1 and 4_Congo_weak2, whose results best approximate the basement depth variations previously reconstructed (Chapter 2 and 3). Indeed, since the 3D numerical simulations do not include the effects of the sedimentation, the modelled surface topography (section 4.3) has been considered as the top of the basement (Fig. 3.1).

4.4.1 Model setup

The forward gravity models have been implemented using the density values computed at x, y, z coordinates for each 3D numerical simulation. For this purpose, I constructed rectangular prisms with the center coincident to each grid point of the numerical models and length, width, and height equal to the half of the inter-node spacing. The gravity is computed at 4 km distance from the top of the numerical model, in order to smooth short-scale near-surface variations induced by the density changes. Furthermore, I excluded from the computation the prisms modelling the sticky air layer, considering only those having a density values > 1000 kg/m^3.

The density values of the two models used as data input for the calculation of the forward gravity modelling are displayed in terms of lateral changes and depth variations at the base of the lithosphere, at the time steps 0.010 Myr and 200 Myr, respectively, in Figs. 4.52 - 4.53. Both models show an initial condition, characterized by a central area with density lower than surroundings (Figs. 4.52 A, 4.52 C, 4.53 A, and 4.53 C). At 200 Myr, the updoming of the hot asthenosphere in the central part of the model causes a density decrease at the bottom of the lithosphere along two zones orthogonal each other (Fig. 4.52 B, 4.52 D, 4.53 B, and 4.53 D). These features overprint a circular zone of higher density (but still lower than that of the external areas), produced by a slower, and thus less hot, mantle upwelling (Figs. 4.52 B and 4.53 B). The described structures have a larger size in 4_Congo_weak2 model, due to the geometry design and initial temperature conditions assumed.

The temporal density variations produce a surface topography depression in the central part of the model, interrupted by sharp uplifts in the 3_Congo_weak1 model, indicating strong lateral density changes within the subsided area. In contrast, in the 4_Congo_weak2 model, there is only a small uplift in the center of a much larger topography depression, due to the upraised hot asthenosphere. In both models, the central subsided area forms consequently to the replacement of the less dense more buoyant cratonic lithosphere with the denser asthenosphere, which cools migrating far from the center. On the other hand, the sudden surface topography increase, at the edges of the subsided area, sharply occurs in correspondence of the lateral density decrease of the mantle lithosphere, at the transition from the deformed central area to the almost stable and stiffer external cratonic part. The edges are more uplifted in 4_Congo_weak2 model, where we observe a thickening of the low-density part of the lithosphere. We can further notice that the lateral density variations,

occurring in the more peripheral parts of the model during the extensional deformation, do not significantly affect the surface topography.

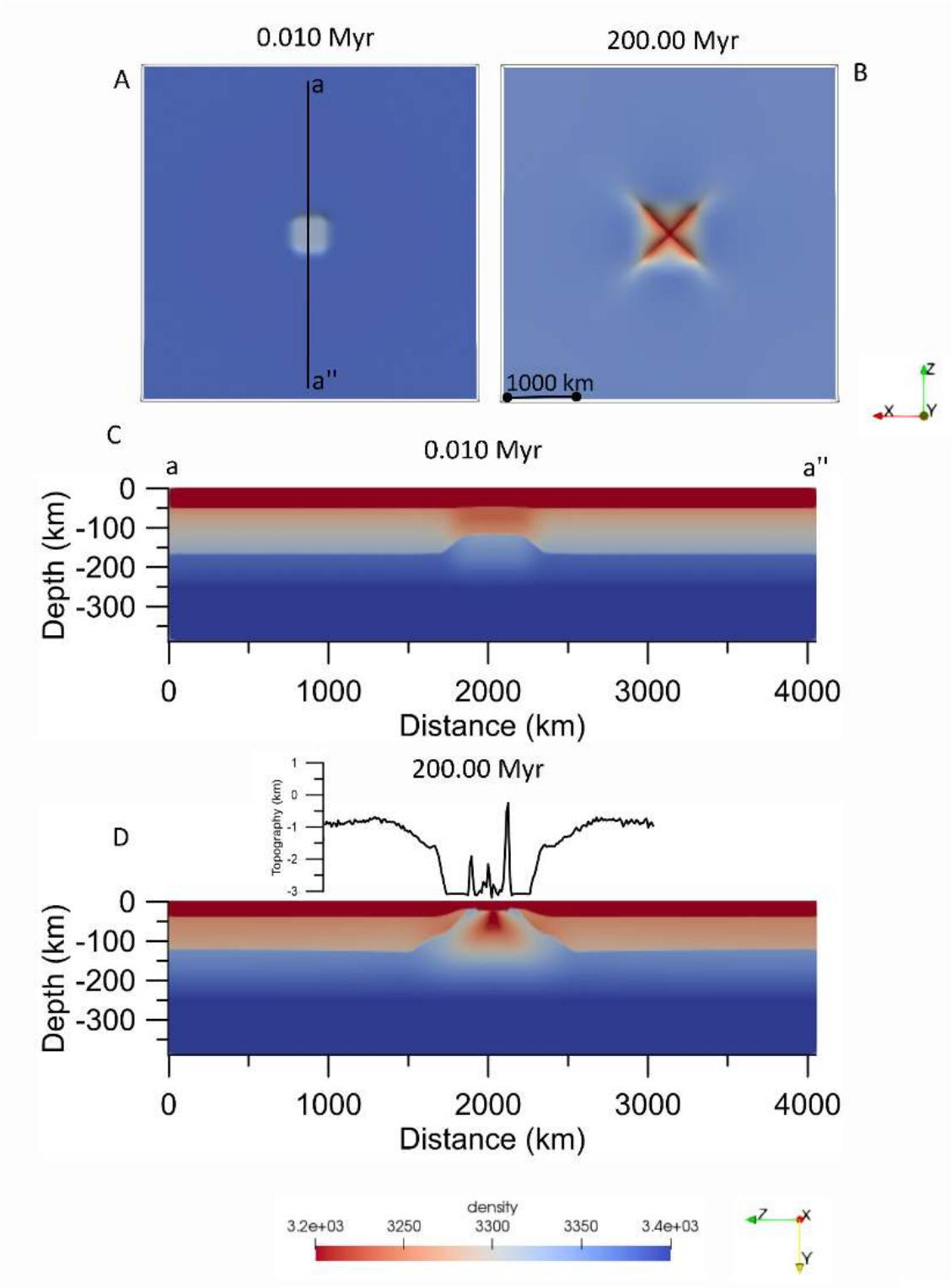

Figure 4.52 - *Model 3_Congo_weak1. Lateral variation of density (kg/m³) at the base of the lithosphere, defined as depth of the isotherm 1573 K, at 0.010Myr (**A**), and 200 Myr (**B**). Depth-density (kg/m³) variation, along the cross-section displayed in A, at 0.010Myr (**C**), and 200 Myr (**D**). Vertical scale increased by 15% with respect to horizontal axis. Black curve represents the lateral variation of surface topography along the central part of the cross-section displaying the depth-density variations.*

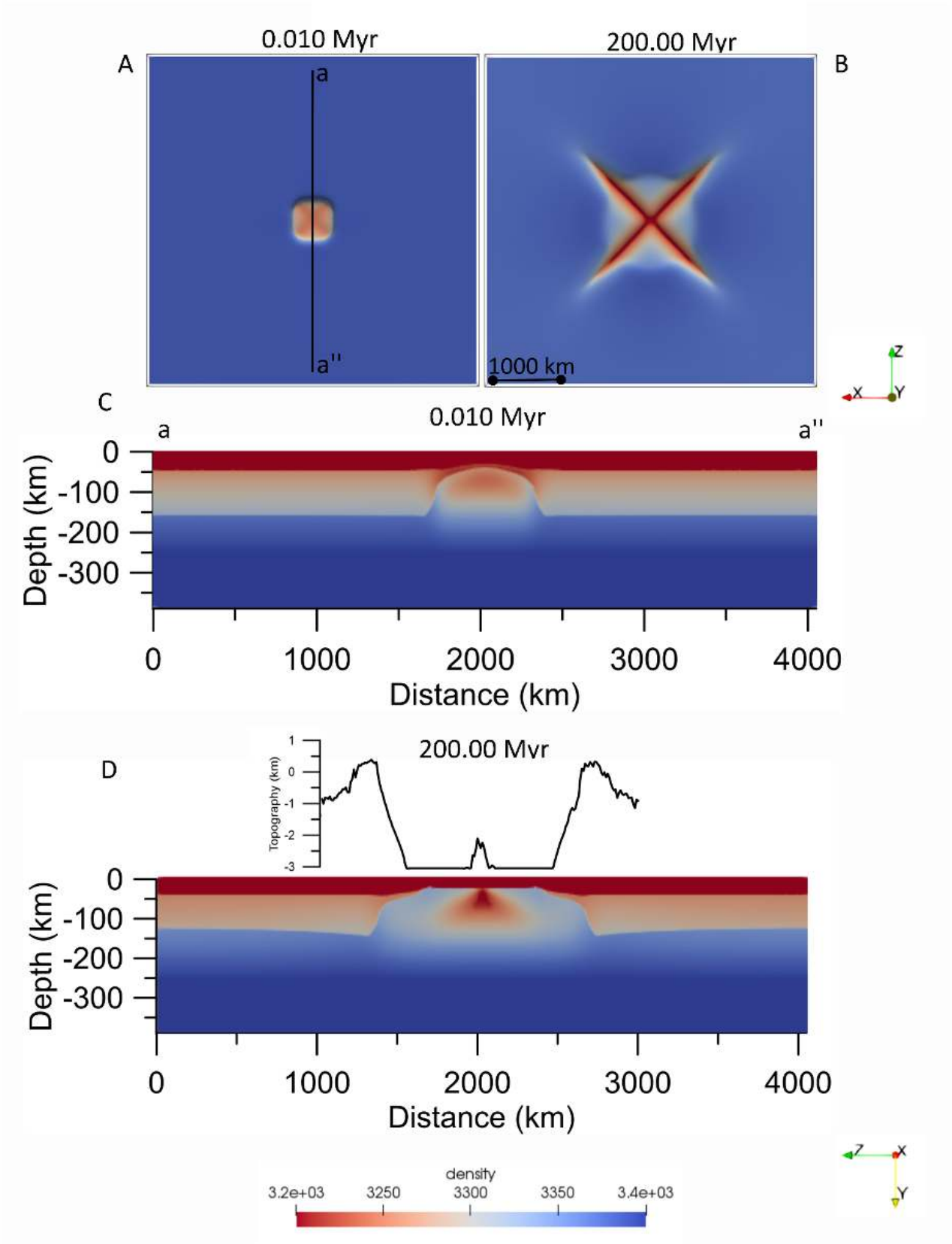

Figure 4.53 - *Model 4_Congo_weak2. Lateral variation of density (kg/m³) at the base of the lithosphere, defined as depth of the isotherm 1573 K, at 0.010Myr (**A**), and 200 Myr (**B**). Depth-density (kg/m³) variation, along the cross-section displayed in A, at 0.010Myr (**C**), and 200 Myr (**D**). Vertical scale increased by 15% with respect to horizontal axis. Black curve represents the lateral variation of surface topography along the central part of the cross-section displaying the depth-density variations.*

4.4.2 Dynamic forward gravity modelling (DFGM)

To observe how the gravity field changed over time, I implemented a DFGM, by computing the difference between the gravity effects of the two numerical models (3_Congo_weak1 and 4_Congo_weak2) at the time step 200 Myr with those produced at 0.010 Myr (Figs. 4.54 A and 4.55 A). The results show strong positive anomalies (between +80 and +300 mGal), related to the mass excess caused by the mantle upwelling, inducing density and topography variations. The amplitude of the anomalies and the features formed by their variations are greater for the 4_Congo_weak2. The highest and lowest values are localized in the uplifted and subsided areas (Figs 4.17-4.25) and, as for the topography variations, form two elongated structures orthogonal each other. We can further notice that the applied multi-extensional stress produces a change in the mass distribution not uniformly distributed, with a series of maxima and minima, affecting both the central and peripheral parts of the models.

Looking at the gravity anomalies along three cross-sections (Figs. 4.54 B and 4.55 B), we can observe in more detail the difference between the two models. In particular, the cross-sections A-B passing through one of the two elongated features of the 4_Congo_weak2 model evidences a minimum value in the central part (+248 mGal) surrounded by two maxima (+260 mGal). In contrast, the same cross-section of the 3_Congo_weak1 model shows a maximum in the center (+215 mGal), surrounded by other two maxima (+200 mGal). The different trend of anomalies indicates that the deformation simulated by 4_Congo_weak2 model reached a more mature rift stage, than that simulated by the first model. Indeed, the maximum in the center observed in 3_Congo_weak1 model is the effect of the mantle upwelling localized in a narrower zone than in 4_Congo_weak2 model, as can be observed in the density-depth distribution (Figs 4.52-4.53).

The cross-section C-D, 45° oriented with respect to the direction of the elongated orthogonal structures, shows that the positive anomaly (> 250 mGal) in the center of the 3_Congo_weak1 model forms a maximum (about +250 mGal) surrounded by two minima of about +100 mGal. In contrast, in the other model, we observe along the same cross-section an alternation of minima and maxima spanning in a smaller range (between +170 and +230 mGal). On the other hand, the trend of the gravity anomalies along the third cross-section, perpendicular to one of the elongated structures (E-F), is the same for both models, showing a minimum in the center, surrounded by two maxima, which have a lower amplitude in 3_Congo_weak1 model. Therefore, the two models considered produce similar anomalies variations in their peripheral parts, while the different geometry design and initial temperature conditions assumed significantly influence the evolution of the deformation in the center, causing a different trend and amplitude of the gravity anomalies.

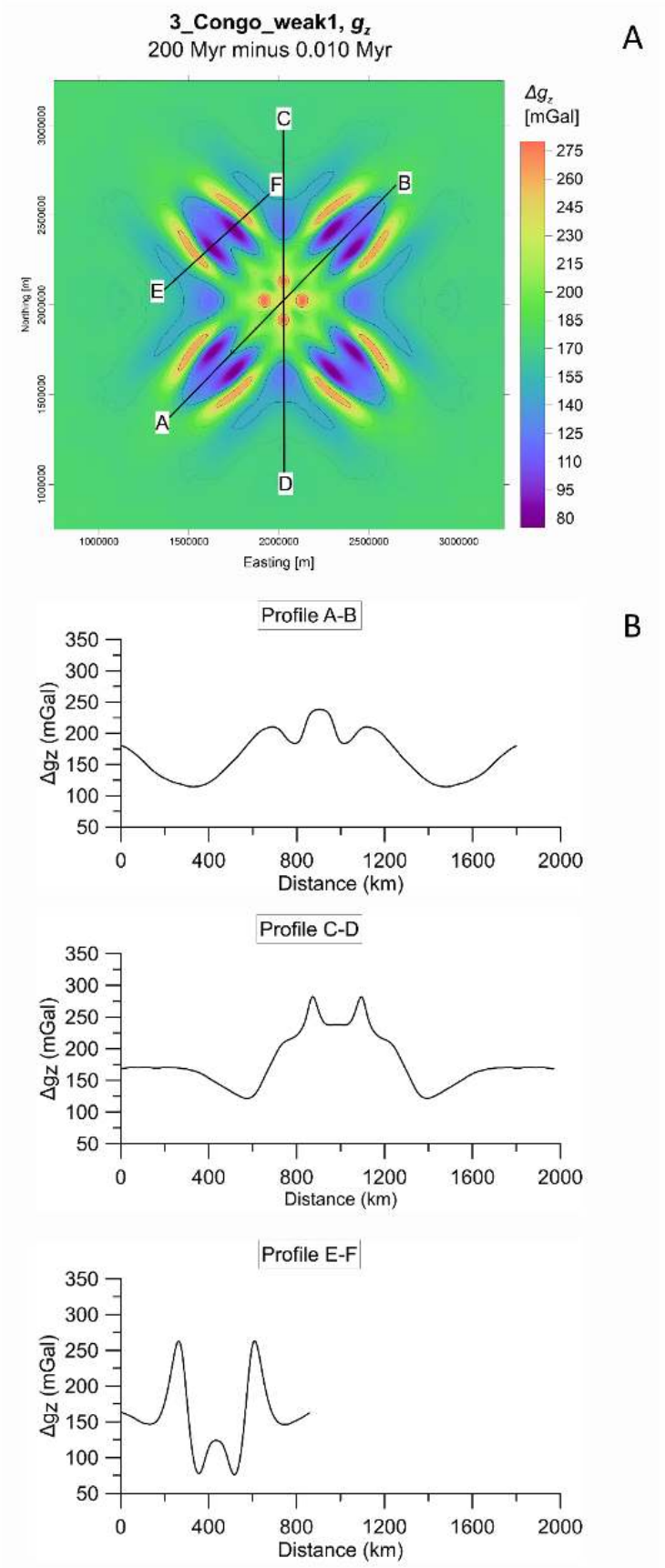

Figure 4.54 - *Dynamic Forward Gravity Modelling (DFGM) of the 3_Congo_weak1 simulation. (**A**) Horizontal plane visualization of the gravity variation; (**B**) Lateral gravity variations along three profiles displayed in A.*

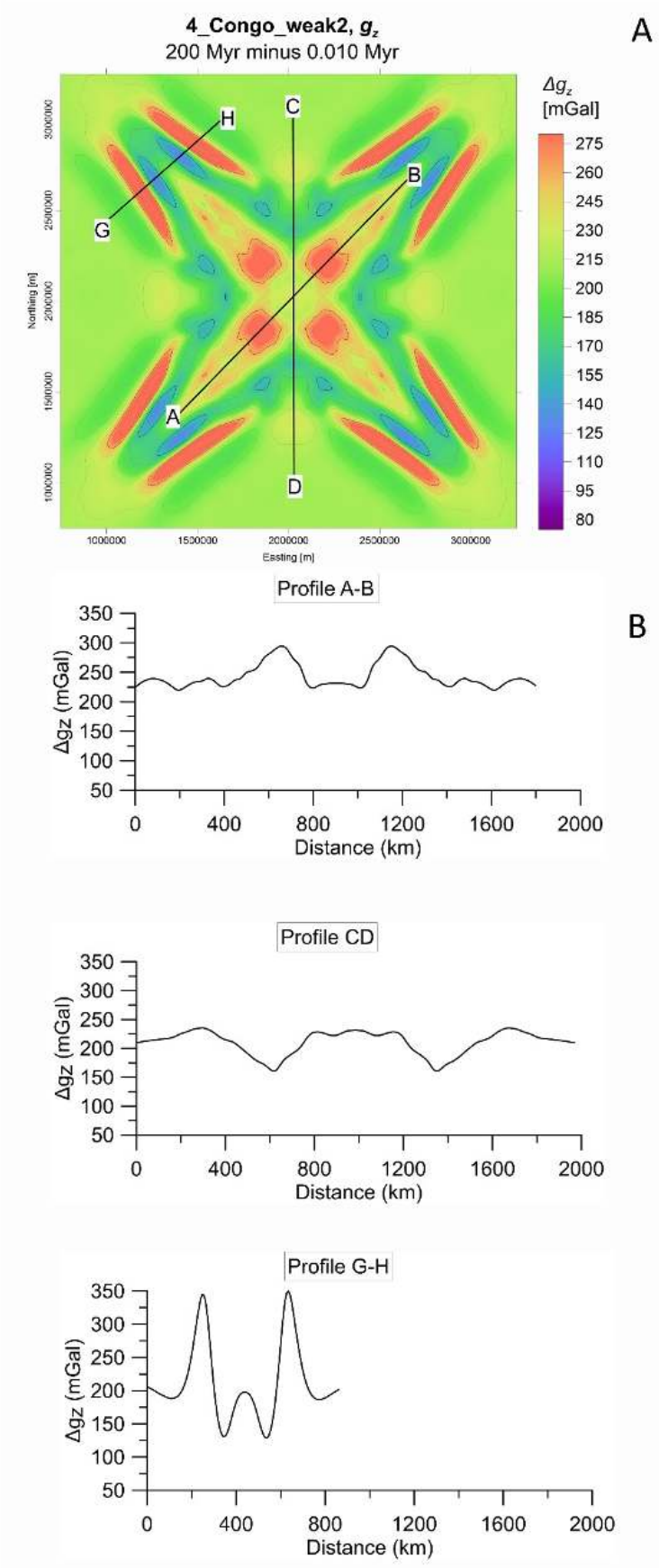

Figure 4.55 - *Dynamic Forward Gravity Modelling (DFGM) of the 4_Congo_weak2 simulation. (**A**) Horizontal plane visualization of the gravity variation; (**B**) Lateral gravity variations along three profiles displayed in A.*

4.4.3 Static forward gravity modelling (SFGM)

I implemented the *SFGM* to observe the gravity anomalies resulting from the gravity effect of the two numerical simulations at 200 Myr, after the removal of the effect of a 1D-reference model calculated at the same time step (Fig. 4.56). The reference model was computed as the average density of the all prisms having the same depths, at the time step 0.010 Myr and 200 Myr, respectively, to show the differences between the initial and final conditions (Fig. 4.56). We can notice that the reference models of 3_Congo_weak1 and 4_Congo_weak2 show very small differences, with respect to the same time step. The reason is that the original different horizontal patterns of the two models are hidden by the computed average. On the other hand, the differences for the same model at the two time steps are relatively large at the crustal depths and more reduced below, according to the larger density variations occurring at the crustal levels during the extension.

The results of the SFGM show positive and negative gravity anomalies localized in the uplifted and subsided areas (Figs 4.57) and, as already observed in the DFGM, form two elongated structures orthogonal each other. In general, the SFGM produce similar structures to those obtained from the DFGM. As before, 4_Congo_weak2 simulation causes anomalies of higher amplitude, distributed on a larger area with respect to those of the 3_Congo_weak1. This can be ascribed to the different geometry design and initial temperature conditions assumed that, in case of 4_Congo_weak2, increase the speed of the extensional deformation simulated and enhance the mantle upwelling on a larger area.

The two SFGMs show that the distribution of the anomalies is very similar (Figs 4.57). In particular, we can observe weak positive anomalies (< 50 mGal) in the central area and along two elongated zones orthogonal each other, characterized by the uprising of the asthenosphere and strong subsidence of the surface topography (Figs. 4.17 D and 4.25 D). These structures are surrounded by zones of strong negative anomalies (-30 mGal to -90 mGal), which are in turn surrounded by zones of strong positive anomalies (between +70 and +130 mGal), corresponding to the areas of subsidence and uplift of the surface topography (Figs. 4.17 D and 4.25 D). These anomalies, reflecting the formation of zones of mass excess and defect, with respect the 1D reference model can be explained by the combined effect of the lateral variations of surface topography and temperature of the upwelling mantle that decreases moving away from the center. To this purpose, we should notice that the uplift of the surface topography is induced by the propagation of the extensional deformation from the central weak zone towards the more rigid cratonic areas and thus it is not accompanied by a crustal thickening (Fig. 4.58 D and 4.59 D). The results of the SFGM in comparison with the gravity disturbance anomalies are discussed in section 4.5.

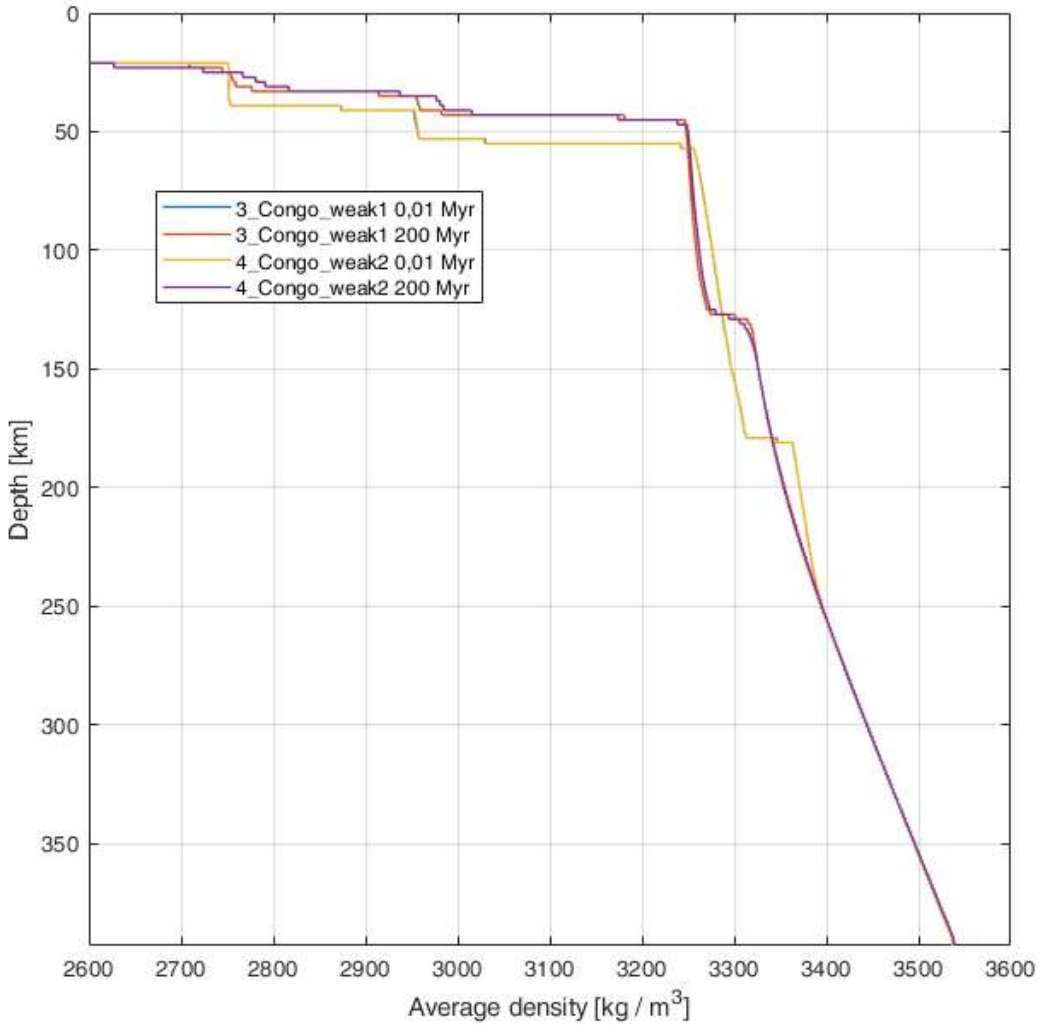

Figure 4.56 *– Depth-density variation of the reference density models, for each time step of 3_Congo_weak1 and 4_Congo_weak2 models. Blue and red curves show the depth-density function of the 3_Congo_weak1* model *at 0.010 Myr and 200 Myr, respectively. Yellow and violet curves show the depth-density function of the 4_Congo_weak2* model *at 0.010 Myr and 200 Myr, respectively.*

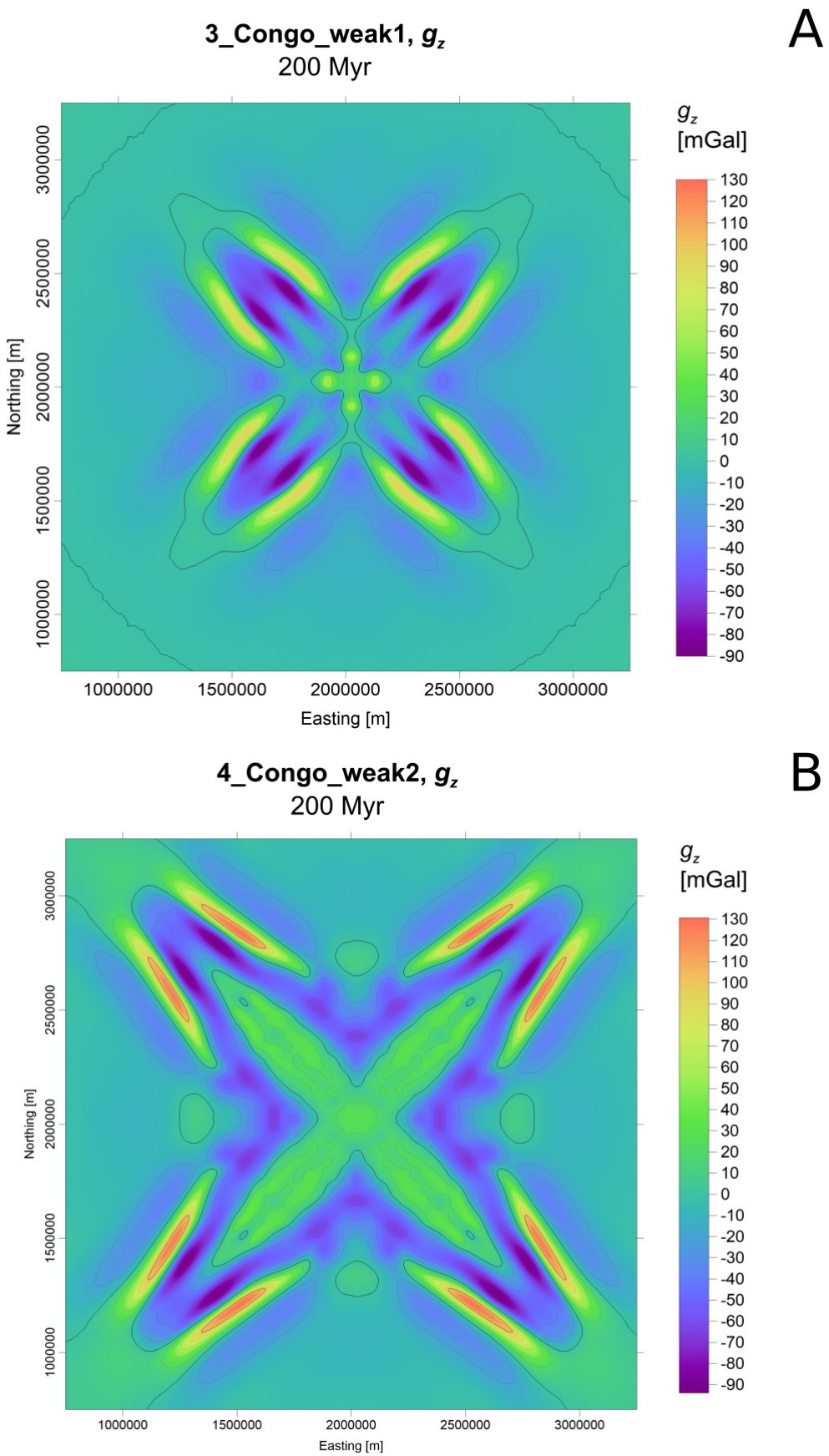

Figure 4.57 *– Horizontal plane visualizations of the Static Forward Gravity Modelling (SFGM) in the 3_Congo_weak1 simulation (**A**) and 4_Congo_weak2 simulation (**B**), respectively.*

4.4.4 Static forward gravity model topography corrected (SFGM_tc)

In order to separate the effects of the topography and density variations induced by the mantle upwelling on the amplitude and trend of the static gravity anomalies, I performed a new forward gravity modelling of the same numerical simulations (3_Congo_weak1 and 4_Congo_weak2) at the time step 200 Myr. In this analysis, I suppressed the effects of the topography variations. To this aim, I removed from the computed gravity the signal produced by the first 23 km, which includes the effect of the sticky layer (first 20 km) and that of the surface topography variations, which are in a range of ±3 km (Figs 4.17 and 4.25). Afterwards, I subtracted a 1D-reference model, computed at the time step 200 Myr and corrected for the topography effect. The new gravity field (named SFGM_tc) shows features similar to those of the static and dynamic models (e.g. two elongated structures orthogonal each other). However, the distribution and amplitude of anomalies within these features is quite different compared to the previous static model. This is due to the enhancement of the effect of the anomalous mass below the reference depth (23 km). In particular, we should notice the strong increase of the positive anomalies (up to +200 mGal) in the central part of the model, which is more affected by the mantle upwelling. In contrast, the edges of the two elongated structures show weak anomalies (± 20 mGal), indicating that the effect of the anomalous mass below 23 km depth is negligible.

Looking at the gravity anomalies along three cross-sections (Figs. 4.58 B and 4.59 B), we can observe in more detail the difference between the gravity effects produced by 3_Congo_weak1 and 4_Congo_weak2, corrected for the topography effect. The first cross-sections A-B evidences in both models a broad area of positive values (> 150 mGal), with the center characterized by a maximum in 3_Congo_weak1 model and a relative minimum in 4_Congo_weak2 model. These differences are related to the variations of the asthenospheric flow occurring during the tectonic extension in the two models. In the second model (4_Congo_weak2), the asthenospheric uprising affects a larger area, producing an excess of mass along two orthogonal directions (Fig. 4.59 A). The gravity anomalies along the cross-section C-D, 45° oriented with respect to the direction of the elongated orthogonal structures, have similar shape and amplitude in both models with a large positive anomaly (~180 mGal) and a minimum in the center (~ 150 mGal). The gravity anomalies along the third cross-section, perpendicular to one of the elongated orthogonal structure (E-F), show also very similar trends and amplitudes in the two models (Figs. 4.58 B and 4.59 B).

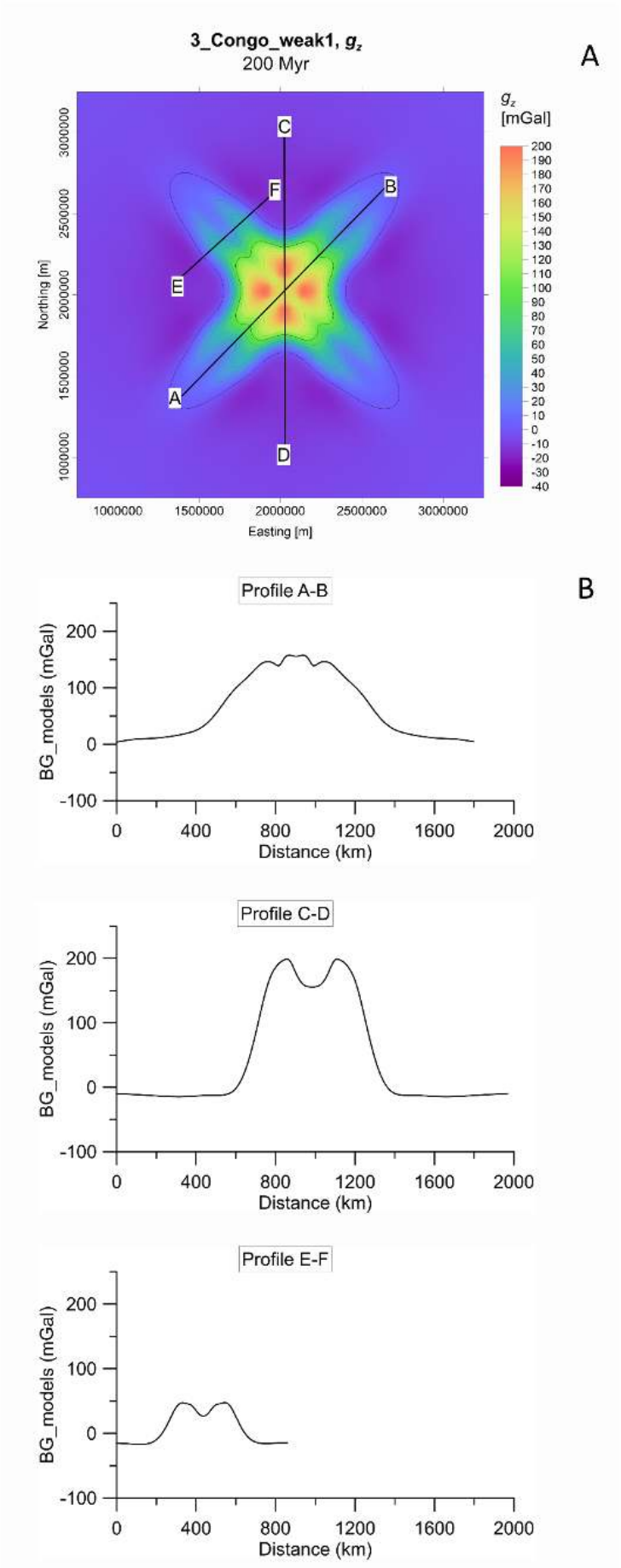

Figure 4.58 - *Static Forward Gravity Modelling corrected for Topography (SFGM_tc) of the 3_Congo_weak1 simulation. **(A)** Horizontal plane visualization, **(B)** along three cross-sections.*

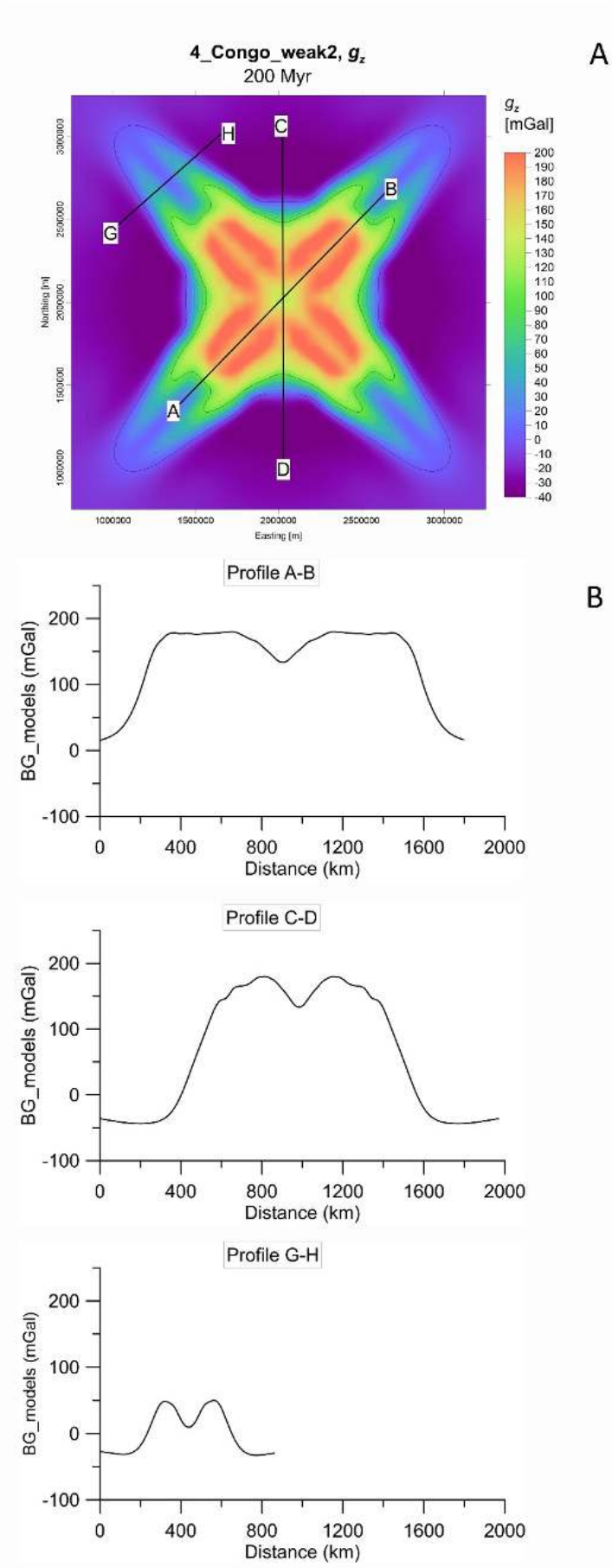

Figure 4.59 - *Static Forward Gravity Modelling corrected for Topography (SFGM_tc) of the 4_Congo_weak2 simulation. (**A**)Horizontal plane visualization, (**B**) along three cross-sections.*

4.5 Discussion

In order to model the first stage of the *CB* evolution as effect of multi-extensional tectonics, I performed seven 3D numerical models having different initial temperature conditions and geometries. They could reproduce the Congo Craton after its formation, characterized by the agglomeration of several cratonic blocks that left a weak 'suture' zone in the central part (De Wit and Linol, 2015).

The multi-extensional tectonics was simulated applying a slow divergent uniform velocity in *N-S* and E-W direction of 2.5 mm/yr for each side, for a maximum time lapse of 200 Myr. I kept the same kinematic boundaries in all the models, considering this extensional velocity suitable for the formation of a continental rift. In this way, I could evaluate if a small, but long-time tectonic event, lead to a basin formation in a cratonic area. The numerical models show how the different geometry designs and initial temperature conditions could influence the upwelling of the asthenospheric mantle, causing variations in temperature, viscosity and density, and thus in the surface topography. After qualitatively comparing the structures formed by the numerical simulations with the tectonic features observed from the interpretation of geology and geophysical data (Chapter 2 and 3), I considered the two simulations 3_Congo_weak1 and 4_Congo_weak2 (section 4.3), which better reproduce these features and more differentiate each other, as reference models. Indeed, from the first two numerical models implemented, composed of four cratonic blocks divided by weak zones, I obtained unrealistic results, consisting in a larger subsidence in the area between two adjacent cratons than in the central part of the model and uplift of the cratonic edges. As we already discussed in section 4.3, the application of multi-divergent velocities produces a circular subsided zone in almost all the early stages of the simulations (time step 0.010 Myr). This almost rounded area increases its size with time, while its topography is affected by significant variation. For these reasons, it can ideally represent the Cuvette Centrale and its heterogeneous basement, characterized by a series of topographic highs and depressions.

The main difference in the results obtained consists in the size of the central deformed area and in the structures formed inside it, which can be ascribed to the input geometry and initial temperature conditions. In particular, 3_Congo_weak1 and 4_Congo_weak2 models differentiate for the geometry design of the central weak zone, which has a doubled size and halved lithospheric thickness in the latter, with respect to the former. The other models implemented are not discussed in detail, because of the similarity in the results produced. Among these models, 5_Congo_weak3 has the same geometry and initial temperature conditions of 4_Congo_weak. It was carried out to test the effect of the variation of the orientation of the weak zone (its vertices are 45° rotated with respect to those of the other models) and the absence of transition zones between the cratonic and not cratonic lithosphere. Since the results of this numerical test compared to the reference models show just a difference in the shape of the asthenospheric upwelling, without further effects on the topography and viscosity variations (Figs 4.29-4.35), I stopped the run at 50 Myr. On the other hand, model 6_Congo_weak4, characterized by the same size of the weak zone of 3_Congo_weak1 model and having a lithospheric thickness equal to that of 4_Congo_weak2 model, shows structures very similar to those of 4_Congo_weak2 model. However, they form with a temporal delay of about 50 Myr, since the initial size of the central weak zone influences the speed of the deformation. In particular, such a delay occurs when the size of the weak zone is reduced to half of that of the 4_Congo_weak2 model. In contrast, the shape of the structures

formed in the central depressed area strongly depends on the initial lithospheric thickness and initial temperature conditions_applied. Furthermore, I implemented a 'hybrid' model (7_ Congo_cratons+weak), composed of four cratonic blocks and a weak zone in the center, which are divided by a lithosphere having a depth and bottom temperature intermediate between these two types (Fig. 4.44). The results show again the formation of the two elongated structures, well pronounced already at time step 50 Myr. Their size significantly increases at 100 Myr, going beyond the limits of the circular depressed area. These features are effect of the presence of an ''intermediate' lithosphere between the weaker central part of the model and more rigid cratonic blocks. However, the extensional stress produces uplift of the edges of the cratonic blocks, as in another model composed of four cratons (Fig. 4.11). Since the shapes of the structures formed are not so much consistent with those of the *CB* basement depths, I have not further analyzed the obtained results.

Looking in more detail at the reference models (3_Congo_weak1 and 4_Congo_weak2), we observe that the maximum subsidence of the surface topography is reached along two elongated structures, orthogonal each other, after a time lapse between 50 and 100 Myr. These zones are characterized by a low viscosity at the base of the lithosphere and Moho. On the other hand, at the time step 200 Myr, along the same zones, we observe an increase of viscosity at the Moho depth, due to the replacement of the crust with mantle material, and an initial uplift of the surface topography induced by the uprising of the asthenosphere at crustal depths (Figs 4.17-4.25). We can notice that these features, in the 4_Congo_weak2 model form 50-100 Myr before than in the other model (3_Congo_weak1). In particular, the edges of the two orthogonal structures initiate to uplift at their corners already at the time step 50 Myr in 4_Congo_weak2 model and are completely uplifted at 100 Myr. This stage of deformation is reached only at 200 Myr in 3_Congo_weak1 model. These elongated structures orthogonal each other converge in a quadruple junction and are very similar to the ridges formed in the numerical experiments of Gerya and Burov (2018). The authors implemented 3D numerical models, using I3ELVIS code, to simulate the nucleation and evolution of triple junctions induced by multi-directional lithospheric extension. The set-up of their models is quite different from those of my simulations, since higher multi-directional velocity rates (within the range 0.5-3.5 cm/yr) are applied to a relatively thin and young oceanic lithosphere (30 km thick), in which a 2 km×2km×2 km highly strained region (weak inclusion) in the lithospheric mantle at 13 km depth, is prescribed.

The quadruple junctions form in all their numerical experiments as transient features, that, according to the higher multi-divergent velocity applied, rapidly (in less than 1 Myr) migrate and evolve in the more stable triple junctions. In my models, the two elongated structures, marked by a significant different viscosity and topography with respect to those of surrounding areas, appear as stable features, becoming evident between 0.010 and 50 Myr and persisting for more than 100 Myr, with a gradual increase of their length (section 4.3). In order to better discuss possible similarities and differences between the modelling results and the main structures of the Cuvette Centrale, I draw three main cross-sections along the surface topography obtained at the time step 200 Myr and compared their trends with that of the basement depth reconstructed from the interpretation of seismic reflection data (Chapter 2). Such a comparison is limited to the cross-sections passing through the central part of the models, representing the Cuvette Centrale.

In doing such a comparison, we should also consider that the present-day basement depth of the *CB* has been shaped, after the first stage of extension, by successive compressional tectonics. In particular, the *CB*

was affected by a compressional deformation at the Neoproterozoic-Paleozoic transition, related to the Gondwana assembly (Pan-African deformation) and at the Triassic-Jurassic transition (far-field intraplate compression, Chapter 2). In addition, also the load variation induced by the sedimentation and erosion that accompanied the tectonic processes and enhanced by the climatic changes, contributed to modify the basement depth. Looking at Fig. 4.60, we can observe that the cross-section A-B, passing through one of the two elongated structures, shows an almost flat central subsided area in 3_Congo_weak1 model, while the same area is fragmented by highs and small depressions in 4_Congo_weak2 model. In contrast, along the profile C-D, 45° oriented with respect to the first profile, the situation is reversed, with the subsided surface topography mostly flat in the second model and disturbed by small sharp variations in the first model (Fig. 4.60). On ther other hand, the edges of the central depressed area are moderately and strongly uplifted in 3_Congo_weak1 and 4_Congo_weak2 model, respectively. Therefore, both models can simulate the formation of a depressed central area of different size, interrupted by minor lows and highs along one preferential direction, and limited by uplifted edges.

Furthermore, the surface topography in both models varies sharply of 2-3 km within a distance of ~ 100 km, along a cross-section perpendicular to the orthogonal structures (E-F, G-H). This demonstrates that the deformation induced by the multi-extensional stress can affect also areas far from the center. As we discussed in Chapter 2, the basement depth of the Cuvette Centrale is very heterogeneous. It is part of the large depression of the Congo Basin and is characterized by an alternation of lows and highs, *NW-SE* oriented, along profile 1 of Fig. 3.22 (Chapter 3) that crosses Bololo Basin, Inongo High, Lokoro Basin, Kiri High, Busira Basin, and Lulonga High and profile 2 of Fig. 3.22, crossing the Gilson and Samba basins, divided by the accommodation zone of the Kiri and Lokonia highs. This alternation resembles that reproduced by the two simulations considered, along the cross-section A-B (4_Congo_weak2) and C-D (3_Congo_weak1) of Fig. 4.60 and thus can be partly ascribed to a multi-extensional tectonics that by acting on the Congo Craton, produced a rift phase during the Mesoproterozoic age.

The resulting basement depth variation is represented in both simulations by the sharp topography change characterizing the central subsided area. On the other hand, the flat subsided area with a high peak in the center, observed along cross-section A-B (3_Congo_weak1) and C-D (4_Congo_weak2) of Fig. 4.60 resembles the shape of the Maringa ridge limiting the Lomami Basin (Fig. 2.9). The transition to the uplifted zones, bordering the subsided central area along the A-B and C-D profiles, reminds the surface topography variation between the Dekese basin and Lokonia High, shown along profile 4 of Fig. 3.22.

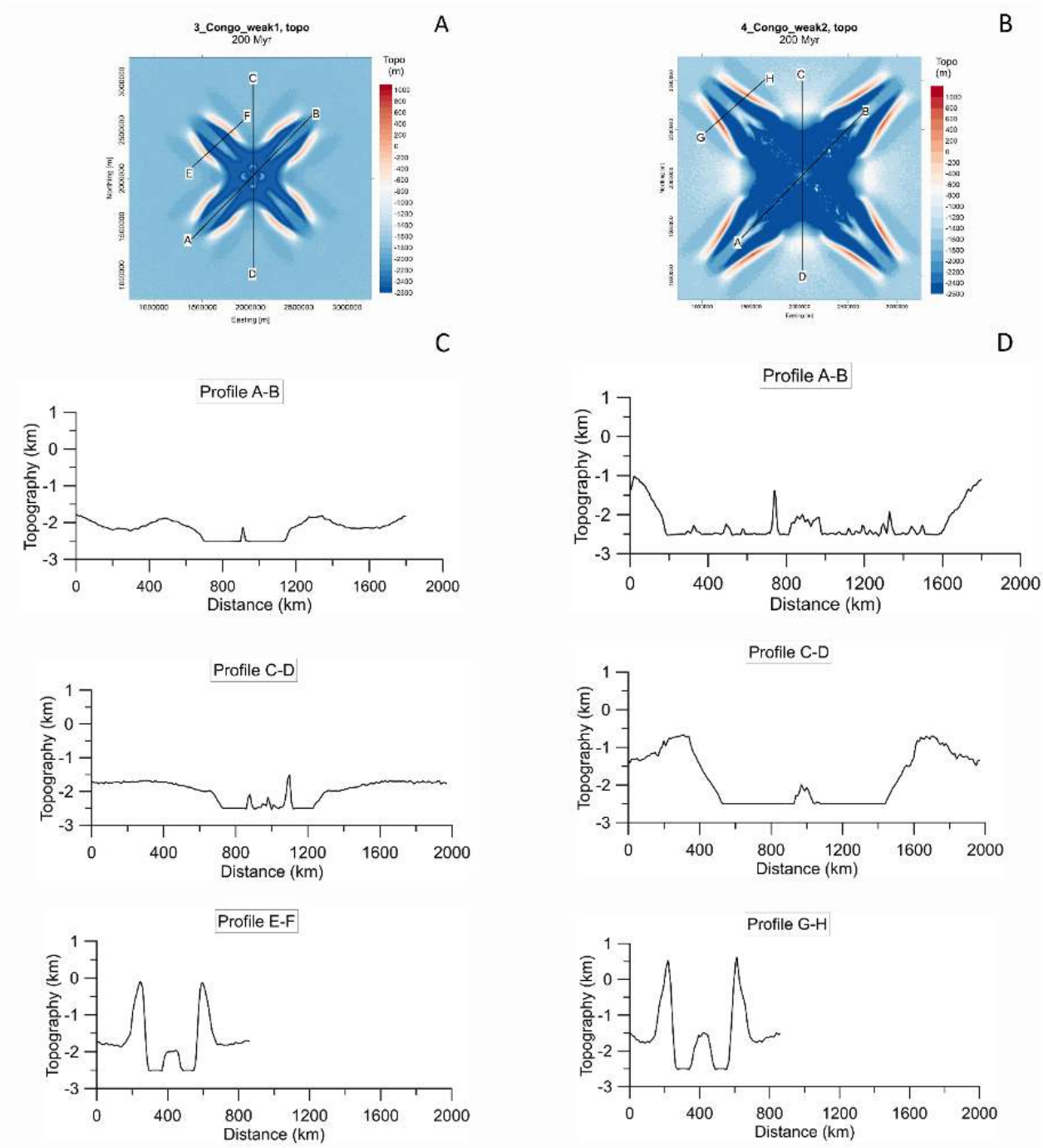

Figure 4.60 *– Surface topography at 200 Myr of the numerical simulations. (**A-B**) Horizontal plane visualization for the model 3_Congo_weak1 and 4_Congo_weak2. Black lines with labels show the location of three chosen cross-sections. (**C-D**) Three cross-sections of the model 3_Congo_weak1 and 4_Congo_weak2, respectively, showing the lateral variations of the topography.*

In order to distinguish the effects of the topography and density variation in the static model of the gravity field, I derived three cross-sections of the *SFGM* and compared the anomaly trends with those of the *SFGM_tc* for both models 3_Congo_weak1 and 4_Congo_weak2. We can notice that along both cross-sections A-B and C-D, the *SFGM*_tc produces anomalies of much larger amplitudes than those of the *SFGM* (Fig. 4.60 and 4.61). Indeed, in the last forward model, the effect of the topography variation (i.e. the formation of a large topography depression) almost counteracts that of the density increase due to the asthenospheric upwelling. On the other hand, along the cross-sections E-F (3_Congo_weak1) and G-H (4_Congo_weak2), the *SFGM_tc* shows quite weak positive anomalies (< 50 mGal), compared to the large range (±100 mGal) of the *SFGM*. This indicates that in the last case, the effect of the sharp topography variations (Fig. 4.60) is much more significant than that of the density changes. The results of the *SFGM* of the two models are also comparable with the gravity disturbance displayed in Chapter 3, taking into account that the last one includes the effect of sediments, not considered in the numerical models. With this aim, I compared the values of the SFGM along three cross-sections with that of the gravity disturbance obtained along several cross-sections (Fig 4.61).

Since the numerical models cannot reproduce all the small heterogeneities of the structures formed during the evolution of the *CB*, the *SFGM* produces a smoother signal with higher amplitude, compared to that of the gravity disturbance. On the other hand, the observed gravity field is characterized by the alternation of weak positive and strong negative anomalies, with a trend similar to that of the *SFGM* along the three cross-sections. For instance, the trend of the cross-section A-B of the 3_Congo_weak1 model and C-D resembles that displayed by the cross-sections A-A' and E-E' of the observed gravity field (Fig 4.61).

In the same way, the trend of the cross-section C-D of the 4_Congo_weak2 model resembles that of the cross-sections BB’ and DD' of the gravity disturbance (Fig. 4.61). However, the observed gravity anomalies are prevalently related to the density variations in the shallow crust, since the topography of the area is quite low (< 300 m, Fig. 4.60). In particular, the minimum values are located in correspondence of the deep sedimentary basins and thus are likely induced by the low density of the sediments. In contrast, the positive values fall in correspondence of the tectonic highs (e.g., Kiri High, Mossaka High), likely characterized by a high-density crystalline crust (Chapter 3). There are also some parts of the Cuvette Centrale, in which the density of the different crustal layers produces small gravity anomalies (between -25 mGal and +10 mGal), as along cross-section C-C’ (Fig. 4.61). This trend is similar to that of the cross-section A-B of the 4_Congo_weak2, which instead reflects the combined effect of the topography subsidence and density increase, due to the asthenospheric uprising (Fig. 4.61).

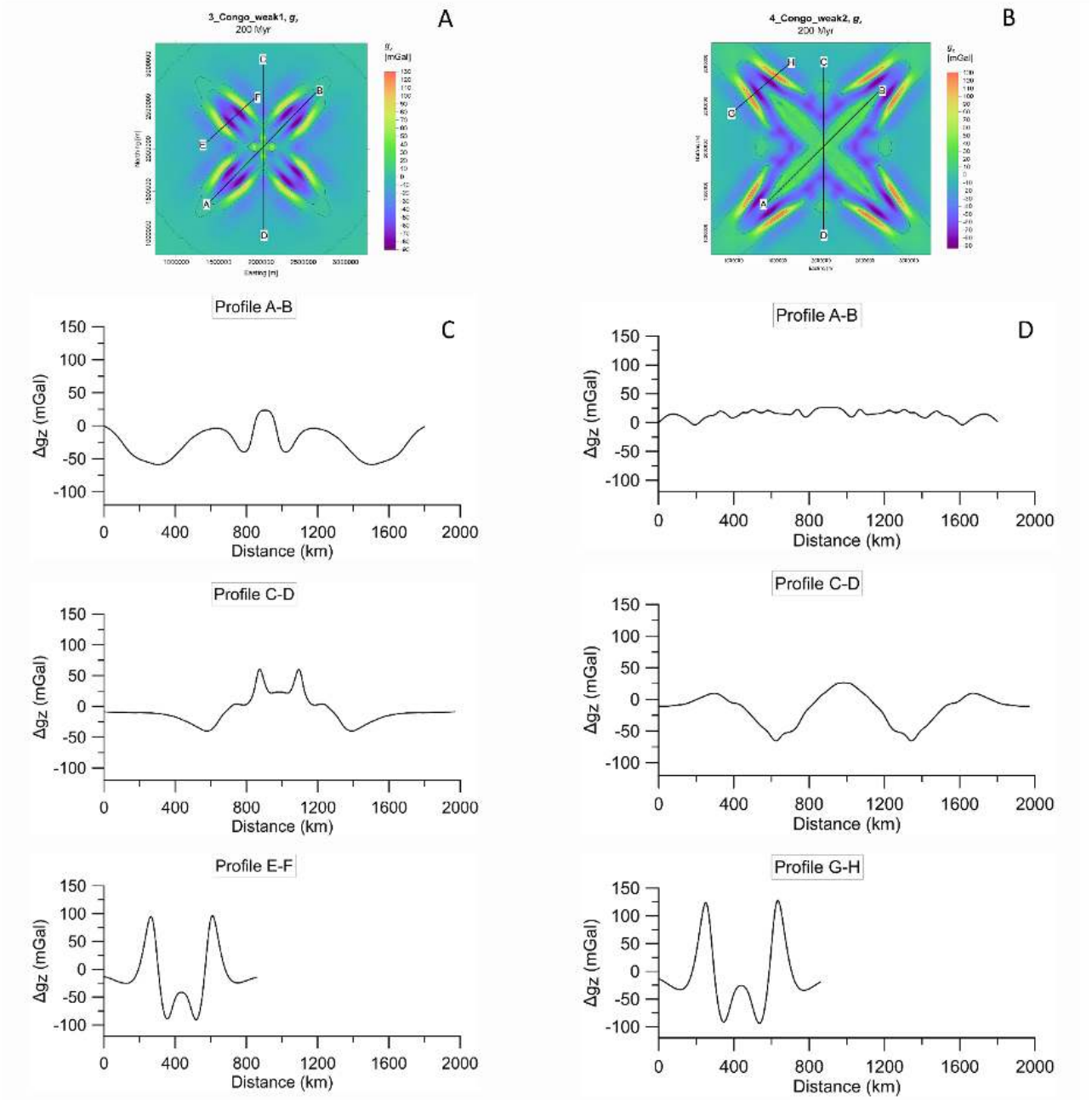

Figure 4.60 - *Static forward gravity modelling (SFGM) of the numerical simulations 3_Congo_weak1 and 4_Congo_weak2, respectively. (**A-B**) Horizontal plane visualization for the model 3_Congo_weak1 and 4_Congo_weak2. Black lines with labels show the location of the three chosen cross-sections. (**C-D**) Three cross-sections of the 3_Congo_weak1 and 4_Congo_weak2 model, showing the lateral variations of the gravity anomalies.*

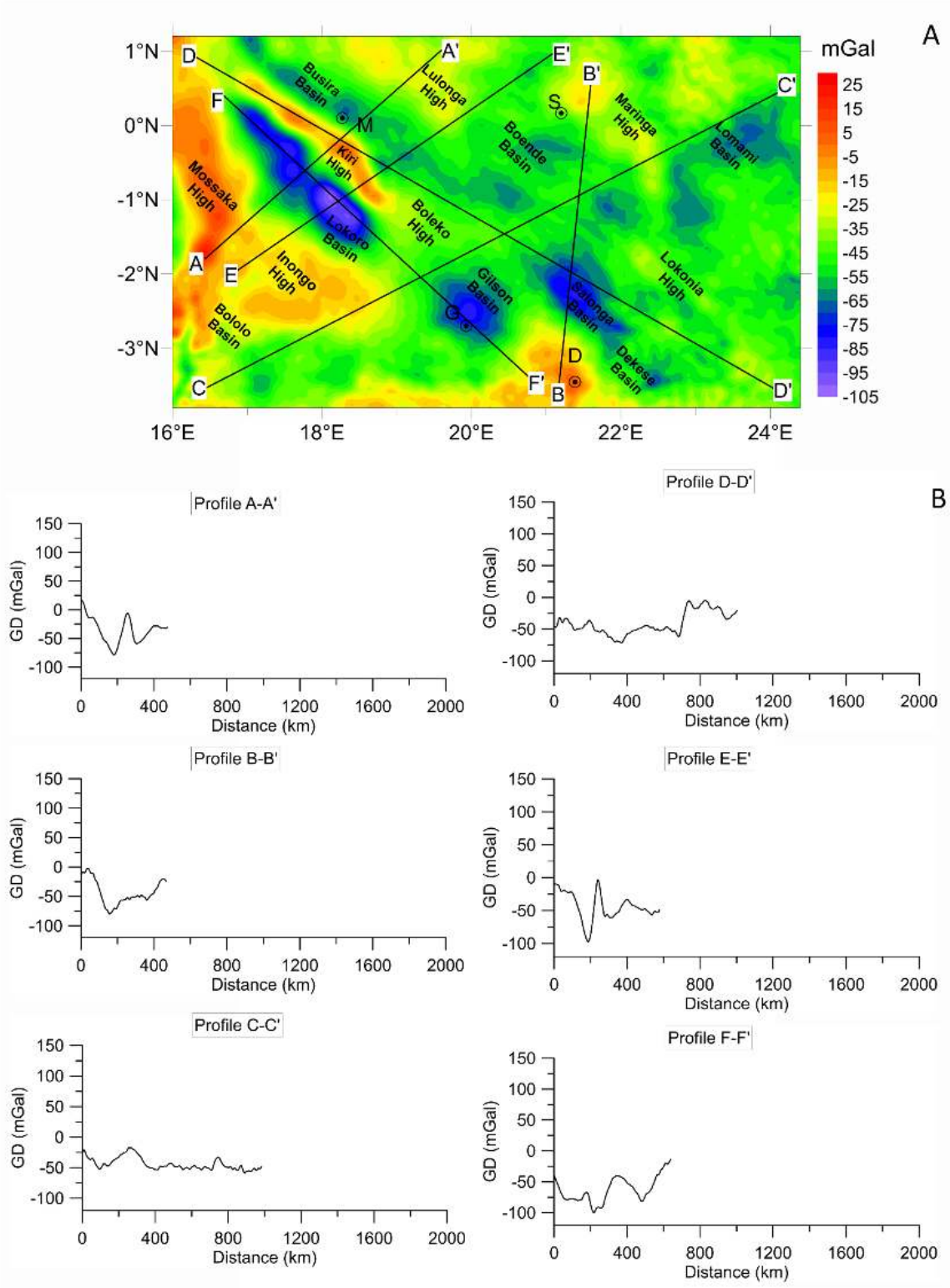

Fig. 4.61 *– Gravity disturbance variation inside the Cuvette Centrale. (**A**) Map visualization of the gravity variation; (**B**) Lateral gravity changes along six profiles displayed in A.*

4.6 Conclusions

In this chapter, I discussed the 3D numerical models implemented to test the hypothesis that multi-extensional velocities, acting on a cratonic area, caused rift phases, signing the initiation of the *CB* formation and producing the first order heterogeneities of the basement depth. For this purpose, I assumed that the amalgamation of the cratonic blocks forming the Congo Craton left a weak 'suture' zone in the center, having a size of 10% or 20% of the total area and a thinner and hotter lithosphere than the surrounding cratonic areas. The results obtained showed that the tectonic structures, formed by applying a multi-divergent uniform velocity of 2.5 mm/yr for each side, for a maximum time lapse of 200 Myr, are principally influenced by the variation of geometry design (size and lithospheric thickness of the weak zone) and initial temperature conditions.

The main results given by the numerical simulations 3_Congo_weak1 and 4_Congo_weak2, consist in the formation of an almost circular subsided area in the central part of the models, as effect of the radial extension, promoting the asthenosphere upwelling. This depressed area, which can represent the first stage of formation of the CB, is the effect of the replacement of the shallow lithosphere with the denser and stiffer mantle material. The strong lateral density variations cause the formation of a series of topographic highs and lows inside the subsided area and significant uplift at the transition zones towards the almost undeformed cratonic parts. The almost circular topographic depression is intersected by two strongly subsided elongated structures, forming quadruple junctions, similar to those produced by the numerical models of Gerya and Burov (2018). The structures formed during the simulated multi-extensional tectonics well represent the first order heterogeneity characterizing the *CB* basement depth, taking into account that the last one has been further modified by other tectonic and climate events. In particular, the *CB* basement depth is characterized by a series of lows and highs, *NW-SE* aligned, similar to those formed in my models in the central depressed part. The alignment of these modelled structures depends on the orientation of the central weak zone, as I shown in 5_Congo_weak3 model. These structures are similar for the two reference models, depending on the initial shape and lithospheric thickness of the central weak zone. In contrast, assuming a greater size of the weak zone (20% of the entire area), it increases the speed of the deformation and size of the structures, which form in an earlier time step than in case the weak zone is reduced to 10% of the model size. In order to check the consistency of the results obtained from 3D numerical modelling, I performed two main types of forward gravity modelling of the two reference numerical simulations. I first carried out 'dynamic' models (*DFGM*), obtained from the difference between the gravity models at 200 Myr and those at 0.010 Myr. These models show positive anomalies induced by the mass excess related to the asthenospheric upwelling, effect of the multi-extensional stress. Afterwards, I performed 'static' forward models at 200 Myr (*SFGM*), obtained by subtracting a reference gravity model, that produce both negative and positive anomalies. The anomalies show a similar distribution to those of the *DFGM*. In particular, the two elongated structures orthogonal each other, observed already from the lateral variations of other parameters (e.g., topography, viscosity) are well distinct in both models.

The comparison between the *SFGM* with the observed gravity anomaly field of the Cuvette Centrale (Chapter 3), shows that the modelled anomalies have a smoother trend and larger amplitude. These results could have been expected, since my simulations do not take into account the effect of sedimentation, which

influences the observed gravity field and could have partly reduced the amplitude of the signal. In addition, the *CB* has been affected by compressional tectonics during the geological time, which has further modified its original structure (e.g., the compression related to the Gondwana assembly). However, comparing the modelled with the observed gravity field along some cross-sections, we can observe a similar alternation of weak positive and strong negative gravity anomalies, which in the models are related to the density and topography variations induced by the upwelling of the asthenosphere. In contrast, in the real case, the anomalies reflect also the combined effect of the variation of the sedimentary thickness and the possible intrusion of mafic bodies, with a consequent crustal thickening. In order to discriminate the effect of the density variations from that of topography in the modelled gravity filed, I implemented another static forward modelling (named *SFGM_tc*), in which I suppressed the effect of topography, subtracting from the *SFGM* the gravity effect induced by the first 23 km, comprehensive of the sticky air layer and topography variations. I noted that the effect of the density variations is enhanced in the central subsided area, where strong positive anomalies are observed, while is negligible in the peripheral part of the two elongated structures.

CHAPTER 5

- What does the Congo Basin tell us? -

5.0 Introduction of the chapter

In this last chapter, I discuss the possible tectonic processes that formed the subsidence of the *CB*, based on the main results of my *PhD* project, with respect to those obtained in previous studies. I also suggest possible outlooks for future researches.

5.1 General discussion

The origin of the intracratonic basins (*ICBs*) is highly debated. Different hypotheses attempted to explain the long-lasting subsidence of the *ICBs*, characterized by prolonged intervals of low rate subsidence, alternating with episodic accelerations in subsidence rates. The most common involve: (1) lithospheric stretching and subsequent thermal contraction; (2) crustal and mantle phase changes, metamorphism and intrusion; (3) changes in the intraplate stress field; (4) convective instabilities in the mantle. However, several *ICBs* originated from one or more rift phases occurred during the continental break-up. A number of long-lived *ICBs* in North America, such as the Michigan, Illinois, and Williston basins, developed as distinct circular or oval depocenters at about 520 Myr (e.g., Klein and Hsui, 1987), associated with the break-up of South America-Laurentia from Gondwanan superassembly. In Australia, a large *ICB*, known as the Neoproterozoic Centralian Superbasin, formed at the time of break-up of Rodinia (ca. 800 Myr. Korsch and Lindsay, 1989).

Supercontinents formation/disruption are closely linked to the whole mantle convection, being them both an effect and a cause of it (Mitchell et al., 2021 and references therein). Indeed, mantle convection can favour supercontinent assembly, but then the newly formed supercontinent produces significant changes to mantle convection patterns. More precisely, continental assembly is driven by the oceanic subductions occurred along the continental margins, which induce downwelling mantle flow. However, after the supercontinent forms, the intensity of local downwelling can reduce, causing both return flow from circum-supercontinent subduction and subcontinental thermal insulation. These conditions would facilitate a plume formation underneath the supercontinent or a thermal anomaly at the base of the lithosphere, which can lead to a rift formation and possibly to a lithospheric break-up, with consequent continental fragmentation. However, this is the case of the Midcontinent rift, a fossil feature within the North American continent, which records a late stage of rifting. Stein et al. (2014) attributed the formation of the Midcontinent rift to Laurentia-Amazonia rifting (1100 Myr), occurred during the Greenville collisional events, leading to the Rodinia assembly (maximum packing between 1000 and 900 Myr). This implies that rift basins could also form in a global compressional tectonic frame, probably at a time when shortening was absent or occurred far away from the rifting place (Stein et al., 2014).

As discussed in Chapter 2, also the *CB* started to form from a rift phase, during the late Mesoproterozoic (about 1200 Myr). The age of its initiation, obtained from the interpretation of the almost 3000 km of seismic reflection profiles (Chapter 2), is older than that assumed in previous studies (Daly et al, 1992; Kadima 2011; Linol et al, 2015), corresponding to a time prior to that of Rodinia assembly. Tectonic reconstructions before the Rodinia assembly are quite uncertain, due to the very limited and sparse geological records. However, the large number of continental collisions dated between 2100 and 1800 Myr records the formation of the Earth's oldest known supercontinent, named Columbia supercontinent, assembled between 2000 and 1600 Myr (Goldberg, 2010). Based on magmatism, paleo magnetism and dike swarms, previous studies dated the initial phase of break-up of this supercontinent just after its maximum packing (1900-1700 Myr), while the final

break-up probably occurred between 1300-1200 Myr (e.g., Nance et al., 2013 and reference therein). In this tectonic scenario, the *CB* formation can be related to one of the final phases of the Columbia break-up, resulted in several-failed rift (e.g., Goldberg, 2010).

At this time, the cratonic blocks, being already dispersed after the fragmentation of Columbia could have been more likely subjected to a multi-extensional tectonics responsible for the *ICBs* formation. To support this hypothesis, we have to refer to the thermo-compositional structure of the underlying *CB* lithosphere, which is apparently similar to those of other old cratonic areas, characterized by thick cold roots. In particular, the recent seismic tomography model of Celli et al. (2019) has shown that the Congo Craton is composed of at least three cratonic blocks, 200-250 km thick, with eroded margins. Furthermore, the lithospheric thermal structure, reflected by the surface heat flow values (Lucazeau et al., 2015) and obtained from inversion of this seismic tomography model, taking into account the mantle compositional variations (Finger et al., 2021), indicate typical cratonic temperatures. On the other hand, mantle density variations, induced by the composition, show small depletion in *Fe* components, which is expressed by the Mg number ([1]Mg # < 91) (Finger et al., 2021). This means that the original Archean lithosphere composing the Congo Craton could have been destroyed and regrowth, or simply rejuvenated. The existing cratons have been previously thought to preserve their original structure, resisting the effect of possible hot asthenosphere/plume upwelling, by spreading the heat to the sides. To this purpose, the numerical models of Koptev et al. (2015) explain the formation of magma-rich and magma-poor rifts along opposite craton sides, by simulating the plume deflection by the cratonic keel, channeling along one of its side. More recently, Liu et al. (2021), based on geochemical data and geodynamic models, introduced the hypothesis that also the lithosphere of cratons, characterized by thick roots, can be affected by cycles of thinning and re-thickening. With this hypothesis, they could reconcile the existence of the thick cratonic roots of the Slave craton and surroundings with the presence of a Mesoproterozoic large igneous province. The processes of recratonization, following significant disruption of the lithospheric roots by Proterozoic mantle plume, could have affected the lithosphere of the Superior Craton, which would have thinned by the midcontinent rift event (1100 Myr) and regrown during the Neoproterozoic. Another example is given by the Kaapval Craton, which would have thinned, producing the Bushveld complex (2000 Myr) and regrown after these events to reach again a thickness of about 200 km (Liu et al., 2021). The re-thickening of the cratons would occur through mantle melts that seal them along existing gaps, even if these thinned parts are far away from the main heat source (Liu et al., 2021).

The rifting and suturing effects linked to mantle plumes should be plausible if we assume large-scale movements of tectonic plates during the supercontinent assembly/breakup (Foley and O'neill 2021; Liu et al, 2021). The destructive or constructive action of a plume might be related to different types of regional tectonic stress (Foley and O'Neill, 2021). In case of regional extensional forces, the cratons can undergo rifting and thus thin their lithosphere, while compressional tectonic forces would prevent the destructive action of a plume. In case of compressional stress, the plume, exerting local extension, can induce an initial rift phase, only with minor thinning of the cratonic roots. In this scenario, plume melts could not reach the surface, but only metasomatized the upper mantle and possibly accretionate at the base of the crust/mantle lithosphere. This

[1] Mg# =100×Mg/(Mg+Fe)

process would also favors the regrowth of the cratonic roots after the local thinning due to the plume action and enhances the topographic subsidence. If this would have been the case of the *CB*, the compressional stress could have been the effect of the ridge push of mid-oceanic rifts, opened during the last pulse of breakup of Columbia, occurred between 1600 and 1200 Myr (Nance et al., 2013 and reference therein). The hypothesis of the interplay of regional compressional stress field with mantle plume is appealing, since it fits the geophysical observations. In particular, it would justify (1) the presence of a crust thicker (about 40 km, Ojo et al., 2021) than it would be in case of isostatic equilibrium; (2) the small *Fe*-components depletion of the lithosphere underlying the *CB* (Finger et al., 2021). In addition, the removal of the lithospheric roots due to the plumes' action and their subsequent restoration has been proposed for both the South American and African cratons by Hu et al. (2018). However, I rule out this hypothesis, due to the absence of a large igneous province of Mesoproterozoic age in the study area and surroundings. Furthermore, no short-scale lateral mantle velocity variations have been detected from seismic tomography within the cratonic blocks composing the Congo Craton, which would mark episodes of thinning and re-thickening of the lithosphere (Liu et al., 2021). In contrast, I can speculate that slow multidirectional divergent velocity, acting on a cratonic lithosphere, could have induced the initial subsidence of the *CB* in a weaker part of the craton. Such a weak zone could have represented the suture between the different cratonic pieces (De Wit and Linol, 2015) or have simply been an inherited heterogeneity from the processes of the cratons formation.

The relatively deep crustal and lithospheric roots (Ojo et al., 2021; Celli et al., 2020) indicate that the extensional stress that initiated the *CB* subsidence has not induced significant crustal/lithospheric thinning, possibly, because it did not act for a sufficient time, being followed, after about 100 Myr, by compressional stress related to the Rodinia assembly. However, the extensional stress has likely caused the intrusion of high-density mafic bodies, whose presence is supported by the gravity models performed in this thesis (Chapter 3). Indeed, the gravity field, reflecting the effect of the crustal and sub-crustal lithosphere (*BG_RES2*), shows strong localized positive anomalies in the southern part of the *CB*, in the Dekese Basin and surroundings. This finding has also been confirmed by the study of Watts et al. (2018), also based on gravity analyses. Since the seismic tomography of Ojo et al. (2021) shows that the shear wave velocities are not very high in the lowermost part of the crust (< 4 km/s), I suppose that most of the crust would not have been thinned during the extensional tectonics and the injection of mafic bodies would have occurred only sporadically. In particular, dense basaltic lavas and dolerites are present in the Mbuji-Maji Supergroup, deposited during the initial rifting stage, in the Mbuji-Maji area, in the southeast continuation of the Dekese and Salonga Basins (Delvaux et al., 2021). They are found on top of the Mbuji-Maji Supergroup in the southwestern branch of the Mbuji-Maji basin, while they are present as a large planar intrusion in the middle of the Mbuji-Maji Supergroup in the northeastern branch. Alternatively, I can hypothesize the presence of a high-density lowermost crust, even if the last one has not been detected by the seismic tomography. Indeed, high-density minerals are not necessarily characterized by anomalous shear-wave velocities. In this case, the high-density anomalies of the *BG_RES2* residuals would be related to mafic bodies composing the lower crust.

I can also speculate that the asthenospheric upwelling induced by the extensional stress has metasomatized the lithospheric cratonic roots, producing weakening and densification of the original cratonic lithosphere. This process that probably caused a small erosion of the lithospheric roots, considering the present-day great

lithospheric thickness (200-250 km, according to the seismic tomography model of Celli et al., 2020), could have enhanced the basin subsidence, initiated by the action of extensional stress. The eroded lithosphere could have been replaced by the cooled asthenosphere, during the post-rift phase, lasting 300 Myr. During this period, there are no signs of tectonic stress related to the Rodinia assembly and break-up. The reconstruction of the basement depths and those of the other seismic horizons show the migration of the *CB* depocenters from the Proterozoic to Jurassic times and lateral thickness variations of the sedimentary layers, with a progressive decrease in the influence of the initial rift structure.

The initial rift phase produced stronger subsidence in the northern part of the Cuvette Centrale, as observed by the greater thickness of the syn-rift sediments located in that part of the basin. On the other hand, the following compressional stress, related to the Gondwana assembly, enhanced the initial subsidence related to the rift extension, in the southern part, forming the deepest depocenters of the *CB* (Lokoro Basin, Gilson Basin, Bololo Basin and Dekese basin). Therefore, both the extensional and compressional phases might not have acted uniformly on the Cuvette Centrale, but along different preferential directions. The succession of compressional events to a rift extension occurred also in other *ICBs*, such as those of North America, producing significant variations in their subsidence trends and morphology (e.g., Klein and Hsui, 1987). Another example is given by the phases of intracontinental orogeny that lead to the separation of the Centralian Superbasin of Australia in four main basins (between 600 and 300 Myr), such as Officer, Amadeus, Ngalia and Georgina basins (e.g., Lindsay, 2002). Following the Gondwana assembly, there were only minor phases of tectonic stress accompanied by climatic changes that further modified the morphology of the Cuvette Centrale. In particular, there was a post-orogenic phase, related to Gondwana super-fan (~500-380 Myr), observed from outcrops and Samba-Dekese well cores that compose the sequences of the Paleozoic Red Beds. In addition, another compressional phase occurred at the base of Triassic age, related to Gondwanide orogeny (~320-200 Myr) and probably at the base Jurassic, where we observe a hiatus coeval with the Gondwana breakup (~200-157 Myr). Among the climatic changes, the new seismo-stratigraphic model evidences the existence of a global glacial event, while the *CB* was drifting from the South Pole to the Equator (Delvaux et al. 2021). The recognized tectonic events allowed me to confirm the division of the stratigraphy of the *CB* into three major stratigraphic units, separated by two major tectonic unconformities related to the Pan-African deformation and far-field intraplate compression at the Jurassic-Cenozoic transition, (Kadima et al., 2015). The re-interpretation of the seismic reflection profiles, integrated with well log and outcrops data, lead me to identify two new seismic horizons in the first stratigraphic unit. The first one divides the Mesoproterozoic sediments into two sequences (Sequence 0 and Sequence 1), composed of coarse siliciclastics, carbonates and dolostones, while the other one separates them from the Neoproterozoic stratigraphic layer (Chapter 2). The present-day *CB* basement topography, revealed by the interpretation of seismic reflection profiles and magnetic and gravity anomalies, is quite heterogeneous, being characterized by a series of topographic depocenters and highs *NW-SE* oriented. This alinement has been detected for the first time in Cahen (1954) and confirmed later by Kadima et al. (2011a and 2015), Buiter et al. (2012), and more recently by Kaban et al. (2021). However, the gravity analysis of Buiter et al. (2012) and Kadima et al. (2011a and 2015) did not provide a reconstruction of the basement depth. In contrast, with my analysis of the gravity fields, using as constraints the seismic data, I could recover the basement depths in the Cuvette Centrale, with more accuracy in the area between the seismic

profiles, suppressing the artefacts due to their interpolation. These new results revealed the continuity of the Kiri High, separating the *CB* into two parts. This is also confirmed by the matching of this feature with the axial magnetic zone, *NW-SE* oriented. In the past, the Kiri High was thought to be the rift axis, successively inverted by the compressional tectonics (Daly et al., 1992; De Wit et al., 1992), while Kadima et al. (2011a, b) and more recently Raveloson et al. (2021), based on a surface wave velocity model, highlighted the role that salt tectonics could play in creating this structure. According to my interpretations, the Kiri High formed consequently to a compressional reactivation (Chapter 2).

The comparison between the basement depths that I reconstructed from the interpolation of seismic data (seismic basement) with those derived from the gravity analyses, shown the existence of common features (Chapter 3). In particular, I could identify three main deep depocenters (Lokoro, Gilson and Boende Basins), where the sedimentary thickness is between 9 and 18 km. These values are greater than the previous ones of Linol et al. (2016) that estimated a maximum thickness near the center of the basin of only 6 km, as well as of those of the very recent study of Raveloson et al. (2021), revealing only two basins ~8 km deep, divided by the Kiri High. However, the deepest depocenters of the Lokoro and Gilson Basin, detected from gravity inversion, are shifted southeast and south, respectively, with respect to the maxima shown in the seismic basement depth. Such a maximum, in case of the Lokoro basin, lies in an area uncovered by seismic profiles (Chapter 3). Furthermore, the gravity basements depths show other basins located in the areas uncovered by the seismic data, such as the Lomami Basin in the northeastern sector of the *CB*. Other basins, identified only when I used in the inversion the greatest superficial density contrast (-0.800 g/cm^3), are located southeast to the Gilson Basin. Along the seismic profiles the seismic and gravity basement show a general good consistency, while the discrepancies could be ascribed to the gravity resolution, not sufficiently high to detect the parts of the basement characterized by sharp lateral variations induced by faults, or to the effect of the crystalline crust not completely removed from the inverted gravity residuals. The most recent basement depth reconstructed by Kaban et al. (2021), which is based on the inversion of the decompensative gravity anomalies and takes into account the variations of the lithospheric rigidity, shows a similar distribution of sedimentary depocenters, with a maximum thickness, exceeding 10 km in Lokoro and Salonga Basins. However, the tectonic features appear better defined in this study, with a clear distinction between the different depocenters.

Other studies have used an integrated approach, based on the analysis of geological and geophysical data, to reconstruct the structure of other *ICBs*. In particular, Perron et al. (2018), used satellite images, geological, and potential field data, to investigate the basement structure of the basins lying on the African metacraton (Reggane, Ahnet, Mouydir and Illizi basins). Their results revealed that these basins and the *CB* are coeval and their evolution has been influenced by some common tectonic and climatic processes. For instance, they have been affected by the Pan African collision that preceded the Paleozoic deposition of the sandstone series (named Red Beds in the *CB* stratigraphy). Furthermore, in these basins as also in other African *ICBs* (e.g., Taoudeni basin, Delvaux et al., 2021), have been found glacial deposits of the age between the Ordovician (Perron et al. 2018) and Late Devonian-Early Carboniferous (Chapter 2). Before this study, 3D numerical models have been mostly performed to understand the effects of the interaction between the mantle plume and lithosphere (e.g., Gerya et al., 2015, Koptev et al., 2015, Koptev et al. 2018a, Koptev et al. 2018b, Baes et al., 2016; 2019; 2020). Some of these studies investigated the hypothesis that the interaction of a mantle

plume with old oceanic lithosphere can initiate subduction. They arrive to the conclusion that the negative buoyancy of the lithosphere is one of the main factor triggering the subduction initiation. Koptev et al. (2015) were the first to study in 3D the rift formation as effect of the interplay of mantle plume with a variable lithospheric thickness. They could explain the heterogeneous topography and magmatic products distribution in the East African Rift, as the effect of the plume location with respect to the lateral variation of the lithospheric thickness. More recently, Koptev et al. (2018b) investigated how the geometry and dynamics of rifting to continental break-up is influenced by the interaction of a continental lithosphere, rheologically stratified with a mantle plume. However, the results of these simulations produced only linear rift structures. Afterwards, the study of Koptev et al. (2018a) demonstrated that the formation in a continental area of simple or interconnected triple junctions are the product of the combined effect of a mantle plume and slab pull forces, generating uniform *E-W* velocity and not uniform northward velocity of similar rates. In contrast, linear rifts formed, when one a significant difference in the rates of the velocities are applied. However, extensional stress due to plate tectonics is the most common mechanism for rift formation at the present-day (Brune et al., 2014).

The recent study of Gerya and Burov (2018) tested the hypothesis that the multi-divergent velocities applied to an oceanic lithosphere could have been responsible for the formation of triple junctions from the evolution of the transient quadruple junctions. Therefore, considering that the formation of the first-order heterogeneities of the basement depth of the *CB* have been induced by an extensional stress (Chapter 2), I implemented 3D numerical models applying uniform multi-divergent velocities to a cratonic lithosphere. To this aim, I modelled the Congo Craton as a single cratonic block with a weak zone in the center (representing a suture zone or an inherited heterogeneity) or as composed of four cratonic blocks surrounded by weak zones. In all the simulations, I applied a uniform velocity of 2.5 mm/yr in *N-S* and *E-W* direction (in agreement with typical velocities of continental rift formation), for a maximum time lapse of 200 Myr. Besides the geometry design, the numerical simulations differ each other for the size, lithospheric thickness, and continental geotherm assumed for the weak zones (Chapter 4). The first two simulations, considering four cratonic pieces surrounded by weak zones, produced, after a time lapse of 100 Myr, more subsidence along the cratonic borders than in the central part of the model. Due to the inconsistencies of the results obtained with the basement depth of the *CB*, I performed a greater number of simulations, considering a simpler geometry design, with only an almost circular zone in the center of a cold cratonic area, composed of a thinner and hotter lithosphere. The results show the formation of a circular central depression, limited by uplifted edges. The formation of a circular basin is a typical effect of the interaction between a plume and the mantle lithosphere, as shown in previous 3D numerical models (e.g., Gerya et al., 2015; Baes et al., 2016; 2019; 2020). On the other hand, according to Koptev et al. (2015), the location of the plume along the cratonic edges determines the formation of quite asymmetric structures, with surface topography variations of different amplitude. The interaction of a plume with a lithosphere having a variable thickness results in the formation of linear rifts with different depths, characterized by igneous products, along the cratonic edge where the lithosphere is thin, and magma devoid, in the central part of the craton. In contrast, in my models, when a multi-divergent velocity is applied to a cratonic lithosphere with a weak central zone, the resulting surface topography within the circular-depressed area is characterized by a series of topographic lows and highs aligned along a preferential direction (Chapter 4). The symmetry of the formed structures is due to the assumed geometry design and low extensional

rate applied. The last one determines also the absence of magmatic products during the rift structures formation. Furthermore, I noticed that the maximum subsidence during the first 50-100 Myr is concentrated along two elongated structures orthogonal each other that form a quadruple junction. This feature does not evolve in a triple junction as in the numerical models of Gerya and Burov (2018), probably because of the low extensional rate assumed in my models. On the other hand, interconnected rifts forming triple junctions are the direct effect of the combination of symmetric and asymmetric divergent velocities applied (Koptev et al., 2018a).

The elongated structures are the direct effect of the asthenospheric upwelling, which replaces the less dense mantle lithosphere and later (after ~100 Myr) the crust (Chapter 4). As soon as the asthenosphere reaches the crustal depths, the surface topography tends to uplift. Since the crust is currently quite thick (Ojo et al., 2020), the results at the last time step (200 Myr) represent a more advanced stage of deformation that was not reached by the *CB* during the rift phase. This makes more difficult the comparison between the modelled and reconstructed present-day basement depth. In addition, we should consider that the *CB* basement depth reflects also the effects of the following tectonic compressional phases and of sedimentation/erosion, which are processes not simulated in this study. We do also not know if the divergent velocity acted uniformly on the Congo craton or more significantly along one direction. However, despite all the assumptions used in the numerical models, the resulting topography heterogeneities resemble those of the current basement depth (Chapter 4). In particular, my models could reproduce the sharp topography variations (2-3 km) within a short distance (about 100 km), which characterize the basement depth of the *CB*, for instance, at the transition between the Dekese basin and Lokonia High (Chapter 2). I could further notice that the effects of the multi-extensional stress propagate also in the peripheral parts of the central weak zone, which become progressively uplifted. These features resemble the mobile belts located around the edges of the *CB*. The comparison of the modelled static gravity fields, implemented using as input the surface topography resulting from two numerical simulations, with the gravity disturbance anomalies (Chapter 4) shows that the former produce a smoother signal with higher amplitude, compared to the latter. In particular, the modelled fields could reproduce a trend of anomalies similar to that observed, but not the shape of all the small anomalies related to the local heterogeneities of the basement. On the other hand, I want to point out that the origin of the modelled anomalies is due to the combined effect of the topography and density variations induced by the mantle upwelling, while the trend of the gravity disturbance is significantly influenced by the sediment distribution, since the topography of the area is quite low. In particular, the minimum negative values of the observed gravity field are located in correspondence of the deep sedimentary basins, while the positive values correspond to the tectonic highs (e.g., Kiri High, Mossaka High), likely characterized by a high-density crystalline crust (Chapter 3). Therefore, from the analyses of all the obtained results, I can state that my numerical models simulate the first stage of the evolution of the *ICBs* formed from a failed rift, reproducing their main tectonic structures.

5.2 Conclusions

In the frame of this *PhD* project, I investigated the formation and evolution of the long tectonic history of the *CB*, using a multidisciplinary approach that applies different methods integrating both geological and geophysical data. In particular, I integrated all available exploration geophysical data (seismic reflection, refraction, and well-log data) with satellite gravity data, outcrops, and results of previous studies. The progressive growth of scientific interest for the *CB*, from 50's (Cahen, 1954) to the present-day, is due to its potential reservoir of hydrocarbons and precious minerals, such as cobalt and diamonds. This lead to the deployment of almost 3000 km of seismic reflection profiles, collection of thousands of samples along the Congo River, and drilling of four boreholes in the central part of the *CB* (Cuvette Centrale). The complete analysis of these large datasets, made for the first time in this thesis, allowed reconstructing in more detail than before the stratigraphic and tectonic history of the basin, putting it in the frame of the evolution of the entire African continent, during the last 1200 Myr. The results shown that the *CB* is a remarkable intracontinental sag basin, which initiated its subsidence during the late Mesoproterozoic, most probably as a failed rift basin. The subsidence was accompanied by a thick deposition of syn- rift clastics in the northern part of the Cuvette Centrale. During the following post-rift phase, occurred the deposition of the (1) dolomitic limestones composing the carbonate ramp (~1040-1000 Myr), (2) the deposits of carbonates and evaporites (~1000-720 Myr), and (3) the siliciclastics sediments during the Rodinia break up (~720-560 Myr). The evolution of the CB during the Paleozoic is marked by compressional tectonic deformations related to Gondwana assembly (~500-560 Myr) that is possible to observe with the seismic reflection profiles along the southwestern sectors of the Cuvette Centrale. The post-orogenic phase is characterized by the deposition of red arkoses called Red Beds, mostly identified in the Samba and Gilson wells. The *CB* evolution was also marked by glacial events, occurred between the end of Devonian and early Carboniferous (~380-320 Myr), during the Gondwana glaciation, when the *CB* was located at the South Pole (Delvaux et al., 2021). The following stratigraphic depositions referred to the "Karoo Supergroup" are characterized by the transition from the glacial-lacustrine sediments (deglacial period ~320-252 Myr) to continental sandstones.

After the Gondwana breakup during the early Jurassic (200-157 Myr), characterized by a stratigraphic hiatus, the sedimentation continuously occurred from the late Jurassic until the end of the Paleogene. The *CB* might also have been locally influenced by distal tectonic events, but the current data available do not allow to precise that. All these tectonic and climatic events caused the migration of the sedimentary depocenters from the Proterozoic until Jurassic age inside the Cuvette Centrale, indicating a different behavior of the basin during its evolution (Chapter 2). Since the seismic data are uneven distributed in the entire Cuvette Centrale, I integrated the knowledge acquired on the main structures of the basin with potential fields analyses. The results confirm the strong heterogeneity of the basement depths, characterized by the formation of highs (i.e. Kiri and Inongo High) and depressions (e.g., Busira and Lokoro basin), and the tectonic trend *NW-SE* oriented within a circular depressed area (*CB*).

The basement depths reconstructed from gravity analyses are quite consistent with that derived from the interpretation of the seismic profiles. However, the new results show the continuity of the Kiri and Boleko High, which appeared in the basement reconstructed only from the interpolation of seismic data separated by

a sedimentary cover. I could also identify some small basins south of Gilson well, in areas uncovered by seismic data. The shallow crustal structures, investigated through the gravity analysis, reveal the possible presence of mafic bodies in the southern part of the Cuvette Centrale.

In order to understand the causes of the formation of the main structures of the *CB*, I performed 3D numerical models, which could simulate the first extensional phase that initiated its subsidence. For this purpose, I tested the hypothesis that multi-divergent velocities, acting on a cratonic area, caused the *CB* formation. The main results show the formation of an almost circular subsided area in the central part of the models, as effect of the radial extension, due to the asthenosphere upwelling. The other structures formed, consisting in a series of lows and highs along specific orientations, resemble the first order heterogeneities characterizing the *CB* basement depth (lows and highs *NW-SE* aligned). The alignment of these modelled structures, as well as the size and time of formation depends on the geometry design and initial temperature conditions assumed for the different simulations.

To check the consistency of the results obtained with the observed *CB* structures, I implemented static and dynamic forward gravity models, using as input the modelled surface topography. The dynamic forward model produced positive anomalies induced by the mass excess related to the asthenospheric upwelling. The static forward model shows positive and negative anomalies localized in the uplifted and subsided areas, respectively. The comparison between these anomalies with those of the gravity disturbance (Chapter 3) shows that they have a similar trend, although the modelled anomalies are smoother and have larger amplitudes. These results could have been expected, since my simulations do not take into account the effect of sedimentation, which influences the observed gravity field and could have partly reduced the amplitude of the signal. In addition, the *CB* has been affected by compressional tectonics during the geological time, which has further modified its original structure (e.g., the compression related to the Gondwana assembly). In order to discriminate the effect of the density variations from that of topography in the modelled gravity field, I implemented another static forward modelling, in which I suppressed the effect of topography. I noticed that in this case the effect of the density variations is enhanced in the central subsided area, where strong positive anomalies are observed, while is negligible in the peripheral part of the extended area.

5.3 Outlooks

The results obtained in this study give the opportunity to continue the research on the causes of the long-term evolution of the continental interiors. In particular, it would be interesting to explore the effects of other tectonic processes, such as the compressional stress related to the supercontinent assembly on the *ICBs* evolution, keeping a similar approach used in this study.

The reconstruction of the stratigraphy allows quantifying the effects of sedimentation/erosion on the basement depth, adding constraints to numerical models that before this study were performed only for theoretical cases. In particular, Cacace and Scheck-Wenderoth (2016) implemented 3D models that simulate basin subsidence by imposing a thermal anomaly in the deep lithosphere and considering the effect of sedimentation. In the simulations, they took into account the flexural rigidity of the lithosphere, constrained by elastic-brittle-plastic rheology. Their results show that the sediments deposition, reducing the heating loss ('blanketing effect'), significantly slows the post-rift subsidence and at the same time favors decoupling of the crust from the mantle lithosphere, causing a more distributed deformation. These effects of sedimentation on the basement depth variations can be investigated in the near future in the *CB*, as well as in any other *ICB*, by implementing numerical models, keeping similar kinematic boundaries and geometry designs used in this thesis.

The modelled thermal history of the basins can be compared with real observations obtained from petroleum exploration campaigns and be the object of future studies. Theoretical subsidence curves have been also reconstructed by Armitage and Allen (2012) that studied the evolution of basins lying on a thick cratonic lithosphere, occurring at low strain rate values. They demonstrated that these conditions were sufficient to produce the long subsidence decay that characterizes the *ICBs*. The hypotheses put forward in these previous studies can be tested through numerical models, using the results obtained in this thesis. In particular, the reconstructed stratigraphy and analysis of well-log data, together with paleo-topography reconstructions, based on future analyses of thermo-chronological data, will make it possible to perform backstripping of the *CB* sediments, to restore the initial basement depth and original thicknesses of the sedimentary layers.

Furthermore, the long- term evolution of intra-cratonic basins is often influenced by a longlasting negative dynamic topography, induced by the deep lithospheric roots (Heine et al., 2008). Therefore, in the near future, it will be interesting to analyze the dynamic topography of the CB, using seimic tomography models and geoid anomalies, in order to improve the plate kinematic frameworks of the central African continent. The computation from 3D numerical models of time-dependant surface topography, induced by the mantle upwelling occurred during the first phase of the CB formation, will help quantify the initial dynamic topography. The link between surface and deep processes acting on a cratonic lithosphere can be further investigated through the analyses of satellite images and digital elevation models (*DEM*), which allows studying fault kinematics or sedimentary structures. In particular, with these analyses will be possible to monitor temporal geomorphological variations of the hydrological basin of the Congo River, in order to distinguish the effect of climatic and tectonic processes.

Previous studies, such as Downey and Gurnis (2009), Crosby et al. (2010), and Buiter et al. (2012), have investigated the origin of the huge negative free-air and geoid gravity anomalies over the entire *CB*,

through the interpretation of seismic tomography models, basin data analyses, and satellite gravity data, without proposing a common hypothesis. In particular, they linked this anomaly to the mantle structure and its dynamics (Downey and Gurnis, 2009; Crosby et al., 2010) or to the effect of sediments (Buiter et al., 2012). The deployment of more seismic stations in the African continent, through the ongoing African Array project (AfricaArray.psu.edu), offers the possibility to increase in the near future our knowledge on the crustal and mantle structures of an area that is still mostly uncovered of seismic data. As soon as this objective is achieved, it will be possible to investigate the origin of the negative gravity anomaly and increase the complexity of the 3D numerical models, by including more structural heterogeneities as already done in 2D models (e.g., Perron et al., 2020).

Appendix A

The well-log data used to reconstruct the stratigraphic columns shown in Chapter 2 are displayed, in terms of lithology, reflectors, and stratigraphy.

MBANDAKA WELL								
Elf-Aquitaine internal report Esso-Zaire SARL 1981b			**Linol et al. 2015b**		**Here**			
Depth (m)	**Lithology**	**Strati.**	**Unit**	**Strati.**	**Seq.**	**Strati.**	**Refl.**	**TWT (sec.)**
169	Sandstones, Shales	Kalahari	M1	Kalahari	S7	Cretaceous	R10 R9	
345	Sandstones	Kwango	M2	Bokungu				0.541
614	Carbonated sandstones	Bokungu						
823	Red shales	Loia	M3	Loia				0.690
844	Red Arkoses		M4	Stanleyville	S6	Stanleyville	R8	0.704
1536	Red Sandstones Red-brown fine sandstones Red-orange conglomerates Dark-grey siltstones		M5	Haute-Lueki	S5	Karoo	R6	1.116
2155			M6		S4	Red Beds	R4	1.405
2610			M7	Lukuga	S3	Siliciclastics	R3	1.832
3408			M8		S2	Carbonates-clastics	R2	2.087
3991	Red-siltstones to conglomerated siltostones		M9	Carbonates-siliciclastics				
4351	Shales, anhydrites, halites		M10		S1	Carbonates	TD	2.134

Table A1 *– Well-log data (Mbandaka well) used to construct the stratigraphic columns displayed in the text (Fig.2.2). (Delvaux et al. 2021).*

DEKESE WELL								
	Cahen et al., 1960			Linol et al., 2015c		Here		
Depth (m)	**Lithology**	**Strati.**	**Unit**	**Unit**	**Strati**	**Seq.**	**Refl.**	**TWT (sec.)**
22	Sands, pebbles	Kalahari	A	D1	Kalahari	S7	R8 R9	0.660
318	Sandstones	Bokungu	B	D2	Bokungu			
398				D3	Loia			
461				D4	Dekese			
705	Clastic sandstones	Loia	C					
714				D5	Stanleyville			
753	Varval clays	Karoo	D	D6	Haute-Lueki	S5	R6	1.182
860	Diamictites		E	D7	Lukuga			
1553	Varval clays		F	D8				
1677	Red Beds Diamictites		G	D9				
1856	Red Arkoses	Red Beds	H	D10	TD	S4	TD	1.265

Table A2 *– Well-log data (Dekese well) used to construct the stratigraphic columns displayed in the text (Fig.2.2). (Delvaux et al. 2021).*

SAMBA WELL								
	Cahen et al., 1960			Linol et al., 2015c		Here		
Depth (m)	**Lithology**	**Strati.**	**Unit**	**Unit**	**Strati**	**Seq.**	**Refl.**	**TWT (sec.)**
86	Sand	Cenozoic	1	S1	Kalhari	S7	R10	0.500
193	Argilleous sandstones	Kwango	2	S2				
517	Red claystones	Bokungu	3	S3	Bokungu			
602				S4	Loia			
845	Sandstones, carbonates, siltstones	Loia	4				R9	0.623
1167	Sand-siltstones	Stanleyville	5	S5	Stanleyville	S6	R8	0.786
2038	Red Arkoses	Red Beds	6	S6	Haute-Lueki	S4	TD	1.226

Table A3 *– Well-log data (Samba well) used to construct the stratigraphic columns displayed in the text (Fig.2.2). (Delvaux et al. 2021).*

Appendix B

The seismic profiles composed of single or several seismic lines are displayed in the following figures. In each figure, the maps show all the seismic lines location (in black) and the interpreted seismic line (in red). The upper, central, and bottom profile is the raw, interpreted, and the depth-converted seismic line, respectively. The colors of reflectors have been chosen consistently with those of Fig. 2.2 (Chapter 2).

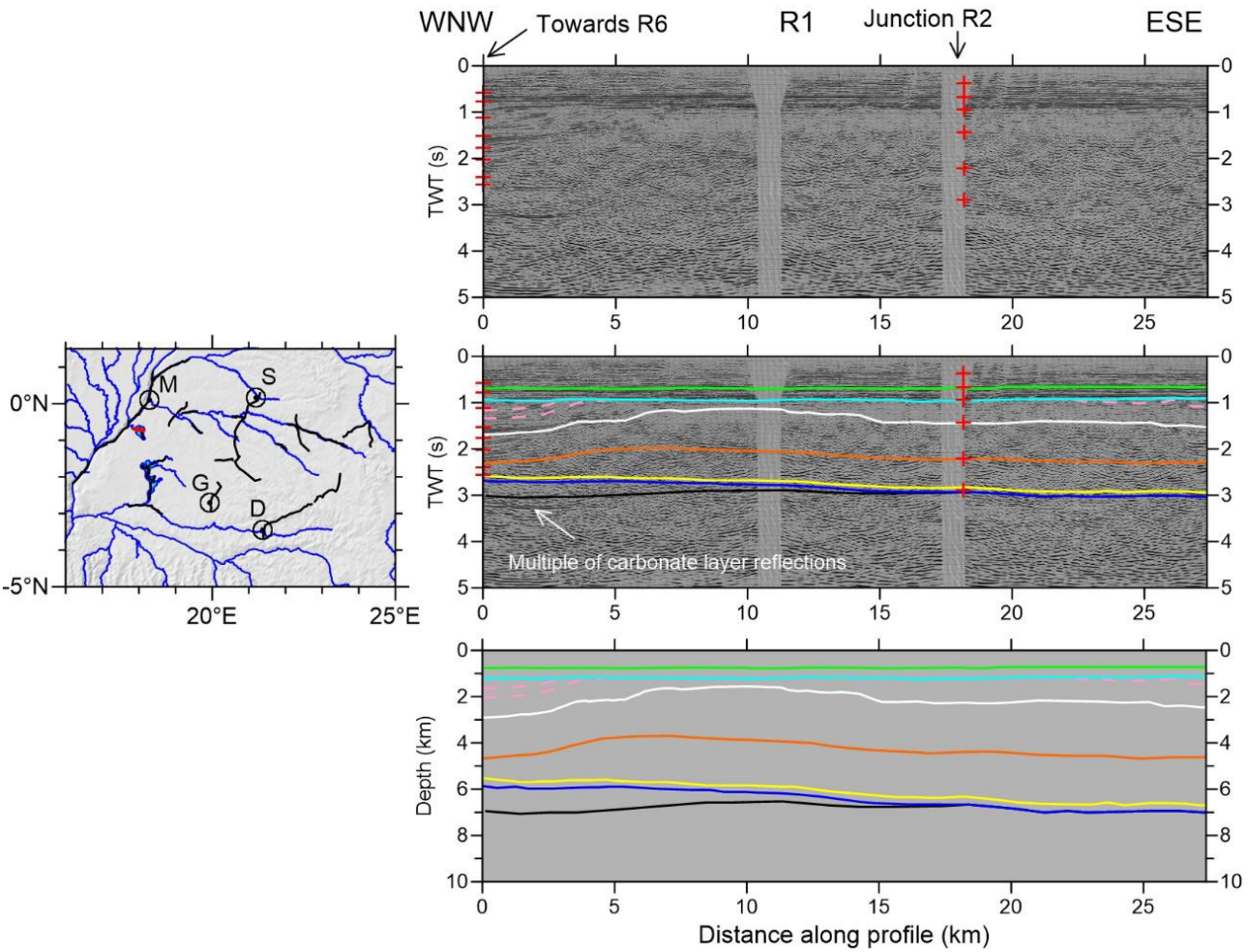

Figure B1 *– Profile R1 (Delvaux et al., 2021)*

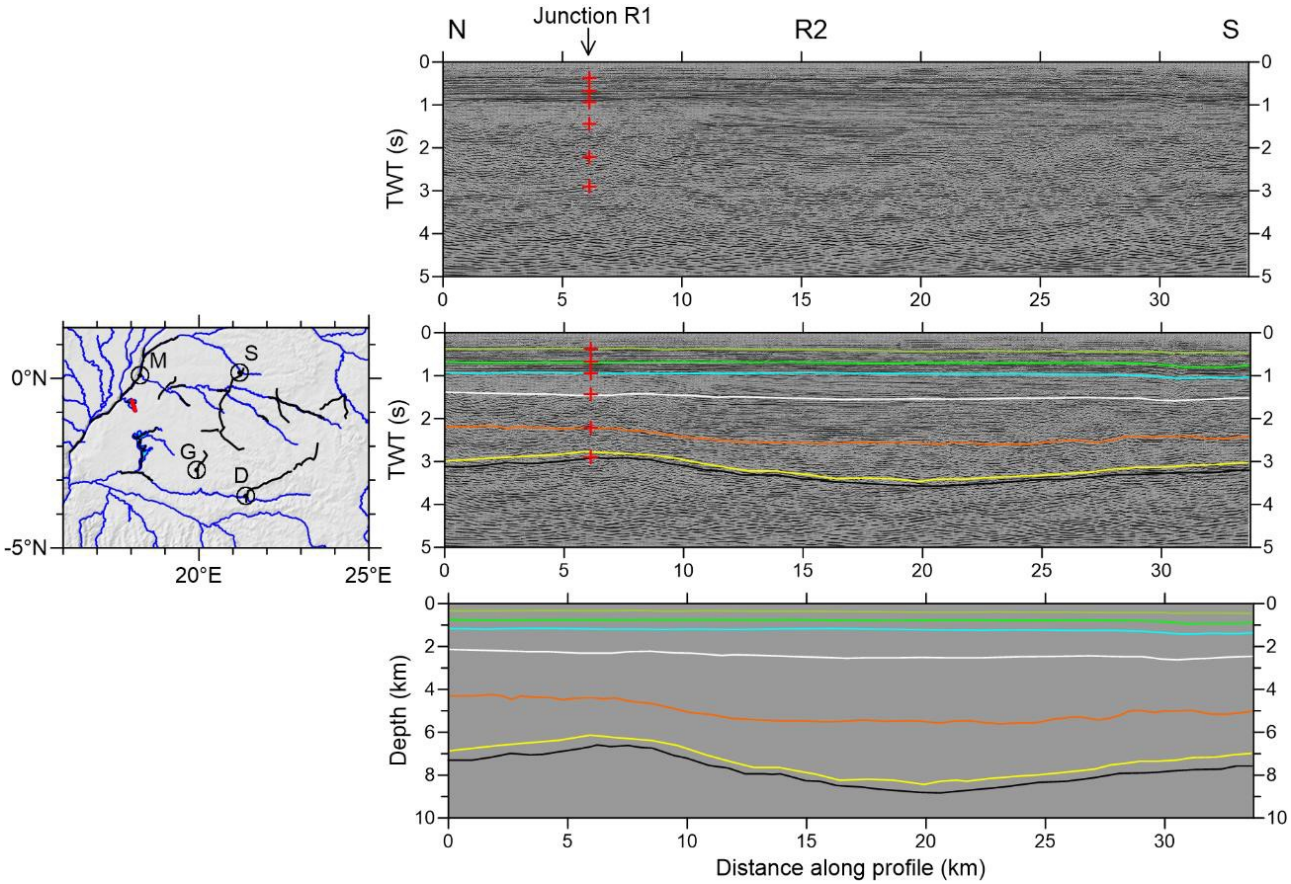

Figure B2 *– Profile R2 (Delvaux et al., 2021)*

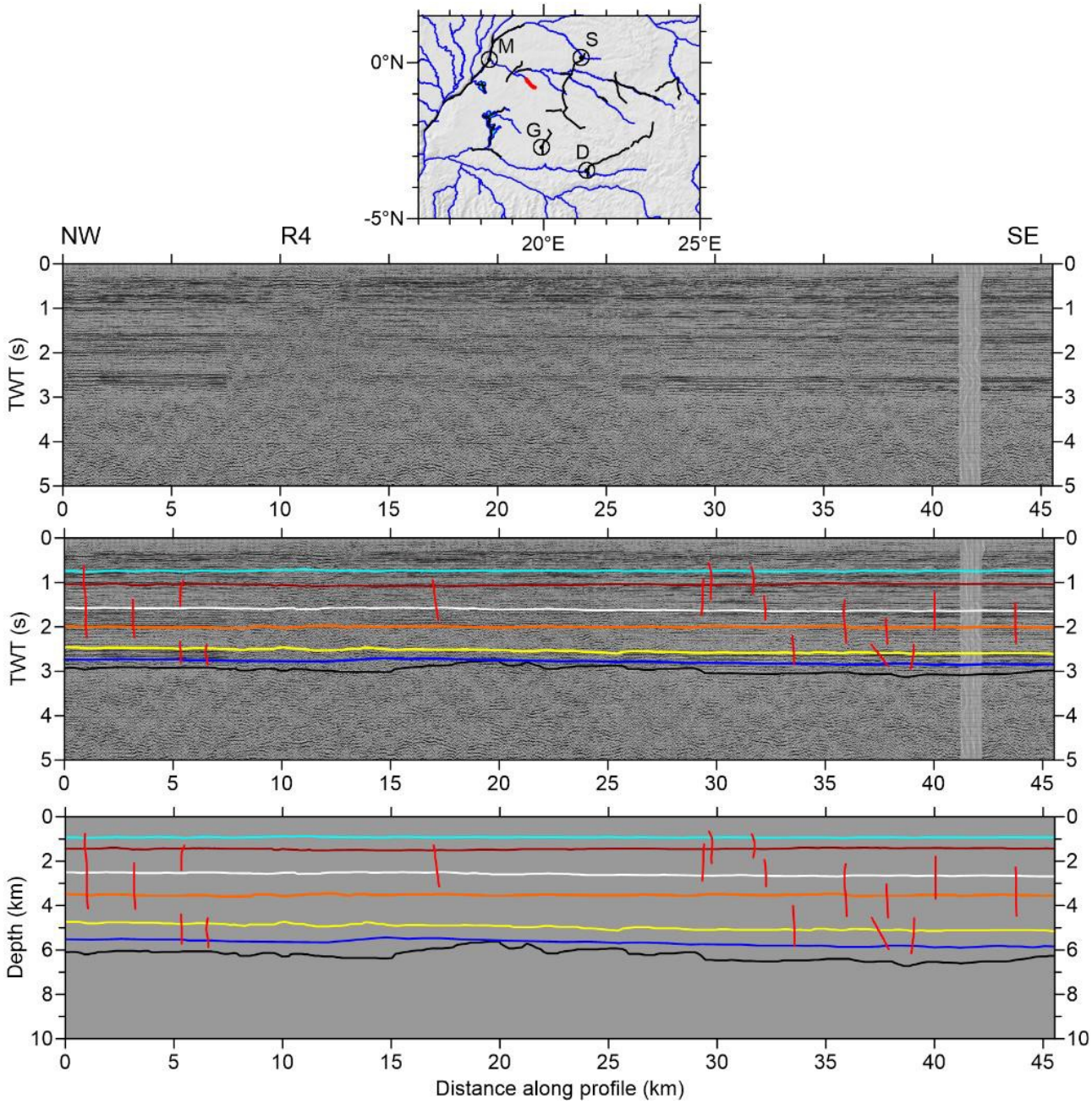

Figure B3 *– Profile R4 (Delvaux et al., 2021)*

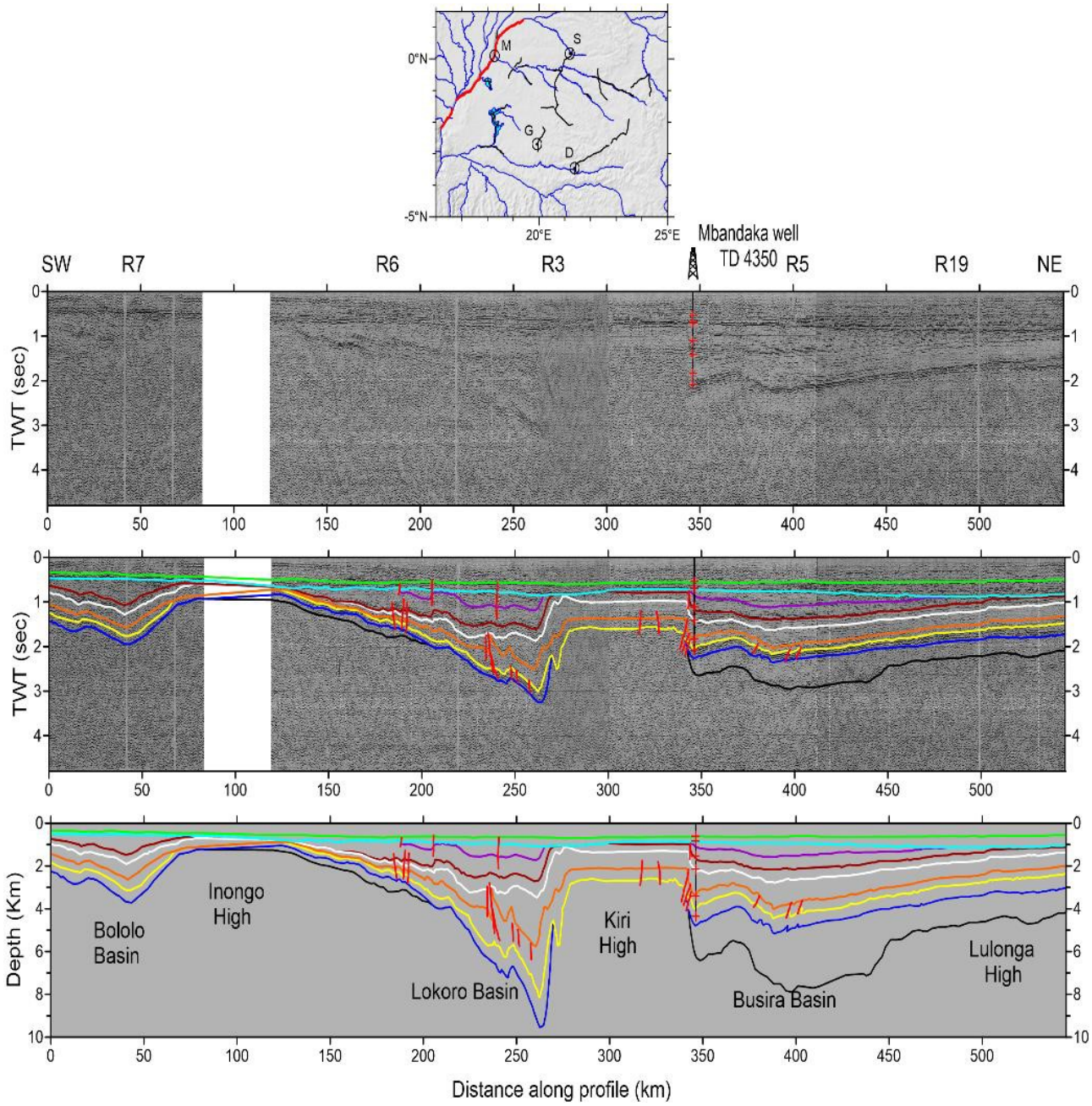

Figure B4 *– Profile R7-6-3-19 (Delvaux et al., 2021)*

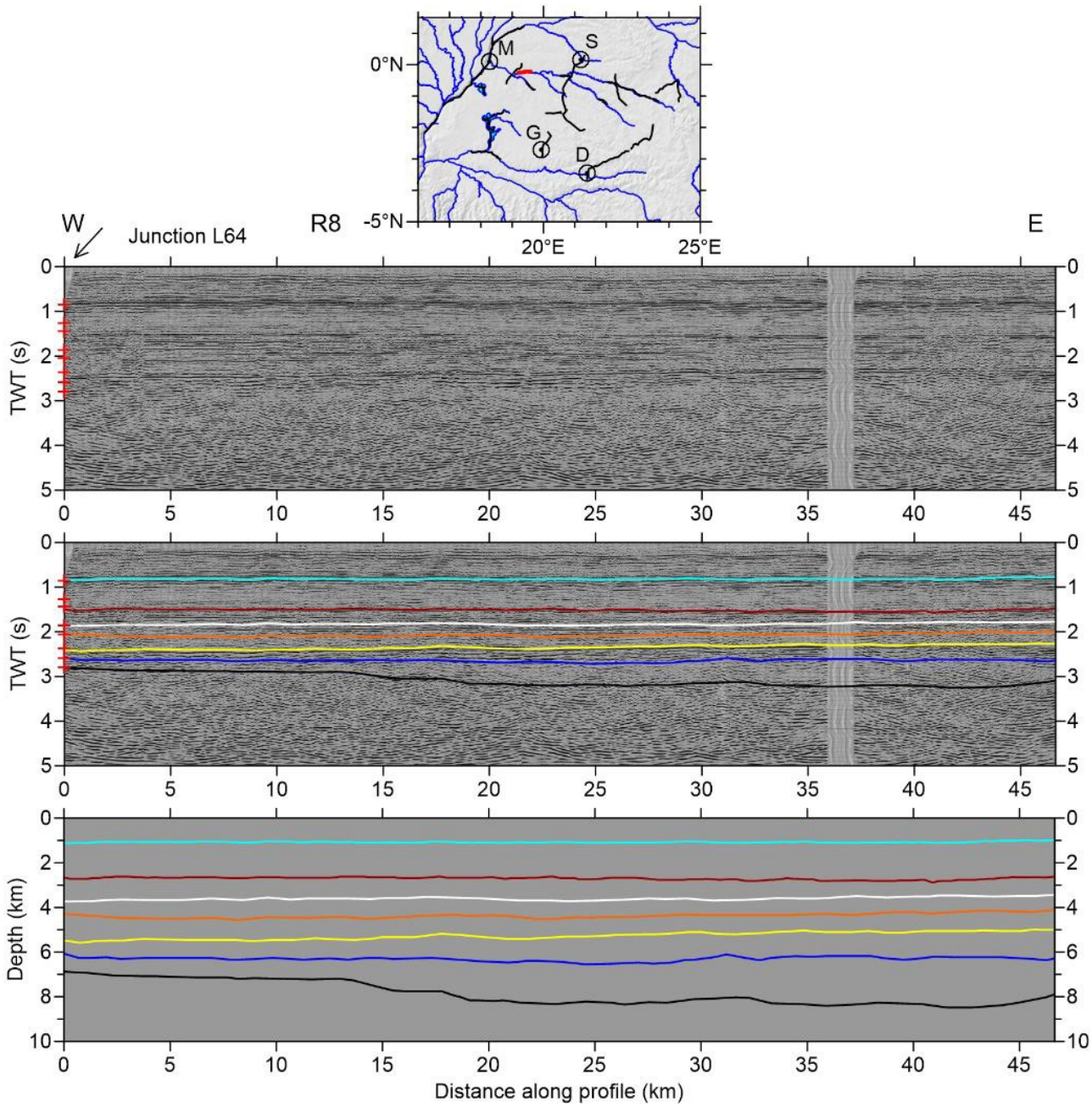

Figure B5 *– Profile R8 (Delvaux et al., 2021)*

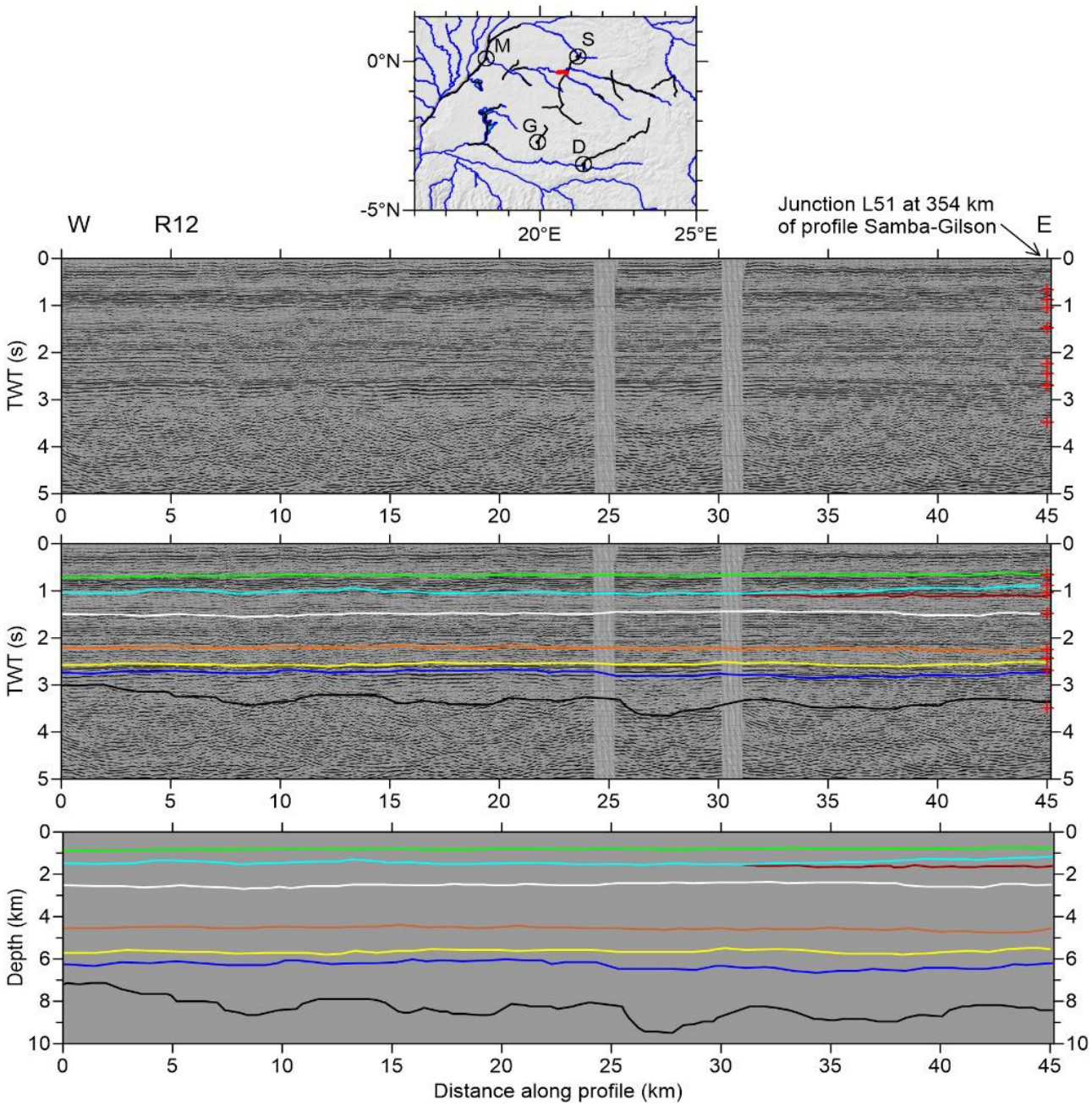

Figure B6 *– Profile R12 (Delvaux et al., 2021)*

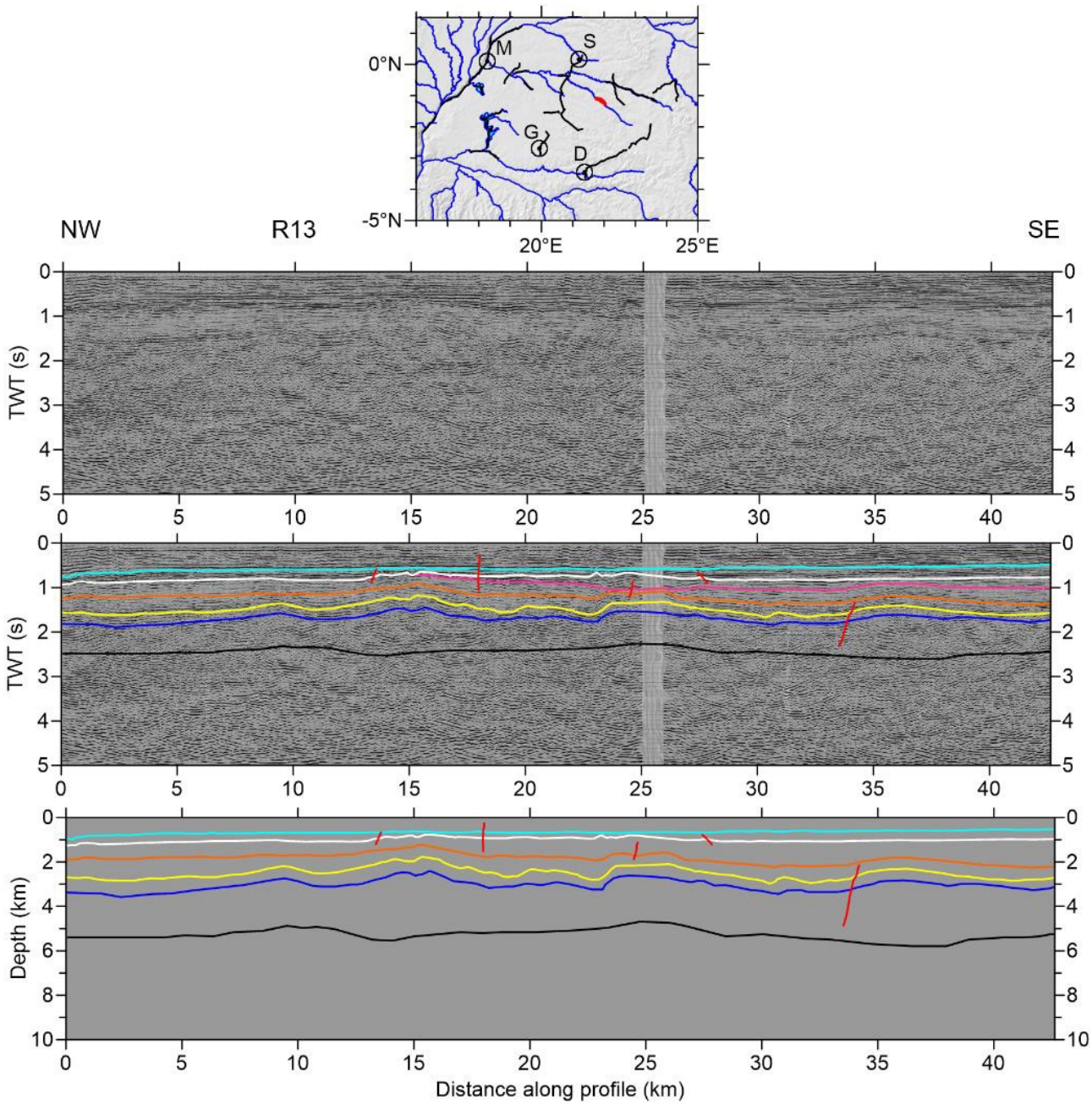

Figure B7 *– Profile R13 (Delvaux et al., 2021)*

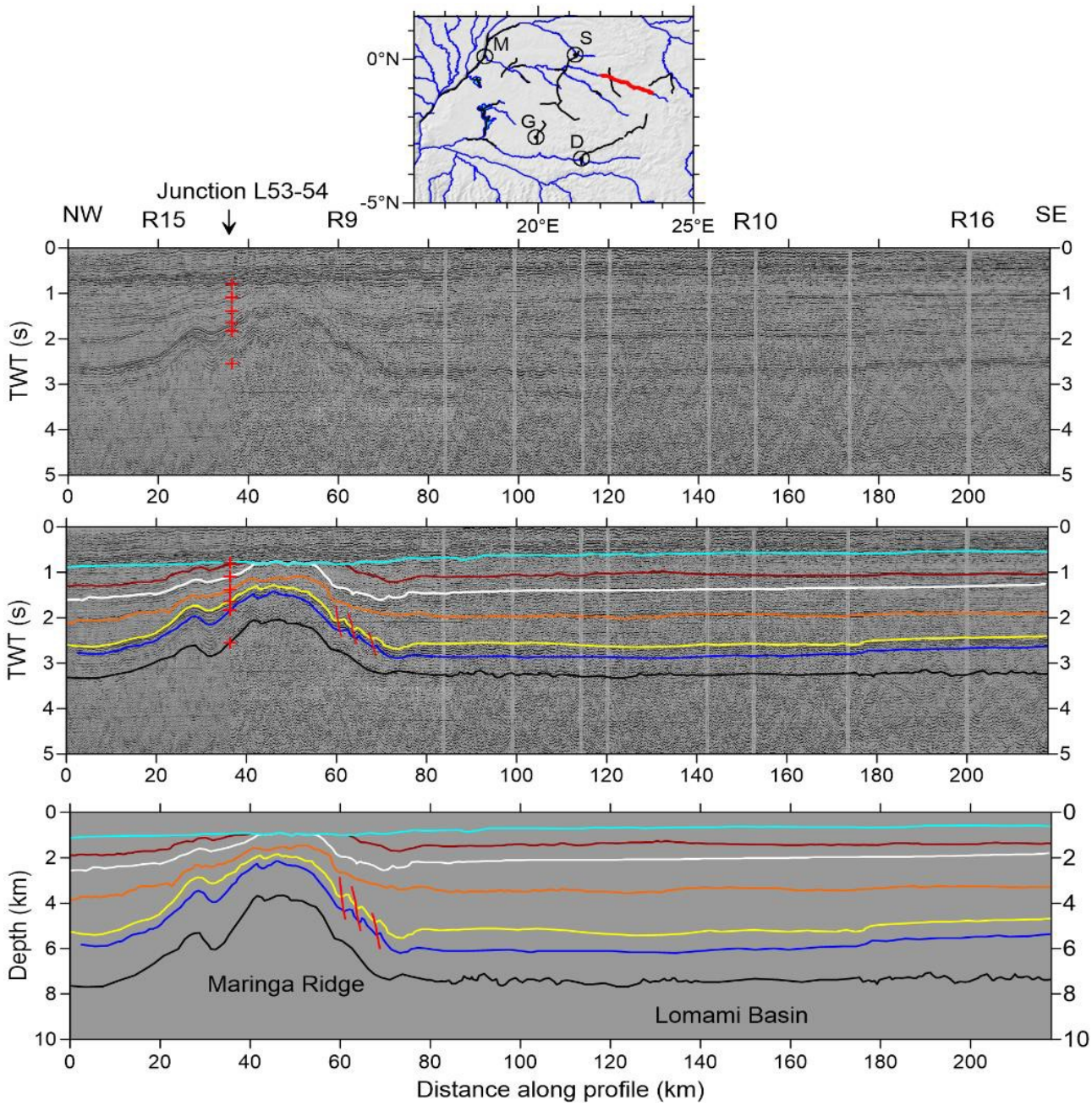

Figure B8 *– Profile R15-9-10-16 (Delvaux et al., 2021)*

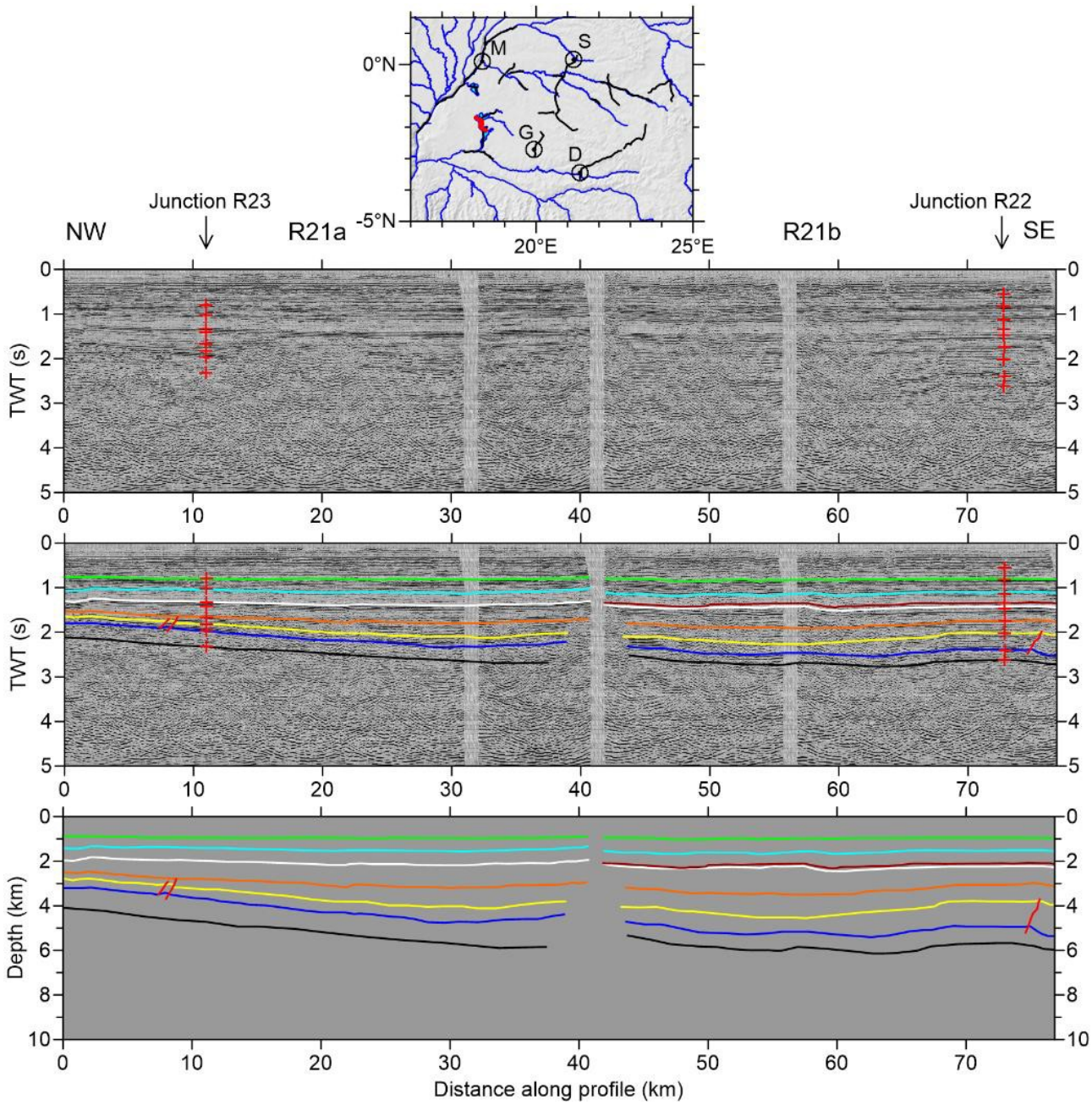

Figure B9– *Profile R21 (Delvaux et al., 2021)*

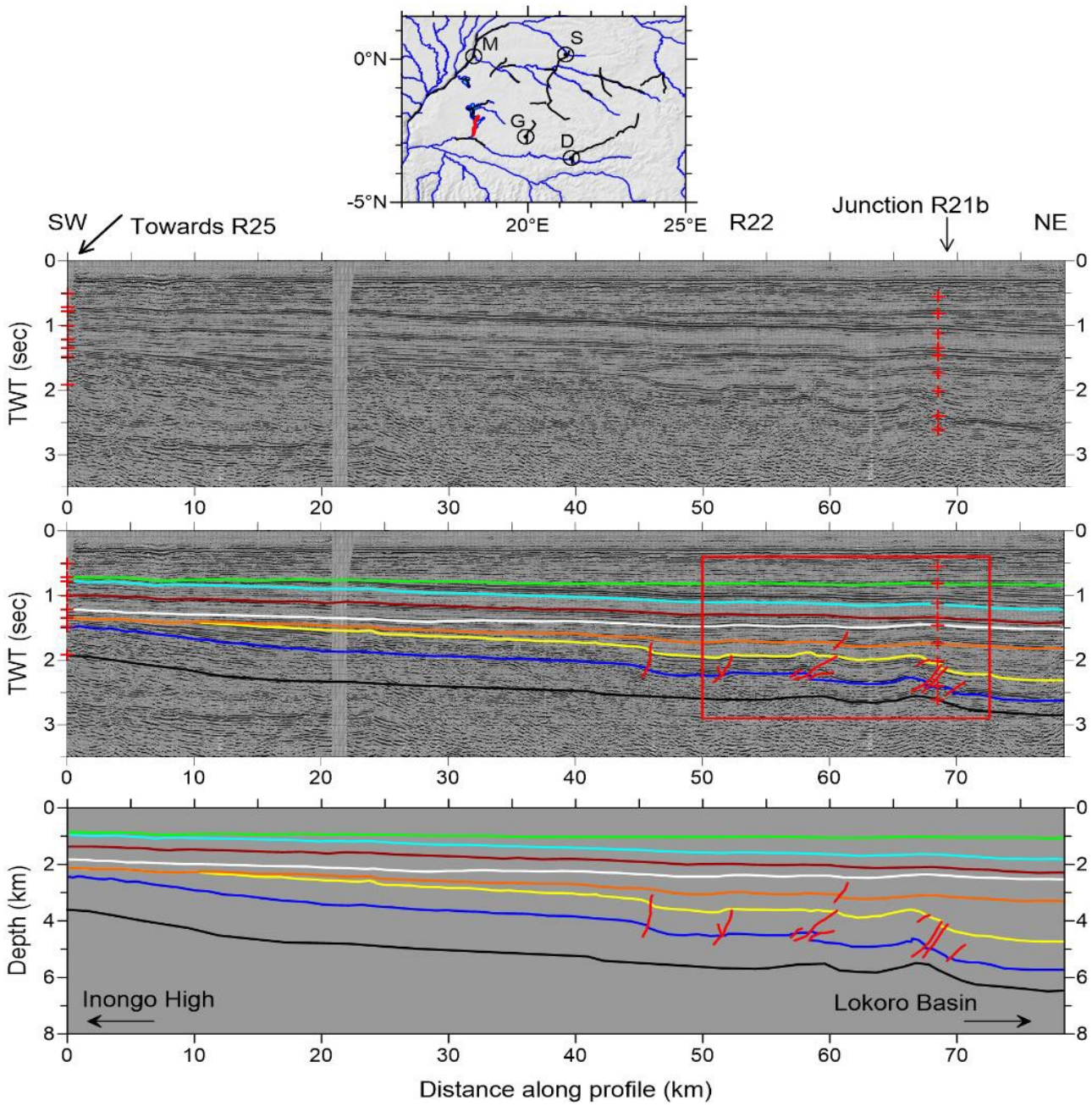

Figure B10 *– Profile R22 (Delvaux et al., 2021)*

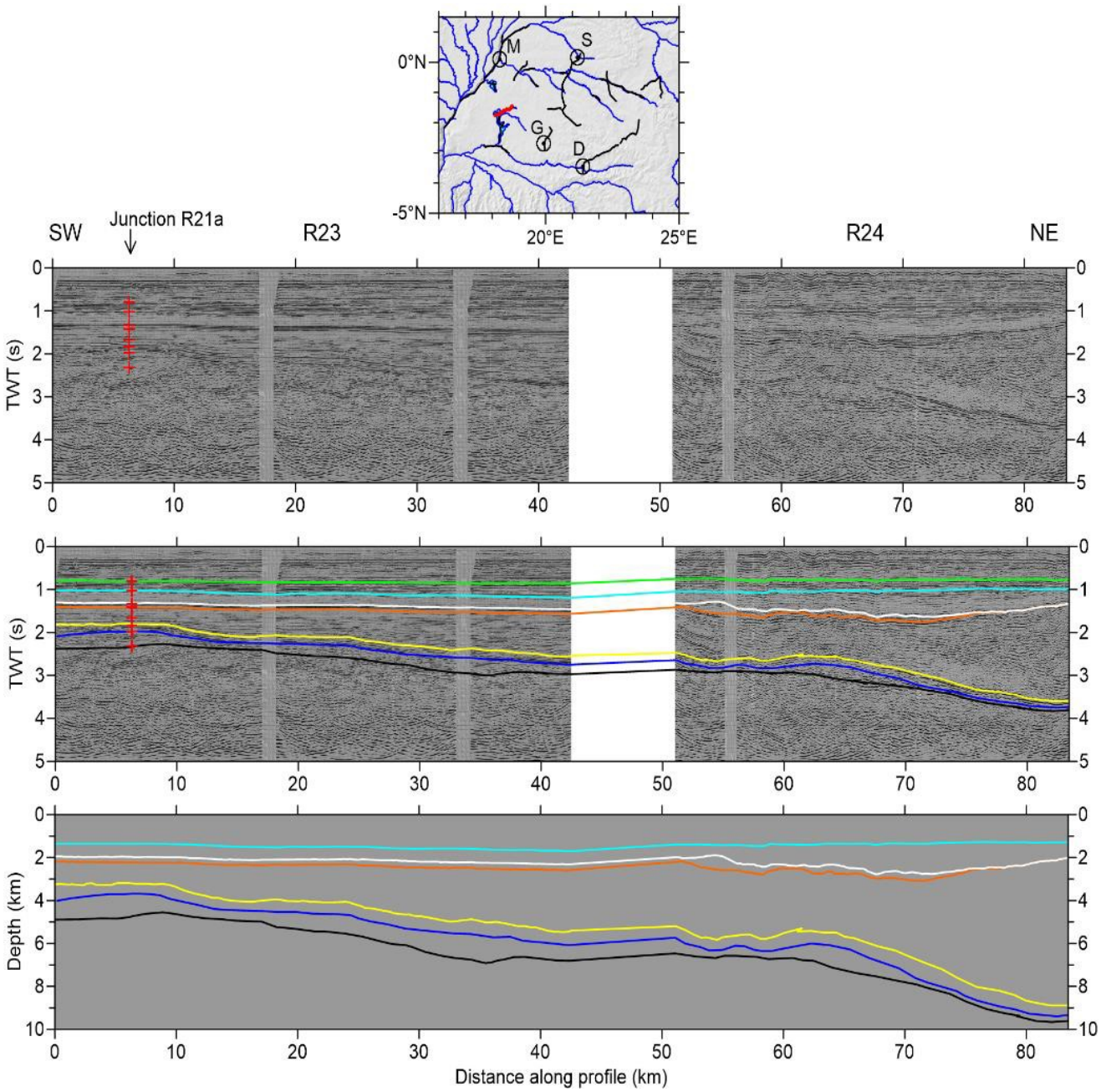

Figure B11 *– Profile R23-24 (Delvaux et al., 2021)*

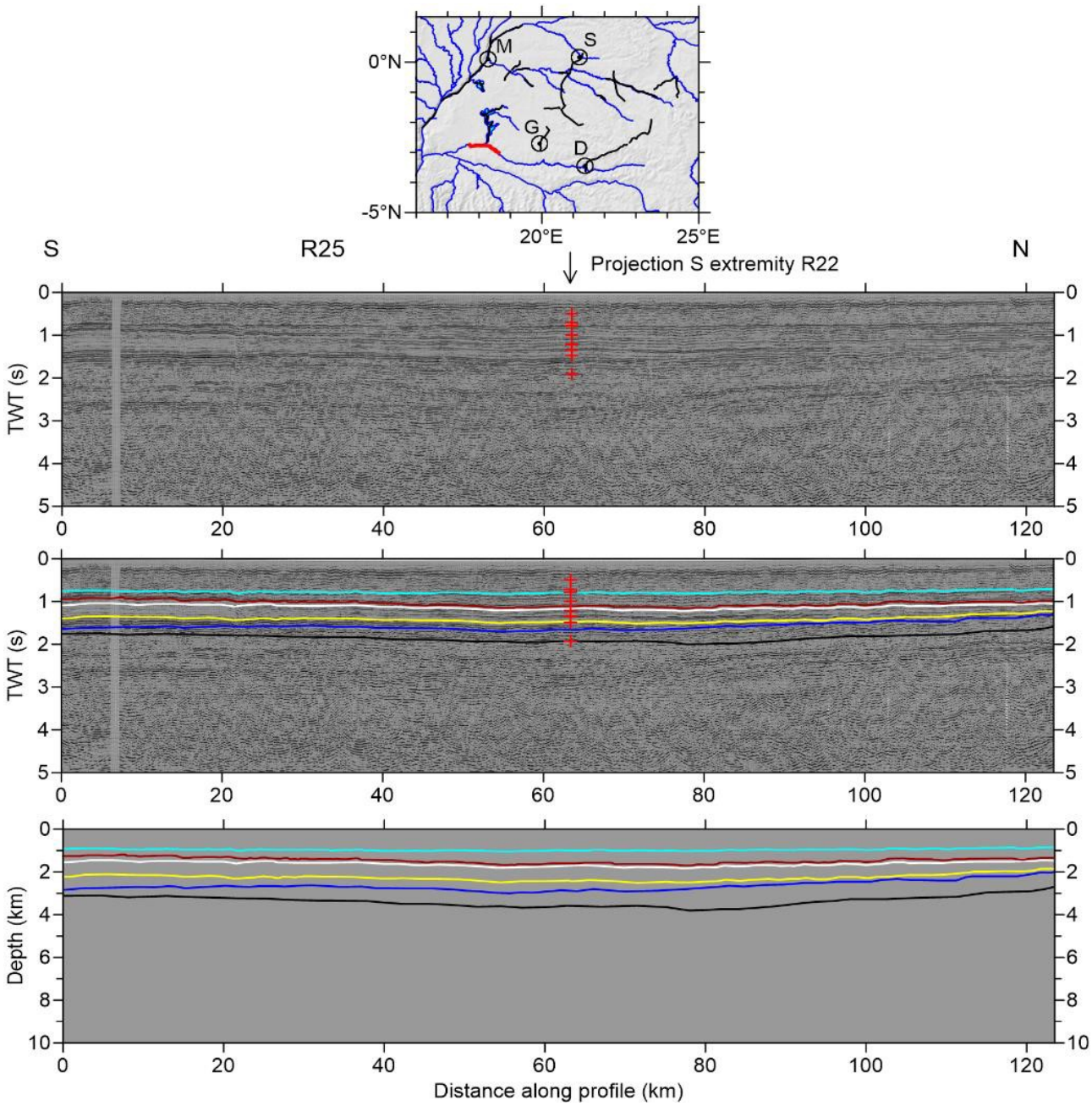

Figure B12 *– Profile R25 (Delvaux et al., 2021)*

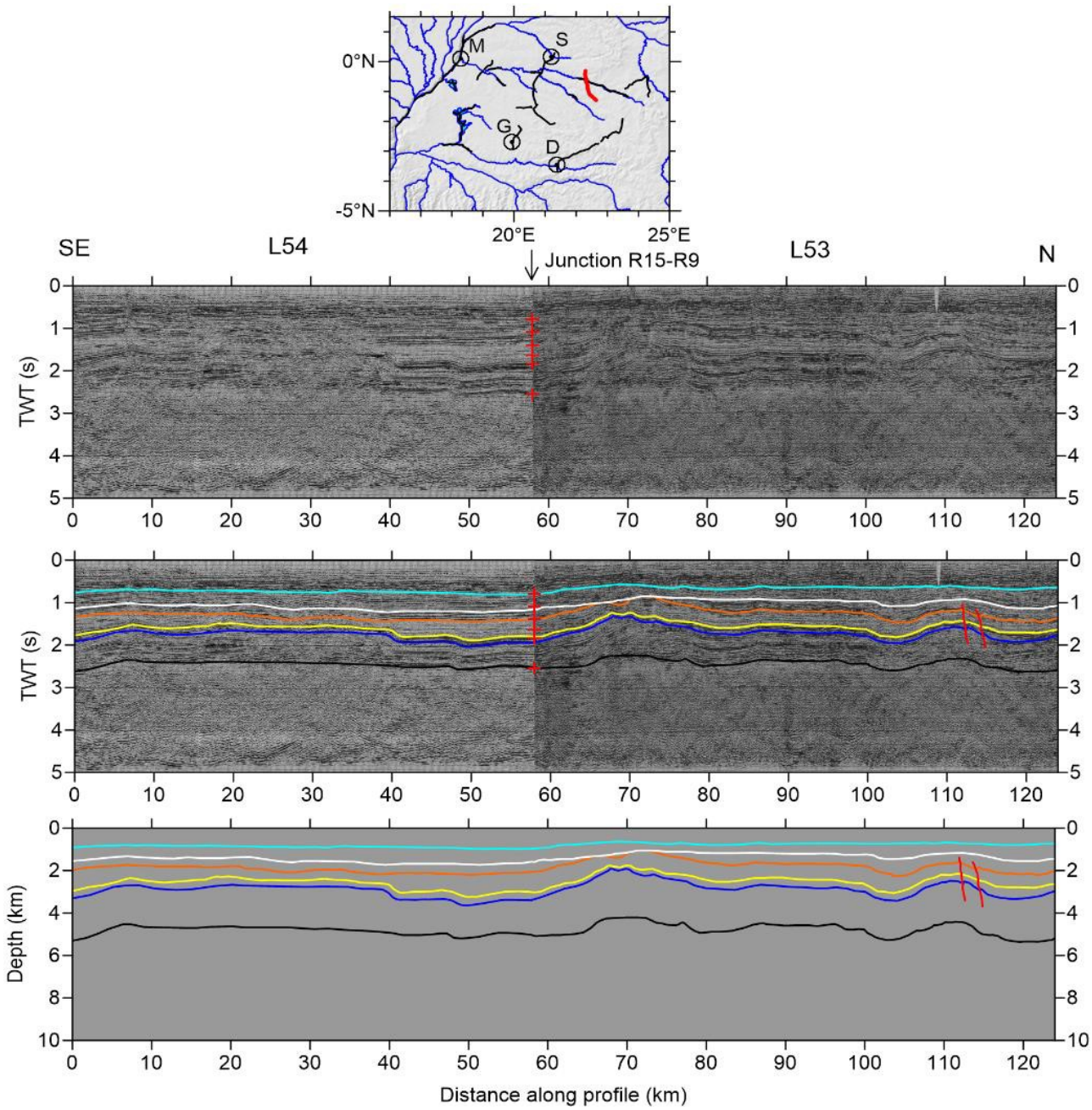

Figure B13 *– Profile L54-53 (Delvaux et al., 2021)*

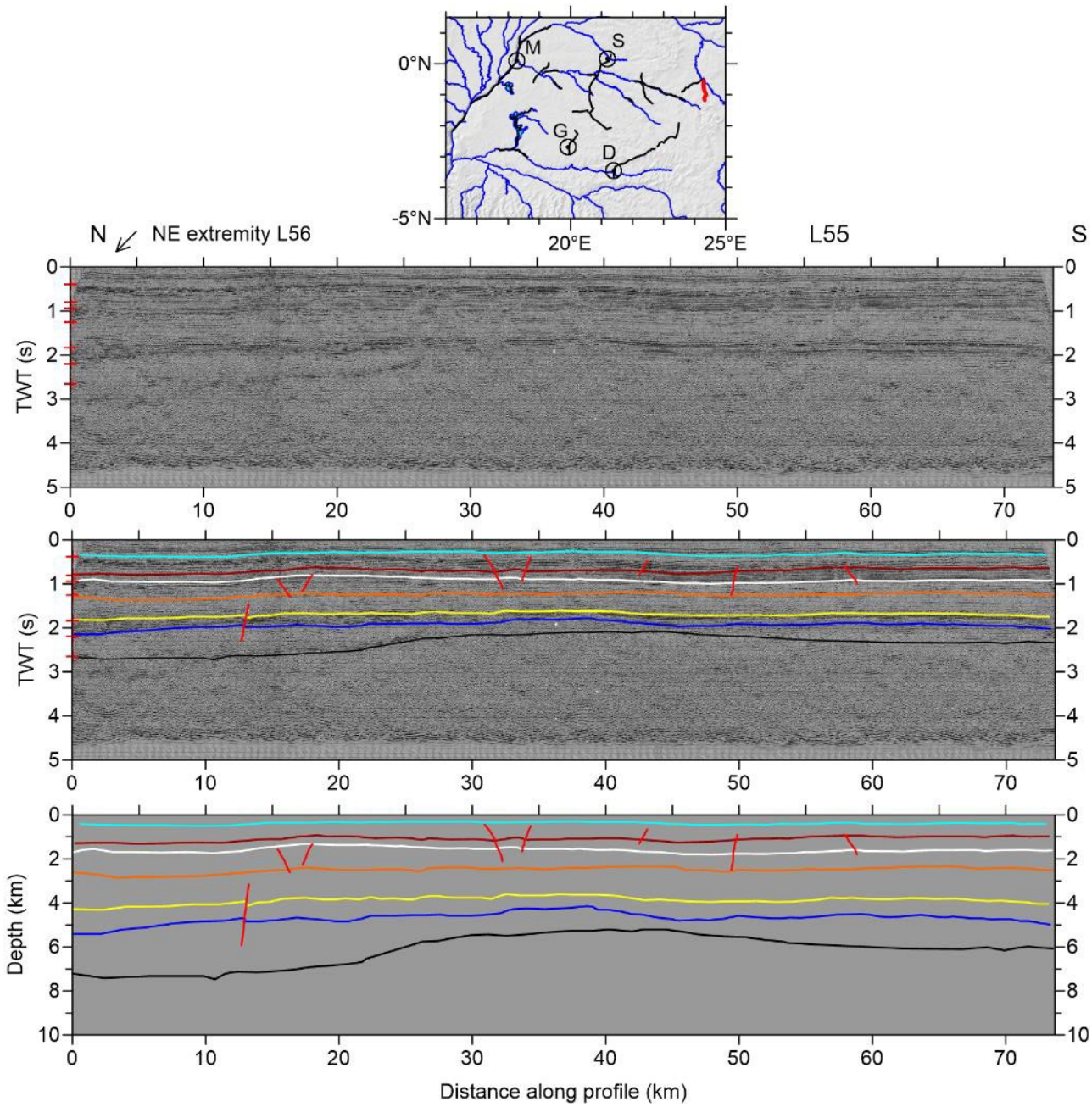

Figure B14 *– Profile L55 (Delvaux et al., 2021)*

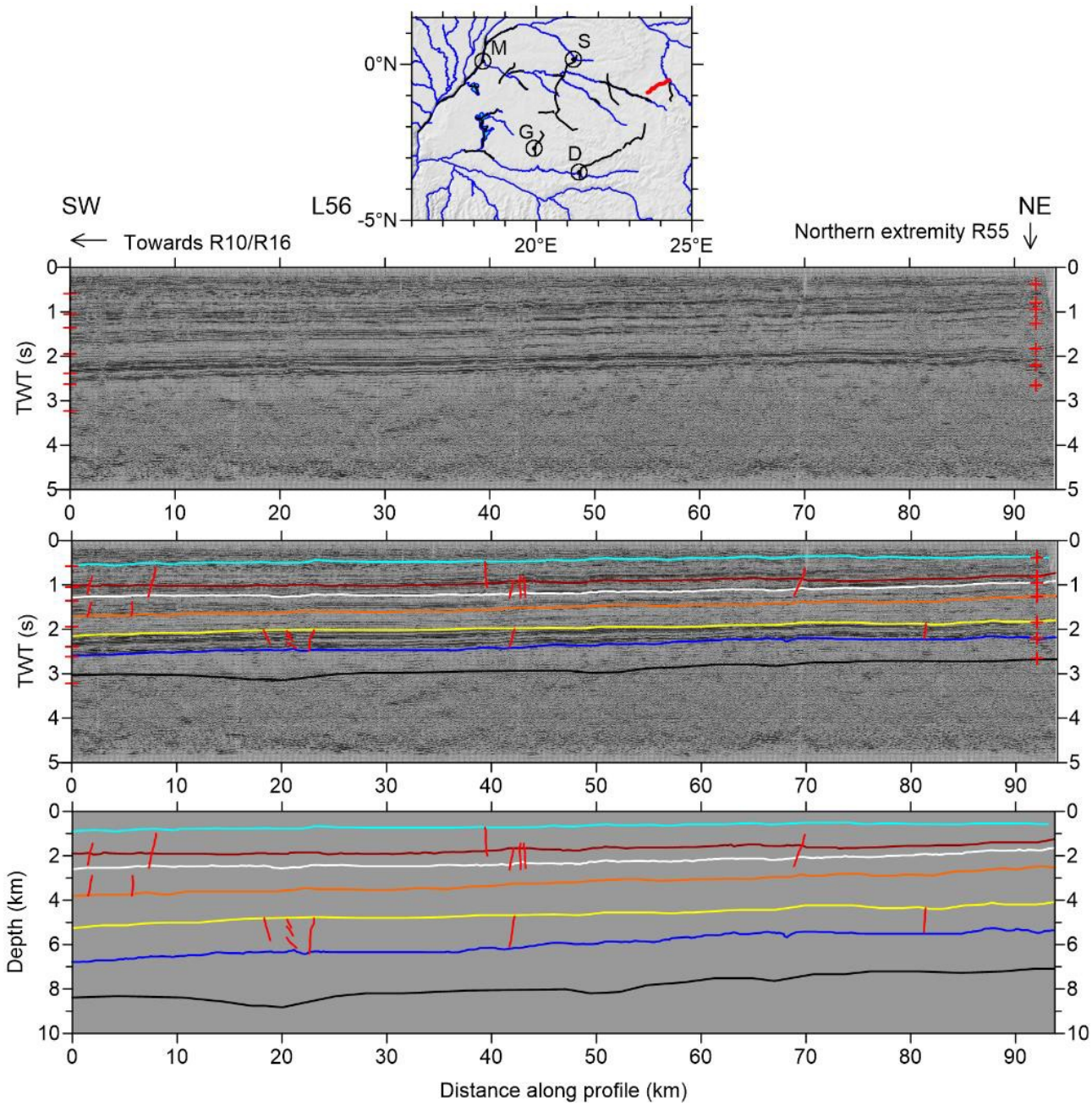

Figure B15 – *Profile L56 (Delvaux et al., 2021)*

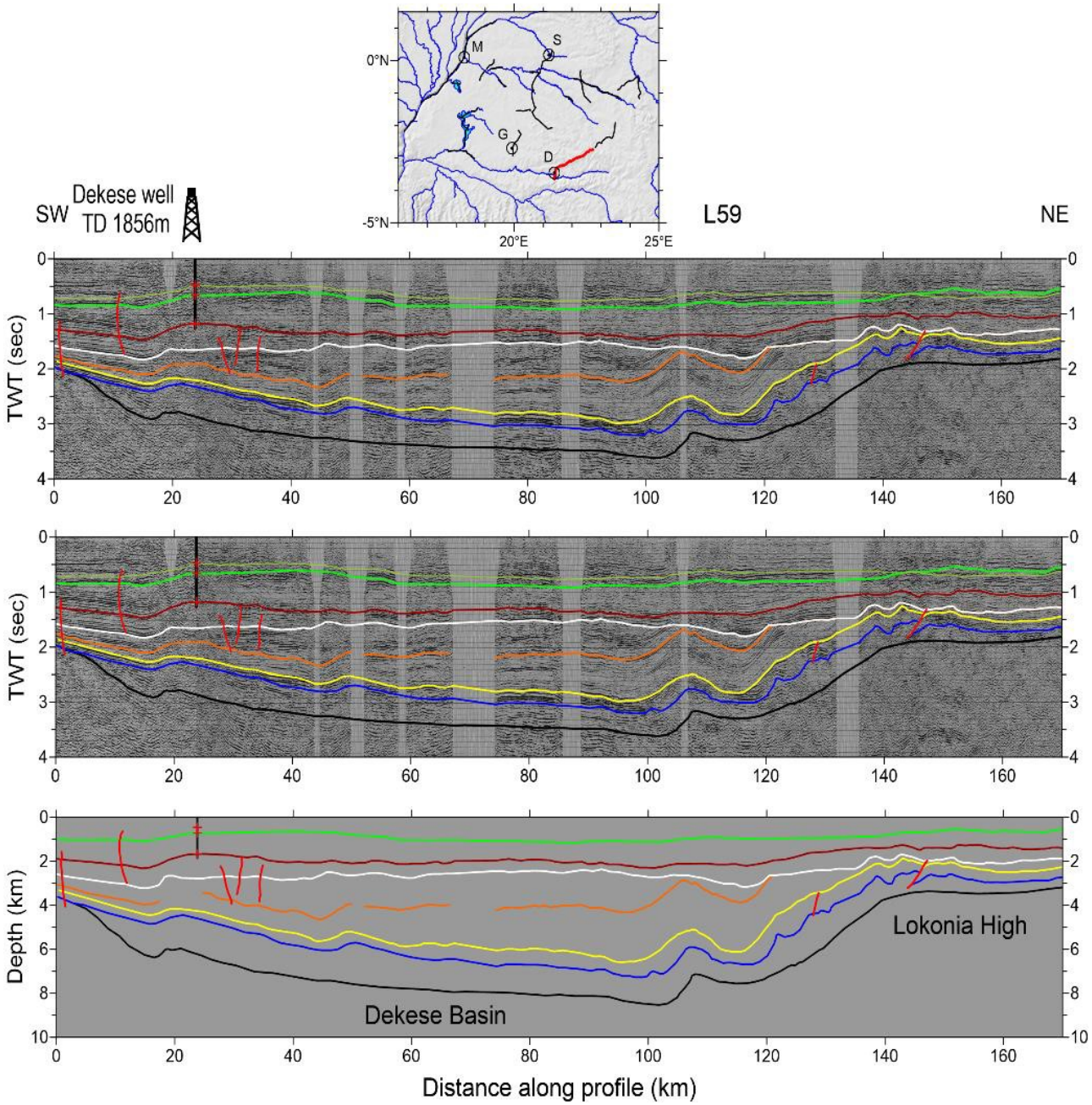

Figure B16 *– Profile L59 (Delvaux et al., 2021)*

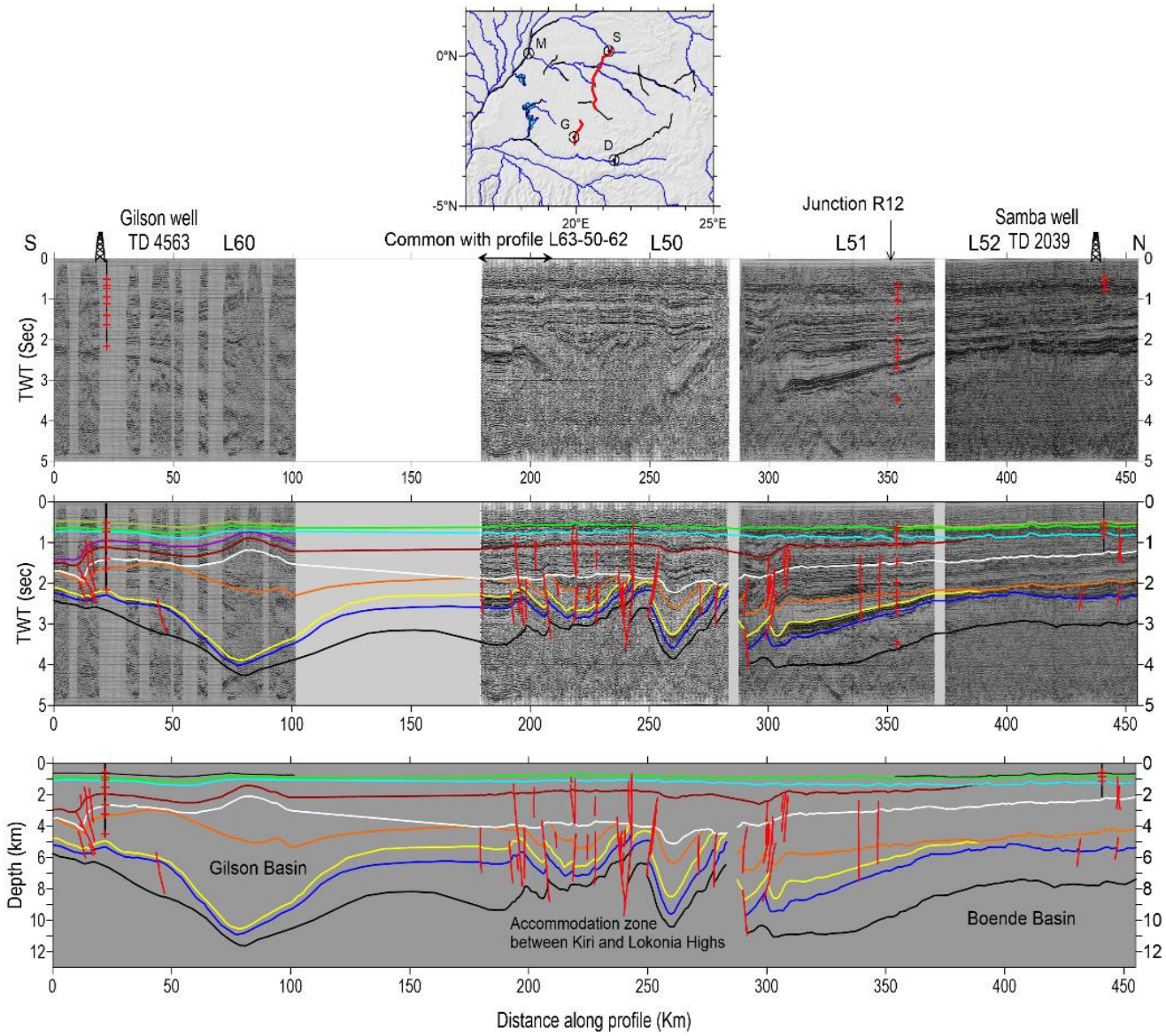

Figure B17 *– Profile L60-50-51-52 (Delvaux et al., 2021)*

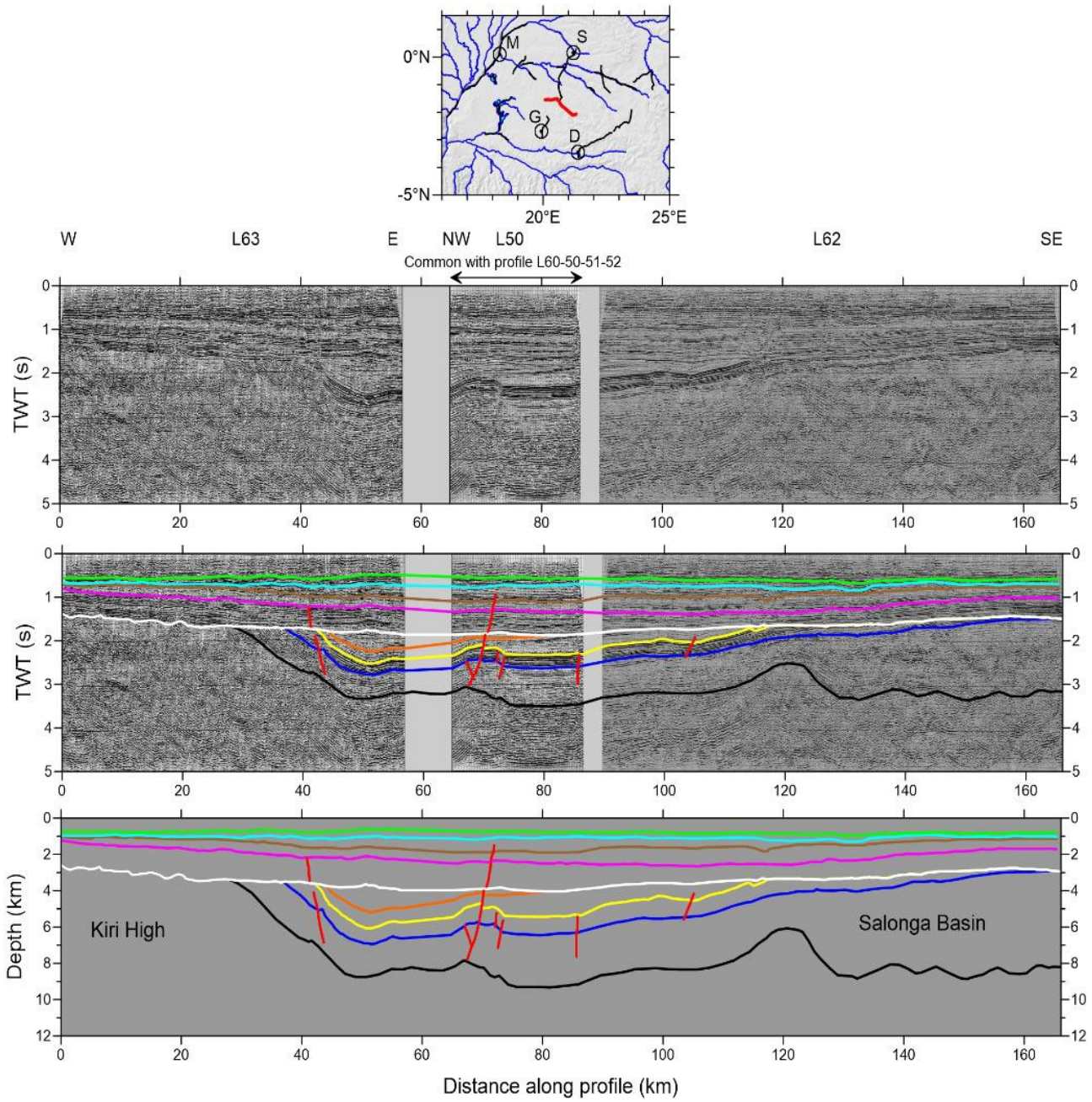

Figure B18 *– Profile L63-50(part)-62 (Delvaux et al., 2021)*

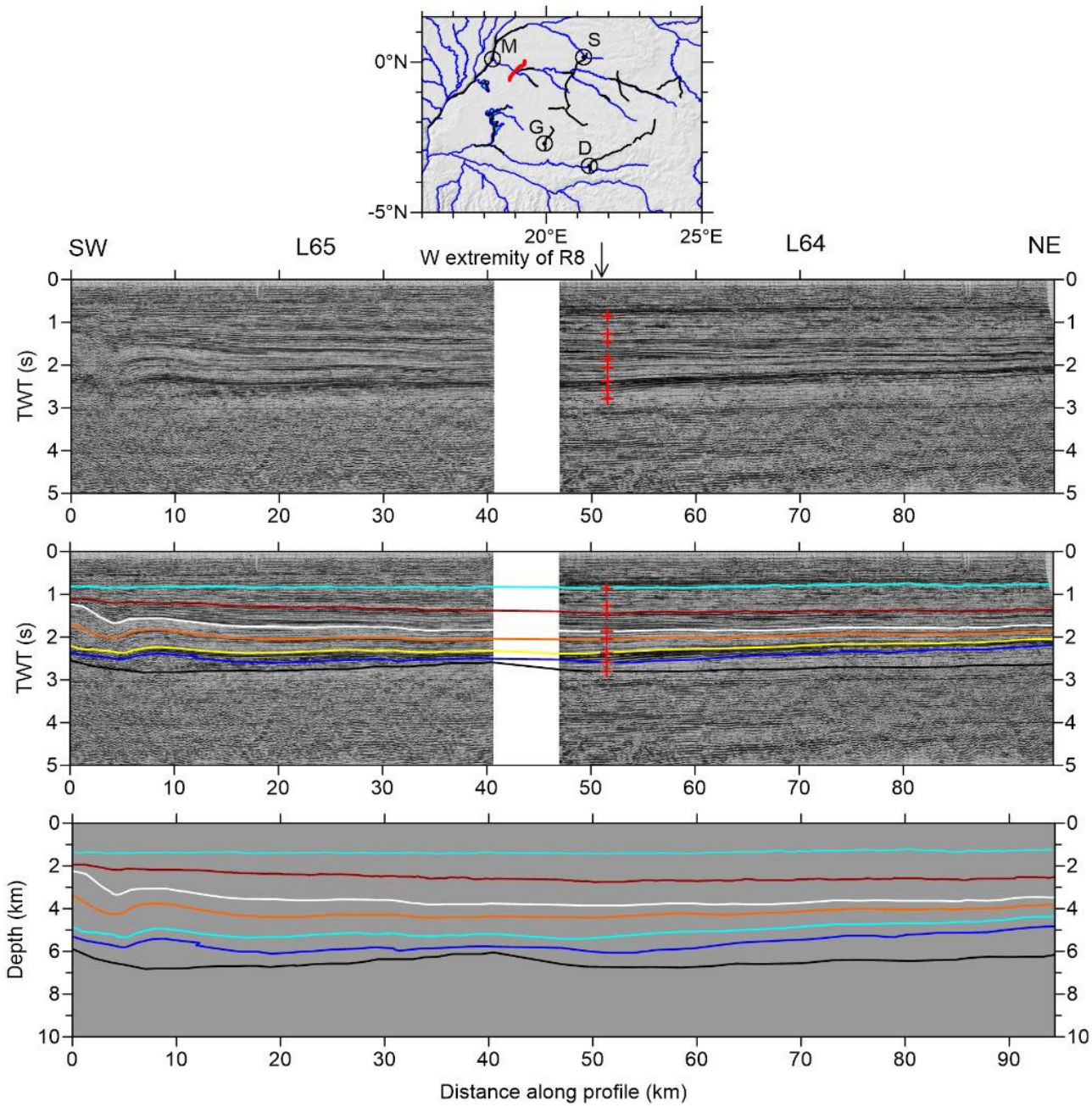

Figure B19 *– Profile L65-64 (Delvaux et al., 2021)*

Appendix C

In this section I present the geotherms used in the numerical simulations and the cross-sections displaying the time evolution of the depth-viscosity variations.

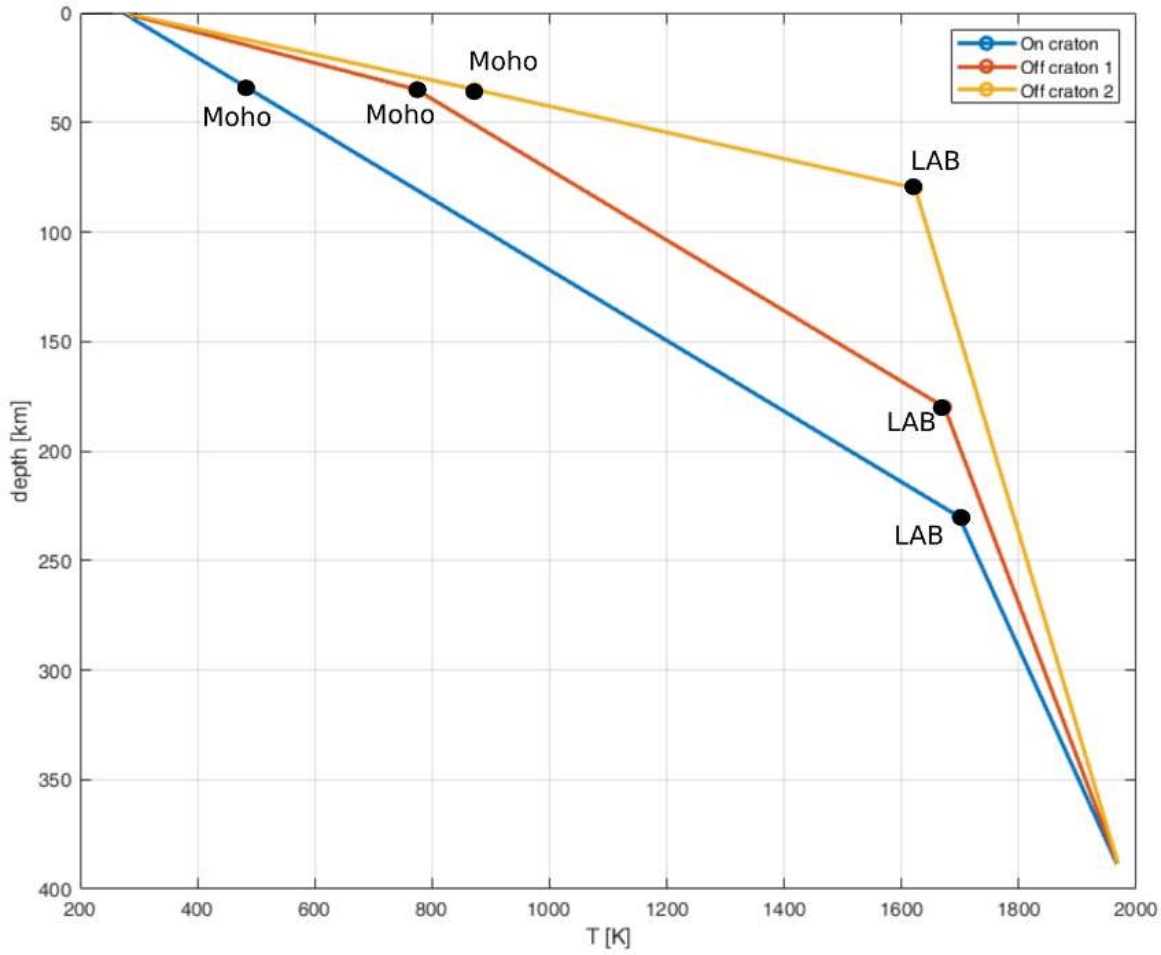

Figure C1 *– Geotherms used in the 3D numerical simulations.* ***On craton****: Geotherm of the cratonic areas.* ***Off craton 1****: First end-member geotherm of the areas outside the cratons, having a lithospheric thickness of 180 km and a temperature at the Moho and base of the lithosphere depth of 873 and 1623 K, respectively.* ***Off craton 2****: Second end-member geotherm of the areas outside the cratons, having a lithospheric thickness of 80 km and a temperature at the Moho and base of the lithosphere depth of 773 and 1673 K, respectively (see Table 4.2).* ***Moho****: Boundary layer between lower crust and upper mantle.* ***LAB****: Lithosphere-Asthenosphere Boundary.*

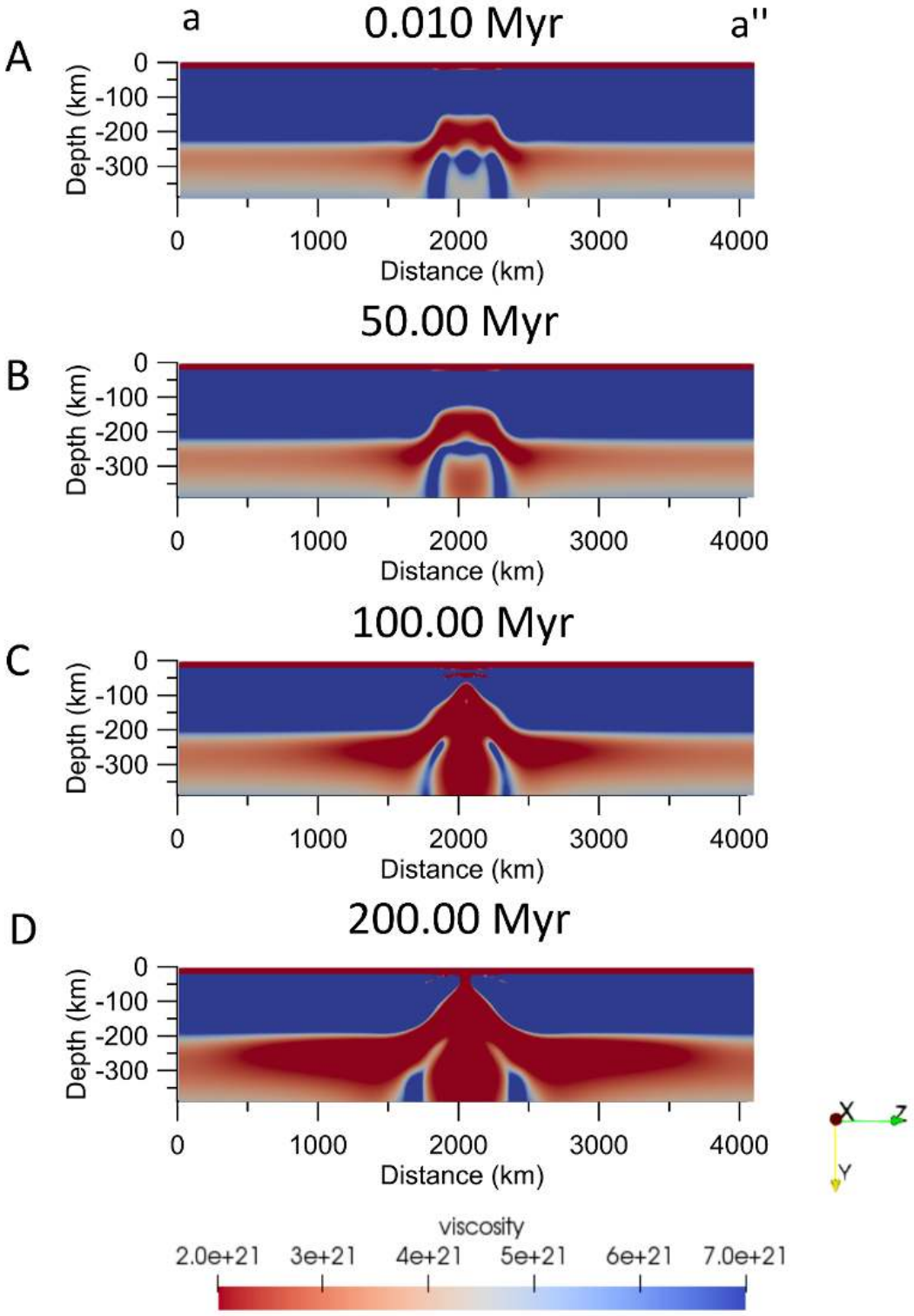

Figure C2a - *Model 3_ Congo_weak1. Depth-viscosity variation at 0.010Myr (**A**), 50Myr (**B**), 100 Myr (**C**), and 200 Myr (**D**). Vertical scale increased by 15% with respect to the horizontal axis.*

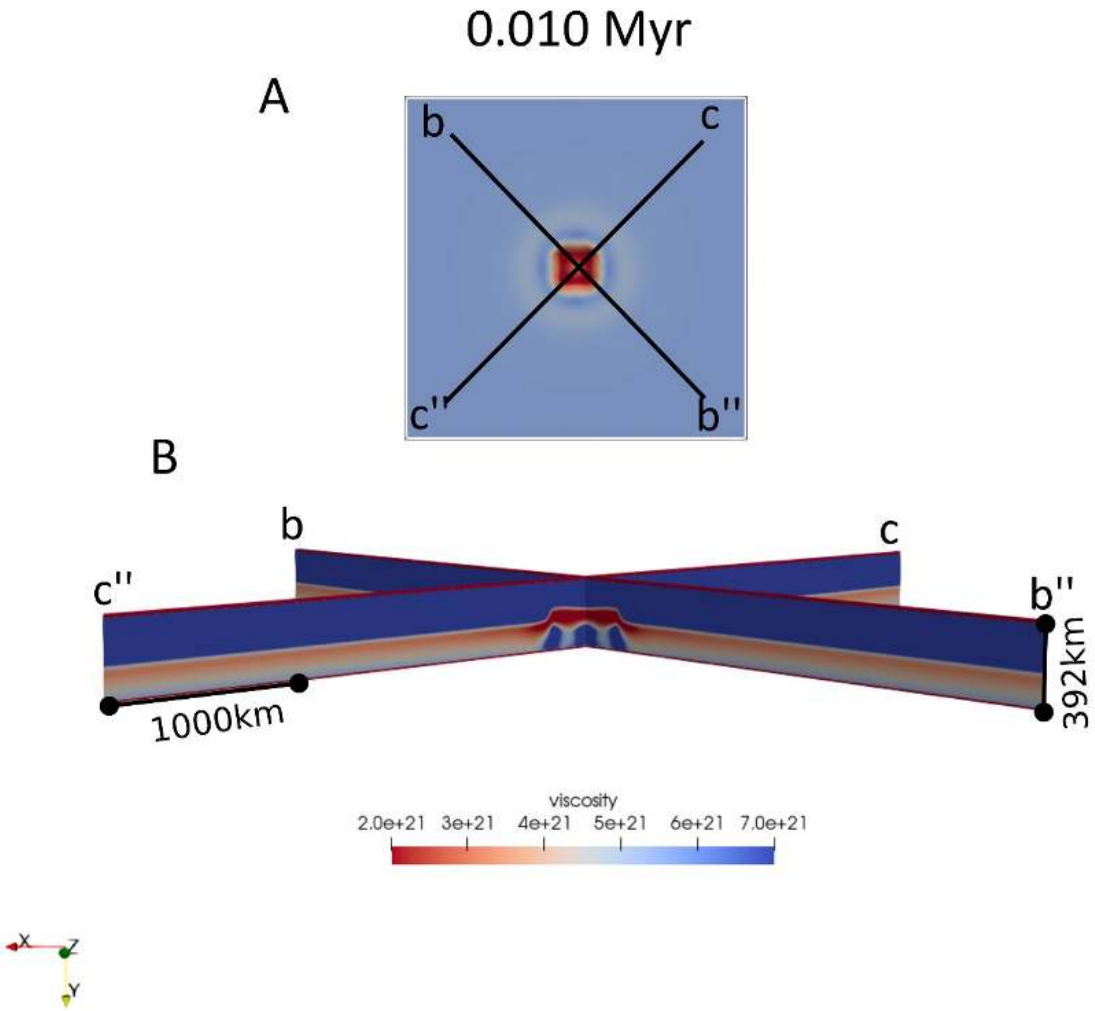

Figure C2b - *Model 3_ Congo_weak1. (**A**) Lateral variation of viscosity (Pa s) at the base of the lithosphere, defined as depth of the isotherm 1573 K at 0.010 Myr (Fig. 4.15 A). (**B**) Diagonal cross-sections of the viscosity variation at 0.010 Myr. Black lines delimited by labels b-b"and c-c", showlocation of the two cross-sections.*

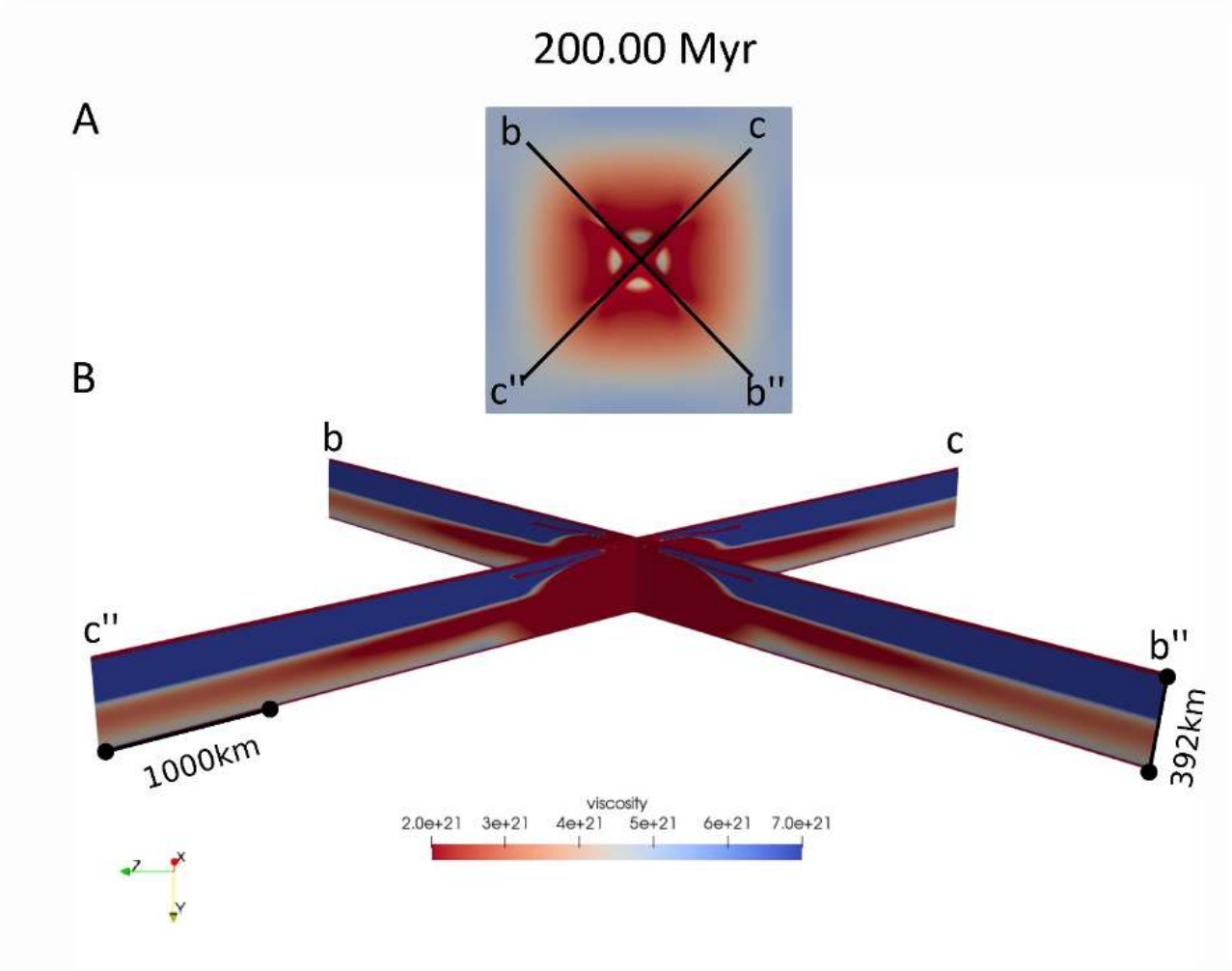

Figure C2c - *Model 3_ Congo_weak1. (**A**) Lateral variation of viscosity (Pa s) at the base of the lithosphere, defined as depth of the isotherm 1573 K at 200Myr (Fig. 4.15 D). (**B**) Diagonal cross-sections of the viscosity variation at 200 Myr. Black lines delimited by labels b-b"and c-c", showlocation of the two cross-sections.*

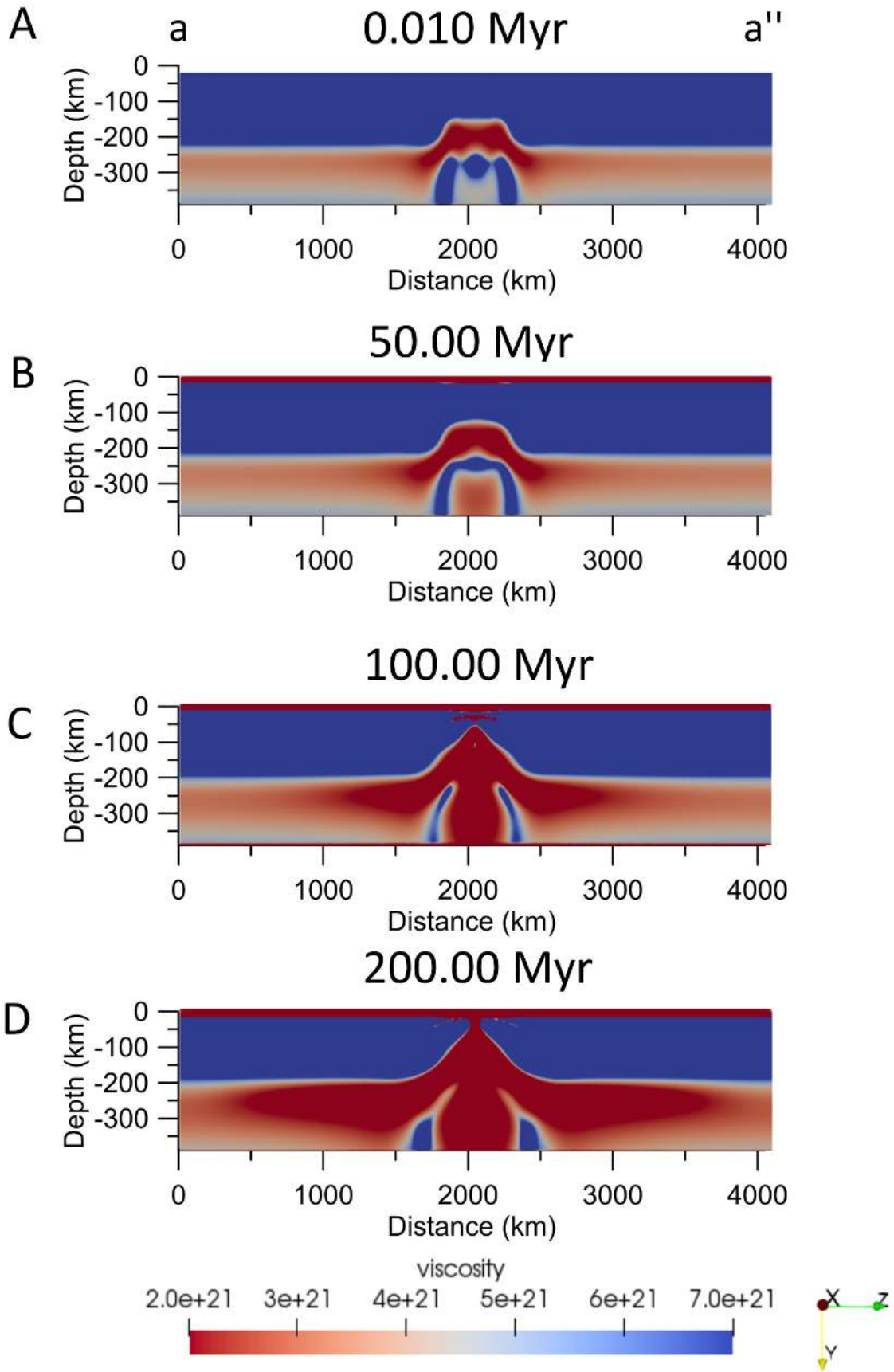

Figure C3a - *Model 4_ Congo_weak2. Depth-viscosity variation at 0.010Myr (**A**), 50Myr (**B**), 100 Myr (**C**), 200 Myr (**D**). Vertical scale increased by 15% with respect to horizontal axis.*

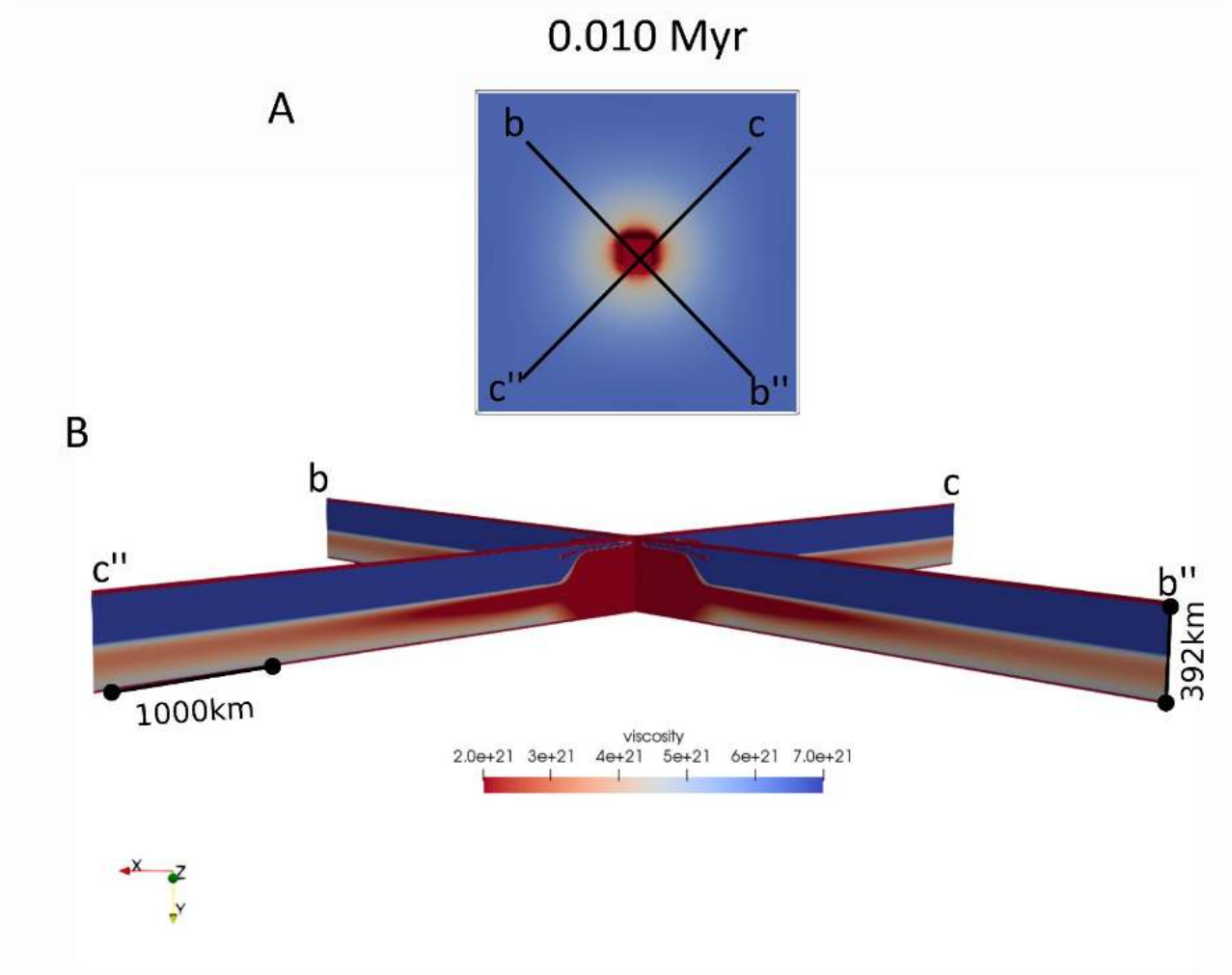

Figure C3b - *Model 4_ Congo_weak2. (**A**) Lateral variation of viscosity (Pa s) at the base of the lithosphere, defined as depth of the isotherm 1573 K at 0.010 Myr (Fig. 4.23 A). (**B**) Diagonal cross-sections of the viscosity variation at 0.010 Myr. Black lines delimited by labels b-b"and c-c", show location of the two cross-sections.*

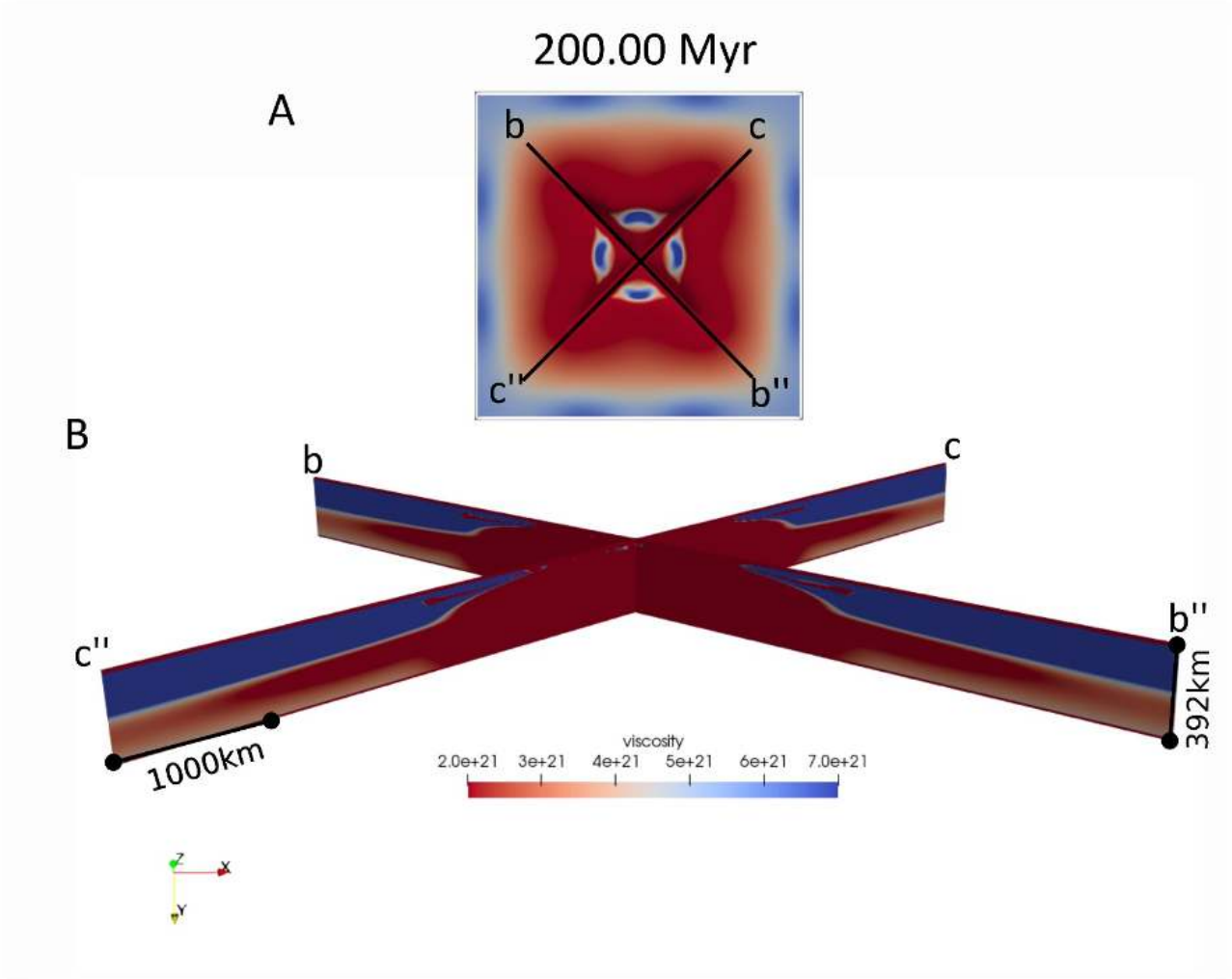

Figure C3c - *Model 4_ Congo_weak2. (**A**) Lateral variation of viscosity (Pa s) at the base of the lithosphere, defined as depth of the isotherm 1573 K at 200Myr (Fig. 4.23 D). (**B**) Diagonal cross-sections of the viscosity variation at 200 Myr. Black lines delimited by labels b-b"and c-c", show location of the two cross-sections.*

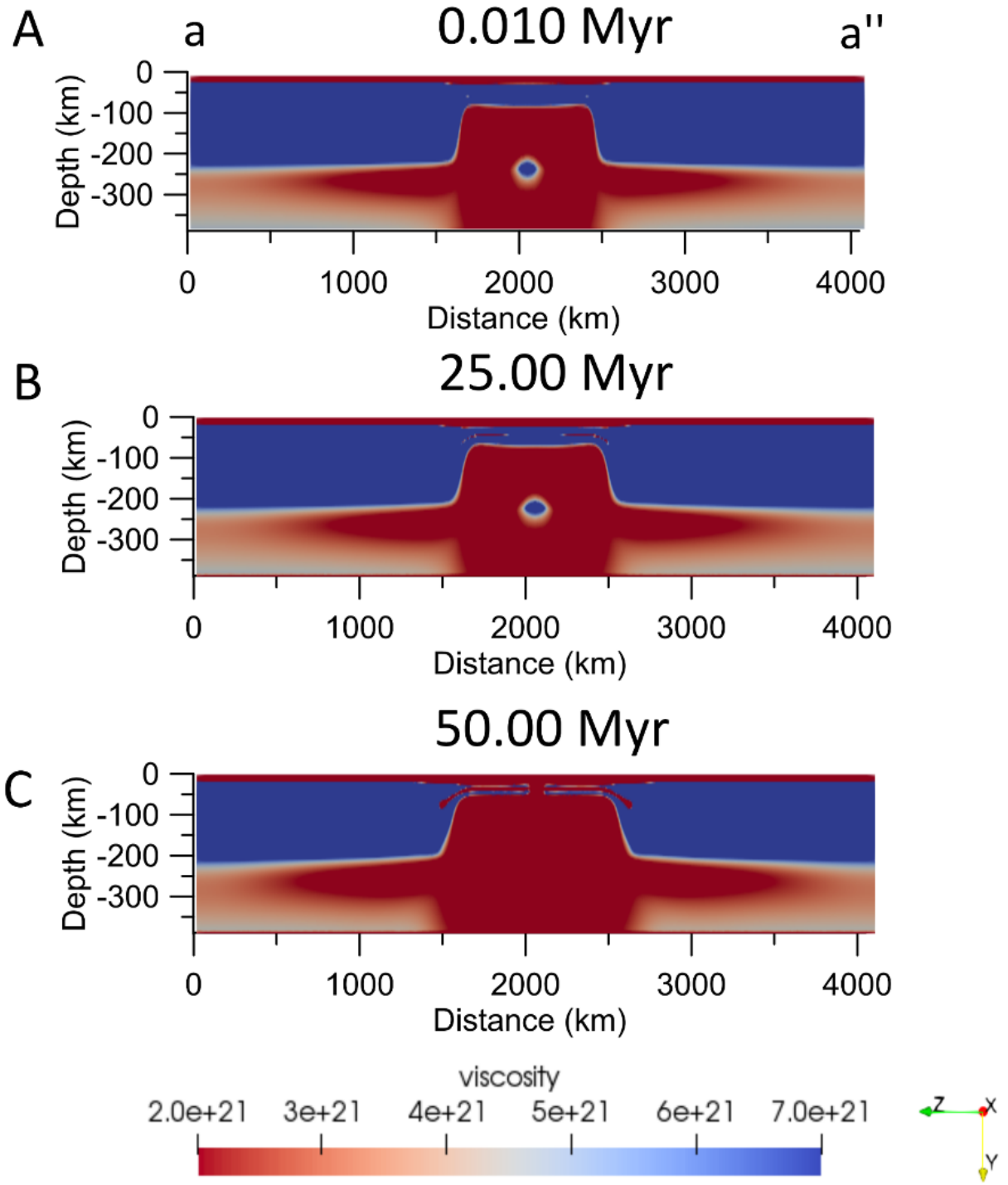

Figure C4a - *Model 5_ Congo_weak3. Depth-viscosity variation at 0.010Myr (**A**), 25Myr (**B**), 50 Myr (**C**). Vertical scale increased by 15% with respect to horizontal axis.*

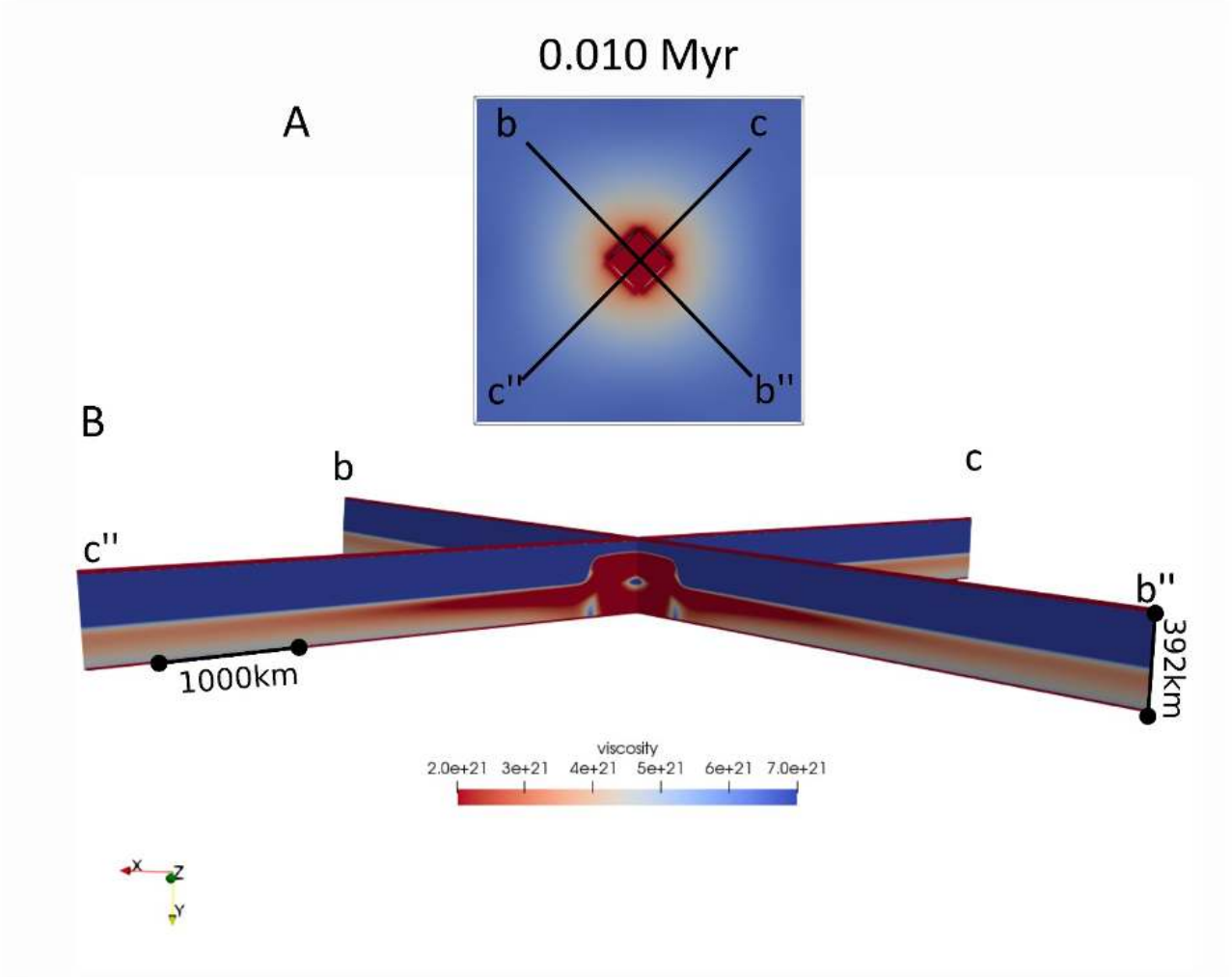

Figure C4b - *Model 5_ Congo_weak3. (**A**) Lateral variation of viscosity (Pa s) at the base of the lithosphere, defined as depth of the isotherm 1573 K at 0.010 Myr (Fig. 4.31 A). (**B**) Diagonal cross-sections of the viscosity variation at 0.010 Myr. Black lines delimited by labels b-b"and c-c", showlocation of the two cross-sections.*

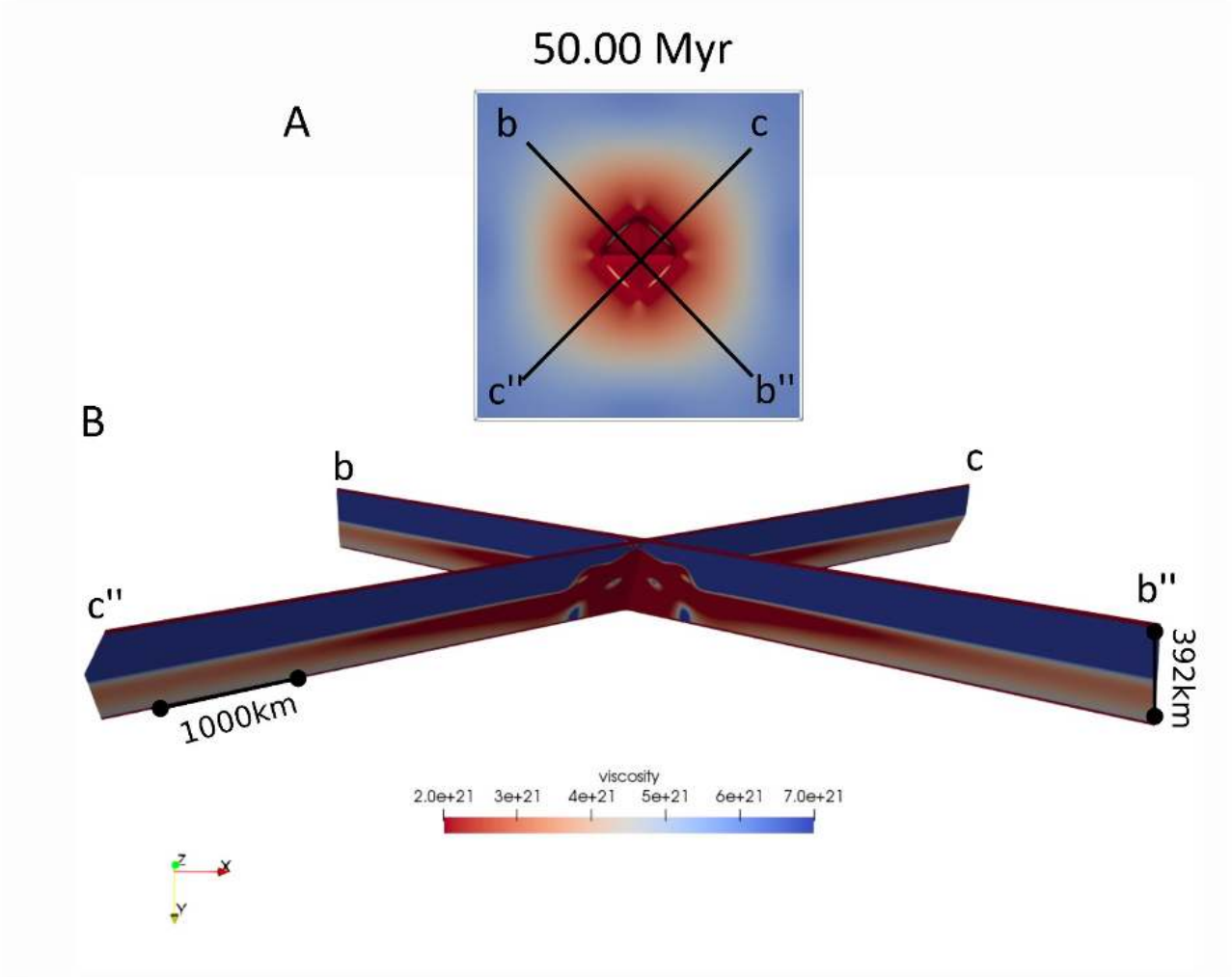

Figure C4c - *Model 5_ Congo_weak3. (**A**) Lateral variation of viscosity (Pa s) at the base of the lithosphere, defined as depth of the isotherm 1573 K at 200 Myr (Fig. 4.31 D). (**B**) Diagonal cross-sections of the viscosity variation at 200 Myr. Black lines delimited by labels b-b"and c-c", showlocation of the two cross-sections.*

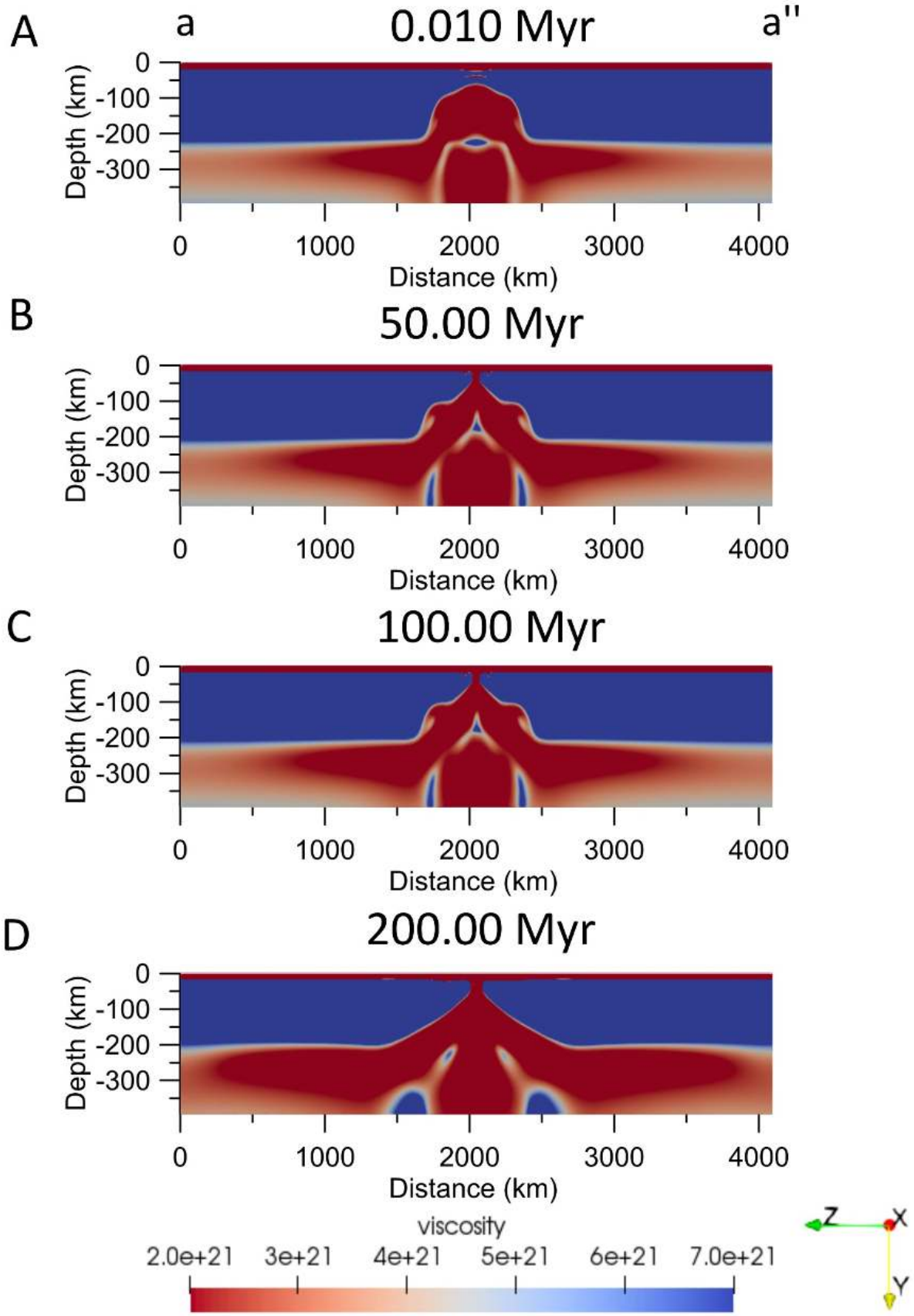

Figure C5a - *Model 6_ Congo_weak4. Depth-viscosity variation at 0.010Myr (**A**), 50Myr (**B**), 100 Myr (**C**), 200 Myr (**D**). Vertical scale increased by 15% with respect to horizontal axis.*

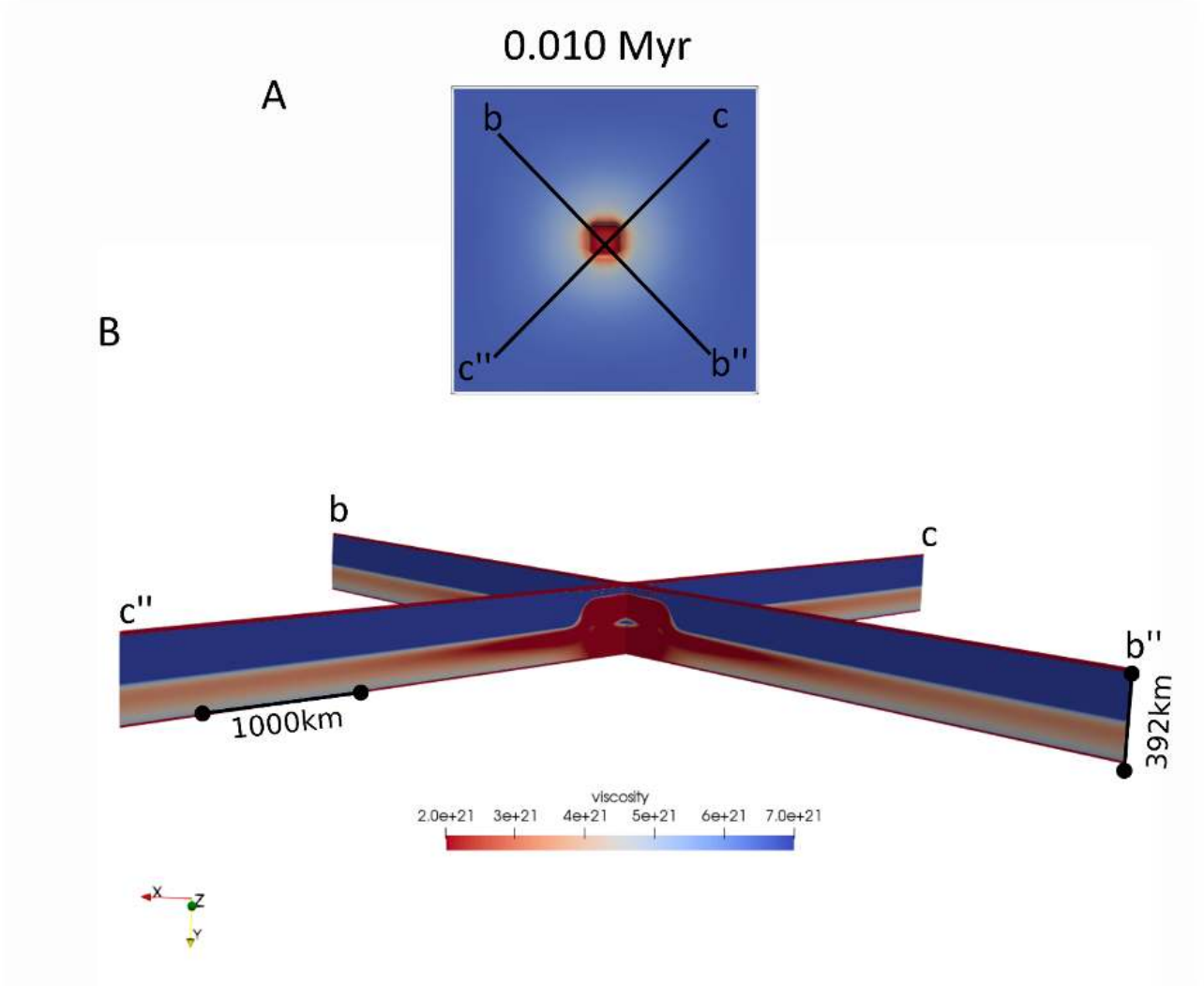

Figure C5b - *Model 6_ Congo_weak4. (**A**) Lateral variation of viscosity (Pa s) at the base of the lithosphere, defined as depth of the isotherm 1573 K at 0.010 Myr (Fig. 4.39 D). (**B**) Diagonal cross-sections of the viscosity variation at 0.010 Myr. Black lines delimited by labels b-b"and c-c", show location of the two cross-setions.*

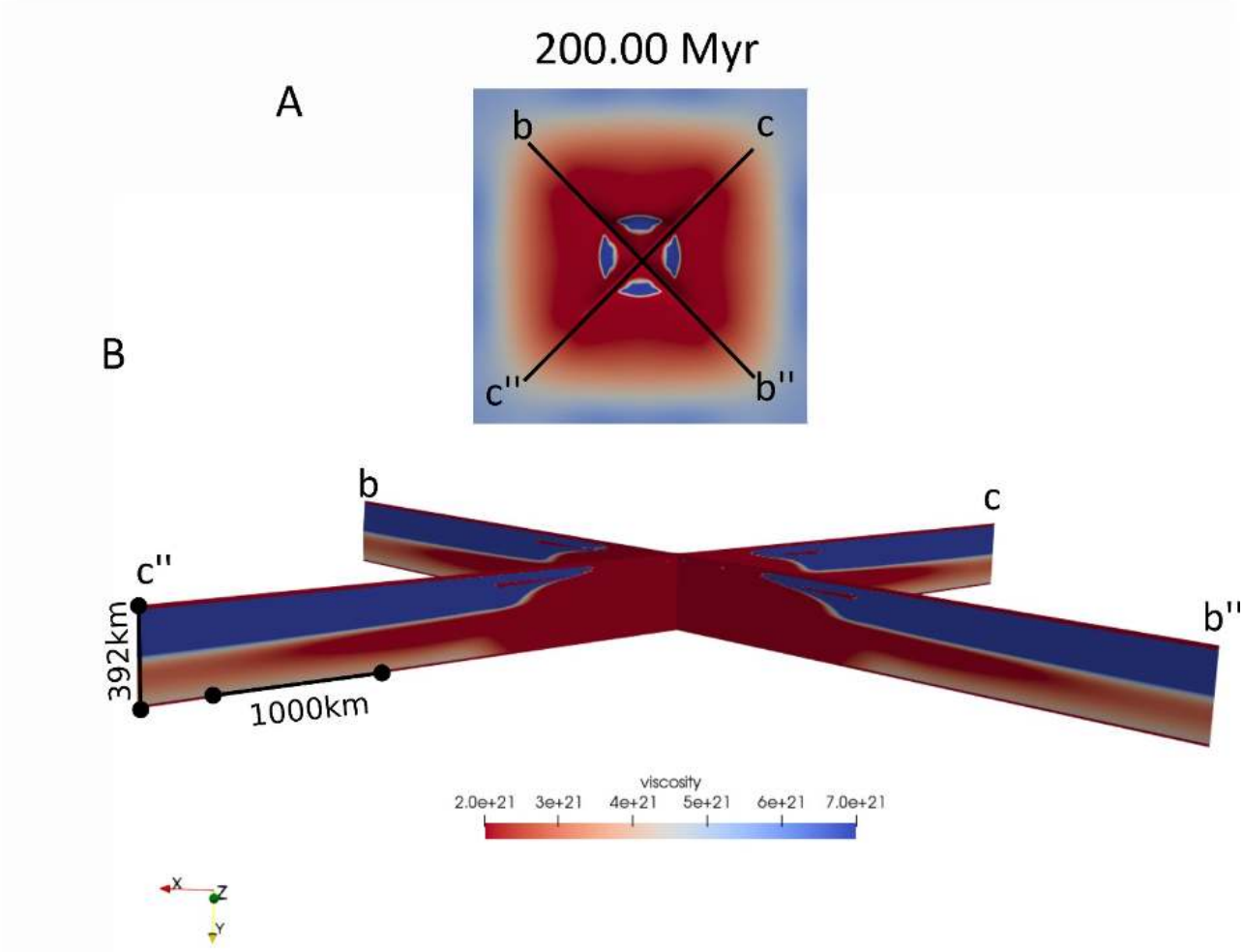

Figure C5c - *Model 6_ Congo_weak4. (**A**) Lateral variation of viscosity (Pa s) at the base of the lithosphere, defined as depth of the isotherm 1573 K at 200Myr (Fig. 4.39 D). (**B**) Diagonal cross-sections of the viscosity variation at 200 Myr. Black lines delimited by labels b-b"and c-c", show location of the two cross-setions.*

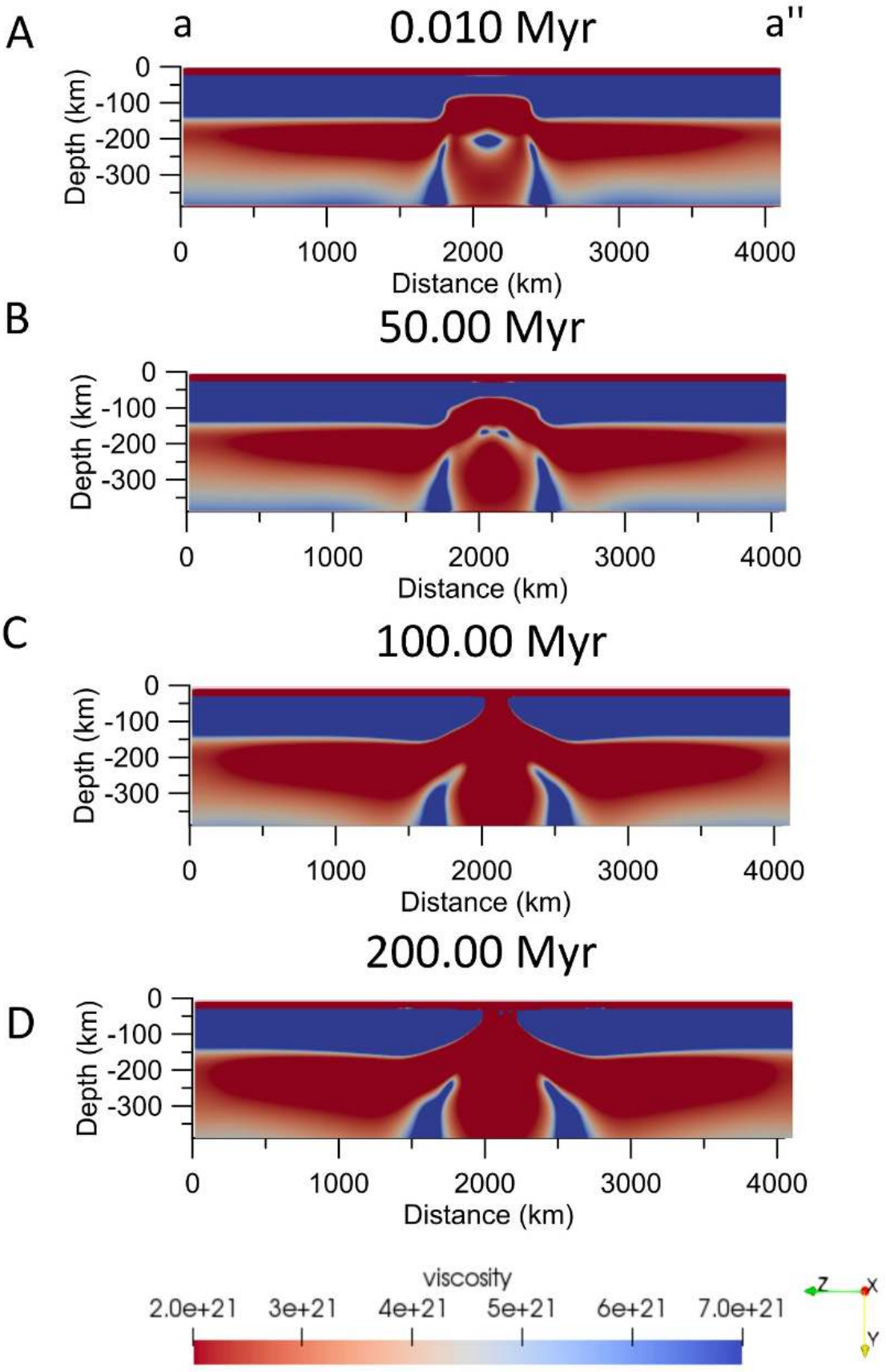

Figure C.6a - *Model 7_ Congo_cratons+weak. Depth-viscosity variation at 0.010Myr (**A**), 50Myr (**B**), 100 Myr (**C**), 200 Myr (**D**). Vertical scale increased by 15% with respect to horizontal axis.*

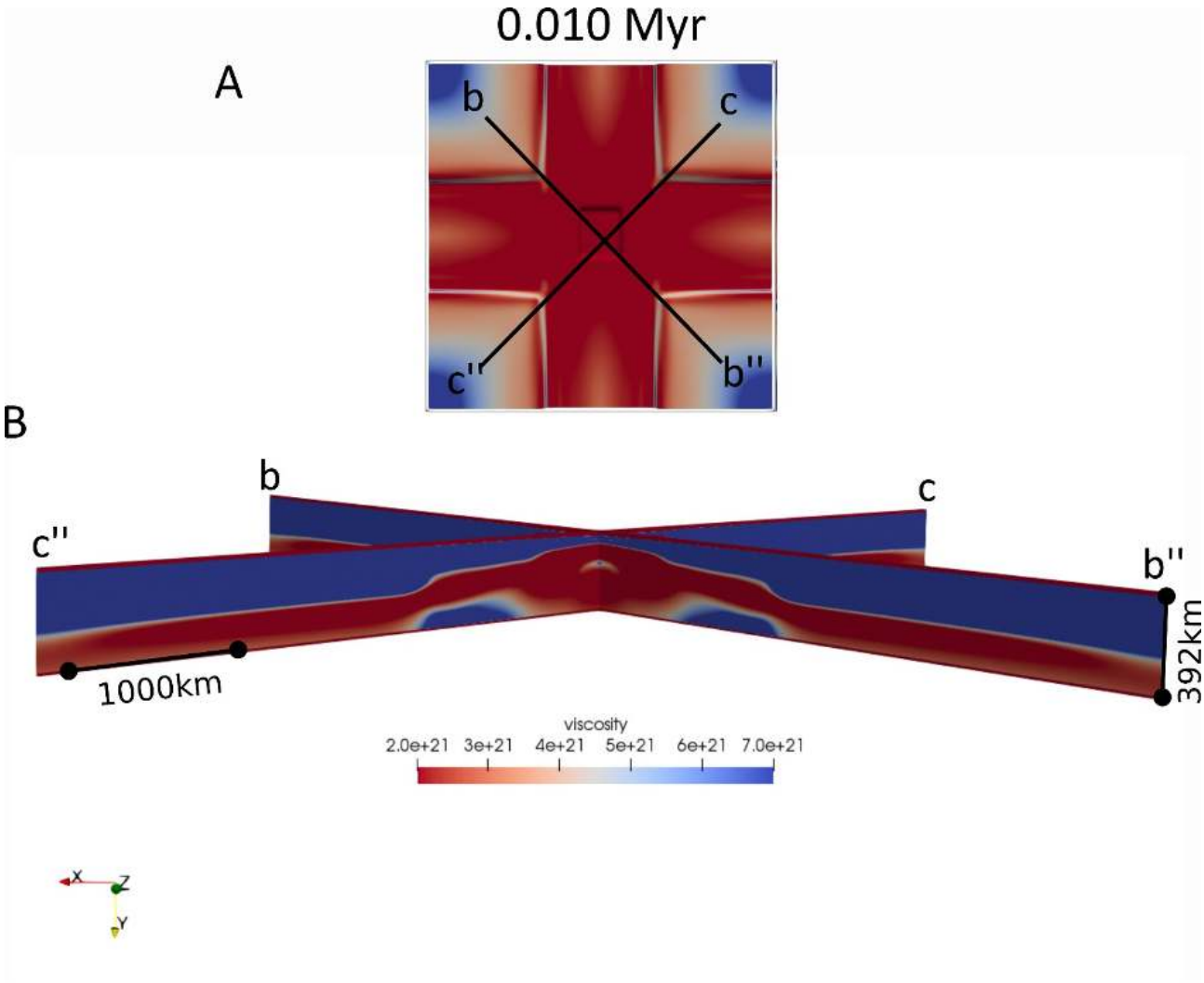

Figure C6b - *Model 7_ Congo_cratons+weak. (**A**) Lateral variation of viscosity (Pa s) at the base of the lithosphere, defined as depth of the isotherm 1573 K at 0.010 Myr (Fig. 4.47 D). (**B**) Diagonal cross-sections of the viscosity variation at 0.010 Myr. Black lines delimited by labels b-b"and c-c", show location of the two cross-sections.*

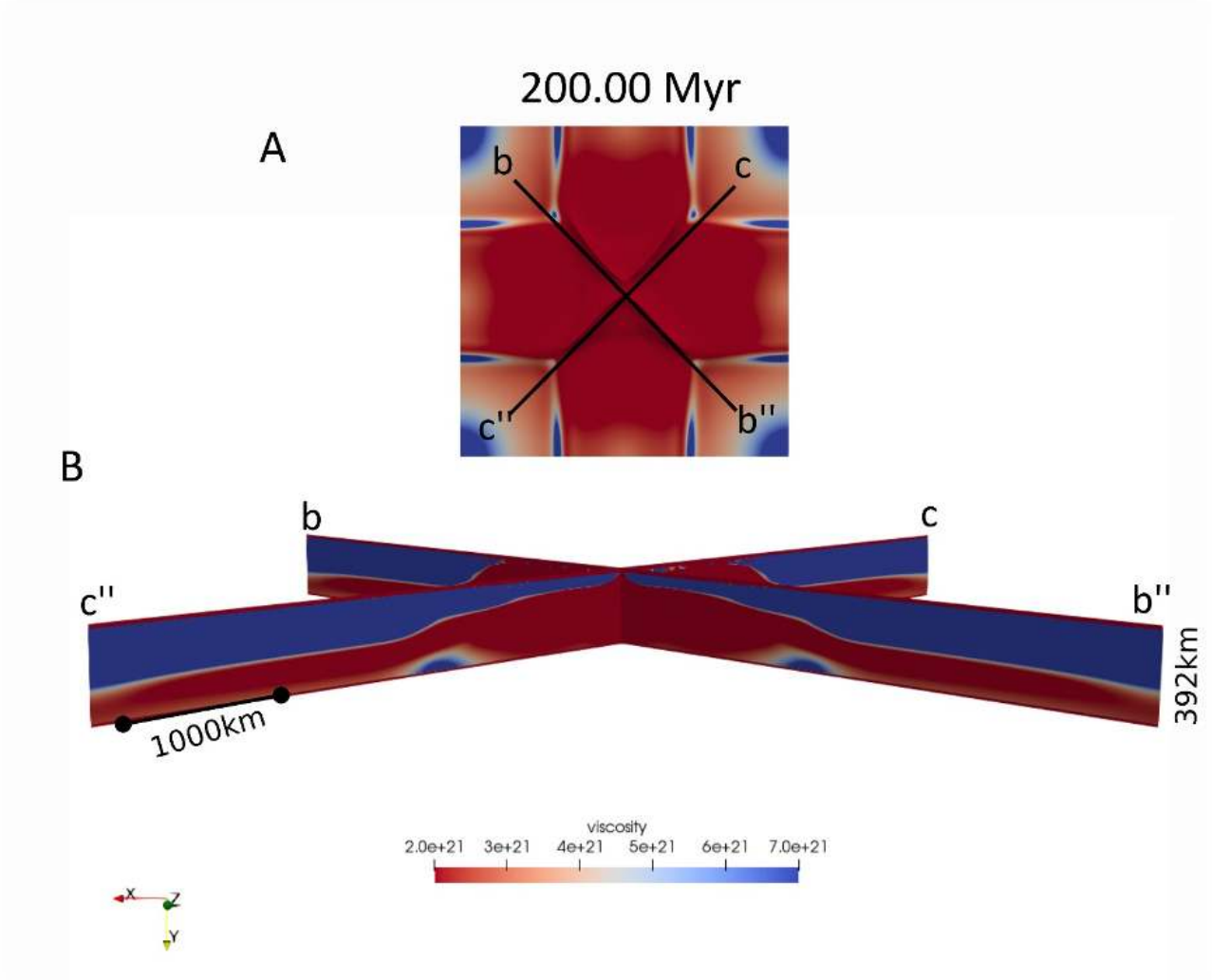

Figure C6c - *Model 7_ Congo_cratons+weak. (**A**) Lateral variation of viscosity (Pa s) at the base of the lithosphere, defined as depth of the isotherm 1573 K at 200Myr (Fig. 4.47 D). (**B**) Diagonal cross-sections of the viscosity variation at 200 Myr. Black lines delimited by labels b-b"and c-c", show location of the two cross-sections.*

Data sources

The geological samples and the exploration geophysics data used come from the Royal Museum of Central Africa (*RMCA*, Tervuren, Belgium). In particular, the well log data used come from available Esso Zaire reports. The seismic profiles were *obtained* from the *CNE*, Kinshasa, and D.R. Congo thanks' to S.M. Kabeya.

The aeromagnetic data provided by D. Fairhead (*GETECH* Group Plc., Kitson House, Elmete Hall, Leeds, *LS8 2LJ*, *UK*).

The release of magnetic data from *GETECH* (GEoscience ta and geospatial TECHnology for delivering the energy transition) has been done in a frame of scientific collaboration between the *RMCA* and *GETECH*.

The satellite data used in terms of global topography, topography and gravity disturbance have been downloaded from *ICGEM* (International Centre for Global Earth Models, (www.icgem.gfz-potsdam.de)).

The 3D numerical simulations have been performed thanks' to the *ETHZ* (Eidgenössische Technische Hochschule Zürich*)* computation facilities (Euler cluster).

The forward modelling of gravity has been performed thanks' to computing resources of the dept. of Mathematics and Geosciences, University of Trieste (*UniTs*). Computation of gravity effects was carried out with the *Tesseroids* software (http://tesseroids.leouieda.com).

Acknowledgements

I would like to thank my supervisors Profs. C. Braitenberg and M. Tesauro, for having patiently taught me during all the phases of this *PhD* project, always giving me the opportunity to get involved in many scientific activities, proposing new ideas and promoting debates.

I am very grateful to Dr. D. Delvaux (*RMCA*) and Prof. T. Gerya (*ETHZ*) who allowed me to join in their research groups, contributing to the realization of this *PhD* thesis project. I would like also to thank Prof. T. Gerya (*ETHZ*) and Prof. M. Scheck-Wenderoth (*GFZ-Potsdam*) for their suggestions during the final revisions of the thesis.

A special thanks to my research group colleagues A. Pastorutti and T. Pivetta for countless helpful discussions on gravity modelling, scientific coding and data analysis.

The *PhD* scholarship that allowed me to carry out this project was provided by Regione Friuli Venezia Giulia (Italy) and University of Trieste through a European Social Fund (*FSE*) 50% cofounded fellowship named "*PO FRIULI VENEZIA GIULIA – FONDO SOCIALE EUROPEO 2014/2020*"

References

Abdelsalaam, M.G., Liégeois, J.-P., Stern, R.J., 2002. The Sahara Metacraton. Journal of African Earth Sciences 34, 119-136. Doi: https://doi.org/10.1016/S0899-5362(02)00013-1

Affaton, P., Kalsbeek, F., Boudzoumou, F., Trompette, R., Thrane, K., Frei, R., 2015. The Pan-African West Congo belt in the Republic of Congo (Congo Brazzaville): Stratigraphy of the Mayombe and West Congo Supergroups studied by detrital zircon geochronology. Precambrian research 272, 185-202. Doi: https://doi.org/10.1016/j.precamres.2015.10.020

Allen, P.A., Allen, J.R., 2005. Basin analysis: Principles and Applications. Blackwell, Maldern, 549p. IBSN: 978-1-118-45030-7

Allen, P.A., Armitage, J.J., 2012. Cratonic basins. In: Busby, C., Azor, A. (Eds.), Tectonics of Sedimentary Basins: Recent Advances. Blackwell Publishing Ltd., pp. 602–620. Doi: https://doi.org/10.1002/9781444347166.ch30

Alvarez P., Maurin J.-C., Vicat J.-P., 1995. La Formation de l'Inkisi (Supergroupe Ouest-Congolien) en Afrique Centrale (Congo et Bas-Zaïre): un delta d'âge Paléozoïque comblant un bassin en extension. Journal of African Earth Sciences 20(2), 119-131. Doi: 10.1016/0899-5362(95)00038-U

Baes, M., Gerya, T. V., Sobolev, S. V. (2016). 3-D thermo-mechanical modeling of plume-induced subduction initiation. Earth and Planetary Science Letters, 453, 193–203. Doi: https://doi.org/10.1016/j.epsl.2016.08.023

Baes, M., Sobolev, S., Gerya, T., Brune, S., 2019. Subduction initiation by plume-plateau interaction: insights from numerical models. Geochemistry, Geophysics, Geosystems, 21, Geophysics, Geosystems, 21, e2020GC009119. Doi: https://doi.org/10.1029/2020GC009119

Baes, M., Sobolev, S., Gerya, T., Brune, S., 2020. Plume-induced subduction initiation: Single-slab or multi-slab subduction. Geochemistry, Geophysics, Geosystems, 21, e2019GC008663. Doi: https://doi.org/10.1029/2019GC008663

Balukiday, B.K., François, C., Sforna, M.C., Beghin, J., Cornet, Y., Storme, J.-Y., Fagel, N., Fontaine, F., Littke, R., Bauder, D., Delvaux, D., Javaux, E., 2018. Raman microspectroscopy, bitumen reflectance and illite crystallinity scale: comparison of different geothermometry methods on fossiliferous Proterozoic sedimentary basins (DR Congo, Mauritania and Australia). International Journal of Coal Geology 191, 80-94, Doi: org/10.1016/j.coal.2018.03.007.

Barritt, S. D. (1993). The African magnetic mapping project. *ITC journal*, (2), 122-131. Doi: 10.1016/S0899-5362(02)00013-1

Begg, G.C. ,W.L. Griffin, L.M. Natapov, S.Y. O'Reilly, S.P. Grand, C.J. O'Neill, J.M.A. Hronsky, Y. Poudjo m Djomani, T. Deen, P. Bowden. (2009). The Lithospheric architecture of Africa. Seismic tomography, mantle petrology and tectonic evolution**.** Geosphere, 5, pp. 23-50. Doi: https://doi.org/10.1130/GES00179.1

Beghin, J., Storme, J.-Y., Blanpied, C., Gueneli, N., Brocks, J.J., Poulton, S.W., Javaux, E.J., 2017a. Microfossils from the late Mesoproterozoic – early Neoproterozoic Atar/El Mreïti Group, Taoudeni Basin, Mauritania, northwestern Africa. Precambrian Research 291, 63–82. Doi: https://doi.org/10.1016/j.precamres.2017.01.009

Beghin, J., Guilbaud, R., Poulton, S.W., Gueneli, N., Brocks, J.J, Storme, J.-Y., Blanpied, C., Javaux, E.J., 2017b. A palaeoecological model for the late Mesoproterozoic – early Neoproterozoic Atar/El Mreïti Group, Taoudeni Basin, Mauritania, northwestern Africa. Precambrian Research 299, 1-14. Doi: 10.1016/j.precamres.2017.07.016

Blewett, S., David, P., 2016. An Overview of Cape Fold Belt Geochronology: Implications for Sediment Provenance and the Timing of Orogenesis. In: Linol. B. and De Wit, M.J. (Eds) Origin and evolution of the Cape Mountains and Karoo Basin. Springer, Berlin, pp. 45-56. Doi: 10.1007/978-3-319-40859-0_5

Bertrand-Sarfati, J., Moussine-Pouchikne, ZA, Affaton, P., Trompette, R., Bellion, Y., 1991. Cover sequences of the West-African Craton. In: Dallmeyer, R.D. Lecorché, J.P. (Eds). The West African Orogens and Circum-Atlantic Correlatives. Springer, Berlin, 65-82. Doi: https://doi.org/10.1007/978-3-642-84153-8_4

Boniface N, Schenk V (2012) Neoproterozoic eclogites in the Paleoproterozoic Ubendian Belt of Tanzania: evidence for a Pan-African suture between the Bangweulu Block and the Tanzania Craton. Precambrian Res 208–211:72–89. Doi: 10.1016/j.precamres.2012.03.014

Boniface, N., Appel, P., 2017. Stenian - Tonian and Ediacaran metamorphic imprints in the southern Paleoproterozoic Ubendian Belt, Tanzania: Constraints from in situ monazite ages. Journal of African Earth Sciences 133, 25-35. Doi: 10.1016/j.jafrearsci.2017.05.005

Boulouard, C., Calendra, F., 1963. Etude palynologique de quelques sondages de la République du Congo (Congo ex-belge). Unpublished report R/ST-no7376, SNPA Direction Exploration et Production Pau, France.

Braitenberg, C., 2015. Exploration of tectonic structures with GOCE in Africa and across-continents. International Journal of Applied Earth Observation and Geoinformation 35(A), 88-95. Doi:10.1016/j.jag.2014.01.013

Bronner, G., Roussel, J., Trompette, R., Clauer, N., 1980. Genesis and geodynamic evolution of the Taoudeni Cratonic Basin (Upper Precambrian and Paleozoic), western Africa. In: Bally, A.W. (Ed.), Dynamics of Plate Interiors. Geodyn. Series 1, 81–90. AGU-GSA. Doi: https://doi.org/10.1029/GD001p0081

Brune, S., C. Heine, and M. Pérez-Gussinyé. (2014). Rift migration explains continental margin asymmetry and crustal hyperextension, Nature, Doi: 10.1038/ncomms5014

Buiter, S.J.H., Steinberger, B., Medvedev, S., Tetreault, J.L., 2012. Could the mantle have caused subsidence of the Congo Basin? Tectonophysics 514-517, 62-80. Doi: http://dx.doi.org/10.1016/j.tecto.2011.09.024

Burke, K., Gunnell, Y., 2008. The African erosion surface: a continental-scale synthesis geomorphology, tectonics, and environmental change over the past 180 million years. Geological Society of America Memoir 201, 66pp. IBSN: 978-0813712017

Cacace, M. Scheck-Wenderoth, M. 2016. Why intracontinental basins subside longer: 3-D feedback effects of lithospheric cooling and sedimentation on the flexural strength of the lithosphere. J. Geophys. Res. Solid Earth, 121, 3742-3761. Doi: 10.1002/2015JB012682

Cahen, L., Mortelmans, G., 1947. Le système de la Bushimae au Katanga. Bull. Société belge de Géologie 56, 217-252.

Cahen, L., 1954. Géologie du Congo Belge. Vaillant-Caramane, Liège, 577pp. (OCoLC)594632320

Cahen, L., Ferrand, J.J., Haarsma, M.J.F., Lepersonne, J., Verbeek, Th., 1959. Description du sondage de Samba. Ann. Mus. Royal Congo Belge, Tervuren (Belgique), Série in-8°, Sc. géol., 29, 210pp.

Cahen, L., Ferrand, J.J., Haarsma, M.J.F., Lepersonne, J., Verbeek, Th., 1960. Description du sondage de Dekese. Ann. Mus. Royal Congo Belge, Tervuren (Belgique), Série in-8°, Sc. géol., 34, 115pp.

Cahen, L., Lepersonne, J., 1971. La stratigraphie de la série des roches rouges et ses relations avec la série de la Haute-Lueki. (Annexe : Coupe du sondage n°11 dans le bassin charbonnier de la Lukuga). Dépt. Géol. Min., Mus. Roy. Afr. Centr., Rapp. Ann., 1970, 94-121.

Cahen, L., Lepersonne, J., 1978 Synthèse des connaissances relatives au Groupe (anciennement Série) de la Lukuga (Permien du Zaïre). Ann. Mus. Roy. Congo belge, Tervuren (Belgique), série in-8, Sci. géol., 82, 115-152.

Cahen, L., 1981. Précisions sur la stratigraphie et les corrélations du Groupe de la Haute-Lueki et des formations comparables (Triassique à Liasique d'Afrique Centrale). Dépt. Géol. Min., Mus. Roy. Afr. Centr., Rapp. Ann. 1980, 81-96.

Cahen, L., 1983a. Brèves précisions sur l'âge des groupes crétaciques post-Wealdien (Loia, Bokungu, Kwango) du Bassin intérieur du Congo (Republique du Zaïre). Rapport annuel du Musée Royal de l'Afrique centrale, Tervuren (Belgique), Département de Géologie et de Minéralogie, pp 61–72.

Cahen, L., 1983b. Le Groupe de Stanleyville (Jurassic supérieur et Wealdien de l'intérieur de la République du Zaïre): Révision des connaissances. Rapport annuel du Musée Royal de l'Afrique centrale, Tervuren (Belgique), Département de Géologie et de Minéralogie, pp 73–91.

Cahen, L., Snelling, N.J., Delhal, J., Vail, J.R., Bonhomme, M. and Ledent, D., 1984. Geochronology and Evolution of Africa. Clarendon, Oxford, 512 p. ISBN: 0-19-857544-0

Caillaud, A., Blanpied, C., Guillocheau, F., Delvaux, D., 2017. The Jurassic Stanleyville formation in the eastern margin of the Congo Basin: an example of a shallow balanced-fill lake basin. Journal of African Earth Sciences 132, 80-98. Doi: 10.1016/j.jafrearsci.2017.05.002

Cailteux, J.L.H., De Putter, T., 2019. The Neoproterozoic Katanga Supergroup (D. R. Congo): State-of-the-art and revisions of the lithostratigraphy, sedimentary basin and geodynamic evolution. Journal of African Earth Sciences 150, 522–531. Doi: 10.1016/j.jafrearsci.2018.07.020

Cartwright, J.A., Haddock, R.C., Pinheiro, L.M., 1993. The lateral extent of sequence boundaries. In: Williams, G.D. Dobb, A. (eds.), Tectonics and Seismic Sequence Stratigraphy. Geological Society, Special Publication 71, 15-34, London. Doi: https://doi.org/10.1144/GSL.SP.1993.071.01.02

Casier, E., 1965. Poissons fossiles de la série du Kwango (Congo). Ann. Mus. royal Afrique centrale, Tervuren (Belgique), série in-8, Sci. géol., 50, 69p.

Celli, N.L., Lebedev, S., Schaeffer, A.J., Gaina, C., 2020. African cratonic lithosphere carved by mantle plumes. Nature Communications 11, 92, Doi:10.1038/s41467-019-13871-2.

Chorowicz, J., Le Fournier, J., Mvumbi, M.M., 1990. La Cuvette Centrale du Zaïre: un bassin initié au Proterozoïque supérieur. Contribution de l'analyse du réseau hydrographique. C. R. Acad. Sci. Paris, t. 311, Serie II, p. 349-356. ISSN 0764-4450

Clauer, N., 1981. Rb–Sr and K–Ar dating of Precambrian clays and glauconies. Precambrian Res. 15, 331–352.

Cloetingh, S., Burov, E.B., Poliakov, A., 1999. Lithospheric folding: primary response to compression? (From central Asia to Paris basin). Tectonics 18, 1064–1083. Doi: 10.1029/1999TC900040

Colin, J.P., 1994. Mesozoic-Cenozoic lacustrine sediments of the Zaïre Interior Basin. In: Gierlowski-Kordesch, E., Kelts, K. (eds.) Global Geological record of lake basins, Vol.1. Cambridge University Press, UK, pp. 31-36.

Collins, A.S., Pisarevsky, S.A., 2005. Amalgamating eastern Gondwana: The evolution of the Circum-Indian Orogens. Earth-Sciences Reviews 71, 229-270. Doi: 10.1016/j.earscirev.2005.02.004

Cox, L.H., 1960. Further Mollusca from the Lualaba Beds of the Belgian Congo. Ann. Mus. Roy. Afr. Cent., Tervuren (Belgique), série in-8, Sci. géol., 37, 15p.

Crameri, F., Schmeling, H., Golabeck, G.J., Duretz, T., Orendt, R., Buiter, S.J.H., May, D.A., Kaus, B.J.P., Gerya, T.V., Tackley, O.J., 2012a. A comparison of numerical surface topography calculations in geodynamic modelling: an evaluation of the « sticky air » method. Geophysical Journal International, 189, 38-54. Doi: https://doi.org/10.1111/j.1365-246X.2012.05388.x

Crosby, A.G., Fishwick, S., White, N., 2010. Structure and evolution of the intracratonic Congo Basin. Geochemistry Geophysics Geosystems 11(6), Q06010, Doi: 10.1029/2009GC003014.

Daly, M.C., Lawrence, S.R., Kimun'a, D., Binga, M., 1991. Late Palaeozoic deformation in central Africa: a result of distant collision? Nature 350, 605-607. Doi: https://doi.org/10.1038/350605a0

Daly, M.C., Lawrence, S.R., Diemu-Tshiband, K., Matouana, B., 1992. Tectonic evolution of the Cuvette Centrale, Zaire. Journal of the Geological Society of London 149, 539-546, Doi:10.1144/gsjgs.149.4.0539.

Daly, M.C., Fuck, R.A., Julià, J., Macdonald, D.I.M., Watts, B., 2018. Cratonic basin formation: a case study of the Parnaíba Basin of Brazil. Geological Society, London, Special Publications, 472, 1-15. https://doi.org/10.1144/SP472.20.

Defrétin-Lefranc, S., 1967. Etude sur les Phyllopodes du Bassin du Congo. Ann. Mus. Roy. Afr. Cent., Tervuren (Belgique), série in-8, Sci. géol., 56, 122p.

Delpomdor, F., Blanpied, C., Virgone A., Préat, A., 2013a. Paleoenvironments in Meso-Neoproterozoic carbonates of the Mbuji-Mayi Supergroup (Democratic Republic of Congo) - Microfacies analysis combined with C-O-Sr isotopes, major-trace elements and REE+Y distributions. Journal of African Earth Sciences 88, 72-100. Doi:10.1016/j.jafrearsci.2013.09.002

Delpomdor, F., Linnemann, U., Boven, A., Gärtner, A., Travin, A., Blanpied, C., Virgone, A., Jelsma, H., Préat, A., 2013b. Depositional age, provenance, and tectonic and paleoclimatic settings of the late Mesoproterozoic–middle Neoproterozoic Mbuji-Mayi Supergroup, Democratic Republic of Congo. Palaeogeography, Palaeoclimatology, Palaeoecology 389, 35-47. D Doi:10.1016/j.palaeo.2013.06.012

Delpomdor, F. and Préat, A., 2015. Overview of the Neoproterozoic sedimentary series exposed along the margins of the Congo Basin. In: De Wit, M., Guillocheau, F., De Wit, M.C.J. (Eds), The Geology and Resource Potential of the Congo Basin. Springer, Berlin, pp. 41-58, Doi: 10.1007/978-3-642-29482-2_3.

Delpomdor, F., Eyeles, N., Tack, L., Préat, A., 2016. Pré- and post-Marinoan carbonate facies of the Democratic Republic of the Congo: Glacially- or tectonically-influenced deep-water sediments Paleogeography, Paleoclimatology, Paleoecology 457, 144-157. Doi: 10.1016/j.palaeo.2016.06.014

Delvaux, D., 2001. Karoo rifting in western Tanzania: precursor of Gondwana breakup In Contributions to Geology and Paleontology of Gondwana. In honour of Prof. Dr. Helmut Wopfner, Cologne, pp. 111-125. ISBN 3-934027-07-5.

Delvaux, D., Barth, A., 2010. African stress pattern from formal inversion of focal mechanism data. Implications for rifting dynamics. Tectonophysics 482, 105-128. D Doi:10.1016/j.tecto.2009.05.009

Delvaux, D., Kervyn, F., Macheyeki, A.S., Temu, E.B., 2012. Geodynamic significance of the TRM segment in the East African Rift (W-Tanzania): active tectonics and paleostress in the Ufipa plateau and Rukwa basin. Journal of Structural Geology 37, 161-180. D Doi: 10.1016/j.jsg.2012.01.008

Delvaux, D., Cloetingh, S., Beekman, F., Sokoutis, D., Burov, E., Buslov, M.M, Abdrakhmatov, E.E. (2013). Basin evolution in a folding lithosphere: Altai-Sayan and Tien Shan belts in central Asia. Tectonophysics 602, 194-222. Doi: https://doi.org/10.1016/j.tecto.2013.01.010

Delvaux, D., Fernandez-Alonso, M., 2015. Petroleum potential of the Congo Basin. In: De Wit, M., Guillocheau, F., De Wit, M.C.J. (Eds.), The Geology and Resource Potential of the Congo Basin. Springer, Berlin, pp. 371-391, Doi: 10.1007/978-3-642-29482-2_18.

Delvaux, D., Maddaloni, F., Tesauro, M., Braitenberg, C., 2021. The Congo Basin: Stratigraphy and subsurface structure defined by regional seismic reflection, refraction and well data. Global and Planetary Change. Doi: 10.1016/j.gloplacha.2020.103407

Deynoux, M., Affaton, P., Trompette, R., Villeneuve, M., 2006. Pan-African tectonic evolution and glacial events registered in Neoproterozoic to Cambrian cratonic and foreland basins of West Africa. Journal of African Earth Sciences 46, 397–426. DOI:10.1016/j.jafrearsci.2006.08.005

De Waele, B., Johnson S.P. and Pisarevsky, S.A., 2008. Palaeoproterozoic to Neoproterozoic growth and evolution of the eastern Congo Craton: Its role in the Rodinia puzzle. Precambrian Research 160, 127-141. Doi: https://doi.org/10.1016/j.precamres.2007.04.020

De Wit, M.J., Ransome, I.G.D., 1992. Regional inversion tectonics along the southern margin of Gondwana. In: De Wit, M.J., Ransome, I.G.D. (Eds.), Inversion Tectonics of the Cape Fold Belt, Karoo and Cretaceous Basins of Southern Africa. Balkema, Rotterdam, pp. 15-21.

De Wit, M.J., Linol, B., 2015. Precambrian basement of the Congo Basin and its flanking terrains. In: De Wit, M., Guillocheau, F., De Wit, M.C.J. (Eds.), The Geology and Resource Potential of the Congo Basin. Springer, Berlin, pp. 19-40, Doi: 10.1007/978-3-642-29482-2_2.

Downey, N.J., Gurnis, M., 2009. Instantaneous dynamics of the cratonic Congo Basin. Journal of Geophysical Research 114, B06401, Doi: 10.1029/2008JB006066.

Downey, N., Gurnis, M., Avouac, J.-P., 2011. Subsidence history and geodynamic evolution of the cratonic Congo Basin. Geophysical Research Abstracts 13, EGU2011-388-1.

Duretz, T., May, D.A., Gerya, T.V., Tackley, P.J., 2011a. Discretization errors and free surface stabilization in the finite difference and mark-in-cell method for applied geodynamics: a numerical study. Geochemistry, Geophysics, Geosystems, 12, Q07004. Doi: https://doi.org/10.1029/2011GC003567

ECL, 1988. Hydrocarbon Potential of the Cuvette Centrale (Republic of Zaire). Exploration Consultants Limited, Cellule Technique Pétrolière, Pétrozaire, unpublished report, 41pp.+figures, tables, appendices and enclosures.

Egoroff, A., Lombard, A.L., 1962. Présence des couches de Stanleyville dans le sous-sol de Léopoldville, République du Congo (Note préliminaire). Ann. Société géologique Belg. 85, 103-109.

Esso-Zaire SARL (1981a) Geological completion report: Gilson-1. Unpublished report

Esso-Zaire SARL (1981b). Geological completion report: Mbandaka-1. Unpublished report

Evrard, P., 1957. Les recherches géophysiques et géologiques et les travaux de sondage dans la Cuvette congolaise. Académie royale des Sciences coloniales, Classe des Sciences Techniques, Mém. En 8°, Nouv. Sér., 7(1), 63p.

Evrard, P., 1960. Sismique. Résultats scientifiques des missions du Syndicat pour l'étude géologique et minière de la Cuvette congolaise. Ann. Mus. Royal Congo Belge, Tervuren (Belgique), Série in-8°, Sc. géol. 33, 87p.

Fernandez-Alonso, M., Cutten, H., De Waele, B., Tack, L., Tahon, A., Baudet, D., Barritt, S.D., 2012. The Mesoproterozoic Karagwe-Ankole Belt (formerly the NE Kibara Belt): The result of prolonged extensional intracratonic basin development punctuated by two short-lived far-field compressional events. Precambrian Research 216-219, 63-86. Doi: 10.1016/j.precamres.2012.06.007

Fernandez-Alonso, M., Kampata, D., Mupande, J.-F., Dewaele, S., Laghmouch, M., Baudet, D., Lahogue, P., Badosa, T., Kalenga, H., Onya, F., Mawaya, P., Mwanza, B., Mashagiro, H., Kanda-Nkula, V., Luamba, M., Mpoyi, J., Decrée, S. and Lambert, A. 2015. Carte Géologique de la République Démocratique du Congo au 1 / 2.500.000 - Notice explicative. Ministère des Mines, République Démocratique du Congo, Kinshasa. ISBN: 978-9-4922-4481-9.

Fernandez-Alonso, M., Kampata, D., Mupande, J.-F., Dewaele, S., Laghmouch, M., Baudet, D., Lahogue, P., Badosa, T., Kalenga, H., Onya, F., Mawaya, P., Mwanza, B., Mashagiro, H., Kanda-Nkula, V., Luamba, M., Mpoyi, J., Decrée, S. and Lambert, A. 2017. Carte Géologique de la République Démocratique du Congo au 1 / 2.500.000 -. Ministère des Mines, République Démocratique du Congo, Kinshasa. ISBN: 978-9-4922-4480-2.

Finger, N.-P., Kaban, M. K., Tesauro, M., Haeger, C., Mooney, W. D., Thomas, M. (2021). A thermo-compositional model of the cratonic lithosphere of South America. Geochemistry, Geophysics, Geosystems, 22, e2020GC009307. Doi: https://doi.org/10.1029/2020GC009307

Fishwick, S., 2010. Surface wave tomography: Imaging of the lithosphere–asthenosphere boundary beneath central and southern Africa. Lithos, November 2010, Pages 63-73. Doi: https://doi.org/10.1016/j.lithos.2010.05.011

Foley, S., O'Neill. 2021. Continents soldered from below. Nature. Vol 592. News and views. Doi: 10.1038/d41586-021-01087-8

Foster, D. A., Goscombe, B. D., Newstead, B., Mapani, B., Mueller, P. A., Gregory L. C., Muvangua E., 2015. U–Pb age and Lu–Hf isotopic data of detrital zircons from the Neoproterozoic Damara Sequence: Implications for Congo and Kalahari before Gondwana, Gondwana Research 28(1), 179-190, Doi:10.1016/j.gr.2014.04.011.

Fourmarier, P., 1914. Le bassin charbonnier d'âge Permo-Triassique de la Lukuga. Ann. Soc. Ge¤ol. Belg., Pub. Rel. Congo belge, 41, C77-C227. URL: https://popups.uliege.be/0037-9395/index.php?id=6583.

Frakes, L.A., Francis, J.E., Syktus, J.l., 1992. Climate Modes of the Phanerozoic. Cambridge University Press, Cambridge, 274p. ISBN: 978-0-521-36627-4

François, C., Baludikay, B.K., Storme, J.Y., Baudet, D., Paquette, J.L., Fialin, M., Javaux, E.J., 2017. Contributions of U-Th-Pb dating on the diagenesis and sediment sources of the lower group (BI) of the Mbuji-Mayi Supergroup (Democratic Republic of Congo). Precambrian Research 298, 202-219. Doi: https://doi.org/10.1016/j.precamres.2017.06.012

Frimmel, H. E., Tack, L., Basei, M. S., Nutman, A. P., Boven, A., 2006. Provenance and chemostratigraphy of the Neoproterozoic West Congolian Group in Democratic Republic of Congo: Journal of African Earth Sciences 46, 221-239. Doi: http://dx.doi.org/10.1016/j.jafrearsci.2006.04.010

Frimmel, H. E., Basei, M. A. S., Gaucher, C., 2011. Neoproterozoic geodynamic evolution of SW-Gondwana: a southern African perspective, International Journal of Earth Sciences, 100, 323-354, Doi: 10.1007/s00531-010-0571-9.

Fritz, H., Abdelsalam, M., Ali, K.A., Bingen, B., Collins, A.S., Fowler, A.R., Ghebreab, W. Hauzenberger, C.A., Johnson, P.R., Kusky, T.M., Macey, P., Muhongo, S., Stern, R.J., Viola, G., 2013. Orogen styles in the East African Orogen: A review of the Neoproterozoic to Cambrian tectonic evolution. Journal of African Earth Sciences 86, 65-106. Doi: https://doi.org/10.1016/j.jafrearsci.2013.06.004

Gerya, T.V., Yuen, D.A., 2003. Characteristics-based marker-in-cell method with conservative finite differences schemes for modelling geological flows with strongly variable transport properties. Physics of the Earth and Planetary Interiors, 140, 293-318. Doi: Doi:10.1016/j.pepi.2003.09.006

Gerya, T.V., Burg, J.P., 2006. Intrusion of ultramafic magmatic bodies into the continental crust: Numerical Simulation. Physics of the Earth and Planetary Interiors 160(2007) 124-42. Doi: Doi:10.1016/j.pepi.2006.10.004

Gerya, T.V., Yuen, D.A., 2007. Robust characteristics method for modelling multiphase visco-elasto-plastic thermo-mechanical problems. Physics of the Earth and Planetary Interiors, 163, 83-105. Doi: https://doi.org/10.1016/j.pepi.2007.04.015

Gerya, T.V., 2010a. Introduction to numerical geodynamic modelling. Book. Cambridge University Press. ISBN 978-0-521-88754-0

Gerya, T.V., 2010b. Dynamical instability produces transform faults at mid-ocean ridges. Science, 329, 1047-1050. Doi: 10.1126/science.1191349

Gerya, T.V., 2013. Three-dimensional thermomechanical modelling of oceanic spreading initiation and evolution. Physics of the Earth and planetary interiors, 214, 35-52. Doi: https://doi.org/10.1016/j.pepi.2012.10.007

Gerya, T.V., Burov, E.T., 2018. Nucleation and evolution of ridge-ridge-ridge triple junctions: Thermomechanical model and geometrical theory. Tectonophysics 746 (2018) pp.83-105. Doi: https://dx-doi.org/10.1016/j.tecto.2017.10.020.

Gerya, T.V., Burov, E.T., 2018. Ridge-ridge-ridge triple junction: failed attemps and “magic” formula. American Geophysical Union, fall meeting 2018, abstract #DI43A-05.

Gerya, T.V., 2019. Introduction to numerical geodynamic modelling. Second edition. Book. Cambridge University Press. ISBN 978-0-521-88754-0

Giresse, P., 2005. Mesozoic-Cenozoic history of the Congo Basin. Journal of African Earth Sciences 43, 301-315. Doi: 10.1016/j.jafrearsci.2005.07.009

Gobbo-Rodrigues, S.R., Coimbra, S.R., Petri, S.R.J.B., 2003. Kwango Series (Congo), Bauru Group (Brazil) and Neuquen Basin (Argentina) ages, based on ostracods and vertebrates. XVIII Congresso Brasiliero de Paleontologia, Brasilia, Brazil, 152-153.

Goldberg, A.S., 2010. Dyke swarms as indicators of major extensional events in the 1.9–1.2 Ga Columbia supercontinent. Journal of Geodynamics, 50 (2010), pp. 176-190. Doi:10.1016/j.jog.2010.01.017

Guillocheau, F., Chelalou, R., Linol, B., Dauteuil, O., Robin, C., Mvondo, F., Callec, Y., Colin, J.-P., 2015. Cenozoic landscape evolution in and around the Congo Basin: Constraints from sediments and planation surfaces. In: De Wit, M., Guillocheau, F., De Wit, M.C.J. (Eds), The Geology and Resource Potential of the Congo Basin. Springer, Berlin, pp. 271-314, Doi: 10.1007/978-3-642-29482-2_14.

Gray, D.R., Foster, D.A., Meert, J.G., Goscombe, B.D., Armstrong, R., Trouw, R.A.J., Passchier, C.W., 2008. A Damara orogen perspective on the assembly of southwestern Gondwana. In: Pankhurst, R.J., Trouw, R.A.J., Brito Neves, B.B., De Wit, M.J. (Eds) West Gondwana: Pre-Cenozoic Correlations across the South Atlantic Region. Geological Society, London, Special Publications, 294, 257–278. Doi:10.1144/SP294.14

Grombein, T., Seitz, K., Heck, B., 2016. The Rock-Water-Ice topographic gravity field model RWI_TOPO_2015 and its comparison to a conventional rock-equivalent version. Surv. Geophys 37(5), 937-976, Doi: 10.1007/s10712-016-9376-0.

Hartley, R.W. and Allen, P.A., 1994. Interior cratonic basins of Africa: relation to continental break-up and the role of mantle convection. Basin Research 6, 65-113. Doi: https://doi.org/10.1111/j.1365-2117.1994.tb00078.x

Heine, C., Zoethout, J., Müller, R.D., 2013. Kinematics of the South Atlantic rift. Solid Earth 4, 215-253. Doi: https://doi.org/10.5194/se-4-215-2013

Heine, C., Müller, R.D., Steinberger, B., Torvisk, T.H., 2008. Subsidence in intracontinental basins due to dynamic topography. Physics of the Earth and Planetary Interiors. 171, 1-4, 252-264. ISSN 0031-9201,https://doi.org/10.1016/j.pepi.2008.05.008.Hirt, C., Rexer, M., 2015. Earth2014: one arc-min shape, topography, bedrock and ice-sheet models – Available as gridded data and degree-10,800 spherical harmonics. Int. J. Appl. Earth Obs. Geoinf. 39, 103-112. Doi: 10.1016/j.jag.2015.03.001.

Hu, J. Faccenda, M., Zhou, Q., Fischer, K.M., Marshak, S, Lundstrom, C., 2018. Modification of the Western Gondwana craton by plume lithosphere interaction. Nat. Geosci. 11, 203–210. Doi: 10.1038/s41561-018-0163-z

Jamotte, A., 1931. Contribution à l'étude géologique du basin charbonnier de la Lukuga. Comité Spécial du Katanga: Annales du Service des Mines, 2, 3-44.

JNOC, 1984. Rapport des investigations géophysiques et géologiques dans la Cuvette Centrale de la République du Zaïre. Japan National Oil Corporation, Report for Department of Mines and Energy, Government of Zaire, Unpublished, 205pp.

Jones, L., Mathieu, P.L. and Strenger, H., 1960. Gravimétrie: Les résultats scientifiques des missions du syndicat pour l'étude géologique et minière de la Cuvette Congolaise et travaux connexes. Ann. Mus. Roy. Congo belge, Tervuren (Belgique), série in-8, Sci. géol. 36, 46pp.

Kaban, M.K., Delvaux, D., Maddaloni, F., Tesauro, M., Braitenberg, C., Petrunin, A., El Khrepy, S., 2021. Thickness of sediments in the Congo Basin based on 1 the analysis of decompensative gravity anomalies. Journal of African Earth Sciences. Doi: https://doi.org/10.1016/j.jafrearsci.2021.104201

Kadima, E.K., 2011. Contribution géophysique à la connaissance du bassin de la Cuvette congolaise. Modélisation de la structure sédimentaire, Mécanisme de subsidence et structure de la lithosphère sous-jacente. PhD thesis, University of Lubumbashi, 278pp.

Kadima, E., Delvaux, D., Sebaganzi, S.M.N., Tack, L., Kabeya, S. M. 2011a. Structure and geological history of the Congo Basin: An integrated interpretation of gravity, magnetic, and reflection seismic data. Basin Research 23, 499-527. Doi: 10.1111/j.1365-2117.2011.00500.x

Kadima, E.K., Sebagenzi, S.M.N., Lucazeau, F., 2011b. A Proterozoic-rift origin for the structure and the evolution of the cratonic Congo Basin. Earth and Planetary Science Letters 304, 240-250. Doi: 10.1016/j.epsl.2011.01.037

Kadima, K.E., Delvaux, D., Everaerts, M., Sebagenzi, S.M.N., Lucazeau, F., 2015. Neoproterozoic to Early Paleozoic sequences of Congo Shield: comparison of Congo Basin with the surrounding marginal basins. In: De Wit, M., Guillocheau, F., De Wit, M.C.J. (Eds), The Geology and Resource Potential of the Congo Basin. Springer, Berlin, pp. 97-109, Doi: DOI 10.1007/978-3-642-29482-2_6

Kaus, B.J.P., Muhlhaus, H., May, D.A., 2010. A stabilization algorithm for geodynamic numerical simulations with a free surface. Physics of the earth and planetary interiors. 181, 12-20. Doi:10.1016/j.pepi.2010.04.007

Kipata, M.L., Delvaux, D., Sebagenzi, M.N., Cailteux, J.-J., Sintubin M., 2013. Brittle tectonic and stress field evolution in the Pan-African Lufilian arc and its foreland (Katanga, DRC): from orogenic compression to extensional collapse, transpressional inversion and transition to rifting. Geologica Belgica 16/1-2, 001-017. ISSN: 1374-8505

Koptev, A., Calais E., Burov E., Leroy S., Gerya T., 2015. Dual continental rift systems generated by plume–lithosphere interaction. Nature Geoscience, 8, 388-392, Doi: 10.1038/NGEO2401.

Koptev, A., Burov, E., Gerya, T., Le Pourhiet, L., Leroy S., Calais, E., Jolivet L., 2018. Plume-induced continental rifting and break-up in ultra-slow extension context: Insights from 3D numerical modeling. Tectonophysics, 746, 121-137. Doi: 10.1016/j.tecto.2017.03.025

Kröner, U., Römer, R.L., 2013. Two plates - Many subduction zones: The Variscan orogeny reconsidered. Gondwana Research 24, 298-329. Doi: 10.1016/j.gr.2013.03.001

Kuribara, Y., Tsunogae, T., Takamura, Y., Tsutsumi, Y., 2018. Petrology, geochemistry, and zircon U-Pb geochronology of the Zambezi Belt in Zimbabwe: Implications for terrane assembly in southern Africa. Geoscience Frontiers 10, 2021-2044, Doi: 10.1016/j.gsf.2018.05.019.

Lawrence, S.R., Makazu, M.M., 1988. Zaire's Central basin: prospectivity outlook. Oil Gas Journal 86(38), 105-108.

Le Gall, B., Tshoso, G., Dyment, J., Kampunzu, A.B., Jourdan, F., Féraud, G., Bertrand, H., Aubourg, C., Vétel, W., 2005. The Okavango giant mafic dyke swarm (NE Botswana): its structural significance within the Karoo large igneous province. Journal of Structural Geology 27, 2234–2255. Doi: 10.1016/j.jsg.2005.07.004

Lepersonne, J., 1945. La stratigraphie du Système du Kalahari et du Système du Karoo au Congo occidental. Bulletin du Service géologique du Congo belge et du Rwanda-Urundi 1, 27-50.

Lepersonne, J. 1974. Carte géologique du Zaïre au 1: 2.000.000 + Notice explicative. Kinshasa, République du Zaïre: Direction de la Géologie/Musée Royal de l'Afrique centrale, Tervuren (Belgique).

Lepersonne, J., 1977. Structure géologique du bassin intérieur du Zaïre. Bulletin de l'Académie royale de Belgique, Classe des Sciences, 5e série, 63(12), 941-965.

Li, Z.X., Bogdanova, S.V., Collins, A.S., Davidson, A., De Waele, B., Ernst, R.E., Fitzsimons, I.C.W., Fuck, R.A., Gladkochub, D.P., Jacoba, J., Karlstrom, K.E., Lu, S., Napatov, L.M., Pease, V., Pisarevsky, S.A., Thrane, K., Vernikovsky, V., 2008. Assembly, configuration, and break-up history of Rodinia: A synthesis. Precambrian Research 160, 179-210. Doi: 10.1016/j.precamres.2007.04.021

Liao, J., Wang, Q., Gerya, T., Ballmer, M.D., 2017. Modeling craton destruction by hydration-induced weakening of the upper mantle. J. Geophys. Res. 122, 7449–7466. Doi: 10.1002/2017JB014157

Lindsay, J.F., 2002. Supersequences, superbasins, supercontinents-evidence from the Neoproterozoic-Early Paleozoic basins of Central Australia. Basin Research 14, 207-223. Doi: 10.1046/j.1365-2117.2002.00170.x

Linol, B. 2013. Sedimentology and sequence stratigraphy of the Congo and Kalahari Basins of south-central Africa and their evolution during the formation and break-up of West Gondwana. PhD thesis, Nelson Mandela Metropolitan University, 375p.

Linol, B., De Wit, M.J., Guillocheau, F., Robin, C., Dauteuil, O., 2015a. Multiphase Phanerozoic subsidence and uplift history recorded in the Congo Basin: a Complex successor basin. In: De Wit, M., Guillocheau, F., De Wit, M.C.J. (Eds). The Geology and Resource Potential of the Congo Basin. Springer, Berlin, pp. 213-227, Doi: 10.1007/978-3-642-29482-2_11.

Linol, B., De Wit, M.J., Bartoon, E., Guillocheau, F., De Wit, M.C.J., Colin, J.P., 2015b. Paleogeography and tectono-stratigraphy of Carboniferous-Permian and Triassic 'Karoo-like" sequences of the Congo Basin In: De Wit, M., Guillocheau, F., De Wit, M.C.J. (Eds), The Geology and Resource Potential of the Congo Basin. Springer, Berlin, pp. 111-134, 111-134, Doi: 10.1007/978-3-642-29482-2_7.

Linol, B., De Wit, M.J., Barton, E., Guillocheau, F., De Wit, M.C.J., Colin, J.P., 2015c. Facies analyses, chronostratigraphy and Paleo-environmental reconstructions of Jurassic to Cretaceous sequences of the Congo Basin. In: De Wit, M., Guillocheau, F., De Wit, M.C.J. (Eds). The Geology and Resource Potential of the Congo Basin. Springer, Berlin, pp. 135-162, 135-161, Doi: 10.1007/978-3-642-29482-2_8.

Linol, B., De Wit, M.J., Milani, E.J., Guillocheau, F., Scherer, C., 2015d. New Regional Correlations between the Congo, Parana´ and Cape-Karoo Basins of Southwest Gondwana. In: De Wit, M., Guillocheau, F., De Wit, M.C.J. (Eds). The Geology and Resource Potential of the Congo Basin. Springer, Berlin, pp. 245-270, Doi: 10.1007/978-3-642-29482-2_13.

Linol, B., De Wit, M.J., Guillocheau, F., De Wit, M.C.J., Anka, Z., Colin, J.-P., 2015e. Formation and collapse of the Kalahari Duricrust ['African Surface'] across the Congo Basin, with implications for changes in rates of Cenozoic offshore sedimentation. In: De Wit, M., Guillocheau, F., De Wit, M.C.J. (Eds). The Geology and Resource Potential of the Congo Basin. Springer, Berlin, pp. 193-212, Doi: 10.1007/978-3-642-29482-2_10.

Linol, B., De Wit, M.J., Barton, E., De Wit, M.C.J., Guillocheau, F., 2016. U–Pb detrital zircon dates and source provenance analysis of Phanerozoic sequences of the Congo Basin, central Gondwana. Gondwana Research 29, 208-219. Doi: 10.1016/j.gr.2014.11.009

Liu, J., Graham Pearson, D., Wang, L.H., Mather, K.A., Kjarsgaard, B.A., Schaeffer, A.J., Inrvine, G.J, Kopylova, M.G., Armstrong, J.P. 2021. Plume-driven recratonization of deep continental lithospheric mantle. Nature. Vol.592. Doi: https://doi.org/10.1038/s41586-021-03395-5

Lombard, A.L., 1961. La série de la Haute-Lueki (partie orientale de la cuvette congolaise). Bulletin de la Société belge de Géologie, de Paléontologie et d'Hydrologie 70, 65-72.

Lucazeau, F., Armitage, J., Kadima, E.K., 2015. Thermal regime and evolution of the Congo Basin as an intracratonic basin. In: De Wit, M., Guillocheau, F., De Wit, M.C.J. (Eds). The Geology and Resource Potential of the Congo Basin. Springer, Berlin, pp. 229-224, Doi: 10.1007/978-3-642-29482-2_12. Doi: 10.1007/978-3-642-29482-2_12

Macgregor, D., 2015. History of the development of the East African Rift System: A series of interpreted maps through time. Journal of African Earth Sciences 101, 232–252. Doi: 10.1016/j.jafrearsci.2014.09.016

Maddaloni, F., Braitenberg, C., Kaban, M.K., Tesauro, M., Delvaux, D., (2021a). The Congo Basin: Subsurface structure interpreted using potential field data and constrained by seismic data. Global and Planetary Change. (in press)

Maddaloni, F., Pivetta, T.F., Braitenberg, C. (2021b). Gravimetry and petrophysics for defining the intracratonic and rift basins of the western-central Africa zone. Geophysics. Doi: 10.1190/geo2019-0522.1

Martin-Monge, A., Baudino, R., Gairifo-Ferreira, L.M., Tocco, R., Badali, M., Ochoa, M., Haryono, S., Soriano, S., El Hafiz, N., Hernan-Gomez, J., Chacon, B., Brisson, I., Grammatico, G., Varade, R., Abdallah, H., 2016. An unusual Proterozoic petroleum play in Western Africa: the Atar Group carbonates (Taoudeni Basin, Mauitania). In: Sabato Ceraldi, T., Hodgkinson, R.A., Backe, G. (Eds) Petroleum Geoscience of the West Africa Margin. Geological Society, London, Special Publications 438. Doi: 10.1144/SP438.5

Martins, C. M., Barbosa, V. C. F., Silva, J. B. C. (2010). Simultaneous 3D depth-to-basement and density-contrast estimates using gravity data and depth control at few points. Geophysics, 75(3), XI21-I28. Doi:10.1190/1.3380225.

Master, S., 2010. Lac Télé structure, Republic of Congo: Geological setting of a cryptozoological and biodiversity hotspot, and evidence against an impact origin. Journal of African Earth Sciences 58, 667–679. Doi:10.1016/j.jafrearsci.2009.07.017

Milani, E.J., De Wit, M.J., 2008. Correlations between the classic Paraná and Cape–Karoo sequences of South America and southern Africa and their basin infills flanking the Gondwanides: du Toit revisited. Geological Society, London, Special Publications 294, 319-342. Doi: 10.1144/SP294.17.

Mitchell, R.N., Zhang, N., Salminen, J., Liu, Y., Spencer, C.J., Steinberger, B., Murphy, B.J., Li, Z.X. 2021.The Supercontinent cycle. Nature. Earth and Environment. Doi: 10.1038/s43017-021-00160-0

Nance, R.D., Murphy, J.B., Santosh, M. 2013. The supercontinent cycle: a retrospective essay. Gondwana Research 25 (2014) 4-29. Doi: 10.1016/j.gr.2012.12.026

Ojo, A.O., Weisen, S., Ni, S., Zhao, L., Xie, J., Kao, H., 2020. Lithospheric Structure of Africa and Surrounding Regions Revealed by Earthquake and Ambient Noise Surface Wave Tomography. Doi: 10.1002/essoar.10504718.1

Passau, G., 1923. La géologie du bassin des schistes bitumineux de Stanleyville (Congo belge). Ann. Société géologique de Belgique. Publ. Rel. Congo belge 45, 91-243.

Pasyanos, M.E., Nyblade, A.A, 2007. A top to bottom lithospheric study of Africa and Arabia. Tectonophysics, Volume 444, Issues 1–4, 2007, Pages 27-44, ISSN 0040-1951. Doi: 10.1016/j.tecto.2007.07.008.

Pedrosa-Soares, A.C., Alkmim, F.F., Tack, L., Noce, C.M., Babinski, M., Silva, L.C., Martins-Neto, M.A., 2008. Similarities and differences between the Brazilian and African counterparts of the Neoproterozoic Araçuaí-West Congo orogeny. Geological Society, London, Special Publications 294, 153-172. Doi: 10.1144/SP294.9

Perron, P., Guiraud, M., Vennin, E., Moretti, I., Portier, É. Le Pourhiet, L. and Konaté, M.: Influence of basement heterogeneity on the architecture of low subsidence rate Paleozoic intracratonic basins (Reggane, Ahnet, Mouydir and Illizi basins, Hoggar Massif), Solid Earth, 9(6), 1239-1275, Doi: 10.5194/se-9-1239-2018, 2018.

Perron, P., Le Pourhiet, L., Guiraud, M., Vennin, E., Moretti, I., Portier, É. and Konaté, M. 2020: Control of inherited accreted lithospheric heterogeneity on the architecture and the low long-lived subsidence rate of intracratonic basins, BSGF - Earth Sciences Bulletin, Doi: 10.1051/bsgf/2020038, 2020.

Phillips, B.R., and Bunge, H.-P., 2007. Supercontinent cycles disrupted by strong mantle plumes. Geology, 35, 846-850. Doi: 10.1130/G23686A.1

Pivetta, T., Braitenberg, C., 2020. Sensitivity of gravity and topography regressions to earth and planetary structures. Tectonophysics 774, 228-299, Doi: 10.1016/j.tecto.2019.228299.

Poidevin, J.-L., 1985. Le Protérozoïque supérieur de la République Centrafricaine. Ann. Mus. Royal Afrique Centrale, Tervuren (Belgique), Série in-8°, Sc. géol. 91, 75p.

Poudjom, Y.H.D., O'Reilly, S.Y., Griffin, W.L., Morgan, P., 2001. The density structure of subcontinental lithosphere through time. Earth and Planetary Science Letters 184 (2001) 605-621. Doi: 10.1016/S0012-821X (00)00362-9

Ranalli, G., 1995. Rheology of the Earth. Chapman & Hall. London. ISBN: 978-0-412-54670-9

Raucq, P., 1957. Contribution à la connaissance du Système de la Bushimay. Ann. Mus. Royal Congo Belge, Tervuren (Belgique), Série in-8°, Sc. géol. 18, 427p.

Raucq, P., 1970. Nouvelles acquisitions sur le système de la Buchimay (Republique Demotratique du Congo). Ann. Mus. Royal Congo Belge, Tervuren (Belgique), Série in-8°, Sc. géol. 69, 156p. INIST: GEODEBRGM722242061

Raveloson, A., Nyblade, A., Fishwick, S., Mangongolo, A., Master, S., 2015. The Upper Mantle Seismic Velocity Structure of South-Central Africa and the Seismic Architecture of Precambrian Lithosphere beneath the Congo Basin, in: De Wit, M.J., Guillocheau, F., De Wit, M.C.J. (Eds.), Geology and Resource Potential of the Congo Basin. Springer Berlin Heidelberg, Berlin, Heidelberg, pp. 3–18. Doi: 10.1007/978-3-642-29482-2_1

Raveloson A., Nyblade A., Durrheim R. 2021. Joint inversion of surface wave and gravity data reveals subbasin architecture of the Congo Basin. Geology. Doi: https://doi.org/10.1130/G48408.1

Rexer, M., Hirt, C. Claessens, S., Tenzer, R., 2016. Layer-Based Modelling of the Earth's Gravitational Potential up to 10-km Scale in Spherical Harmonics in Spherical and Ellipsoidal Approximation. Surv in Geophy 37, Doi: 10.1007/s10712-016-9382-2.

Roberts, E.M., Jelsma, R. E., Hegna, T.A., 2015. Mesozoic sedimentary cover sequences of the Congo Basin in the Kasaï Region, Democratic Republic of Congo. In: De Wit, M., Guillocheau, F., De Wit, M.C.J. (Eds). The Geology and Resource Potential of the Congo Basin. Springer, Berlin, pp. 163-191, Doi: 10.1007/978-3-642-29482-2_9.

Rooney, A.D., Selby, D., Houzay, J.-P., Renne, P.R., 2010. Re-Os geochronology of a Mesoproterozoic sedimentary succession, Taoudeni basin, Mauritania: Implications for basin-wide correlations and Re-Os organic-rich sediments systematics. Earth and Planetary Science Letters 289, 486-496. Doi: 10.1016/j.epsl.2009.11.039

Sachse, V.F, Delvaux, D., Littke, R., 2012. Petrological and geochemical investigations of potential source rocks of the Central Congo Basin, DRC. AAPG bulletin 96 (2), 277-300. Doi: 10.1306/07121111028

Santiago, R., de Andrade Caxito, F., Neves, M.A., Dantaz, E.L., de Medeiros Junior, E.B., Queiroga, G.N., 2020. Two generations of mafic dyke swarms in the Southeastern Brazilian coast: reactivation of structural lineaments during the gravitational collapse of the Araçuaí-Ribeira Orogen (500 Ma) and West Gondwana breakup (140 Ma). Precambrian Research 340, 105344. Doi: 10.1016/j.precamres.2019.105344

Saha-Fouotsa, A.N., Vanderhaeghe, O., Barbey, P., Eglinger, A., Tchameni, R., Zeh, A., Fosso Tchunte, P., Negue Nomo, E., 2019. The geologic record of the exhumed root of the Central African Orogenic Belt in the central Cameroon domain (Mbé – Sassa-Mbersi region). Journal of African Earth Sciences 151 286-314, Doi: 10.1016/j.jafrearsci.2018.12.008.

Schmeling, H., 1987. On the relation between initial condition and late stages of Rayleigh-Taylor instabilities. Tectonophysics, 133, 65-80. Doi: 10.1016/0040-1951(87)90281-2

Schmeling, H., Babeyko, A. Y., Enns, A., Faccenna, C., Funiciello, F., Gerya, T.V., Golabeck, G.J., Grigull, S., Kaus, B.J.P., Morra, G., Schmalholz, S.M., van Hunen, J., 2008. A benchmark comparison of spontaneous subduction models – towards a free surface. Physics of the Earth and Planetary Interiors, 171, 198-223. Doi: https://doi.org/10.1016/j.pepi.2008.06.028

Scotese, C.R., Boucot, A.J., Mckerrow, W.S., 1999. Gondwanan paleogeography and paleoclimatology. Journal of African earth Sciences 28(1), 99-114. Doi: 10.1016/S0899-5362(98)00084-0

Sebai, A., Stutzmann, E., Montagner, J.P., Sicilia, D., Beucler, E., 2006. Anisotropic structure of the African upper mantle from Rayleigh and Love wave tomography, 14 April 2006, Pages 48-62 Doi: 10.1016/j.pepi.2005.09.009

Sinha, S. T., Saha, S., Longacre, M., Basu, S., Jha, R., Mondal, T., 2019. Crustal architecture and nature of continental breakup along a transform margin: New insights from Tanzania-Mozambique margin. Tectonics 38, Doi: 10.1029/2018TC005221.

Smithson, S.B., 1971. Densities of metamorphic rocks. Geophysics 36(4), 690-694. Doi: 10.1190/1.1440205

Stein, C.A., S. Stein, M. Merino, G. Randy Keller, L.M. Flesch, D.M. Jurdy. (2014). was the Midcontinent Rift part of a successful seafloor-spreading episode? Geophys. Res. Lett., 41 (5), pp. 1465-1470. Doi: 10.1002/2013GL059176

Stein, S. , C.A.; R. Elling, J. Kley, G.R. Keller, M. Wysession, T. Rooney, A. Frederiksen, R. Moucha. (2018). Insights from North America's failed Midcontinent Rift into the evolution of continental rifts and passive continental margins. Tectonophysics, 744, pp. 403-421. Doi: 10.1016/j.tecto.2018.07.021

Straathof, G.B., 2011. Neoproterozooic low latitude glaciations: an African perspective. PhD thesis, University of Edinburg, 285p. URI: http://hdl.handle.net/1842/9607

Taverne, L. (1975a). A propos de trois Téléostéens Salmoniformes du Crétacé inférieur (Wealdien) du Zaïre, précédemment décrits dans les genres Leptolepis et Culpavus (Pisces Teleostei). Rev. Zool. Afr. 89, 481-504.

Taverne, L. (1975b). Etude ostéologique de Leptolepis caheni, Téléostéen fossile du Jurassique supérieur (Kimméridgien) de Kisangani (ex-Stanleyville, Zaïre) précédemment décrit dans le genre Paraclupavus. Rev. Zool. Afr. 89, 821-853.

Torsvik TH, Cocks LR, 2011. The Paleozoic paleogeography of central Gondwana. In: Van Hinsbergen, D.J., Buiter, S.J.H., Torsvik, T.H., Gaina, C., Webb, S.J. (eds).The formation and the evolution of the Africa: a synopsis of 3.8 Ga of earth history. Geological Society, London, Special publications 357, 137-166. Doi: 10.1144/SP357.8

Torsvik, T.H., Cocks, L.R., 2013. Gondwana from top to base in space and time. Gondwana Research 24, 999-1030. Doi: 10.1016/j.gr.2013.06.012

Toteu, S.F., Penaye, J., Poudjom Djomani, Y., 2004. Geodynamic evolution of the Pan-African belt in central Africa with special reference to Cameroon. Can. J. Earth Sci. 41, 73–85. Doi : 10.1139/E03-079

Trompette, R., 1973. Le Précambrien supérieur et le Paléozoïque inferieur de l'Adrar de Mauritanie (bordure occidentale de Bassin de Taoudeni, Afrique de l'Oust). Un exemple de sédimentation de craton. Etude stratigraphique et sédimentologique. Travaux des laboratoires des Sciences de la Terre St.-Jérome, Marseille B-7, 702.

Trouw, R.A.J., De Wit, M.J., 1999. Relation between the Gondwanide Orogen and contemporaneous intracratonic deformation. Journal of African Earth Sciences 28, 203–213.

Uieda, L., V. Barbosa, and C. Braitenberg (2016), Tesseroids: Forward-modeling gravitational fields in spherical coordinates, Geophysics, F41-F48, Doi:10.1190/geo2015-0204.1.

Veach, A.C., 1935. Evolution of the Congo Basin. Mem. Geol. Soc. Am., 3, 184p.

Verbeek, T., 1970. Géologie et lithologie du Lindien (Précambrien Supérieur du nord de la République Démocratique du Congo). Ann. Mus. Roy. Afr. Cent., Tervuren (Belgique), série in-8, Sci. géol., 66, 311p.

Watts, A.B. (2001), Isostasy and flexure of the lithosphere. Cambridge University Press, Cambridge ; New York. ISBN: 978-0-521-62272-1 978-0-521-00600-2

Watts, A.B., Tozer, B., Daly, M.C., Smith, J. 2018. A comparative study of the Parnaíba, Michigan and Congo cratonic basins. In: Daly, M.C., Fuck, R.A., Julià, J., Macdonald, D.I.M., Watts, A.B. (Eds) Cratonic Basin Formation: A Case Study of the Parnaíba Basin of Brazil. Geological Society, London, Special Publications, 472. Doi: 10.1144/SP472.6

Weinberg, R.B., Schmeling, H., 1992. Polydiapirs: multiwavelength gravity structures. Jurnal of Structural Geology, 14, 425-436.

Wopfner, H., 1999 The Early Permian deglaciation event between East Africa and northwestern Australia. Journal of African earth Sciences 29(1), 77-90.

Dedication

“ … Je n'ai pas peur de la route
Faudrait voir, faut qu'on y goûte
Des méandres au creux des reins
Et tout ira bien là
Le vent nous portera … ”

“*Le vent nous portera*”, *album:* “*Des visages des figures*”, *The Noir Désir*, *2001*.

Con i versi di una canzone della band francese Noir Désir voglio cominciare l’ultima sezione di questo mio lavoro di tesi di dottorato, espressione massima di ciò che è stato il mio progetto di ricerca scientifica, nonché il riassunto di quasi quattro anni continui di duro lavoro, perseveranza e sacrifici. Di questo periodo ho amato soprattutto poter viaggiare e vivere all’estero non come una semplice turista, ma come una vera e propria ricercatrice: confrontando il mio lavoro con altri colleghi della comunità scientifica, creando “ponti” fra le persone e mettendomi in gioco durante i convegni a cui ho partecipato, mostrando metodologie di indagine e risultati ottenuti interessanti ed alternativi. Negli anni di dottorato quindi posso dire di aver amato la città di Bruxelles per i suoi Jazz Clubs, i boschi, i musei, le case in stile fiammingo e le corse mattiniere intorno l’immenso parco del Royal Museum of Central Africa nella quale lavoravo. Di Zurigo invece ho amato follemente tutte le attività culturali promosse in collaborazione con il Politecnico (*ETH-Z*), le passeggiate lungo il lago, i tuffi nel Limmat in autunno ma soprattutto il folto gruppo di ricerca internazionale con la quale collaboravo. Porterò sempre nel cuore l’amicizia con i miei due colleghi di ufficio Antonio e Daniela e tutte le risate che uno spagnolo, una portoghese ed un’italiana possono aver fatto.

Con questo manoscritto dunque, concludo il mio percorso accademico, un capitolo di vita inevitabilmente molto lungo ed intenso. Nell’arrivare fino a qui però di certo non sono stata sola ma anzi, devo ammettere che sono talmente tante le persone incontrate e conosciute con cui ho condiviso momenti splendidi, che metterle per iscritto tutte forse non basterebbero altre cento pagine. Pertanto, mi limiterò a ringraziare dedicando queste parole a tutti coloro che negli ultimi tempi hanno avuto la pazienza di aiutarmi, ascoltarmi e sostenermi. Gli anni di pandemia globale infatti sono stati veramente difficili da affrontare, non solo dal punto di vista lavorativo ma anche psicofisico. Ciononostante, si può dire di essere ancora qui per superarli e raccontarli, con la speranza di poter andare avanti ricordando ed imparando sia dai momenti belli, che dagli errori o i torti commessi e subiti.

Arrivata al termine di questo progetto di dottorato di ricerca quindi, ringrazio in primis la mia famiglia: mia nonna Maria, mia madre Rossana, mio padre Vitaliano e mio fratello Giovanni, i quali hanno sempre sostenuto le mie scelte e supportato le mie idee, soprattutto quando sembravano assurde, eclettiche o bizzarre. Insieme a loro non posso che non coinvolgere anche le mie due “bestiole” con cui ormai convivo da due anni

e che si sono aggiunte come nuovi membri familiari: la mia gatta Moho e la mia cagna Airy, le amo immensamente. A tal proposito quindi ringrazio Deborah ed Alessandro per la pazienza, i consigli e la loro presenza soprattutto quando Airy era una cucciola esuberante. Con loro non mi sono mai sentita sola, soprattutto durante il periodo di piena pandemia.

Ringrazio poi i miei colleghi Alberto Pastorutti e Tommaso Pivetta, nonché Federico Morsut con cui non solo ho condiviso lo studio e il lavoro in team, ma anche momenti di amicizia fraterna e riflessioni. I loro consigli e le loro intuizioni sono stati di grande aiuto durante il tutto il periodo trascorso insieme. Ricorderò sempre con affetto i nostri "*venerdì del collega*" davanti ad un bel bicchiere fresco di birra o di spritz bianco.

Dedico poi questo lavoro a tutte le amicizie mantenute, incontrate e ritrovate nel tempo, sia vivendo a Trieste, che durante il periodo di missioni all'estero trascorso tra il Belgio e la Svizzera. In particolare quindi, dedico questo progetto di tesi ad Andrea B., caro amico con cui spero di tornare a viaggiare presto per mari e monti al suono di canzoni revival anni 70',80' e 90'. Insieme a lui mando un pensiero a tutti gli amici piemontesi che mi aspettano ogni volta che torno a casa. A tal proposito quindi, ringrazio Matteo S., Fabio P. e Luca G. unitamente agli amici laziali Luca A., Damiano B., Gabriele B. e Alessandro DL., per le chiacchierate serali quotidiane su "Discord", i film guardati insieme e le discussioni "*nerd*" portate avanti per giorni. Unitamente a loro ringrazio di cuore i miei amici e amiche veneto-friulane-giuliane: Alessandra V., Barbara B., Daniela C., Giulia V., Francesca I., Gabriele P., Gaia P., Irene R., Maddalena S., Massimiliano "Max" S., Silvia M., Simona D.N. e Valentina C., per la loro amicizia e tutti i momenti speciali che mi hanno fatto vivere da quando le conosco. Insieme a loro dedico un ringraziamento anche alla mia insegnante di "ginnastica metabolica" Susanna V., per avermi ascoltata e motivata durante periodi in cui era il momento di fare scelte di vita importanti. A tal proposito quindi aggiungo anche la dottoressa Barbara W., terapeuta eccellente la quale mi ha aiutato a superare tutte le difficoltà che il 2020 è stato in grado di farmi vivere. Dedico poi questo lavoro anche a Lorenzo V., una nuova amicizia del tutto inaspettata, incontrata casualmente in un giorno di esami universitari, che poi era anche il mio compleanno. Senza di lui le festività trascorse in questi ultimi tempi di lockdown e pandemia, sarebbero state decisamente più tristi e sole. Grazie anche all'artista romano Federico Russo per aver disegnato la copertina di questa tesi.

Ai the Cure, Smashing Pumkins, Editors, Zen Circus, Noir Desir e i Depeche Mode. Al Golden Virginia (giallo), il buon vino e la mia fantastica Fujifilm x100F, i quali sono stati tutti degli ottimi strumenti di concentrazione e terapia.

Ad A. Fania, amore immenso dei miei 30 anni, conosciuto in una sera di pioggia e ritrovato dopo un pomeriggio di sole. "…*Tout disparaîtra, mais le vent nous portera"*.